Construction of Semiconductor-Based Photosystem for CO_2 Reduction and Water Oxidation towards Artificial Photosynthesis

（人工光合成を目指した半導体光触媒による CO_2 還元および酸素生成に関する研究）

Hong Pang

Functional Materials Chemistry Unit

Graduate School of Chemical Sciences and Engineering

Hokkaido University

2019

CONTENTS

Abstract

Mimicking the natural plant, artificial photosynthesis offers a promising strategy to close the carbon cycle on the earth. Involved with the challenging CO_2 fixation over Photosystem I and the sluggish water oxidation over Photosystem II, the processes do not occur readily. Zinc sulfide (ZnS) and the photosynthetic membrane protein are regarded as the most promising catalysts for CO_2 reduction reaction (CO_2RR) and oxygen evolution reaction (OER) for their negative conduction band and high turnover frequency (TOF), respectively. However, previous efforts have demonstrated the superior CO_2RR activity of colloidal ZnS nanocrystals and the OER activity of *Photosystem II* but their performance is limited by light absorption. Furthermore, the active sites and reaction mechanism are worth deep understanding for future materials design. Thus, this thesis focused on constructing half reactions of CO_2RR and OER using visible-light responsive photocatalysts with an emphasis on the active site-regulated CO_2RR process.

In chapter 1, an overview of artificial photosynthesis and the semiconductor-based photocatalysis are introduced. The general principle for designing the photocatalysts for CO_2RR and OER are given. The chapter also briefly summarized the development and application of zinc sulfides in hydrogen evolution reaction (HER) and CO_2RR in the past years. Several commonly used strategies for constructing efficient CO_2RR and the *Photosystem II*-based systems are also briefly reviewed.

In chapter 2, well-designed colloidal Cu-doped ZnS (ZnS:Cu) nanocrystals were synthesized and operated as a promising visible-light-responsive photocatalyst in all-inorganic reaction system. Two functional elements, Cu and Cd, are respectively used as dopant and cocatalyst of ZnS nanocrystal for selective CO_2 reduction. Cu doping expands the photoabsorption of ZnS into visible light region and the simultaneous Cd^{2+} surface modification significantly improves the activity of CO_2RR with 99% formic acid selectivity.

In chapter 3, aqueous colloidal Ni-doped ZnS (ZnS:Ni) nanocrystals were constructed as another

excellent photocatalyst for CO_2RR into formate under solar light irradiation and as a case study to investigate the interplay between Ni doping and sulfur vacancies. It is revealed that the abundant sulfur vacancies and extended visible light absorption of the constructed colloidal ZnS:Ni nanocrystals contribute to the prominent performance for CO_2RR; excessive doping of Ni does not guarantee an increase of photocatalytic CO_2RR due to a diminish of sulfur vacancies.

In chapter 4, the mechanism by which the colloidal ZnS nanocrystals loaded with Cd^{2+} induced a remarkable enhancement in the selective production of formate was investigated. We present the spectroscopic evidence of the Cd status using the X-ray absorption fine structure (XAFS) and electron behaviors associated with sulfur vacancies, deep dopants and surface Cd sites by photoluminescence (PL) spectroscopy and transient absorption spectroscopy (TAS). *Ab initio* calculations reveal that a higher density of states near band-edge from Cd s orbital accounts for the favorable charge transfer and disclose the pathways during CO_2 activation and reduction, together with the *in situ* attenuated total reflectance-infrared (ATR-IR) spectroscopic observation.

In chapter 5, cation vacancy-rich ZnS was constructed to create Zn vacancies (V_{Zn}) as active sites instead of the anion vacancies for CO_2RR on the surface while reserving the charge transport capability in the bulk. With no co-catalyst, the ZnS acquired a high selectivity of formate production (> 85%). *In situ* attenuated total reflection-infrared (ATR-IR) spectroscopy and first-principle calculations have been used to elucidate the pathways of CO_2RR into formate and prove the surface V_{Zn} as favorable active sites by greatly lowering the barrier of the CO_2RR process and precluding the proton adsorption, clarifying the origin of the highly selective CO_2RR into formate in the presence of competitive hydrogen evolution reaction (HER).

In chapter 6, a bio-hybrid photoanode of a photosynthetic membrane protein (*Photosystem II*), the exclusive photosynthetic complex responsible for OER were fabricated on mesoporous WO_3 film for water oxidation. The *Photosystem II* membrane proteins have been communicated with the WO_3 electrode in the absence of any soluble redox mediators and sacrificial reagent under the solar spectrum even to 700 nm and

a maximum incident photon-to-current conversion efficiency (IPCE) reaches 15.24% at 400 nm. This work represents a preliminary effort towards construction of the monoclinic artificial photosynthetic leaf.

In chapter 7, an overall summary and the future prospects of this dissertation work are presented. This thesis carried out a systematic study on the half reactions of CO_2RR and OER over "Photosystem I" and "Photosystem II", respectively. Doping effect, surface vacancies and isolated co-catalyst are demonstrated of great significance on the photocatalytic CO_2RR activity over ZnS photocatalyst; their impacts are disclosed experimentally and theoretically, deepening the understanding of the CO_2RR pathways. Initial efforts on OER are also paid on constructing *Photosystem II*| mesoporous WO_3 film as the other segment of one monoclinic artificial leaf. This study potentially provides new inspirations for facile synthesis and rational design of more efficient photocatalysts towards artificial synthesis in the future research.

Chapter 1 Introduction

1.1 Overview of artificial photosynthesis

Ever increasing global warming and energy crisis have been two major issues all over the world in recent decades.[1, 2] The excessive exploration and utilization of fossil fuels lead to the shortage and depletion of the natural resources at a far greater pace.[3-5] The sun, winds, tides, biomass and other power from nature have been increasingly recognized as the new energy by scientists and a growing number of research projects were invested to convert the natural energy to electricity and value-added feedstocks.[6, 7] Because of the infinite reservoir and environmental beingness of solar energy, huge strides have been taken to develop the solar-driven systems making use of sunlight to close the carbon cycles.[8-10] However, as the low conversion efficiency and the high cost to satisfy sufficient supply, the research to construct the artificial leaves and mimic the green plant or algae factory are still faced with great challenges.[11]

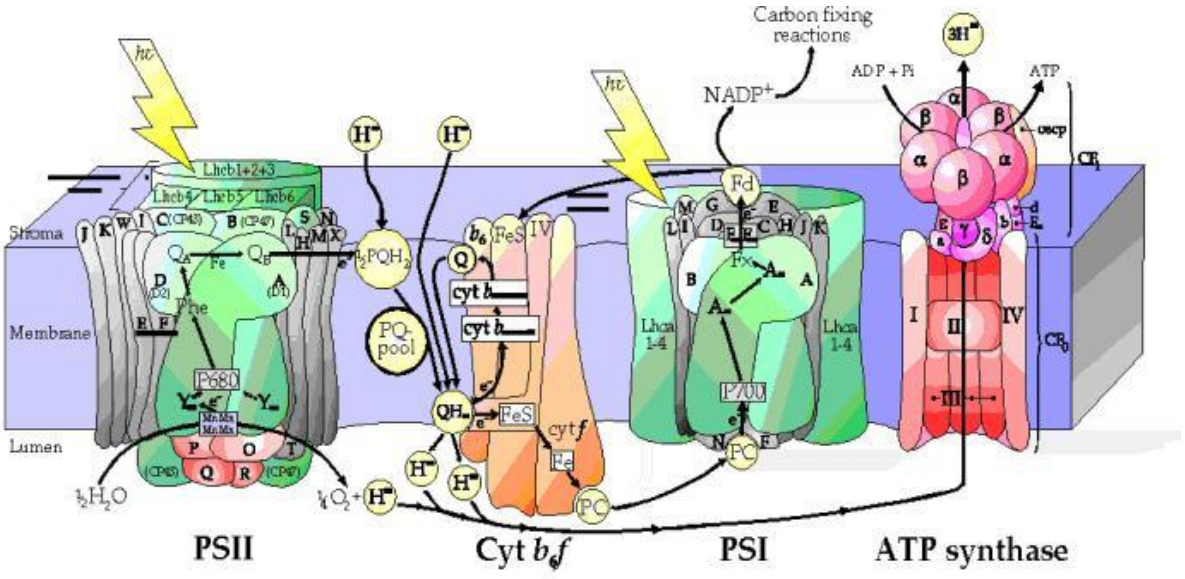

Figure 1.1 Architecture and mechanism of the photosynthetic apparatus[12]

Since Honda and Fujishima discovered the water photolysis over TiO_2 electrode under UV,[13] "artificial photosynthesis" using sunlight as energy source through photocatalytic or photoelectrochemical reactions has witnessed a long journey of developments. Basically, the photocatalytic and photoelectrochemical reactions are analogous in terms of the widely accepted three stages, namely light absorption, charge separation and surface redox reactions.[14] Upon illumination with photon energy larger than the bandgap, the photogenerated electrons are excited from the valence band to conduction band; then the electrons and holes migrate to the different places on the surface of photocatalyst; the oxidative and reductive reactions take place with the holes and electrons, respectively given that the valence band and conduction band has sufficient chemical potentials for each reaction. However, during this procedure, severe recombination of charge carriers usually occurs, leading to a low efficiency of the photocatalytic reaction, which raises the highest concern in such reactions. Therefore, in terms of the steps mentioned above, photocatalytic researchers aim at enhancing the light absorption, charge migration and separation as well as the favorable thermodynamics and kinetics in redox reactions.[14]

The photocatalytic researches are mainly in the following fields: i) photo-degradation of volatile organic compounds (VOC); ii) artificial photosynthesis (water splitting, carbon/nitrogen fixation); iii) photoelectrochemical conversion; iv) self-cleaning and photo-induced superhydrophilicity.[14] Note that from the view of thermodynamics, except the reaction i) and iv) which can proceed spontaneously with negative change in Gibbs free energy ($\Delta G<0$), the ii) and iii) are involved with uphill reactions ($\Delta G>0$) that necessitate extra driving force.[15] To mimic the natural photosynthetic apparatus as shown in Figure 1.1, which are consisted "Photosystem I" for CO_2 reduction and of "Photosystem II" for water oxidation, the research in ii) and iii) are worth investigating to construct the artificial leaves.

The ultimate goal of the artificial photosynthesis is to drive the standalone artificial leaves with sunlight as the sole input energy to produce hydrocarbons. Towards a sustainable overall process, a complete photosynthetic system should couple the Photosystem I with Photosystem II, which means

to couple the subsystem for CO_2 reduction

$$CO_2 + 2\ e^- \rightarrow CO + 1/2\ O_2$$

with subsystem for H_2O oxidation

$$H_2O + 2\ h^+ \rightarrow 1/2\ O_2 + 2\ H^+$$

Actually, the ultimate products of CO_2 reduction are beyond CO to liquid products or multi-carbon fuels.[16] One system that can carry out both CO_2 reduction and water oxidation is ideal. But as either reaction requires great barrier to overcome, few semiconductors have the sufficiently large bandgap that can straddle the redox potentials. To solve this issue, Z-scheme model was proposed to couple two light-absorbing components for separate CO_2 reduction and water oxidation in Figure 1.2.[17] Figure 1.2a presents the Z-scheme electron transfer in the natural photosynthetic apparatus and Figure 1.2b presents an example to mimic the Z-scheme approach using metal sulfides as "Photosystem I" for reduction reactions and oxides as "Photosystem II" for water oxidation. The conductive reduced graphene oxide (RGO) undertakes the function for electron transfer between "Photosystem I" and "Photosystem II". However, involved with the challenging CO_2 fixation over "Photosystem I" and the sluggish water oxidation over "Photosystem II", even the realization of the half reaction does not occur readily. The activation of the reactant species, the charge transfer, the light absorption, etc. make the half reaction more complicated than a problem of thermodynamic issue. Therefore, before constructing a monoclinic artificial leaf, the in-depth studies and rational design of the half reactions are imperative. In this thesis, both half reactions of CO_2 reduction and water oxidation using visible-light responsive photocatalysts are investigated and constructed as a step towards future artificial photosynthesis.

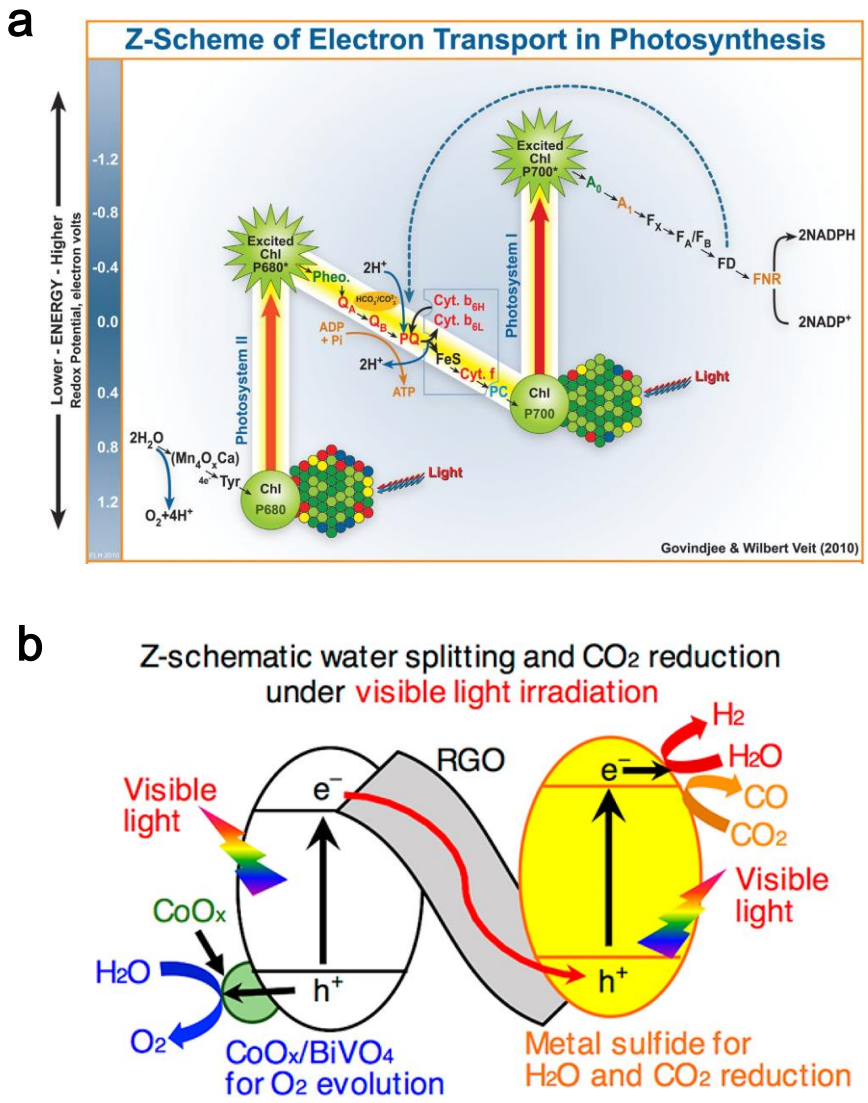

Figure 1.2 (a) The Z-Scheme for electron transport from water-$NADP^+$ in photosynthesis. There are two Photosystems—Photosystem I (PS I) and Photosystem II (PS II) connected in series.[18] (b) Z-scheme system for water splitting consisting of a Pt-loaded metal sulfide photocatalyst and an RGO-CoO_x/$BiVO_4$ composite photocatalyst.[17]

1.2 "Photosystem I" for CO_2 reduction

There are several solar-driven pathways to convert CO_2 to chemicals including biocatalysis,[19] photoelectrocatalysis, photothermocatalysis[20] and photocatalysis[14, 21]. Either biocatalysis,

photoelectrocatalysis or photothermocatalysis entails other external supplies like biomass, electric bias and heat. In contrast, photocatalysis is more cost-effective and facile to operate without any other energy consumption except solar energy. In this thesis, photocatalysis are solely discussed for CO_2 reduction.

1.2.1 Fundamental principles of photocatalytic CO_2 reduction

Intrinsically, CO_2 is a molecule of highly stability with two symmetric C=O bonds in a short line based on the fact that breaking the initial carbonyl bond in CO_2 requires a quite high energy of ~ 750 kJ/mol[22, 23]. The carbon atom in CO_2 molecule occupies the highest valence so that there are a variety of reduced products in different oxidation states ranging from reported gaseous carbon monoxide (CO), methane (CH_4) and other multi-carbon chains (*e.g.* C_2H_4, C_3H_8) to liquid chemicals such as carboxylic acid (HCOOH, CH_3COOH) and methanol (CH_3OH), etc[24]. Moreover, it should be noted that protons reduction is able to occur at the potentials required for CO_2 reduction. Hydrogen evolution reaction (HER) usually competes with CO_2 reduction in aqueous solution, resulting in the low selectivity and efficiency of the desired reaction, which can be elucidated from a thermodynamic perspective. [25]

From a thermodynamic view, the standard redox potential of transformation from CO_2 to different C1-carbon fuel products with respect to the standard hydrogen electrode (SHE), are given in Table 1.1. [22, 26-28]

Table 1.1 Formal electrochemical redox potential for the reaction of CO_2 reduction to related products in aqueous media

Reaction	E^o vs. SHE (V)	eqn
$2H_2O\,(l) + 2e^- \rightarrow H_2\,(g) + 2OH^-(aq)$	− 0.41	(1-1)
$CO_2\,(g) + 4H_2O\,(l) + 8e^- \rightarrow CH_4\,(g) + 8OH^-(aq)$	− 0.24	(1-2)
$CO_2\,(g) + 5H_2O\,(l) + 6e^- \rightarrow CH_3OH\,(l) + 6OH^-(aq)$	− 0.38	(1-3)
$CO_2\,(g) + 3H_2O\,(l) + 4e^- \rightarrow HCHO\,(l) + 4OH^-(aq)$	− 0.48	(1-4)
$CO_2\,(g) + H_2O\,(l) + 2e^- \rightarrow CO\,(g) + 2OH^-(aq)$	− 0.52	(1-5)
$CO_2\,(g) + H_2O\,(l) + 2e^- \rightarrow HCOO^-(aq) + OH^-(aq)$	− 0.42	(1-6)
$CO_2\,(g) + e^- \rightarrow CO_2^{\bullet -}$	− 1.9	(1-7)

As the reductive potential ranges in the negative potentials, it is apparent that the CO_2 reduction is thermodynamically favored over semiconductors that bear more negative potential than the formal redox potentials. But it is more difficult to carry out the CO_2 reduction in practice than hydrogen evolution as the activation of H_2O molecules is generally much easier than the activation of CO_2 molecules. Therefore, besides the redox potentials, it is well worth noting the activation during the initial steps of CO_2 reduction.

Based on the widely used d-band theory, when the gaseous molecules, for instance, CO_2, is chemisorbed to the transition metal-based catalyst surface, the interaction between the oxygen 2p orbitals of CO_2 and the 3d orbitals of transition metal in the surface will result in a filled low-lying bonding d-σ orbital and an empty antibonding (d-σ)* state. The catalytic activity correlating highly with the extent of filling of the (d-σ)* is demonstrated both theoretically and experimentally. An increased filling of the antibonding (d-σ)* state corresponds to a destabilization of the metal-adsorbate interaction. The higher the d-band with respect to the Fermi level (E_F), the less filling of the (d-σ)* state and the more stabilization of the catalyst-adsorbate system is, to translate, the stronger interaction between the catalyst and the adsorbed CO_2. As the filling extent highly depends on the electronic structure of the metal, special attention should be paid to the electronic structure of the metal where CO_2 reduction reaction takes place.[29, 30]

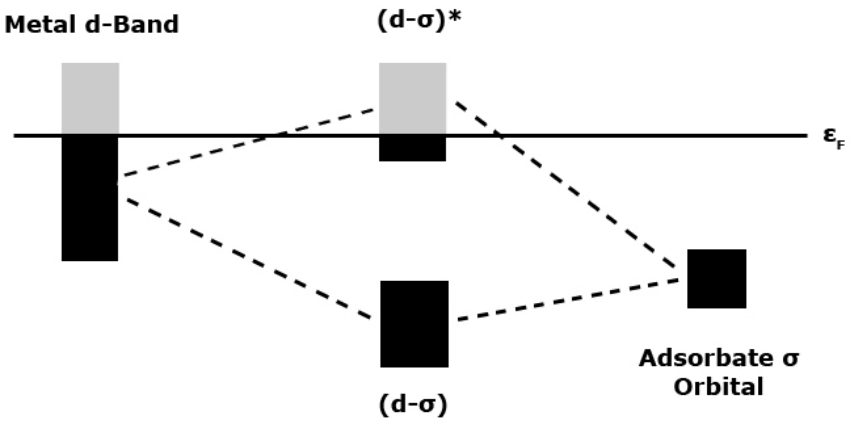

Figure 1.3 Scheme of the metal-adsorbate model in the d-band theory.[29]

Except the initial interaction between the gaseous molecule and the catalyst, two-electron transfer are involved in the reduction of CO_2 to CO and formate and multi-electrons transfer are involved in the CO_2 reduction to HCHO, CH_4 or CH_3OH. From the kinetic perspective, typically, every chemical reaction occurs stepwise and the electrons transfer one-by-one, going through intermediate transition states. In each step there is a compromise of the binding strength of the reactant to the catalyst, so it is necessary to find an optimal state of the key intermediate that is neither too strong nor too weak binding to the catalyst surface according to Sabatier principle.[31] Activity volcano model was hence developed to find out the optimal catalyst at or near the top.[32] According to the scaling rules, simultaneous transfer of multi-electrons means extremely high intersection point of the energy configuration of reactants and products in the coordination.[33] Thus, numerous efforts poised on the less electron transfer reactions for monocarbon products despite an expectation of the multicarbon species from CO_2 reduction. Even for the simplest two-electron transfer reaction for the formate and CO production, the efficiency and rate is still far from satisfactory.

At the initial stage in the pioneering work by Hori et al., it is prevalently thought that CO_2 first reduced to $CO_2^{\bullet-}$ radical anion at a quite negative potential approximately at −1.90 V vs. NHE which holds back the subsequent reactions with large kinetic barriers.[34, 35] Then later phenomena made such statement suspect that it was likely to occur at a more positive potential than the CO_2/ $CO_2^{\bullet-}$ redox potential.[34, 35] The proton-coupled electron transfer (PCET) steps are thus developed. Whether the PCET proceeds as a sequential proton-electron transfer (SPET) pathway or concerted proton-electron transfer (CPET) pathway is determined by whether the proton transfer (PT) follows electron transfer (ET) or both occur in a concerted manner.[33] Generally, ET happens in a reduction reaction if the intermediate has a high electron affinity while PT happens in an oxidation reaction because the intermediate has a low proton affinity. Although the majority of surface reaction follows SPET, it is assumed the CPET is only the feasible pathway to avoid high-energy intermediate when the off-diagonal states are energetically unfavorable. But it only stands for part of the pathways identification. More investigations are necessitated for the development of theory

together with the advanced *in situ* observation techniques.

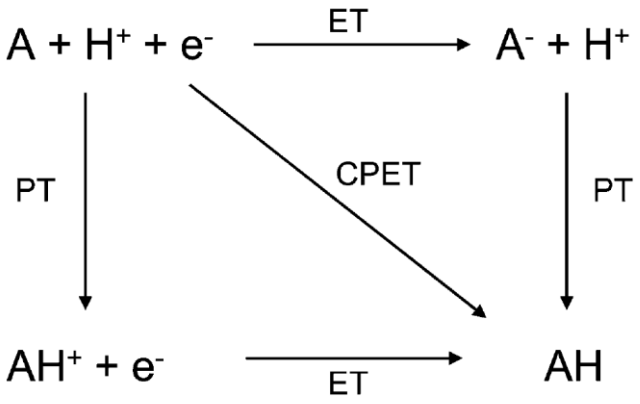

Figure 1.4 Square scheme for proton-coupled electron transfer. ET = electron transfer, PT = proton transfer, CPET = concerted proton–electron transfer.[36]

1.2.2 Previous research on semiconductors for CO_2 reduction

CO_2 reduction reaction taking place on a light-harvesting semiconductor has been considered as a direct avenue to convert sunlight into high-energy solar fuels and received substantial interest since the first report in 1970s.[37] The purpose of these studies is to produce carbon species from CO_2 and water using solar energy input, mimicking the photosynthetic factory in nature. Over the past decades, numerous progresses have been made in the development of semiconductors towards CO_2 reduction. To realize the solar-powered CO_2 reduction, semiconductors for base are required to have a bandgap to match well with the solar spectrum and have enough negative conduction band edge to supply sufficient overpotential for CO_2 reduction. To satisfy the band potential suggested in Table 1.1, the mostly employed semiconductors are listed in Figure 1.5 with a reference of redox potentials of CO_2 reduction, hydrogen evolution and water oxidation, which are presented beside the band diagram.

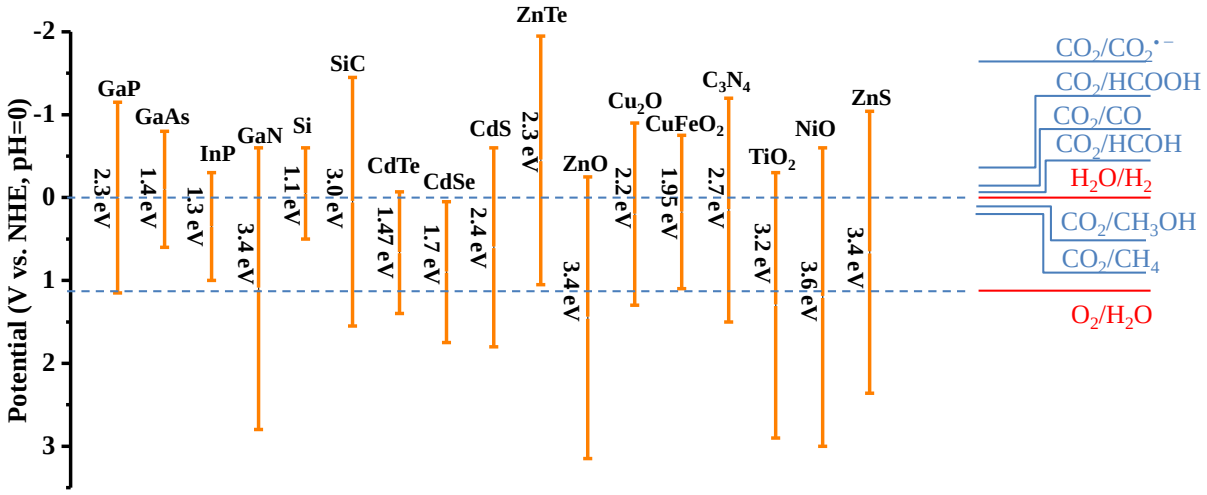

Figure 1.5 Conduction and valence band potentials of several commonly used semiconductors at pH = 0 versus a normal hydrogen electrode (NHE). Thermodynamic potentials for CO_2 reduction and water splitting to different products at pH = 0 versus an NHE are shown beside the band edge positions of semiconductors.

In the first attempt, M. Halmann carried on the photo-assisted electrolytic CO_2 reduction over p-type III-V compounds in aqueous lithium carbonate (Li_2CO_3) and found that the Zn-doped p-type gallium phosphide (GaP, 2.25eV) photocathode can produce formic acid, formaldehyde and methanol. Through the phenomenon that lithium deposited on the illuminated GaP surface to form Li_xGaP, he postulated that the deposited lithium reduced the CO_2 to $CO_2^{\bullet-}$ anion radical at the initial step[37]. CO_2 reduction to C-C bond hydrocarbons was able to proceed together with electricity generation driven by 450 W xenon source with p-GaP in the aprotic solvent of DMF[38]. First-principles DFT calculations by Muñoz-Garc á and Carter clarified the role of p-GaP (110) surface surrounded by H_2O molecules in electrochemical reaction[39]. Their result suggested both Ga and P atoms had strong affinity for electrons and contact with electrons donor. But the readily corrosion and large bandgap of p-GaP limited its potential use as a key problem of the inadequate matching to the solar spectrum and low conversion efficiency.

Similar problem occurred over InP with a great corrosion as a result of hydrophilic nature of the electrode surface in a way the oxygen atom of a water molecule coordinated to a metal site of the semiconductors.[25] Despite an optimal band matching, the research of GaAs was also suspended due to the involvement of toxic As and the not facile synthetic method. GaN was ever reported as a promising material for overall water splitting with a bandgap of 3.4 eV and a band structure straddling the redox potentials of the H_2 evolution and O_2 evolution[40-42]. So GaN has been considered as one of the few materials that can simultaneously satisfy the CO_2 reduction and water oxidation but it requires great cost and high crystallinity.

Among widely used materials, Si also stands out as the one of the most promising semiconductors as it has a quite negative conduction band, suitability of bandgap (1.12 eV) with solar spectrum, excellent conductivity and the great reservation on earth.[43] As Si is readily to be oxidized, the surface control of Si is very crucial. Organic moieties to stabilize the surface and extra electric energy are necessary when preparing the Si photocatalysts. Compared with its applications in photocatalysis, its photoelectrochemical application in water splitting and CO_2 fixation is more attractive and widely studied[43]. This also greatly limits its use in photocatalytic CO_2 reduction.

Binary or ternary Cu(I)-based oxide occupies a significant position in CO_2 reduction as an earth-abundant, non-toxic and relatively stable semiconductor with high charge carrier mobility. But it should be noted that due to the excitation from $3d^{10}$ valence band to the primary 4*s* conduction band, Cu is prone to suffer the self-reduction.[44] Therefore in the previous research, the electrochemical studies are much more than that in photocatalysis. Kanan et al. uncovered the oxide-derived Cu electrode, instead of directly partially oxidized Cu, bears a dramatically improved selectivity than polycrystalline Cu and Cu_2O, reaching a faradaic efficiency of >90% when electrocatalytically reducing CO to liquid fuels like ethanol.[45] Such fascinating phenomena were also observed on the Au_2O_3-derived Au[46] and Ag_2O-derived Ag[47] with a faradaic efficiency to CO of >98% and >80%, respectively. The superior catalytic performance was accounted from the created sufficient crystal boundaries as the potential reaction sites. Effective

electrocatalytic reduction of CO_2 was also discovered on other partially oxidized compounds such as Sn/SnO[48] and atomically thin-layered CoO[49].

Free from the utilization of metals, graphitic carbon nitride (g-C_3N_4) and their derivatives have sparked an interest in photocatalysis.[50] Possessing a bandgap of 2.7 eV, g-C_3N_4 shows visible light response and moderate charge transfer capabilities. With a conduction band located higher than -1.0 V vs. NHE, g-C_3N_4 is capable of reducing water to hydrogen and CO_2 to carbon species. Normally the graphitic planes of g-C_3N_4 stem from the pyrolysis of tri-s-triazine-based or melon-based polymeric compounds and the oligometric units are in-plane amino groups. Binding with a binuclear ruthenium complex (RuRu ′) via hydrogen bonding, carbon nitride nanosheets (NS-C_3N_4) could break up the inert nature of the amino group terminal on the surface of the carbon nitride as usual.[51] With the modification of Ag nanoparticles, it undergoes a promoted CO_2 reduction towards formate with a high selectivity of 98 % in aqueous solution containing EDTA·2Na (10 mM). Combining with the cobalt species, $Co(bpy)_3Cl_2$ as a reductive catalyst and triethanolamine (TEOA) as the electron donor and hydrogen source, CO_2 was converted into CO instead of formate, which was also demonstrated applicable in other conjugated carbon-based polymers.[52]

Despite a low reduction potential and large bandgap, TiO_2 is still considered as one of the most efficient photocatalysts. Extensive research have been conducted and there are plenty of review papers about the CO_2 reduction over TiO_2.[22, 23, 35, 53] Instead, with a more positive oxidation potential at 2.8 V vs. NHE than the other semiconductors, TiO_2 is more promising as a photocatalyst for water oxidation and photoanode from the thermodynamic point.

At last, our attentions were switched to the group of II-VI compounds and chalcogenide. The S 2p or Se 2p provides a relatively high valence band orbitals compared with O 2p. Thus, the majority of materials in this group hence have a red shift of absorption edge and visible light absorption. With most negative conduction band edge (−1.65 vs. RHE, pH=7.5), ZnTe exhibits appreciable capability in reduction reaction. Polypyrrole-coated ZnTe (Ppy/ZnTe) demonstrated the highest faradaic efficiency of 37.2 % for formic acid.[54] Au nanoparticles coupled ZnTe/ZnO nanowire arrays later developed by the same group were

reported a dramatic enhancement in photoelectrochemical CO_2 reduction with a faradaic efficiency of 68% to CO and the IPCE shot up to 98% at −0.7V *vs.* RHE.[55] However, the highly toxicity of Te and Se makes the related materials prohibitive. Compared with CdS, the higher potential of ZnS is more attractive for the reductive reactions. Thus in this thesis, ZnS is selected as the host material for photocatalytic CO_2 reduction.

Basically, the intermediate of $CO_2^{\bullet-}$ proceeds in different manner according to the inherent characteristic of catalyst to carbon monoxide (CO) or formate ion ($HCOO^-$).The detailed steps are as followed[34, 35]:

$$CO_2 + e^- \rightarrow \bullet CO_2^-{}_{ad} \quad (1\text{-}8)$$

$$H + e^- \rightarrow H_{ad} \quad (1\text{-}9)$$

$$\bullet CO_2^-{}_{ad} + Had \rightarrow HCOO^- \quad (1\text{-}10)$$

$$\bullet CO_2^-{}_{ad} + H_2O + e^- \rightarrow HCOO^- + OH^- \quad (1\text{-}11)$$

$$HCOO^- + e^- \rightarrow CO + OH^- \quad (1\text{-}12)$$

$$\bullet CO_2^-{}_{ad} + \bullet CO_2^-{}_{ad} \rightarrow 2CO \quad (1\text{-}13)$$

$$\bullet CO_2^-{}_{ad} + CO_2 + e^- \rightarrow CO + CO_3^{2-} \quad (1\text{-}14)$$

These suggest that the water-mediated proton transfer occurs to form $HCOO^-$ as (1-8) (1-9) (1-10). The subsequent electron binds differently on oxygen atom of $\bullet CO_2^-$ for Au, Ag, Cu, Zn, Fe, Ni, Pt, leading to HCOOH as the product or on carbon atom of $\bullet CO_2^-$ for heavy p-block metals (In, Sn, Pb, Hg), evolving CO.[35, 56] In a word, the primary product of the CO_2 reduction over Zn should be formate. So in the starting scenario of CO_2 reduction, to understand the formate production with CO_2 as the raw material has great importance. Furthermore, formic acid is employed as a raw material in industry for sodium formate, methyl formate, ethyl formate, etc. with considerable economic value. As a facile approach to synthesize formic acid, the fundamental investigation of formate production from CO_2 over ZnS is of great significance and interest.

From another aspect, H_2 evolution at the semiconductor surface may compete with CO_2 reduction and affect the rate of the desirable CO_2 reduction reaction. According to the different rate-determing step, there

is a discrepancy of product distribution. For example, if the CO_2 reduction proceeds under mass transport control but H_2 evolution occurs under activation control, higher energy in the conduction band of semiconductor will lead to a higher H_2 evolution efficiency.[25] Substantial efforts should be devoted to understand the competitive H_2 evolution accompanying the CO_2 reduction, from both theoretically and experiments to instruct the design of the CO_2 photocatalysts and better control the CO_2 reduction reaction.

1.2.3 Zinc sulfide photocatalysts

1.2.3.1 Structure and properties

Zinc sulfide (ZnS) is an important II-VI group semiconductor and has been extensively studied in a variety of fields including light-emitting diodes (LED), flat panel displays, visible and infrared window, sensors, lasers and other devices.[57] The excellent carrier transportation, durable thermal stability, non-toxicity, water insolubility and comparatively inexpensive cost make it one of the most promising photocatalysts in artificial photosynthesis.

Basically, ZnS has two phase structures, sphalerite (cubic) and wurtzite (hexagonal) (in Figure 1.6). The cubic sphalerite form of ZnS has a bandgap of about 3.54 eV while the hexagonal wurtzite structure has a bandgap of 3.91 eV.[58] The comparatively wide bandgap determines the intrinsic semiconductor of ZnS is only responsive to ultraviolet irradiation in the solar spectrum. But the conduction band electrons and valence band holes possess strong redox potentials, indicating the thermodynamic feasibility of water splitting and CO_2 reduction. Therefore, considerable efforts have been devoted to developing the visible-light-responsive ZnS-derived photocatalysts. Metal ion doping, non-metal ion doping, composite construction and dye sensitization are the widely engaged strategies to extend ZnS in the application in visible light region.[15, 53]

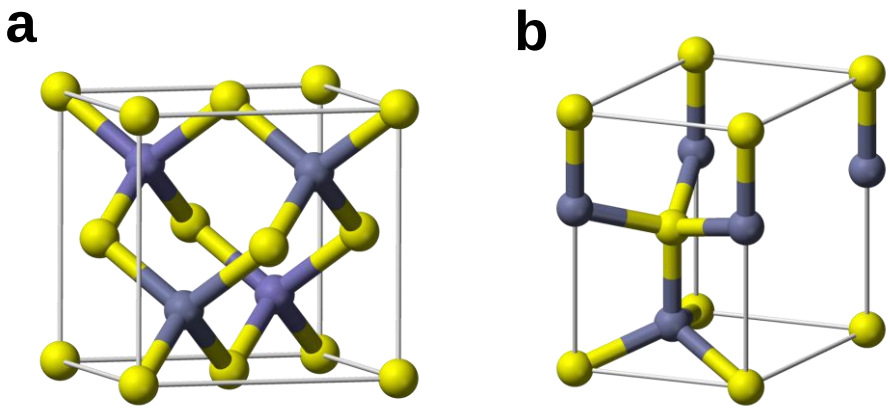

Figure 1.6 Sphalerite (a) and wurtzite (b) phase of ZnS. (blue: Zn atom, yellow: S atom)

1.2.3.2 Zinc sulfide photocatalysts in H_2 evolution

Metal sulfides are one of the most important photocatalysts for H_2 evolution in the presence of sacrificial reagent. With no sacrificial, sulfide photocatalysts are susceptible to photo-corrosion by their own photogenerated holes. To overcome this problem, sulfide/sulfite solutions (Na_2S/Na_2SO_3), lactic acid, ascorbic acid are usually used as the electron donors.

Based on ZnS, ternary semiconductors, such as $Zn_{1-x}Cd_xS$, $Zn_{1-x}Cu_xS$, $Zn_{1-x}Ni_xS$ and $Zn_{1-x}Cr_xS$, or multicomponent sulfides solid-solutions of $AgInS_2$-ZnS, $CuInS_2$-ZnS and $CuInS_2$-$AgInS_2$-ZnS were developed.[15] The activity of representative ZnS-based photocatalysts are listed in the Table 1.2.

Table 1.2 Representative ZnS-based photocatalysts for H_2 evolution from aqueous solutions in the presence of sacrificial reagents

Photocatalysts	Lamp	Reaction solution	H_2 evolution (μmol/h)	ref
ZnS:Cu	300W Xe>420nm	K_2SO_3	450	[59]
ZnS:Ni	300W Xe>420nm	Na_2S+ K_2SO_3	280	[60]
ZnS:Pb,Cl	300W Xe>420nm	Na_2S+ K_2SO_3	40	[61]
CdS-ZnS	300W Hg>420nm	Na_2S+ Na_2SO_3	250	[62]
Pt/$AgInZn_7S_9$	300W Xe>420nm	Na_2S+ K_2SO_3	940	[63]
Pt/$Cu_{0.09}In_{0.09}Zn_{1.82}S_2$	300W Xe>420nm	Na_2S+ K_2SO_3	1200	[64]

$Pt/Cu_{0.25}Ag_{0.25}In_{0.5}ZnS_2$	300W Xe>420nm	$Na_2S+ K_2SO_3$	2300	[65]
$Pt/[In(OH)_yS_z]$:Zn	300W Xe>420nm	$Na_2S+ Na_2SO_3$	67	[66]
$RGO-Zn_{0.8}Cd_{0.2}S$	AM 1.5G	$Na_2S+ Na_2SO_3$	1824	[67]
$S^{2-}-(ZnS)_{0.4}(AgInS_2)_{0.6}$	400W Xe>400nm	$Na_2S+ Na_2SO_3$	5000	[68]
$Cu_{1.94}S-Zn_{0.23}Cd_{0.77}S$	300W Xe>420nm	$Na_2S+ Na_2SO_3$	154.7	[69]

These ZnS-based photocatalysts have been fully proved to be a low-toxic, and cost-effective visible-light driven photocatalysts with high efficiency for H_2 production from water splitting. And herein, doping with impurities and introduction of the defects deserves more attention. Metal cations like Cu, Bi, Pb, Ni, Fe were doped to give rise to a visible light response. Non-metals such as C, B, N, S, F, Cl, Br are most effective anion impurity levels located near the valence band.[15]

Except the doping, utilizing the phase transformation between sphalerite (S) and wurtzite (W) and constructing the phase junction of S-W was also proved effective to regulate the sulfur vacancies and the charge-transfer kinetics. The S-W phase junction with a type II- band structure realized the visible-light-driven photocatalytic H_2 evolution, providing an insightful approach for modifying the wide bandgap semiconductors.[70]

Controlling the amount of intrinsic sulfur vacancies was also achieved as a manipulation method on ZnS spheres for efficient visible light H_2 evolution activity.[71] The density functional characterization of the defect states uncovered the local electronic structure around a sulfur vacancy as seen in Figure 1.7. According to the theoretical model of the wurtzite ZnS, the Zn-S bonding is consisted of a filled sp^3 orbitals of S^{2-} and an empty sp^3 orbital of Zn^{2+}. When one sulfur vacancy is adjacent to four Zn atoms, the interaction between the four dangling bonds will create a 1a and 1t level just below the conduction band. After relaxation, the 1a level becomes closer to the valence band top and filled with double electrons. The empty 1t level is split into three levels near the conduction band bottom, trapping the photogenerated electrons that can be excited to conduction band, thereby enhancing the visible light absorption.

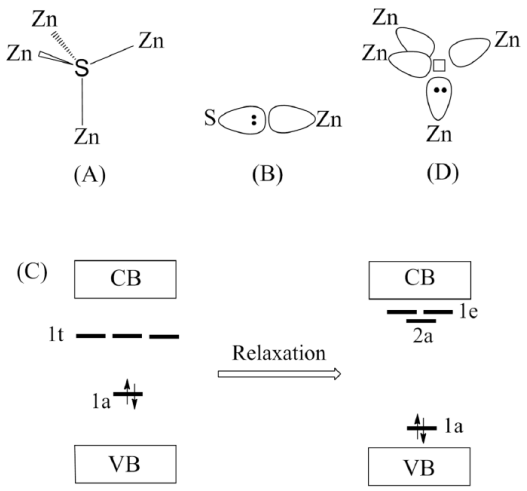

Figure 1.7 The examination of the relaxed structures. (A) SZn_4 tetrahedron of ZnS. (B) Zn-S bonding as a combination of a filled sp^3 hybrid orbital of S^{2-} with an empty sp^3 orbital of Zn^{2+}. (C) Schematic diagram showing the midgap defect states of ZnS created by an S vacancy before (left) and after (right) relaxing the structures around the vacancy site. (D) Overall effect of an S vacancy showing the formation of one of the four ZnS_3 pyramids surrounding the S vacancy getting two electrons. The VB and CB refer to valence and conduction bands, respectively.[71]

1.2.3.3 Zinc sulfide photocatalysts in CO_2 reduction

The photochemical CO_2 reduction over ZnS was pioneered by Yoneyama and Inoue, *et al*. As stated before, the photocatalytic reduction reactions over ZnS necessitated the sacrificial reagents. Commonly used hole scavengers were S_2^{-}/SO_3^{2-}, S_2^{-}/PO_2^{2-}, triethylamine (TEA), triethanolamine (TEOA), methanol, ethylene glycol, oxalate, isopropanol and glycerol.[72, 73]

As we know, there are two phase forms of ZnS: sphalerite and wurtzite. Heagy et al. first conducted the comparative study into the photocatalytic behavior of the two forms taking into consideration of the size, surface area and bandgap in the photoreduction of HCO_3^{-}.[70] Under AM 0 solar simulation irradiation, the nanoparticle-W and microparticle-W showed 6 and 10 times formate production than the counterparts of the sphalerite in a linear manner.

Despite a larger production over the W-microparticles, earlier work on the photochemical reduction of

CO_2 over monodispersed ZnS nanocrystallites (average size *ca*. 2 nm) had attracted more attentions by Yanagida, et al. Using Zn perchlorate and Na_2S as the precursors, ZnS nanocrystallites were synthesized and investigated in organic solvents including *N,N*-dimethylformamide (DMF), acetonitrile (AN) or methanol (MeOH) under UV light (λ> 290 nm). [74, 75] It was found the coordination of the positively charged Zn on the surface with the solvents caused a diversity in product distribution. In ZnS-DMF nanocrystallites, the excessive Zn^{2+} eliminated the sulfur sites and led to CO formation. Thus, the sulfur vacancies could act as the active sites for both CO and H_2 production. As a result, it gave rise to the competition between CO_2 reduction and H_2 evolution. In addition, DMF provided the proton source with S-H form on the surface, which suppressed the sulfur vacancy sites and led to the formate as the exclusive product.

It was also claimed that the ZnS quantum crystallites with low density of surface defects lead to formic acid conversion from CO_2 at pH=7 with NaH_2PO_2 and Na_2S as sacrificial electron donors due to the stabilization of electron-hole against recombination and elimination of the deactivation of the electrons trapped by the surface defects.[72] In the absence of anionic species, the vacancies on the surface trap the conduction band electrons and the trapped electrons are not able to reduce CO_2 but able to reduce H_2 with a more positive reduction potential. In the presence of SH^-, the electrons localized on the sulfur vacancies were scavenged, resulting in the fast surface recombination through hole-anion pairs and reservation of the conduction band electrons. Therefore the CO_2 reduction proceeds with a higher yield of HCO_2^-.[72]

The polyhydroxy compounds are expected to mimic the natural photosynthesis as the plant always give out sugar as the products. In the presence of tetramethylammonium (TMA) salt, the carbon dioxide radical anion with one electron could be protonated to form formate, disprotonated to CO, or dimerized to oxalate, glyoxylate, glycolate, tartrate and malate.[76] Except for the bulk semiconductors of $SrTiO_3$, $BaTiO_3$, ZnO and SiC, CdS and ZnS, which were readily stated in the colloidal crystallites with diameters around 2-4 nm, were also tested as well. The hole acceptors were examined over iodide, TSCoPc, $Fe(CN)_6^{3-}$, hydroquinone, sulphite, propanol, RuO_2, hypophosphite at pH=4 CdS suspensions. Among them, RuO_2 and

TSCoPc were the oxidation catalysts, instead of the electron donors. After addition of TMA salts, it will form an aprotic layer outside the colloidal particles to exclude water. As an ion with a low charge density, negligible Lewis acid effect was occurred on the TMA-capped surface. The Saveant mechanism explained the formation of the polyhydroxy compounds, which claimed that self-coupling of the $CO_2^{\cdot -}$ anion radical forms oxalate; CO formed from oxygen-carbon coupling of $CO_2^{\cdot -}$ with CO_2; the residual water protonated the $CO_2^{\cdot -}$ to form formate. Low proton solvent media like dimethylformamide, dimethyl sulfoxide and propylene carbonate were also applicable to the Saveant mechanism. To improve the quantum efficiency, fixation of ZnS on a large-surface-area support such as SiO_2 was conducted.[77] It was found the 13 % coverage gave the most active reduction of CO_2 to formate using dihydrofuran (2,5-DHF) as a reducing agent.

There is a critical issue on the carbon source when the organic chemicals are utilized in the CO_2 reduction reactions. Since the residual of the organics in the synthesis of the photocatalysts, the organic solvents and the organic sacrificial reagents all can contribute to the overall production, it is necessary to confirm the carbonaceous products are derived from CO_2 instead of the involved organics using the isotope tracer.[53] On the other hand, the involvement of the organics will interference the identification of the products as Guzman also emphasized previously.[79] If possible, the avoidance of carbonaceous consumption can be more effectively free from the unexpected contamination and applies to the target of solar-driven CO_2 reduction.

Recently, Meng et al. developed a facile method for the colloidal ZnS nanocrystals in the aqueous solution at room temperature and utilized the as-prepared photocatalysts in all-inorganic environment.[78] In the presence of Cd^{2+}, the colloidal ZnS photocatalysts acquired a remarkable 76% apparent quantum efficiency at 280 nm with K_2SO_3 as the only hole scavengers. The large amounts of surface sites furnished by the loose aggregated structure were responsible for the high efficiency of the reaction. However, the photocatalyst was limited by ultraviolet absorption response. To make it more applicable, visible light-responsive ZnS colloidal nanocrystals are more demanded in the future development.

In many important aspects, the microscopic local structure on the surface of photocatalysts plays vital role determining the catalytic properties. Except for the electronic structure, crystalline structure, and reaction environment, the surface states are particularly important to be taken into consideration for CO_2 reduction on semiconductor.

1.2.4 Surface modulation methods in CO_2 reduction

As the adsorption and activation of CO_2 plays vitally important role on the surface CO_2 reduction. Over the past decades, great efforts have been made in the development of surface structures towards CO_2 reduction. Herein it is emphasized a selection of strategies which promises to bring substantial improvements of the photocatalysts including the decoration with cocatalysts and the incorporation of the surface defects. For each of the strategy, the details will be discussed in separate sections as following.

1.2.4.1 Cocatalysts

Cocatalysts mainly play several important roles in photocatalytic reactions, *i.e.* improving the charge separation and transfer, enhancing the stability of the catalysts, boosting the activity and selectivity as well as suppressing the back reactions.[80] Therefore, three aspects for designing the highly efficient cocatalyst-photocatalyst photosystems are worth mentioning: (1) the smaller Gibbs free energy for both adsorption and desorption; (2) the smaller particle size of the cocatalysts; and (3) the lower Schottky barriers after combining with semiconductors.

Generally the inorganic cocatalysts are divided into two categories: noble metal-based cocatalysts, i.e., Pt, Ag, Pd, Ru, Rh, Au, or alloys, etc.; noble metal-free cocatalysts, *i.e.*, Cu, Ni, Co, etc. -containing species or nanocarbons. According to the product selectivity, Y. Hori has classified the metals into four groups in electrochemical CO_2 reduction (Figure 1.8). Pb, Hg, In, Sn, Cd, Tl and Bi give out formate as the dominant product; Au, Ag, Zn, Pd and Ga mainly form CO from CO_2; Cu is the exclusive metal that is able to produce hydrocarbons such as CH_4, C_2H_4 and alcohols; H_2 occurs in fierce competition with CO_2 reduction over Ni, Fe, Pt, Ti.[35, 56]

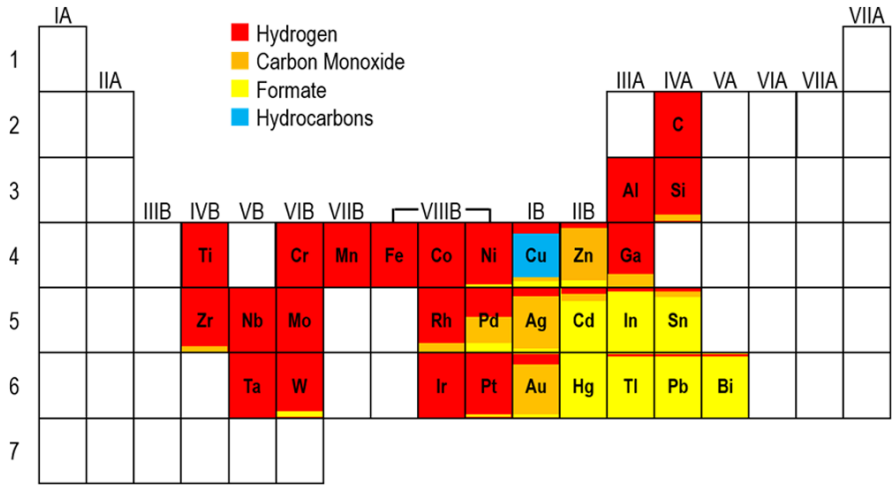

Figure 1.8 Periodic table depicting the primary reduction products in CO_2-saturated aqueous electrolytes on metal and carbon electrodes.[35]

Although the classification might not be applicable to all the cocatalysts in photocatalytic CO_2 reduction, it gives inspiration to the design towards suitable cocatalyst. In practical experiment, Pt is able to generate CH_4 from CO_2 reduction in the presence of H_2O.[81] Pt, Pd, Au, Rh, Ag photodeposited on TiO_2 showed a CH_4 generation activity in the order of Ag < Rh < Au < Pd < Pt, same with the trend in the work function of the noble metals and the electron accepting abilities.[23] However, CO generation didn't increase much, and even decreased. This might be related to the selectivity and competition between CH_4 and CO. As the CO_2 to CH_4 undergoes the 8-electron transfer process and CO_2 to CO is a 2-electron transfer process, the more reductive electrons go to reduce CO_2 to CH_4 while the comparatively weak electrons reduce CO_2 to CO.

However, things change over the colloidal ZnS nanocrystals previously mentioned in the section 1.2.3.3. Grafting the noble metals, such as Pd, Pt, Ag, Au, which are considered promoting the CO_2 activation and reduction, the photocatalytic CO_2 activity turned to be suppressed adversely.[78] The passivation of the active sites by the formed noble metal sulfides were supposed to suppress the activity of the colloidal ZnS nanocrystals. Only Cd^{2+} and Al^{3+} could effectively enhanced the HCOOH production to ~20 and ~ 2 times, respectively, with respect to the counterparts of the bare colloidal ZnS nanocrystals.

Although ion exchange between $Cd^{2+}$and Zn^{2+} have been proposed as a possible reason according to the K_{sp} of the species of CdS and ZnS, no experimental evidence was presented for the process. Thus, the charge dynamics need further investigation together with the kinetic aspect over the surface of Cd^{2+} modified ZnS.

The noble metal-free cocatalysts mainly include Cu-based species and Ni-based species. Cu, CuO_x, Cu_2O, Cu clusters, $CuCo_2O_4$, Ni, NiO, Ni/NiO are most widely loaded on the surface of photocatalysts.[82] According to DFT calculation, the activation of CO_2 is more favorable on Cu nanoparticles as the electrons migrate readily from the *d* orbitals to (C-O) π^* orbitals. A mixture of Cu powder and TiO_2 was reported able to form CH_3OH, HCHO, CH_4 and CO.[83] Coupled with oxygen vacancies on the surface of H_2-pretreated Cu-TiO_2, the Cu^+/Cu^0 species could boost the capture of electrons and holes at different sites.[84] NiO/$InTaO_4$[85] and Ni/NiO/$InVO_4$[86] were reported effective in CO_2 conversion into CH_3OH.

Basically, the smaller particles and higher dispersion will result in a larger enhancement of photocatalytic performance. Single-atom catalysts (SACs), with isolated metal sites anchored on the matrix by strong interaction, are developed as approach of utmost utilization of the metal catalytic atoms.[87] The metal-organic frameworks (MOF), a newly emerging class of crystalline micro-mesoporous hybrid materials, can be incorporated with single atoms.[5] The great advantage of the SACs in such catalysts lies in the even distribution of the effective active sites derived from their intrinsic frameworks and the increase of the adsorption and activation for the adsorbates. With suitable linkers towards CO_2-philicity, and the ability of light absorption and excitation, the MOF materials have drawn a great deal of interest for their application in CO_2 reduction. By introducing single atoms into the MOF matrix, the MOF was an excellent and promising alternative for biocatalysts in nature to carry out the artificial photosynthesis under mild reaction conditions.[88] However, the high cost of the precursors and the low yield for the MOF preparation greatly limits their application in the future.

As an alternative of matrix, with cheaper precursors and easier preparation method, g-C_3N_4 is another promising class of matrix for CO_2 reduction. The single-atom dispersion of Pd and Pt on g-C_3N_4 was predicted to greatly enhance the visible light absorption and CO_2 reduction to HCOOH and CH_4 by DFT

theory.[89] And there is an increasing trend to anchor the transition metals into the g-C_3N_4 matrix for the reduction of utilization of metals and the efficient use of catalytic active sites.[90]

Inspired by the idea of the single atoms in the carbon-based materials, the single catalytic atoms are expected to implant into the surface of the conventional semiconductors that have been demonstrated highly efficient and promising for CO_2 reduction. Modified with the tetracoordinated Co(II) species derived from the decarboxylation of the Co-EDTA (in Figure 1.9), CdS exhibited a selective reduction into CO with a remarkable TOF of 7.94 h^{-1}, which provides a well-dispersed model to fully utilize the transition metal cocatalyst.[91] However, the low coordination and the weak interaction between the Co species and CdS might cause a great electron and energetic transfer barrier in the CO_2 reduction. More intimate interaction is expected to allow for the facile charge transfer and their participation in the reaction. Until now, it is a pity that few researches have set foot in the area of fabricating single-atom or isolated sites for photocatalytic CO_2 reduction over inorganic semiconductors and hence it is imperative to keep an eye on the fabrication and function of SACs to disclose the potential of more efficient and selective isolated cocatalysts over ZnS.

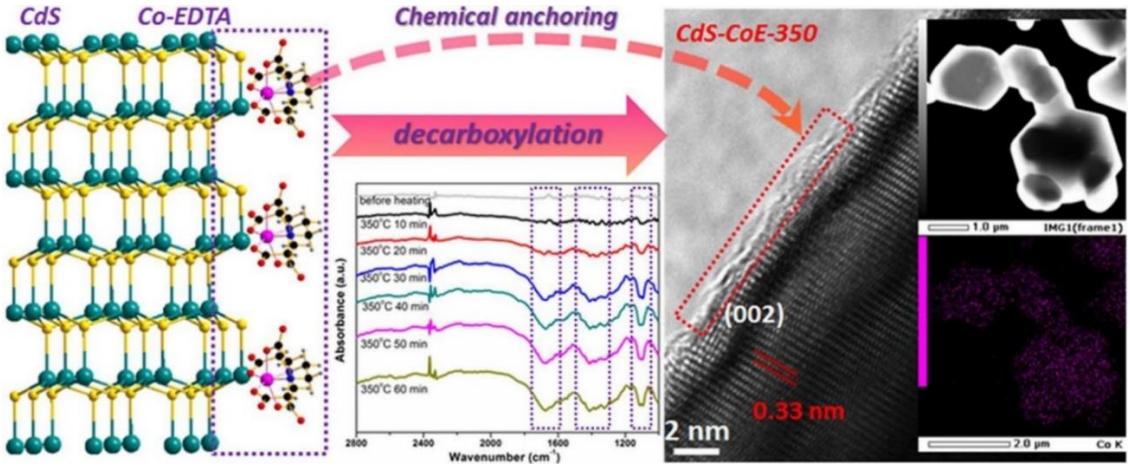

Figure 1.9 Schematic illustration for the chemical anchoring of the Co species on the CdS surface through the controlled decomposition of Co-EDTA precursor. Middle: *in situ* FTIR spectra measured during the calcination of Co-EDTA at 350 °C; right: HRTEM of resulted CdS-CoE-350; inset: STEM image and EDS elemental mapping of CdS-CoE-350.[91]

1.2.4.2 Surface vacancies

For a long time, the vacancies in the materials are considered as the "invisible" agents to carry out a variety of reactions in catalysis.[92] Manipulating the nature and concentration of the defects, the defect engineering is able to tune the electrical, chemical and physical properties. Anion vacancy is one of the most important and prevalent defect within many semiconductors.[92] In many oxides, a missing O atom from the surface or bulk resulted in two trapped electrons localized around the cavity center, giving rise to an excitation in the visible light region of the spectrum.[92] As stated before, with controlled amount of S vacancies modulated in concentrated NaOH solution with $NaBH_4$, enhanced photocatalytic H_2 production under visible light was realized over ZnS crystallites without loading any cocatalyst.[58]

Anion vacancies have been extensively used in CO_2 reduction. Partially oxidized four-atom-thick layers of cobalt oxide materials realized a stable current density of 10 $mA \cdot cm^{-2}$ and 90% formate selectivity at 0.24 V, a quite low overpotential in electrochemical CO_2 reduction.[49] Compared with the oxygen-vacancy-poor layer, the oxygen-deficient cobalt oxide single-unit-cell layers exhibited a current density of 2.7 $mA \cdot cm^{-2}$ with 85 % formate selectivity. The presence of oxygen vacancy can stabilize the intermediate, formate anion radical ($COOH^{-}$*) and lowers the rate-determining activation barrier.[93] Oxygen vacancy in $SrTiO_3$,[94] TiO_2,[95] ZnO,[96], Zn-Ge-O,[97] , ReO_2[98] all have been established with the stronger capacity for CO_2 adsorption and conversion kinetics.

The oxygen vacancies on simple compounds are much easier to be defined. However, when another element is involved as a dopant, the interplay of the foreign elements and anion vacancies and their synergistic impact on the photocatalytic CO_2 reduction is a pending problem. The chemical state of the dopant may be affected by the anion vacancies; the multiple roles of the dopants on light absorption and the activation of chemisorbed species as well as their impact on the distribution of anion vacancies are seldom discussed previously. To refine the defect states of anion vacancies via doping, Mo-doped $W_{18}O_{49}$ ultrathin nanowires were employed as a model to study for N_2 fixation. It was concluded the Mo−W centers was the active sites for chemisorbing N_2 molecules and the doped Mo species level up the defect band

center towards Fermi level, supplying more robust photoexcited electrons for N_2 reduction.[99]

In another case, the role of oxygen vacancies and the surface hydroxyl was investigated over $In_2O_{3-x}(OH)_y$ nanoparticles for the reduction of CO_2 to CO via the reverse water–gas shift reaction. Both hydroxides and oxygen vacancies were the active sites to facilitate the reduction of CO_2. Moreover, they also played a significant influence on the charge relaxation pathways as shown in Figure 1.10. The midgap level associated with the oxygen vacancies can serve as electrons or holes traps to facilitate the charge separation; they can also act as the recombination centers of the photoinduced charges and influence the lifetime of the photoexcited-states. Clarifying the charge dynamics affected by the defect states is also necessary for the rational design and synthesis of efficient photocatalysts.[100]

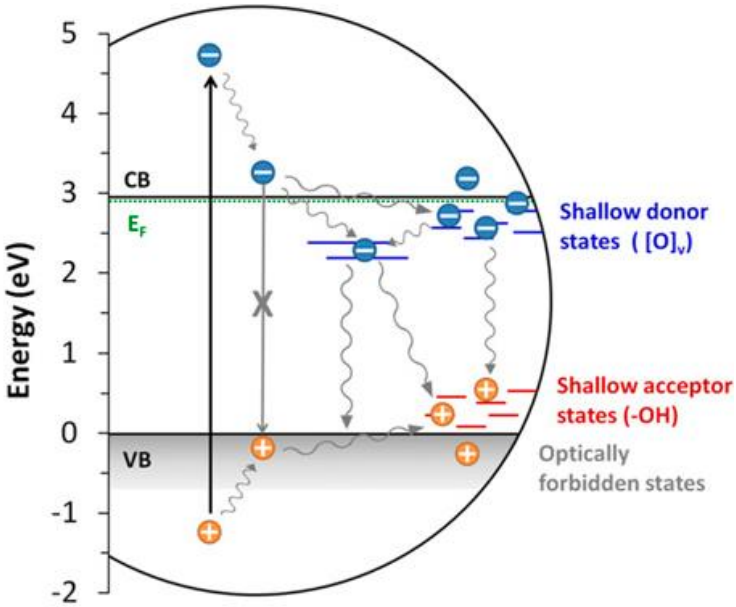

Figure 1.10 A schematic illustration of charge carrier recombination pathways in $In_2O_{3-x}(OH)_y$ nanoparticles. The vertical black arrow indicates initial excitation from the pump pulse. The wavy gray arrows illustrate different nonradiative relaxation processes. Blue and red lines indicate midgap states created by oxygen vacancies and surface hydroxyl groups, respectively.[100]

Very recently, different from the susceptibly oxidized anion vacancies, cation vacancies have aroused

the interest of researchers in various field of materials such as ferromagnetic properties[101], oxygen evolution reaction[102] and hydrogen evolution[103]. On one hand, as the cation vacancy-rich materials are more difficult to prepare compared with the anion vacancy-rich materials,[102] the facile synthetic methods are desirable for the extensive use of such manipulation. On the other hand, despite a handful of studies associated with the cation vacancy modulation in photocatalytic CO_2 reduction, the incisive understanding of the defects are deficient. As reported, the defective one-unit-cell $ZnIn_2S_4$ atomic layer ensures a high concentration of Zn vacancy.[104] With cation vacancies, the $ZnIn_2S_4$ atomic layers exhibit a CO_2 conversion into CO with a formation rate of 33.2 $\mu mol \cdot g^{-1} \cdot h^{-1}$, nearly 3.6 times higher than that with poor Zn vacancies. When the two-dimensional $BiVO_4$ layer was synthesized with rich vanadium vacancies, the non-catalytic material under normal conditions could be able to reduce CO_2 to methanol with stoichiometric O_2 generation.[105] The methanol production rate reached up to 398.3 $\mu mol \cdot g^{-1} \cdot h^{-1}$ and an apparent quantum efficiency of 5.96 % at 350 nm. The examples disclose the possibilities of cation vacancy sites in promoting the solar-driven CO_2 reduction and provide an alternative way to design materials. But both studies attribute the superior performance to the longer-lived photogenerated electrons reserved by the cation vacancies. From my point of view, it is more necessary to deeply understand the role of the cation vacancies in the CO_2 pathways and molecular kinetics, which are still unclear, especially in the presence of the more thermodynamically feasible hydrogen reduction as a competative reaction. The exact pathways over the photocatalysts remain to be established using more advanced techniques, such as the *in situ* spectroscopic observations and the theoretical calculation methods.

1.2.5 *In situ* spectroscopic observation

The transformation of C1 molecules on solid surface is necessary to uncover for understanding the mechanism of the heterogeneous catalytic reaction. Different pathways of the CO_2 reduction in aqueous solvents are still not fully understood, particularly in the presence of a proton source such as water. Nowadays, *in situ* techniques and theoretical calculations afford direct and powerful avenues for us to detect

the intermediates in the CO_2 reduction process and better understand the detailed catalytic transformation processes.[106-108] The *in situ* infrared spectroscopy including the attenuated total reflection-infrared (ATR-IR) mode[78, 109, 110] and diffuse reflection infrared fourier transform spectroscopy (DRIFTS) mode[111, 112] have been gradually applied to the investigation of the catalytic reaction.

The main pathway for electrochemical reduction of CO_2 to acetate over N-doped diamond/ Si rod arrays (NDD/Si RAs) electrode was studied by *in situ* infrared spectroscopy with external reflection mode. From the time-dependent infrared spectrum in Figure 1.11a, the peak of COO^- and the OOC-COO increased along with the peak of C-H and C-OH after electrolysis started, while the CO_2 decreased. Combined with the product distribution and the faster kinetics of C-C coupling than $CO_2^{\bullet-}$ protonation, the pathways are proposed as illustrated the Figure 1.11b.[113]

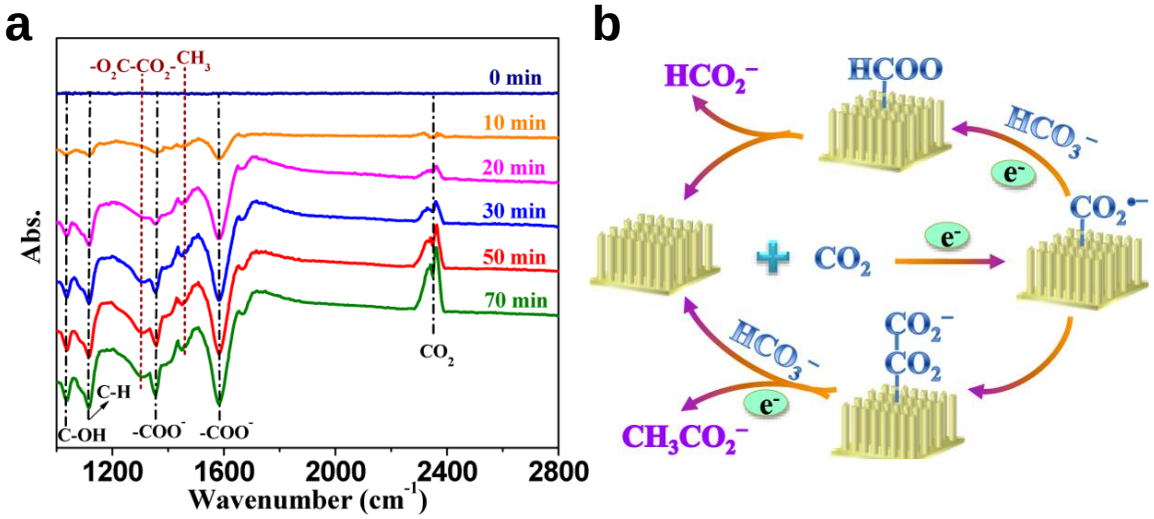

Figure 1.11 (a) *In situ* infrared spectrum of CO_2 reduction on NDD/Si RA electrode at -1.0 V with different electrolytic time (CO_2 saturated 0.5 mol L^{-1} $NaHCO_3$ solution). (b) Schematic pathway for electrocatalytic CO_2 reduction on NDD/Si RA electrode.[113].

To date, the *in situ* attenuated total reflection-infrared (ATR-IR) spectroscopy has also been used in photocatalytic CO_2 reduction. The increasing intensity of the peak at 2100 cm^{-1} indicating the gradual formation of CO was observed over the illuminated boron catalysts.[110] Meanwhile, the growing

absorption bands at 700-1700 cm^{-1}, attributed to C=O, C-H, and C-OH vibrations, indicated the formation of some intermediate products of CO_2 reduction, such as aldehydes and bidentate carbonates. A two-electron, two-proton reaction pathway $CO_2 \rightarrow HCOOH \rightarrow HCHO \rightarrow CH_3OH \rightarrow CH_4$ was also disclosed through the *in situ* FT-IR spectroscopy over the O-doped graphitic carbon nitride (g-C_3N_4) nanotubes (OCN-Tube).[109] Though Meng et al. uncovered two absorption bands at 1364 cm^{-1} and 1640 cm^{-1}, assigned to C-O stretching and C=O stretching of CO_3^{2-} to confirm the maintained local pH environment on the surface of ZnS nanocrystals under continuous light irradiation[78], the more specific pathways of CO_2 transformation remains unclear. More collection and interpretation of the *in situ* IR spectra should be made to push ahead the deeper understanding of the intermediate and mechanism. Therefore in this thesis, the home-made *in situ* attenuated total reflection-infrared (ATR-IR) spectroscopy is used to conduct the research of this area. The setup can be referred to Figure 1.12.

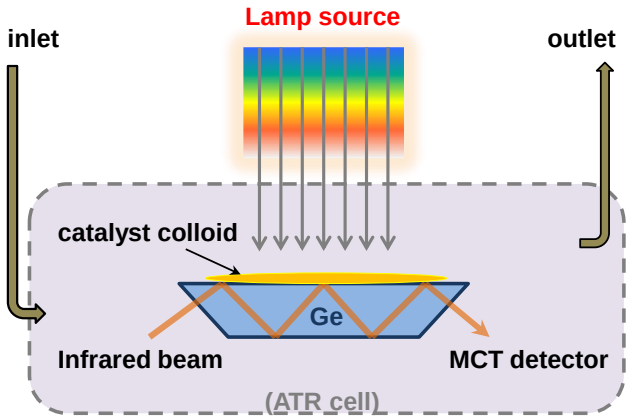

Figure 1.12 Schematic figure of the setup of attenuated total reflection-infrared (ART-IR) spectroscopy used in photocatalytic reaction. (MCT=mercury cadmium telluride. N_2 is the carrier gas. The incidence angle is 45°)

1.3 "Photosystem II" for water oxidation

To couple the CO_2 reduction over "Photosystem I" and close the photosynthetic cycle, the half reaction for water oxidation also necessitates exploitation. However, involved with a four-electron transfer process,

the water oxidation is kinetically sluggish.

Although hundreds of individual light-harvesting complex are found to regulate the process, the fascinating machinery of *Photosystem II* (the italic type indicate the enzyme) is at the heart of this process. The natural *Photosystem II* (Figure 1.13), found in the thylakoid membrane of higher plants, algae and cyanobacteria, is considered as the benchmark photocatalyst for solar water oxidation with a high turnover frequency up to 1000 s^{-1} and a small overpotential, far surpassing the manmade materials. [114, 115] With the attractive efficiency, sophisticated light-harvesting and energy transduction systems, the *Photosystem II* enzymes have aroused the attention of researchers. A great deal of efforts have been made to mimic the Mn_4Ca clusters.[114] Since it is too difficult to completely mimic the intricate proteins in nature, it seems more promising to develop the bio-hybrid architecture between the natural protein and the artificial photocatalysts.

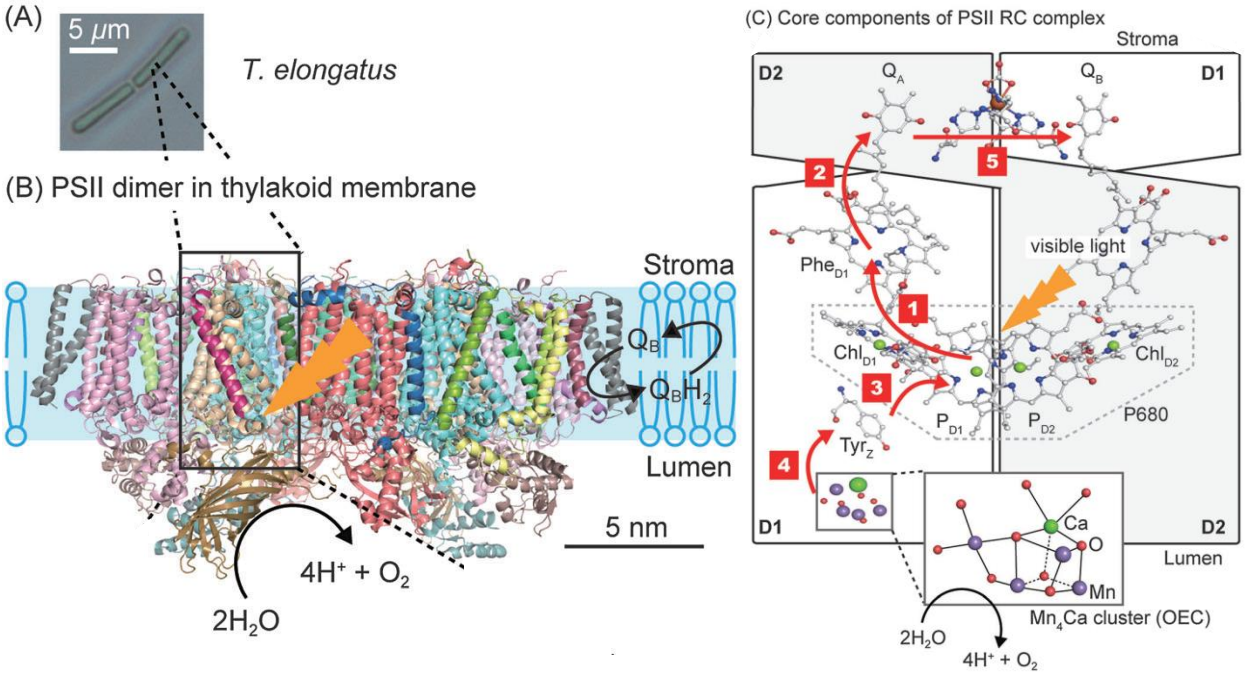

Figure 1.13 (A) Optical micrograph of the thermophilic cyanobacterium *Thermo-synechococcus elongatus* (*T. elongatus*). (B) Schematic representation of the PSII dimer (Protein Data Bank ID: 3ARC) embedded

in the thylakoid membrane. (C) Simplified schematic representation of the RC complex with the D1 (PsbA), D2 (PsbD) subunits and core components involved in photosynthetic electron transfer. Red arrows indicate the direction of electron transfer.[114]

With the expectation to construct the Z-scheme system, *Photosystem II* in *Spinach* has been engaged for water oxidation system and to couple with semiconductors. However, our initial efforts failed to detect the oxygen evolution over the photosystem II membrane protein exclusively in water under one-sun. The small yield of *Photosystem II* extracted from plants and the shorter lives after isolation from the cell might account for the problem.

Compared with photocatalysis, photoelectrochemical method provides a higher sensitivity and the ability to probe the small changes of the catalyst surface and just a small amount of catalysts can yield a good data.[116] In previous studies, the majority of *Photosystem II*-based electrodes are hybridized with gold electrodes[116, 117] or carbon nanomaterials[118-120] as the substrates. Although the modification or hybridization can improve the photoresponse of *Photosystem II* by promoting the electron transfer between the proteins and electrodes, the non-responsive electrodes or nanotubes/graphene made no contribution to the photocurrent under illumination, and prevented the affinity of protein coverage. Thus, researchers in the photocatalytic field are motivated to hybridize the *Photosystem II* enzymes with light-responsive semiconductors.

Also, the redox mediators are usually involved to fulfill the cyclic electron flows to overcome the poor electron trasfer, which, however, are not environmentally friendly and expected in artificial leaf. Hybridizing the enzyme with a suitable semiconductor might allow for a favorable electron and energy transfer. In the past four decades, research on metal oxides semiconductors such as TiO_2, [14] Fe_2O_3,[121, 122] WO_3,[123, 124] $SrTiO_3$,[125, 126] $BiVO_4$[127-129] and other oxides have sprout out for photo-driven water oxidation. Until now, only a few published reports have engaged semiconductors to enhance the photocurrents of *Photosystem II*-based photoanodes. TiO_2 and Fe_2O_3 were attempted as the prominent

photocatalysts to couple with *Photosystem II* but only the photocurrents in the scale of nanoampere were produced.[130] More exquisite design and optimized assemblies between semiconductors and the high-specificity photosynthetic biocatalytic organisms for efficient electron transfer are expected to push forward the construction of the "Photosystem II".

1.4 Research motivation and thesis organization

Mimicking the natural plant, artificial photosynthesis offers a promising strategy for the management of carbon balance on the earth. The harnessment of solar energy and photocatalytic conversion into value-added chemical fuels is an attractive and sustainable approach to alleviate the global energy and environmental problem. Involved with the challenging CO_2 fixation and sluggish water oxidation, the processes do not occur readily. Towards the ultimate goal to construct artificial leaf for photosynthesis, either "Photosystem I" or " Photosystem II" necessitates investigation and rational design. With a fairly negative conduction band edge, zinc sulfide (ZnS) is regarded as a promising photocatalyst to carry out the CO_2 reduction. With a high TOF in oxygen evolution, the photosynthetic membrane protein is attempted to assemble with semiconductors as the "Photosystem II". However, the limited light absorption and lack of active sites incentivize us to carefully examine the two promising catalysts into effective apparatus. Thus, the thesis focused on investigation of ZnS photocatalysts and *Photosystem II* with modulation on active sites and light absorption towards efficient catalytic performance for photosynthesis.

The dissertation is divided into seven chapters. A summary of the remaining six chapters is as follows:

Chapter 2. Fabricating colloidal ZnS:Cu nanocrystal photocatalyst for highly efficient solar-light-powered CO_2 reduction

Though ZnS is an excellent host for photocatalytic CO_2 reduction, the wide bandgap and ultraviolet absorption limits its efficiency. In this chapter, colloidal Cu-doped ZnS (ZnS:Cu) nanocrystals are constructed in the aqueous solution and performed as an excellent visible-light-responsive photocatalyst. With surface area and large amount of sulfur vacancies, CO_2 is successfully photocatalytically converted

into formic acid (HCOOH) over the ZnS:Cu nanocrystals in all-inorganic reactant environment under solar irradiation.

Chapter 3. Probing the role of nickel dopant in aqueous colloidal ZnS nanocrystals for efficient solar-driven CO_2 reduction

With the consideration that the formation energy of sulfur vacancy doping with Cu and Ni are different, another visible-light responsive aqueous colloidal Ni-doped ZnS (ZnS:Ni) is constructed and loaded with Cd^{2+}. A high selectivity and a remarkable quantum efficiency are obtained over Cd^{2+}/ZnS:Ni colloidal. This chapter also highlights that the presence of Ni dopant can modulate the amounts of anion vacancies (sulfur vacancies) induced by the loose structure of colloidal aggregates architecture as well as the electronic states of sulfur vacancy in the vicinity of dopants by density functional theory (DFT) calculation, electron spin resonance (ESR) and photoluminescence (PL) spectroscopy.

Chapter 4. Zinc-cadmium exchange induced isolated sites for efficient CO_2 conversion in aqueous solution

From the previous work, it was found the Cd^{2+}-loaded ZnS bear a high activity and selectivity of CO_2 conversion to formate acid. However, the mechanism by which the colloidal ZnS nanocrystals loaded with Cd^{2+} induced a remarkable enhancement in the selective production of formate was elusive. This chapter focuses on the Cd status and investigates its effect systematically. To elucidate the origin of the high CO_2 reduction rate over the Cd^{2+} modified photocatalysts, spectroscopic evidences are presented using the X-ray absorption fine structure (XAFS), photoluminescence (PL) spectroscopy and transient absorption spectroscopy (TAS). The charge densities and CO_2 adsorption of Cd^{2+} modified ZnS (111) and (110) planes are computed by DFT method. In addition, the CO_2 reduction pathways are disclosed by *in situ* attenuated total reflectance-infrared (ATR-IR) spectroscopy and free energetic configurations.

Chapter 5. Cation vacancy-initiated CO_2 photoactivation over ZnS for efficient formate production

In this chapter, cation surface vacancies are exclusively incorporated on the outmost layers of ZnS by

acid etching, reserving the charge transportation capability in the bulk. Photoluminescence (PL) spectra, electron paramagnetic resonance (EPR) spectra and X-ray photoelectron (XPS) spectra are used to confirm the vacancy species as the Zn vacancies, which act as the trap and activation sites for CO_2 molecules. *In situ* attenuated total reflection-infrared (ATR-IR) spectroscopy and density functional theoretical (DFT) calculations are employed to give a better understanding of the role of surface cation vacancies in the photocatalytic CO_2 reduction reaction and the high selectivity in the presence of HER.

Chapter 6. Interfacing photosynthetic membrane protein with WO_3 for solar water oxidation

Among the hundreds of photosynthetic complex, the membrane protein, *Photosystem II* (PS II), is exclusively responsible for oxygen generation from water. But previous PS II-based inorganic photoanodes were either involved with non-photo-responsive substrates or merely producing photocurrents in the scale of nanoampere. Also, redox mediators were often engaged to fulfill the electron redox cycles between proteins and the inorganic substrates. In this chapter, mesoporous WO_3 photoelectrode, of which the conduction band lies further than the above substrates from the reduction potential of PS II, was constructed as the matrix to interface with PS II, letting the electron transfer along the energy cascade and achieving higher efficiency of water oxidation under solar light.

Chapter 7. General conclusion and future prospects

This chapter makes an overall summary and conclusion of the dissertation. The future prospects based on this work are also presented in this chapter.

References

[1] S.C. Roy, O.K. Varghese, M. Paulose, C.A. Grimes, ACS Nano, 4 (2010) 1259-1278.

[2] D.T. Whipple, P.J.A. Kenis, J. Phys. Chem. Lett., 1 (2010) 3451-3458.

[3] N.S. Spinner, J.A. Vega, W.E. Mustain, Catal.Sci. Technol.y, 2 (2012) 19-28.

[4] D. Kim, K.K. Sakimoto, D. Hong, P. Yang, Angew. Chem. Int. Ed., 54 (2015) 3259-3266.

[5] H. Zhang, G. Liu, L. Shi, H. Liu, T. Wang, J. Ye, Nano Energy, 22 (2016) 149-168.

[6] G.A. Olah, G.K.S. Prakash, A. Goeppert, J. Am. Chem. Soc., 133 (2011) 12881-12898.

[7] J. J. Concepcion, R.L. House, J.M. Papanikolas, T.J. Meyer, Proc. Natl. Acad. Sci., 109 (2012) 15560-15564.

[8] A. J. Bard, J. Photochem., 10 (1979) 59-75.

[9] R.E. Blankenship, D.M. Tiede, J. Barber, G.W. Brudvig, G. Fleming, M. Ghirardi, M.R. Gunner, W. Junge, D.M. Kramer, A. Melis, T.A. Moore, C.C. Moser, D.G. Nocera, A.J. Nozik, D.R. Ort, W.W. Parson, R.C. Prince, R.T. Sayre, Science, 332 (2011) 805.

[10] P.D. Tran, L.H. Wong, J. Barber, J.S.C. Loo, Energy Environm. Sci., 5 (2012) 5902-5918.

[11] R.L. Cook, R.C. MacDuff, A.F. Sammells, J. Electrochem. Soc., 135 (1988) 3069-3070.

[12] C. Chapados, D. Germain, R.M. Leblanc, Biophys. Chem., 12 (1980) 189-198.

[13] A. Fujishima, K. Honda, Nature, 238 (1972) 37-38.

[14] H. Tong, S. Ouyang, Y. Bi, N. Umezawa, M. Oshikiri, J. Ye, Adv. Mater., 24 (2012) 229-251.

[15] A. Kudo, Y. Miseki, Chem. Soc. Rev., 38 (2009) 253-278.

[16] W. Kim, B.A. McClure, E. Edri, H. Frei, Chem. Soc. Rev., 45 (2016) 3221-3243.

[17] A. Iwase, S. Yoshino, T. Takayama, Y.H. Ng, R. Amal, A. Kudo, J. Am. Chem. Soc., 138 (2016) 10260-10264.

[18] P.K. Mohapatra, N.R. Singh, Photosynth. Res., 123 (2015) 105-114.

[19] S.K. Ravi, S.C. Tan, Energy Environ. Sci., 8 (2015) 2551-2573.

[20] X. Meng, T. Wang, L. Liu, S. Ouyang, P. Li, H. Hu, T. Kako, H. Iwai, A. Tanaka, J. Ye, Angew. Chem. Int. Ed., 53 (2014) 11478-11482.

[21] X. Meng, L. Liu, S. Ouyang, H. Xu, D. Wang, N. Zhao, J. Ye, Adv. Mater., 28 (2016) 6781-6803.

[22] X. Chang, T. Wang, J. Gong, Energy Environ. Sci., 9 (2016) 2177-2196.

[23] S. Xie, Q. Zhang, G. Liu, Y. Wang, Chem. Commun., 52 (2016) 35-59.

[24] J. Qiao, Y. Liu, F. Hong, J. Zhang, Chem. Soc. Rev., 43 (2014) 631-675.

[25] H. Yoneyama, K. Sugimura, S. Kuwabata, J. Electroanal. Chem. Interfacial Electrochem., 249 (1988) 143-153.

[26] D.D. Zhu, J.L. Liu, S.Z. Qiao, Adv. Mater., 28 (2016) 3423-3452.

[27] I. Willner, D. Mandler, J. Am. Chem. Soc., 111 (1989) 1330-1336.

[28] W.M. Latimer, The oxidation states of the elements and their potentials in aqueous solutions, Prentice-Hall, inc., New York, 1938.

[29] B. Hammer, J.K. Norskov, Nature, 376 (1995) 238-240.

[30] B. Hammer, J.K. Nørskov, Theoretical surface science and catalysis—calculations and concepts, Advances in Catalysis, Academic Press2000, pp. 71-129.

[31] G. Ertl, H. Knözinger, F. Schüth, J. Weitkamp, Handbook of heterogeneous catalysis: 8 volumes, wiley-vch2008.

[32] M.T.M. Koper, J. Electroanal. Chem., 660 (2011) 254-260.

[33] M.T.M. Koper, Phys. Chem. Chem. Phys., 15 (2013) 1399-1407.

[34] Y. Hori, H. Wakebe, T. Tsukamoto, O. Koga, Electrochim. Acta, 39 (1994) 1833-1839.

[35] J.L. White, M.F. Baruch, J.E. Pander Iii, Y. Hu, I.C. Fortmeyer, J.E. Park, T. Zhang, K. Liao, J. Gu, Y. Yan, T.W. Shaw, E. Abelev, A.B. Bocarsly, Chem. Rev., 115 (2015) 12888-12935.

[36] M.T.M. Koper, Chem. Sci., 4 (2013) 2710.

[37] Y. Taniguchi, H. Yoneyama, H. Tamura, Bull. Chem. Soc. Jpn., 55 (1982) 2034-2039.

[38] V. Guruswamy, J.O.M. Bockris, Int. J. Energy Res., 3 (1979) 397-399.

[39] A.B. Muñoz-García, E.A. Carter, J. Am. Chem. Soc., 134 (2012) 13600-13603.

[40] N. Arai, N. Saito, H. Nishiyama, K. Domen, H. Kobayashi, K. Sato, Y. Inoue, Catal. Today, 129 (2007) 407-413.

[41] D. Wang, A. Pierre, M.G. Kibria, K. Cui, X. Han, K.H. Bevan, H. Guo, S. Paradis, A.R. Hakima, Z. Mi, Nano Lett., 11 (2011) 2353-2357.

[42] M.G. Kibria, S. Zhao, F.A. Chowdhury, Q. Wang, H.P. Nguyen, M.L. Trudeau, H. Guo, Z. Mi, Nat. Commun., 5 (2014) 3825.

[43] M. Szklarczyk, J. Sobkowski, J. Pacocha, J. Electroanal. Chem. Interfacial Electrochem., 215 (1986) 307-316.

[44] I. Sullivan, B. Zoellner, P.A. Maggard, Chem. Mater., 28 (2016) 5999-6016.

[45] C.W. Li, J. Ciston, M.W. Kanan, Nature, 508 (2014) 504-507.

[46] Y. Chen, C.W. Li, M.W. Kanan, J. Am. Chem. Soc., 134 (2012) 19969-19972.

[47] M. Ma, B.J. Trześniewski, J. Xie, W.A. Smith, Angew. Chem. Int. Ed., 55 (2016) 9748-9752.

[48] Y. Chen, M.W. Kanan, J. Am. Chem. Soc., 134 (2012) 1986-1989.

[49] S. Gao, Y. Lin, X. Jiao, Y. Sun, Q. Luo, W. Zhang, D. Li, J. Yang, Y. Xie, Nature, 529 (2016) 68-71.

[50] X. Wang, K. Maeda, A. Thomas, K. Takanabe, G. Xin, J.M. Carlsson, K. Domen, M. Antonietti, Nat. mater., 8 (2009) 76-80.

[51] R. Kuriki, H. Matsunaga, T. Nakashima, K. Wada, A. Yamakata, O. Ishitani, K. Maeda, J. Am. Chem. Soc.y, 138 (2016) 5159-5170.

[52] J. Lin, Z. Pan, X. Wang, ACS Sustain. Chem. Eng., 2 (2014) 353-358.

[53] K. Li, B. Peng, T. Peng, ACS Catal., 6 (2016) 7485-7527.

[54] D.H. Won, J. Chung, S.H. Park, E.-H. Kim, S.I. Woo, J. Mater. Chem. A, 3 (2015) 1089-1095.

[55] Y.J. Jang, J.-W. Jang, J. Lee, J.H. Kim, H. Kumagai, J. Lee, T. Minegishi, J. Kubota, K. Domen, J.S. Lee, Energ. Environ. Sci., 8 (2015) 3597-3604.

[56] Y. Hori, Electrochemical CO2 Reduction on Metal Electrodes, in: C.G. Vayenas, R.E. White, M.E. Gamboa-Aldeco (Eds.) Modern Aspects of Electrochemistry, Springer New York, New York, NY, 2008, pp. 89-189.

[57] R. Zhou, M.I. Guzman, J. Phys. Chem. C, 118 (2014) 11649-11656.

[58] Z. Fang, S. Weng, X. Ye, W. Feng, Z. Zheng, M. Lu, S. Lin, X. Fu, P. Liu, ACS Appl. Mater. Interfaces, 7 (2015) 13915-13924.

[59] A. Kudo, M. Sekizawa, Catal. Lett. 58 (1999) 241-243.

[60] A. Kudo, M. Sekizawa, Chem. Commun., (2000) 1371-1372.

[61] I. Tsuji, A. Kudo, J. Photochem. Photobiol. A: Chem., 156 (2003) 249-252.

[62] C. Xing, Y. Zhang, W. Yan, L. Guo, Int. J. Hydrogen Energy, 31 (2006) 2018-2024.

[63] I. Tsuji, H. Kato, H. Kobayashi, A. Kudo, J. Am. Chem. Soc., 126 (2004) 13406-13413.

[64] I. Tsuji, H. Kato, H. Kobayashi, A. Kudo, J. Phys. Chem. B, 109 (2005) 7323-7329.

[65] I. Tsuji, H. Kato, A. Kudo, Chem. Mater., 18 (2006) 1969-1975.

[66] Z. Li, T. Dong, Y. Zhang, L. Wu, J. Li, X. Wang, X. Fu, J. Phys. Chem. C, 111 (2007) 4727-4733.

[67] J. Zhang, J. Yu, M. Jaroniec, J.R. Gong, Nano Lett., 12 (2012) 4584-4589.

[68] M. Jagadeeswararao, S. Dey, A. Nag, C.N.R. Rao, J. Mater. Chem. A, 3 (2015) 8276-8279.

[69] Y. Chen, S. Zhao, X. Wang, Q. Peng, R. Lin, Y. Wang, R. Shen, X. Cao, L. Zhang, G. Zhou, J. Li, A. Xia, Y. Li, J. Am. Chem. Soc., 138 (2016) 4286-4289.

[70] D.P. Leonard, H. Pan, M.D. Heagy, ACS Appl. Mater. Interfaces, 7 (2015) 24543-24549.

[71] G. Wang, B. Huang, Z. Li, Z. Lou, Z. Wang, Y. Dai, M.H. Whangbo, Sci. Rep., 5 (2015) 8544.

[72] M. Kanemoto, T. Shiragami, C. Pac, S. Yanagida, J. Phys. Chem., 96 (1992) 3521-3526.

[73] H.K. Petra Johne, J. Photochem. Photobiol. A: Chem., 111 (1997) 223-228.

[74] Y.i. S. Yanagida, Y. Miyake, T. Shiragami, C. Pac, J. Phys. Chem, 93 (1989) 2576-2582.

[75] M. Kanemoto, H. Hosokawa, Y. Wada, K. Murakoshi, S. Yanagida, T. Sakata, H. Mori, M. Ishikawa, H. Kobayashi, J. Chem. Soc., Faraday Trans., 92 (1996) 2401-2411.

[76] B.R. Eggins, P.K. Robertson, E.P. Murphy, E. Woods, J.T. Irvine, J. Photochem. Photobiol.y A: Chem., 118 (1998) 31-40.

[77] H. Kisch, P. Lutz, Photochem. Photobiol. Sci., 1 (2002) 240-245.

[78] X. Meng, Q. Yu, G. Liu, L. Shi, G. Zhao, H. Liu, P. Li, K. Chang, T. Kako, J. Ye, Nano Energy, 34 (2017) 524-532.

[79] D. Guzmán, M. Isaacs, I. Osorio-Román, M. Garcá, J. Astudillo, M. Ohlbaum, ACS Appl.Mater. Interfaces, 7 (2015) 19865-19869.

[80] J. Yang, H. Han, C. Li, Acc. Chem. Res., (2012).

[81] H. Pang, L. Liu, S. Ouyang, H. Xu, Y. Li, D. Wang, Int. J. Photoenerg., 2014 (2014) 1-6.

[82] J. Ran, M. Jaroniec, S.Z. Qiao, Adv. Mater., 30 (2018).

[83] K. Adachi, K. Ohta, T. Mizuno, Sol. Energy, 53 (1994) 187-190.

[84] L. Liu, F. Gao, H. Zhao, Y. Li, Appl. Catal. B: Environ., 134-135 (2013) 349-358.

[85] P.-W. Pan, Y.-W. Chen, Catal. Commun., 8 (2007) 1546-1549.

[86] C.-W. Tsai, H.M. Chen, R.-S. Liu, K. Asakura, T.-S. Chan, J. Phys. Chem. C, 115 (2011) 10180-10186.

[87] X.-F. Yang, A. Wang, B. Qiao, J. Li, J. Liu, T. Zhang, Acc.Chem. Res., 46 (2013) 1740-1748.

[88] H. Zhang, J. Wei, J. Dong, G. Liu, L. Shi, P. An, G. Zhao, J. Kong, X. Wang, X. Meng, J. Zhang, J. Ye, Angew. Chem. Int. Ed., 55 (2016) 14310-14314.

[89] G. Gao, Y. Jiao, E.R. Waclawik, A. Du, J. Am. Chem. Soc., 138 (2016) 6292-6297.

[90] Z. Chen, E. Vorobyeva, S. Mitchell, E. Fako, M.A. Ortuno, N. Lopez, S.M. Collins, P.A. Midgley, S. Richard, G. Vile, J. Perez-Ramirez, Nat. nanotechnol., 13 (2018) 702-707.

[91] G. Zhao, W. Zhou, Y. Sun, X. Wang, H. Liu, X. Meng, K. Chang, J. Ye, Appl. Catal. B: Environ., 226 (2018) 252-257.

[92] G. Pacchioni, Chemphyschem, 4 (2003) 1041-1047.

[93] S. Gao, Z. Sun, W. Liu, X. Jiao, X. Zu, Q. Hu, Y. Sun, T. Yao, W. Zhang, S. Wei, Y. Xie, Nat. Commun., 8 (2017) 14503.

[94] K. Xie, N. Umezawa, N. Zhang, P. Reunchan, Y. Zhang, J. Ye, Energ. Environ. Sci., 4 (2011) 4211-4219.

[95] L. Liu, Y. Jiang, H. Zhao, J. Chen, J. Cheng, K. Yang, Y. Li, ACS Catal., 6 (2016) 1097-1108.

[96] Z. Geng, X. Kong, W. Chen, H. Su, Y. Liu, F. Cai, G. Wang, J. Zeng, Angew. Chem. Int. Ed., 57 (2018) 6054-6059.

[97] B. Wang, X. Wang, L. Lu, C. Zhou, Z. Xin, J. Wang, X.-k. Ke, G. Sheng, S. Yan, Z. Zou, ACS Catal., 8 (2017) 516-525.

[98] F. Wang, S. He, H. Chen, B. Wang, L. Zheng, M. Wei, D.G. Evans, X. Duan, J. Am. Chem. Soc., 138 (2016) 6298-6305.

[99] N. Zhang, A. Jalil, D. Wu, S. Chen, Y. Liu, C. Gao, W. Ye, Z. Qi, H. Ju, C. Wang, X. Wu, L. Song, J. Zhu, Y. Xiong, J. Am. Chem. Soc., 140 (2018) 9434-9443.

[100] L. B. Hoch, P. Szymanski, K.K. Ghuman, L. He, K. Liao, Q. Qiao, L.M. Reyes, Y. Zhu, M.A. El-Sayed, C.V. Singh, G.A. Ozin, Proc. Natl. Acad. Sci., 113 (2016) E8011-E8020.

[101] L. Pan, S. Wang, W. Mi, J. Song, J.-J. Zou, L. Wang, X. Zhang, Nano Energy, 9 (2014) 71-79.

[102] D. Chen, M. Qiao, Y.-R. Lu, L. Hao, D. Liu, C.-L. Dong, Y. Li, S. Wang, Angew. Chem. Int. Ed., 57 (2018) 8691-8696.

[103] S. Wang, L. Pan, J.J. Song, W. Mi, J.J. Zou, L. Wang, X. Zhang, J. Am. Chem. Soc., 137 (2015) 2975-2983.

[104] X. Jiao, Z. Chen, X. Li, Y. Sun, S. Gao, W. Yan, C. Wang, Q. Zhang, Y. Lin, Y. Luo, Y. Xie, J. Am. Chem. Soc., 139 (2017) 7586-7594.

[105] S. Gao, B. Gu, X. Jiao, Y. Sun, X. Zu, F. Yang, W. Zhu, C. Wang, Z. Feng, B. Ye, Y. Xie, J. Am. Chem. Soc., 139 (2017) 3438-3445.

[106] M. F. Baruch, J.E. Pander, J.L. White, A.B. Bocarsly, ACS Catal., 5 (2015) 3148-3156.

[107] J. E. Pander, M.F. Baruch, A.B. Bocarsly, ACS Catal., 6 (2016) 7824-7833.

[108] H. Sheng, M.H. Oh, W.T. Osowiecki, W. Kim, A.P. Alivisatos, H. Frei, J. Am. Chem. Soc., 140 (2018) 4363-4371.

[109] J. Fu, B. Zhu, C. Jiang, B. Cheng, W. You, J. Yu, Small, 13 (2017).

[110] G. Liu, X. Meng, H. Zhang, G. Zhao, H. Pang, T. Wang, P. Li, T. Kako, J. Ye, Angew. Chem. Int. Ed., 56 (2017) 5570-5574.

[111] S. Bai, Q. Shao, P. Wang, Q. Dai, X. Wang, X. Huang, J. Am. Chem. Soc., 139 (2017) 6827-6830.

[112] H. Song, X. Meng, T.D. Dao, W. Zhou, H. Liu, L. Shi, H. Zhang, T. Nagao, T. Kako, J. Ye, ACS. Appl. Mater. Interfaces., 10 (2018) 408-416.

[113] Y. Liu, S. Chen, X. Quan, H. Yu, J. Am. Chem. Soc., 137 (2015) 11631-11636.

[114] M. Kato, J.Z. Zhang, N. Paul, E. Reisner, Chem. Soc. Rev., 43 (2014) 6485-6497.

[115] Y. Umena, K. Kawakami, J.-R. Shen, N. Kamiya, Nature, 473 (2011) 55-60.

[116] J. Maly, J. Masojidek, A. Masci, M. Ilie, E. Cianci, V. Foglietti, W. Vastarella, R. Pilloton, Biosens. Bioelectron., 21 (2005) 923-932.

[117] T. Noji, H. Suzuki, T. Gotoh, M. Iwai, M. Ikeuchi, T. Tomo, T. Noguchi, J. Phys. Chem. Lett., 2 (2011) 2448-2452.

[118] J. O. Calkins, Y. Umasankar, H. O'Neill, R. P. Ramasamy, Energ. Environ. Sci., 6 (2013) 1891.

[119] H. A. Dewi, G. Sun, L. Zheng, S. Lim, Phys. Chem. Chem. Phys., 17 (2015) 3435-3440.

[120] P. Cai, X. Feng, J. Fei, G. Li, J. Li, J. Huang, J. Li, Nanoscale, 7 (2015) 10908-10911.

[121] J. E. Thorne, S. Li, C. Du, G. Qin, D. Wang, J. Phys. Chem. Lett., 6 (2015) 4083-4088.

[122] Q. Yu, X. Meng, T. Wang, P. Li, J. Ye, Adv. Funct. Mater., 25 (2015) 2686-2692.

[123] T. Kako, X. Meng, J. Ye, Appl. Catal. A: Gen., 488 (2014) 183-188.

[124] B. M. Klepser, B. M. Bartlett, J. Am. Chem. Soc., 136 (2014) 1694-1697.

[125] S. Ouyang, H. Tong, N. Umezawa, J. Cao, P. Li, Y. Bi, Y. Zhang, J. Ye, J. Am. Chem. Soc., 134 (2012) 1974-1977.

[126] A. Yamakata, M. Kawaguchi, R. Murachi, M. Okawa, I. Kamiya, J. Phys. Chem. C, 120 (2016) 7997-8004.

[127] G. Xi, J. Ye, Chem. Commun., 46 (2010) 1893-1895.

[128] S. Murcia-López, C. Fàbrega, D. Monllor-Satoca, M.D. Hernández-Alonso, G. Penelas-Pérez, A. Morata, J. R. Morante, T. Andreu, ACS Appl. Mater. Interfaces, 8 (2016) 4076-4085.

[129] R. Li, F. Zhang, D. Wang, J. Yang, M. Li, J. Zhu, X. Zhou, H. Han, C. Li, Nat. Commun., 4 (2013) 1432.

[130] W. Wang, Z. Wang, Q. Zhu, G. Han, C. Ding, J. Chen, J. R. Shen, C. Li, Chem. Commun., 51 (2015) 16952-16955.

Chapter 2 Fabricating Colloidal ZnS:Cu Nanocrystal Photocatalyst for Highly Efficient Solar-Light-Powered CO_2 Reduction

2.1 Introduction

Solar fuel production from photocatalytic CO_2 represents a promising solution for sustainable energy supply and environmental mitigating on greenhouse gas emission. Unfortunately, the performance of most of semiconductor photocatalysts are far from satisfied in this respect. Due to the harsh requirements from both thermodynamics and kinetics aspects, high conduction band (CB) potential and good activation ability to CO_2 molecules are indispensable when an efficient CO_2 photoreduction is expected. In order to realize appreciable reaction rate of CO_2 photoreduction under visible light, a popular strategy in the recent studies attempts to couple high CB inorganic semiconductors with organic complexes as photosensitizer/electrocatalyst in the presence of organic reaction medium and organic sacrificial donors.[1, 2] For such organic environment, firstly, valuable sacrificial organic compounds are generally necessary and make the overall CO_2 reduction reaction uneconomical. Secondly, organic matters can also lead to serious interference of CO_2 reduction product identification. Lastly, the functional organic complexes are apt to be deactivated by the photo-corrosion of themselves or photo-oxidation of adjacent inorganic semiconductors, impairing their long term reaction durability.[3] Therefore, it remains very attractive and challenging to develop a photocatalyst that can achieve efficient and stable CO_2 conversion in all-inorganic aqueous reaction medium under mild irradiation input, such as visible light at laboratory or solar light.

Early studies have shown that quantum efficiency of semiconductors for CO_2 photoreduction under excitation wavelength is closely related to CB potentials.[4] Exactly for this reason, among various inorganic semiconductors, colloidal ZnS shows matchless performance. High CB potential and active surface structure enable colloidal ZnS to be a veritably “efficient photocatalyst” for CO_2 conversion.[5]

However, the large band gap of colloidal ZnS determined that it can only be operated under UV light. In order to design an exceptionally efficient and solar light active CO_2 reduction photocatalyst, an ideal strategy is to take the advantages of ZnS matrix and further modulate its energy band structure and surface reactivity. Many ZnS based visible light active photocatalysts have been developed previously at the aim of photocatalytic hydrogen evolution reaction (HER), such as ZnS-$CuInS_2$-$AgInS_2$ and ZnS-CdS solid solution systems, and Ni or Pb doped ZnS, etc.[6] For preparing these sulfide photocatalysts, hydrothermal or heat treatment is required to get high crystallinity. Although a crystalline structure decreased the recombination of photo-excited carriers and increased the activity of photocatalytic HER, it unexpectedly reduced the amount of intrinsically reactive surface structure for selective CO_2 reduction during crystallization process.[5] Therefore, a CO_2-reduction-oriented ZnS photocatalyst should be more favorably prepared by heating-free procedure to retain its reactive surface structure.

Cu doped ZnS (noted as ZnS:Cu for clarity) can be easily prepared in aqueous phase at room temperature.[7] HER can proceed over ZnS:Cu in aqueous solution in the absence of noble metal co-catalysts and sulfur ion (S^{2-}) as sacrificial electron donor, only requiring sulfite ion (SO_3^{2-}) as electron donor which can be obtained from the industrial SO_2 exhaust. It is generally considered that the 3*d* orbital of the formed Cu^+ dopant in ZnS:Cu created an electron donor level above a valence band of ZnS.[7, 8] Since the doping of Cu narrows the band gap without decreasing CB level, in principle, high reduction potential of ZnS can be retained for potentially efficient CO_2 reduction. Motivated by such speculation, we developed an exceptionally efficient and solar-light-active photocatalyst based on colloidal ZnS for CO_2 reduction in all-inorganic aqueous reaction system. Two functional elements, Cu and Cd, which are adjacent to the Zn in periodic table, were respectively used as dopant to modulate the band structure and cocatalyst for selective CO_2 reduction (noted as Cd/ZnS:Cu for clarity). Cu doping expanded the photoabosorption of photocatalyst into visible light region and the simultaneous Cd^{2+} surface modification significantly improved the activity of CO_2 reduction with excellent formic acid selectivity (see scheme 2.1).

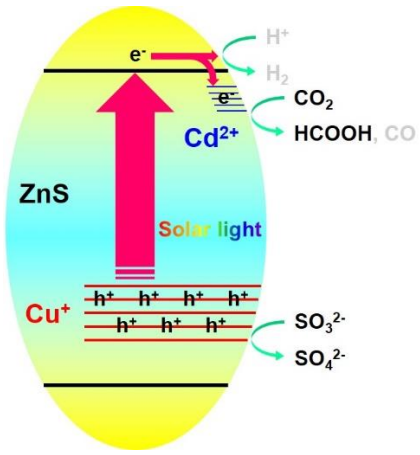

Scheme 2.1 Design principle of efficient solar light active colloidal Cd/ZnS:Cu photocatalyst.

2.2 Experimental section

2.2.1 Synthesis of ZnS:Cu colloidal nanocrystals

Colloidal Cu-doped ZnS (ZnS:Cu) photocatalysts were fabricated by pouring the Na_2S solution (0.5 M) into equivalent volume of the mixture solution of $ZnSO_4$ (0.5 M) and a certain amount (0.1%, 0.2%, 0.5%, 1.0%, 2.0%, 4.0%) of $CuSO_4$ under vigorous stirring. After stirring overnight, the resulted suspensions were rinsed with water and centrifuged. The fresh precipitates were then dispersed in 100 mL ultrapure water (Direct-Q® 3UV) for further photocatalytic activity evaluation.

2.2.2 Characterization

X-ray diffraction (XRD) patterns were recorded on an X-Pert diffractometer equipped with graphite monochromatized Cu-Kα radiation. Transmission electron microscopy (TEM) images were taken by a Tecnai G2 F30 high-resolution transmission electron microscopy. The diffuse reflection spectra of catalysts were measured by UV-Vis spectrophotometer (UV-2600, Shimadzu Co., Japan). The fluorescence spectra were measured by fluorescence spectrophotometer JASCO FP-6500. The excitation wavelength is 280 nm. All the suspensions for the fluorescence spectrum measurements contain 1 $g \cdot L^{-1}$

colloidal ZnS:Cu (0.2%) or colloidal 2.0% Cd/ZnS:Cu (0.2%) in water or CO_2 saturated 0.5 mol·L^{-1} $KHCO_3$ in water.

2.2.3 Photocatalytic CO_2 reduction reaction

The photocatalytic CO_2 reductions over the aqueous colloidal Cu-doped ZnS nanocrystalline suspensions were carried out in a Pyrex glass reaction cell with an upside quartz window linked to a gas-closed circulation system connected to a gas chromatography (GC) (GC-8A, Shimadzu Co., Japan, Carrier gas: Ar) with a thermal conductivity detector (TCD) for online analysis of the H_2 production. 0.001 mol photocatalyst was suspended in 100 mL aqueous solution containing 0.5 M $KHCO_3$ and 0.5 M K_2SO_3 sacrificial reagents. For the formate production, 2.0 wt% $CdSO_4$ cocatalyst were added into the reaction solutions. Prior to the photoreaction, the solution was evacuated until no O_2 and N_2 can be detected. The high-purity CO_2 (99.999%) was purged into the system for several times until the CO_2 adsorption was saturated. An AM 1.5 G solar simulator (WXS-80C-3 AM 1.5G) were used as the light source. The light intensity was measured on a spectroradiometer (Ushio Spectroradiometer, USR-40) for the measurement of apparent quantum efficiency.

2.2.4 Carbon-species products analysis

The CO and CH_4 in the reaction system were sampled and measured with a gas chromatograph (GC-14B, Shimadzu) equipped with a flame ionization detector (FID) according to the standard curves. The contents of H_2 were measured with an online gas chromatograph (GC-8A, Shimadzu) with a TCD detector according to the standard curve. The liquid product HCOOH was quantified by JEOL ECS 400 MHz nuclear magnetic resonance (NMR) spectrometer, in which 0.5 ml electrolyte was mixed with 0.1 ml D_2O (deuterated water), and 0.05 μL dimethyl sulfoxide (DMSO, Sigma, 99.99%) was added as an internal standard. Generally, the production amount of HCOOH was analyzed after the reaction completion of each sample testing.

2.2.5 Isotope tracing

In isotope tracing experiment, $^{13}CO_2$ was injected to the evacuated reaction system and pre-absorbed by reaction solution only containing 0.1 g colloidal ZnS and 0.1 mol L^{-1} K_2SO_3. $KHCO_3$ was not added to the reaction solution to maintain the purity of ^{13}C isotope in carbon source for photocatalytic reaction. In the presence of $KHCO_3$, the carbon source may be contaminated through the exchange effect in equilibrium $CO_2(aq)+H_2O(l)\leftrightarrow H^+(aq)+HCO_3^-(aq)$. Isotope tracing experiments for the identification of ^{13}CO were performed by gas chromatography-mass spectrometry (GC-MS, JMS-K9, JEOL Co., Japan), while $H^{13}COOH$ was confirmed by NMR as described above.

2.2.6 Computational methods

All calculations were performed with Vienna Ab initio Simulation Package (VASP) based on the density-functional theory (DFT). The generalized gradient approximation (GGA-PBE) was used for the exchange-correlation energy with a cutoff energy of 450 eV. The total energy convergence was set to 1×10^{-5} eV/atom, and all atoms are relaxed until the residual force was less than 0.01 eV/Å.

Formation energy calculations for Cu doped ZnS

The supercells for Cu doped ZnS, which consists of 2×2×2 unit cells, are shown in Figure 2.1. For the formation energy calculations, the equation below was used:

$$E_f = E_{Sv} - E_{perfect} + E_S \quad (2\text{-}1)$$

where E_f is the formation energy, E_{Sv} and $E_{perfect}$ are the total energies of supercells with and without S vacancy, E_S is the energy of S atom in bulk sulfur crystal. In this work, the formation energies of S vacancy in perfect supercells and supercells with one or two Cu dopants are calculated.

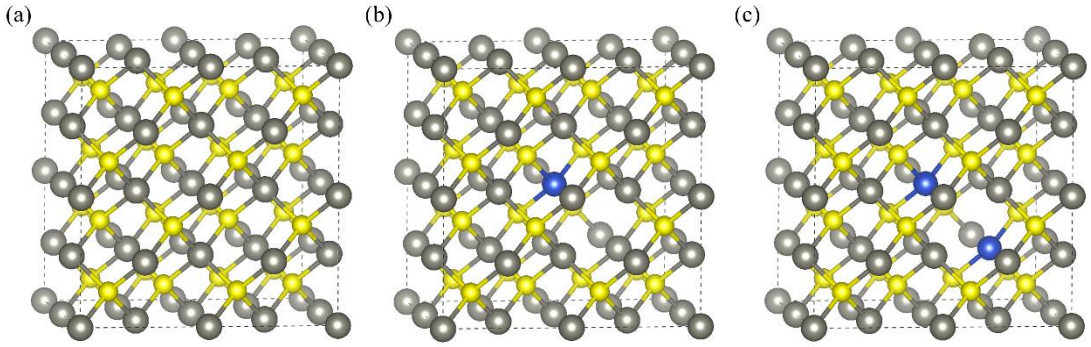

Figure 2.1 The structural models of (a) perfect ZnS supercell, (b) ZnS with one Cu dopant and one S vacancy, and (c) ZnS with two Cu dopants and one S vacancy. The gray, yellow and blue balls indicate Zn, S and Cu atoms, respectively.

2.3 Results and discussion

2.3.1 Characterization of colloidal ZnS:Cu nanocrystals

The freshly prepared colloidal ZnS showed an amorphous feature and large band gap (3.8 eV).[5] These colloidal photocatalysts after continuous stirring during photocatalytic reaction showed broad diffraction peaks of zinc blende structure in their X-ray diffraction (XRD) analysis (Figure 2.2a). Meanwhile, the band gap of the undoped colloidal ZnS reduces from 3.8 eV to 3.6 eV (ca. 345 nm, Figure 2.2b and 2.2c). With increasing the doping concentration of Cu, the colloidal photocatalysts exhibit stronger photoabsorption in visible light region (Figure 2.2b and 2.2c), making enhanced photocatalytic performance possible due to better utilization of solar light.

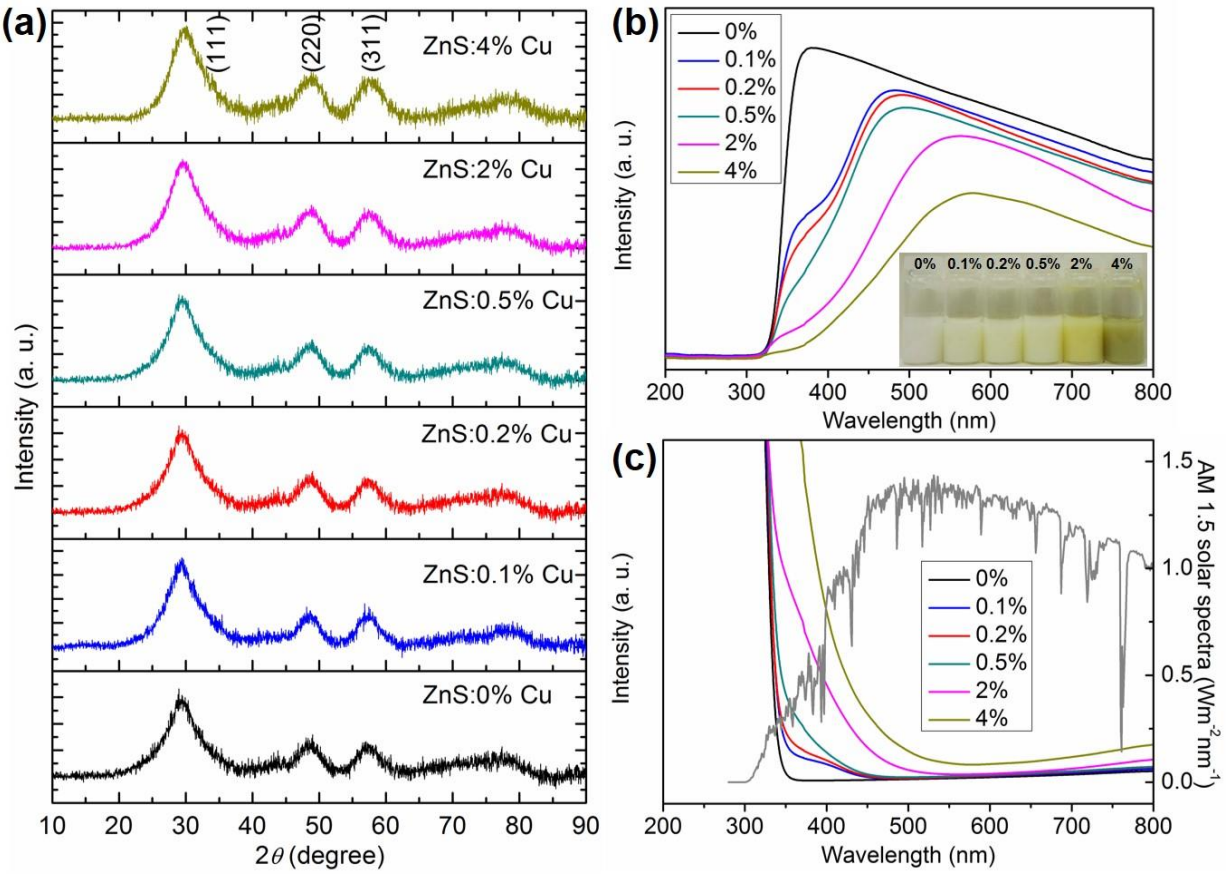

Figure 2.2 Characterizations of colloidal ZnS and ZnS:Cu in the state of wet gel (i.e., precipitate obtained by centrifugation). (a) XRD patterns. (b) UV–Vis reflection spectra of colloidal photocatalysts after reaction. The photographs of photocatalyst suspensions are shown in the inset. (c) UV–Vis absorption spectrum after KM transformation of b.

2.3.2 Photocatalytic activity of colloidal ZnS:Cu nanocrystals

The photocatalytic synthesis gas (CO and H_2 mixture) and formic acid (mainly in the form of formate $HCOO^-$ in the present reaction suspension with pH 7~8) production under solar light are dependent on the doping amount of Cu in colloidal ZnS (Figure 2.3). The optimized doping amount of Cu is 0.2% ~ 0.5%, where both the synthesis gas and formic acid reach their highest production rates. For sulfides, the activation of both proton reduction for HER and CO_2 reduction for CO production are associated with the surface sulfur vacancies (V_S).[9-11] As ZnS:Cu inherits the structure of colloidal ZnS, large amount of surface

defects, especially V_S, can be retained. This is responsible for the high synthesis gas production rate of colloidal ZnS and ZnS:Cu. Moreover, density functional theory (DFT) calculations show that the V_S formation energies could be significantly lowered when Cu substitutes Zn in ZnS, as listed in Table 2.1. This implies that more V_S will form at both surface and bulk of ZnS nanocrystal during Cu doping. Closely resembling the scenario of $Zn_{0.5}Cd_{0.5}S$:Cu analogue in our previous report,[8] two Cu^+ ions will be produced in ZnS when one V_S forms for the reason of charge compensation. Therefore, Cu doping is bifunctional, i.e., narrowing the band gap of ZnS by creating Cu^+ 3*d* energy level (Scheme 2.1) and increasing reactive V_S on ZnS surface for synthesis gas production. A higher Cu doping amount will take adverse effect to the photocatalytic performance possibly because excessive Cu doping has produced too many V_S as the recombination centers of photo-excited carriers in ZnS:Cu nanocrystals.

Table 2.1 Formation energies of S vacancy in undoped and Cu doped ZnS supercells.

	Undoped	One Cu dopant	Two Cu dopants
Formation energy (eV)	2.39	1.58	-0.46

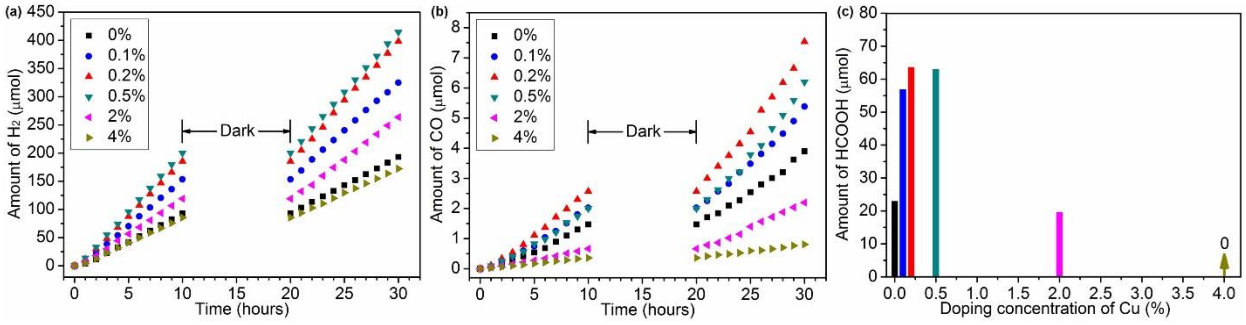

Figure 2.3 Time course of photocatalytic (a) H_2 and (b) CO evolution, and (c) HCOOH production after 20 hours' solar light irradiation over colloidal ZnS and ZnS:Cu.

To confirm the carbon source of products, $^{13}CO_2$ was used as reactant in isotope experiment and injected into the reaction system only containing 0.1 M K_2SO_3 and ZnS:0.2% Cu for pre-absorption. $KHCO_3$ was not added in isotope experiment to maintain the purity of ^{13}C isotope in reaction system. The

gas chromatography-mass spectroscopy (GC-MS) result (Figure 2.4a) clearly shows the formation of ^{13}CO (m/z = 29). Because a little amount of air was inevitably mixed into syringe during the transfer of gas sample into GC-MS, N_2 (m/z = 28) and O_2 (m/z = 32) can be also identified. Analysis of product at liquid phase give an obvious ^{13}C nuclear magnetic resonance (NMR) peak at 170.5 ppm assigned to $H^{13}COO^-$, and a ^{1}HNMR doublet, corresponding to the proton coupled to the ^{13}C in $H^{13}COO^-$ (Figure 2.4b and 2.4c).

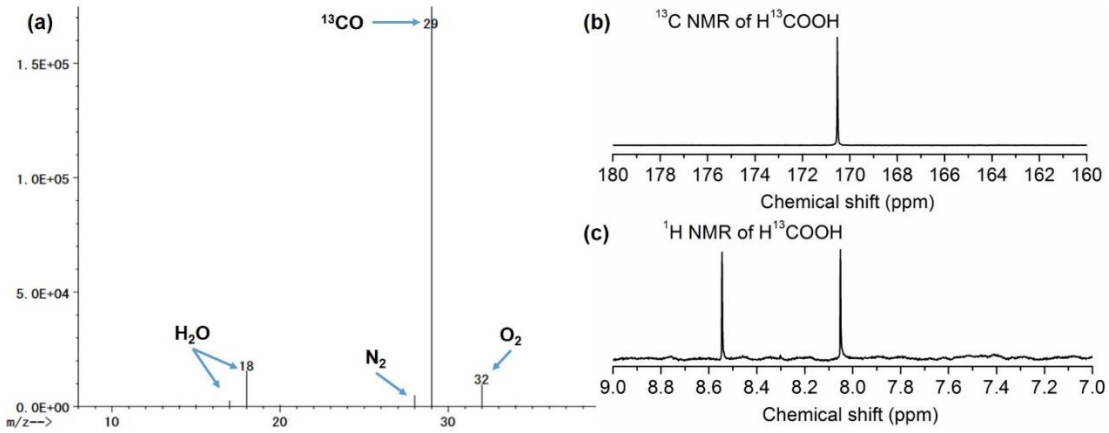

Figure 2.4 Mass spectrum of (a) ^{13}CO, (b) ^{13}C NMR, and (c) ^{1}H NMR spectra of $H^{13}COOH$ produced in isotope tracing experiment.

In order to increase the utilization of photo-generated electrons for selective CO_2 reduction, a 2.0 mol% Cd^{2+} modified ZnS:0.2% Cu photocatalyst was designed (noted as 2.0% Cd/ZnS:0.2% Cu for clarity). The sample can be readily prepared by quantitatively adding cadmium sulfate solution into the reaction suspension containing colloidal ZnS:0.2% Cu. Cd^{2+} modification remarkably improved the CO_2 reduction for selective HCOOH production with respect to synthesis gas (Figure 2.5a-c). The HCOOH production amount of 2.0 % Cd/ZnS:0.2% Cu is 46.7 times higher than ZnS:0.2% Cu. The apparent quantum yield (AQY) of HCOOH was measured under monochromatic UV (381.8 nm, $\lambda_{1/2}$=24.4 nm) and visible light (417.9 nm, $\lambda_{1/2}$=14.4 nm) according to the equation AQY (HCOOH) = N(HCOOH)×2/N(Photons)×100%, where N(HCOOH) and N(Photons) signify the number of HCOOH molecules and the number of incident

photons, respectively. The AQYs of HCOOH over 2% Cd/ZnS:0.2% Cu are 17.8% (381.8 nm) and 5.8% (417.9 nm), and that over 2% Cd/ZnS:0.5% Cu are 23.3% (381.8 nm) and 13.2% (417.9 nm), indicating that, at the wavelength region longer than the absorption edge of colloidal ZnS (345 nm), the AQY rises when increasing the doping amount of Cu from 0.2% to 0.5%. This also implies that the AQY at the wavelength shorter than 345nm should decrease at the same time. Control experiment shows that the CO_2 reduction performance of 2% Cd/ZnS:0.2% Cu is much superior to the homogeneous 2% Cd doped sample, i.e., ZnS:(0.2% Cu+2% Cd), indicating that Cd^{2+} is more favorably used as cocatalyst through surface modification.

Moreover, under present reaction condition, the visible light active colloidal CdS photocatalyst only shows negligible activity for both synthesis gas and HCOOH production, showing that 2% Cd/ZnS:0.2% Cu is a very optimized design. In this work, Cd^{2+} modification on colloidal ZnS:Cu shows exactly same enhancement effect as Cd^{2+} modified colloidal ZnS,[5] revealing that Cu doping did not interfere the unique function of Cd^{2+} ion as an excellent CO_2 reduction selective cocatalyst. In consideration of that the solubility products K_{sp} of CdS ($pK_{sp} \approx 26$) is smaller than that of ZnS ($pK_{sp} \approx 22$), Zn^{2+} at the surface of ZnS nanocrystals will be exchanged by Cd^{2+} ion. It can be estimated that there are only ~16.6 Cd^{2+} ions per ZnS nanocrystal (in 5 nm particle size with 2 mol% Cd loading). However, the fluorescence spectra show that such a few Cd^{2+} ions modification leads to obvious quenching of the broad emission at 380-500 nm resulting from the recombination of photoexcited carries at V_S, which can be further quenched in the presence of carbon source (Figure 2.5d). Therefore, Cd^{2+} modification can effectively separate photogenerated electrons for selective HCOOH production.

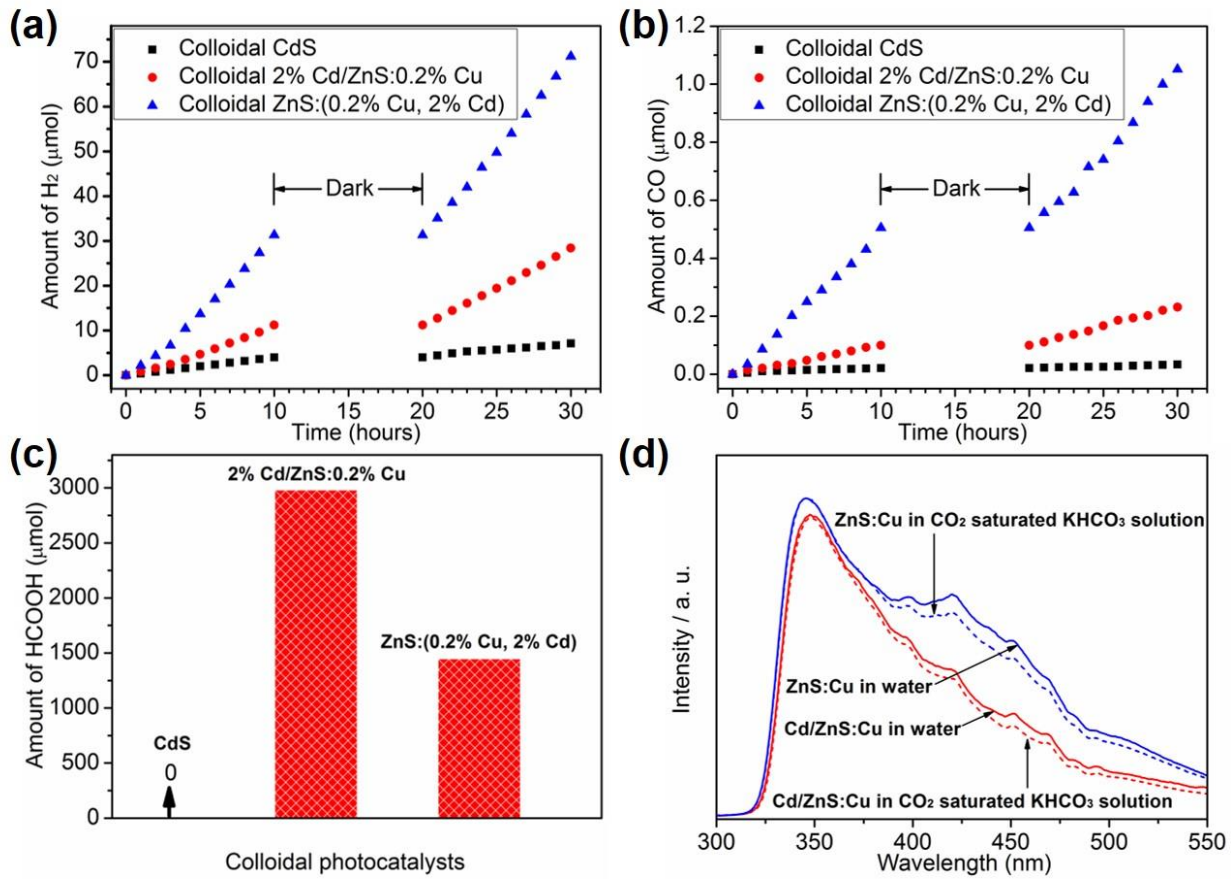

Figure 2.5 Time course of photocatalytic (a) H_2 and (b) CO evolution, and (c) HCOOH production after 20 hours' solar light irradiation over colloidal CdS and 2% Cd/ZnS:0.2% Cu, and ZnS:(0.2% Cu+2% Cd). (d) Fluorescence spectra of ZnS:0.2% Cu and 2% Cd/ZnS:0.2% Cu in water and CO_2 saturated $KHCO_3$ solution.

2.4 Conclusion

In conclusion, we have developed a Cd/ZnS:Cu photocatalyst for efficient photocatalytic CO_2 reduction under solar light. The rationally-designed Cd/ZnS:Cu nanocrystals take both the solar light harvest and CO_2 reduction kinetics into consideration through Cu doping and Cd grafting, respectively. It should be highlighted that Cd/ZnS:Cu possibly represents one of the most active and optimized design of sulfide photocatalysts so far for photocatalytic CO_2 reduction under solar light. Cd/ZnS:Cu as well as the all-inorganic reaction system displays many advantages over the other photocatalysts or reaction systems, including i) high CB potential of photocatalyst (thermodynamic requirement), ii) efficient CO_2 reduction

selective cocatalyst (kinetic requirement), iii) much better solar light absorption compared with bare colloidal ZnS, iv) noble metal and organic medium free, and v) extraordinary convenience in material preparation and photocatalytic reaction procedures. Compared with ZnS:Cu, the other potential constituent elements (such as Ag, Ga, and In) of sulfide photocatalysts are difficult to be prepared by heating-free method to design active sulfide photocatalysts.[6] Due to aforementioned advantages, Cd/ZnS:Cu or ZnS:Cu can be used as an ideal model catalysts for the studies related to photocatalytic CO_2 reduction in future.

References

[1] R. Kuriki, H. Matsunaga, T. Nakashima, K. Wada, A. Yamakata, O. Ishitani, K. Maeda, J. Am. Chem. Soc., 138 (2016) 5159-5170.

[2] K. Sekizawa, K. Maeda, K. Domen, K. Koike, O. Ishitani, J. Am. Chem. Soc., 135 (2013) 4596-4599.

[3] Y. Kou, Y. Nabetani, D. Masui, T. Shimada, S. Takagi, H. Tachibana, H. Inoue, J. Am. Chem. Soc., 136 (2014) 6021-6030.

[4] B.R. Eggins, P.K.J. Robertson, E.P. Murphy, E. Woods, J.T.S. Irvine, J. Photochem. Photobio. A, 118 (1998) 31-40.

[5] X. Meng, Q. Yu, G. Liu, L. Shi, G. Zhao, H. Liu, P. Li, K. Chang, T. Kako, J. Ye, Nano Energy, 34 (2017) 524-532.

[6] A. Kudo, Y. Miseki, Chem. Soc. Rev., 38 (2009) 253-278.

[7] A. Kudo, M. Sekizawa, Catal. Lett., 58 (1999) 241-243.

[8] Z. Mei, B. Zhang, J. Zheng, S. Yuan, Z. Zhuo, X. Meng, Z. Chen, K. Amine, W. Yang, L.W. Wang, W. Wang, S. Wang, Q. Gong, J. Li, F.S. Liu, F. Pan, Nano Energy, 26 (2016) 405-416.

[9] B.-J. Liu, T. Torimoto, H. Yoneyama, J. Photochem. Photobio. A, 113 (1998) 93-97.

[10] H. Li, C. Tsai, A.L. Koh, L. Cai, A.W. Contryman, A.H. Fragapane, J. Zhao, H.S. Han, H.C. Manoharan, F. Abild-Pedersen, J.K. Norskov, X. Zheng, Nat. Mater., 15 (2016) 48-53.

[11] H. Fujiwara, H. Hosokawa, K. Murakoshi, Y. Wada, S. Yanagida, Langmuir, 14 (1998) 5154-5159.

[12] Y. Hori, Electrochemical CO_2 Reduction on Metal Electrodes, in: C. Vayenas, R. White, M. Gamboa-Aldeco (Eds.) Modern Aspects of Electrochemistry, Springer New York 2008, pp. 89-189.

Chapter 3 Probing the Role of Nickel Dopant in Aqueous Colloidal ZnS Nanocrystals for Efficient Solar-Driven CO_2 Reduction

3.1 Introduction

Through constructing an all-inorganic reaction system comprised of the colloidal ZnS, we have achieved a breakthrough of CO_2 conversion into formate with 76% apparent quantum efficiency (280 nm) and 95% HCOOH selectivity.[1] Without any organic surface stabilization, the ZnS particles are quantized with an average diameter of *ca.* 3 nm. The shortened diffusion length within the ultra-small colloidal nanocrystals can slow down the recombination rates of photogenerated electrons and holes.[2] However, its intrinsic wide bandgap of about 3.7 eV determines it exclusively responsive to ultraviolet (UV) region which merely accounts for 4% solar spectrum.[3] It is necessitated to extend its light absorption to visible light region or longer wavelengths. Transition-metal dopants such as Bi, Fe, Pb, Cu, Ni, were reported capable of introducing an additional energy level within the band gap and narrowing the bandgap of ZnS.[4, 5] Thus in the previous chapter, Cu was doped into the colloidal ZnS nanocrystals to narrow the bandgap and realize the visible light response.

Introducing oxygen vacancies has already been demonstrated as an effective avenue to boost the performance of oxide photocatalysts as the vacancy formation can activate the adsorbates and trap the photoexcited electron to suppress the charge recombination, favorable for the catalytic reaction.[6-17] On account of the preparation method, it is envisaged that sulfur vacancies (V_S) intrinsically exist within the synthesized colloidal ZnS samples because S atoms are apt to escape in the form of H-S in such aqueous system, which account for the active sites and exceptional performance. Therefore, the role of elemental dopants is actually quite complicated beyond the light absorption. Previous work pointed out that Cu dopant

changed to Cu^+ and formed one V_S adjacently.[18] But our theoretical calculation surprisingly found the Ni dopant not beneficial for the V_S formation due to an increase of the formation energy.

Herein, Ni, as a noble-metal-free and non-toxic dopant, is selected to modify the electronic structure of ZnS. In this chapter, we constructed another colloidal system of Ni-doped ZnS (ZnS:Ni) nanocrystals in aqueous solutions with loose aggregate architecture furnishing with sufficient surface area and active sites. The interplay between dopant and vacancy also attracts us to look into the effect of Ni doping on V_S where rare reports set foot in, except the modulation of electronic structure. It is investigated and elucidated the correlation between the amount of foreign dopants and the CO_2 reduction performance. Some new perspectives into the CO_2 reduction photocatalyst underpinning the relationship between dopants and vacancies are also given.

3.2 Experimental section

3.2.1 Synthesis of Ni-doped colloidal ZnS nanocrystals

Colloidal ZnS:Ni photocatalysts were fabricated by pouring the Na_2S solution (0.5 M) into equivalent volume of the mixture solution of $ZnSO_4$ (0.5 M) and a certain amount (0.1%, 0.2%, 0.5%, 1.0%, 2.0%, 4.0%) of $NiSO_4$ under vigorous stirring. After stirring overnight, the resulted suspensions were rinsed with water and centrifuged. The fresh precipitates were then dispersed in 100 mL ultrapure water (Direct-Q® 3UV) for further photocatalytic activity evaluation.

3.2.2 Characterization

X-ray diffraction patterns (XRD) were obtained on an X-ray diffractometer (X'pert powder, PANalytical B.V., Netherlands) with Cu-Kα radiation. The morphologies were observed on a field-emission scanning electron microscopy (FE-SEM, S-4800, Hitachi) and a transmission electron microscopy (TEM, FEI Tecnai G2 F30) with a 300 kV accelerating voltage. The diffuse reflectance spectra (DRS) were measured on a Shimadzu UV-2500 spectrophotometer with an integrating sphere.

The absorption spectra were transformed from the DRS spectra via Kubelka-Munk method. The Brunauer–Emmett–Teller (BET) surface area and CO_2 adsorption isotherms were obtained at 77K and room temperature, respectively, over BELsorp II mini (BEL Japan Inc.). The *in situ* attenuated total reflection-Fourier transform infrared (ATR-FTIR) spectroscopy was performed over JASCO FT/IR-6300 with a mercury-cadmium-telluride (MCT) detector and a Ge crystal substrate. The fluorescence (PL) spectra were measured by a fluorescence spectrometer (JASCO FP-6500) with the excitation wavelength of 280 nm over the colloidal ZnS:Ni suspensions of 1.0 $g \cdot L^{-1}$. The time-resolved fluorescence measurements were carried out with the colloidal precipitates over a home-made ps-time resolved luminescence spectroscopy (Marubun Corporation, Japan). X-ray photoelectron spectroscopy (XPS) (PHI Quantera SXM, ULVAC-PHI Inc., Japan) was used to analyse the compositions and valence states of the samples. Electron spin resonance (ESR) measurements were performed on JEOL JES-FA-200 at room temperature.

3.2.3 Photocatalytic CO_2 reduction reaction

The photocatalytic CO_2 reductions over the aqueous colloidal ZnS:Ni nanocrystal suspensions were carried out in a Pyrex glass reaction cell with an upside quartz window linked to a gas-closed circulation system connected to a gas chromatography (GC) (GC-8A, Shimadzu Co., Japan, Carrier gas: Ar) with a thermal conductivity detector (TCD) for online analysis of the H_2 production. 0.001 mol photocatalyst was suspended in 100 mL aqueous solution containing 0.5 M $KHCO_3$ and 0.5 M K_2SO_3 sacrificial reagents. For the formate production, 2.0 wt% $CdSO_4$ cocatalyst was added into each reaction solution. Prior to the photo-reaction, the solution was evacuated until no O_2 and N_2 can be detected. The high-purity CO_2 (99.999%) was purged into the system for several times until the CO_2 adsorption was saturated. An AM 1.5 G solar simulator (WXS-80C-3 AM 1.5G) and 300 W Xe lamp were used as the light source. The light intensity was measured on a spectroradiometer (Ushio Spectroradiometer, USR-40) for the measurement of apparent quantum efficiency.

3.2.4 Carbon-species products analysis

The produced CO and CH_4 were sampled and analysed by GC (GC-14B, Shimadzu Co., Japan) equipped with a flame ionization detector (FID). The formate ions concentration were determined by proton (^1H) spectra on a 400 MHz nuclear magnetic resonance (NMR) spectrometor (ESC-400, JEOL, Japan) using 0.5 mL post-reaction solution supernatant mixed with 0.1 mL deuterated water (D_2O) and 0.05 μL dimethyl sulfoxide (DMSO, Sigma, 99.99%). For isotope tracer measurement, $^{13}CO_2$ was purged in the system. To avoid the confusion of carbon source, the aqueous suspensions only contain 0.5 M K_2SO_3 sacrificial reagents apart from 0.001 mol photocatalyst and a certain amount of Cd^{2+} cocatalyst. The identification of ^{13}CO was conducted on a gas chromatography-mass spectrometry (GC-MS, JMS-K9, JEOL Co., Japan). $H^{13}COOH$ was identified on the carbon (^{13}C) spectrum on the NMR.

3.2.5 Electrochemical measurements

Photoelectrochemical measurements were conducted on a CHI electrochemical workstation ALS/CH model 650A using a three-electrode system with 0.5 M Na_2SO_4 electrolyte (pH=7). For the preparation of working electrode, 1.0 ml of 2.5 mg • mL^{-1} colloidal ZnS suspensions were mixed with 30 μL Nafion® perfluorinated resin solution (Sigma-Aldrich) and sonicated. For the photocurrent measurement, the as-prepared suspensions were deposited on the indium tin oxide (ITO) substrates by spin coating. Platinum and Ag/AgCl (RE-1C; BAS Inc.) were employed as the counter electrode and reference electrode, respectively. An AM 1.5 solar simulator lamp was set as the light source with a light on/off cycle of 10 s. The flatband potential (E_{fb}) of the undoped and doped ZnS was obtained from Mott–Schottky plots at different frequencies (500, 1000, and 2000 Hz).

3.2.6 Theoretical calculations

The calculations of electronic structure were performed based on the plane-waved density functional theory as implemented in a Vienna Ab initio Simulation Package (VASP) code. The generalized gradient

approximation (GGA) in a Perdew-Burke-Ernzerhof (PBE) functional were used for the exchange-correlation potential with a cutoff energy of 450 eV for the valence electrons. For the optical absorption calculations, the HSE06 hybrid functional was used to present the accurate band gap. Substitution of Zn atoms with Ni atom was conducted with a doping percentage of about 3.125 %. The ZnS:Ni (110) surface was simulated using a 2×2 slab model consisting of five atomic layers of ZnS and a 16 Å vacuum region to avoid the interaction between two adjacent slabs. For the calculation of the density of states, 2×2×1 Monkhorst *k*-point meshes were chosen to sample for the Brillouin-zone integrations of the slab model. All atoms are relaxed with the convergence tolerance set to 1×10^{-5} eV per atom and the residual force less than 0.02 eV/Å.

3.3 Results and discussion

3.3.1 Morphology and structure characterization

The colloidal ZnS:Ni photocatalysts with 0 %, 0.1 %, 0.2 %, 0.5 %, 1.0 %, 2.0 % and 4.0 % doping amounts were directly synthesized by controlling the $NiSO_4$ precursor amount in an aqueous-phase co-precipitation process. The morphologies were observed by transmission electron microscopy (TEM) (Figure 3.1a). Figure 3.1a displays that the majority of nanoparticles in colloidal ZnS:Ni are easily agglomerated due to their extremely small dimensions and high surface energy. Despite the severe agglomeration under dehydrated conditions for TEM observation, several isolated nanocrystals are still distinguished as seen in Figure 3.1b. The high-angle annular dark-field (HAADF) image and the energy-dispersive X-ray spectroscopy (EDX) elemental mappings under scanning transmission electron microscopy (STEM) mode exhibits a highly uniform distribution of Zn, S, Ni elements as shown in Figure 3.1c-f, indicating Ni elements are homogeneously doped into the colloidal ZnS:Ni nanocrystals. Observation under the high-resolution TEM (HRTEM) found that the colloidal ZnS:Ni nanocrystals gradually crystallized under the electron beams and showed distinct lattice fringes. The interplanar spacing of the Ni-ZnS is 3.21 Å as marked in Figure 3.1g, in accordance with the analytic result of the selected area

electron diffraction (SAED) in Figure 3.1h which shows the radius of the most distinguished diffraction ring is 0.310 nm, corresponding to (111) crystal plane of the cubic ZnS. Closer examination of the second and third diffraction rings are identified with interplanar spacing of 0.185 nm and 0.158 nm, well assigned to (220) and (311) crystal planes. This result is in well agreement with the three intensive peaks located at 28.6 °, 47.8 °, 56.6 °indexed to 111, 220, 311 diffraction, respectively, in X-ray diffraction (XRD) pattern as present in Figure 3.1i. The XRD pattern clearly showed the as-synthesized ZnS:Ni colloidal nanocrystals are indexed to a typical cubic sphalerite structure (JCPDS No. 77-2100) though the diffractogram is broad. There is no obvious deviation of the peak positions of the XRD patterns with the doping amount increasing from 0 % to 4.0 %, which might be attributed to the reason that the ionic radius of the four-coordinated Ni^{2+} (0.69 Å) is close to that of the Zn^{2+} (0.74 Å).[19] No other discernable impurity peaks are detected, indicating Ni doping well retains the crystal structural phase of cubic ZnS nanocrystals in colloidal system.

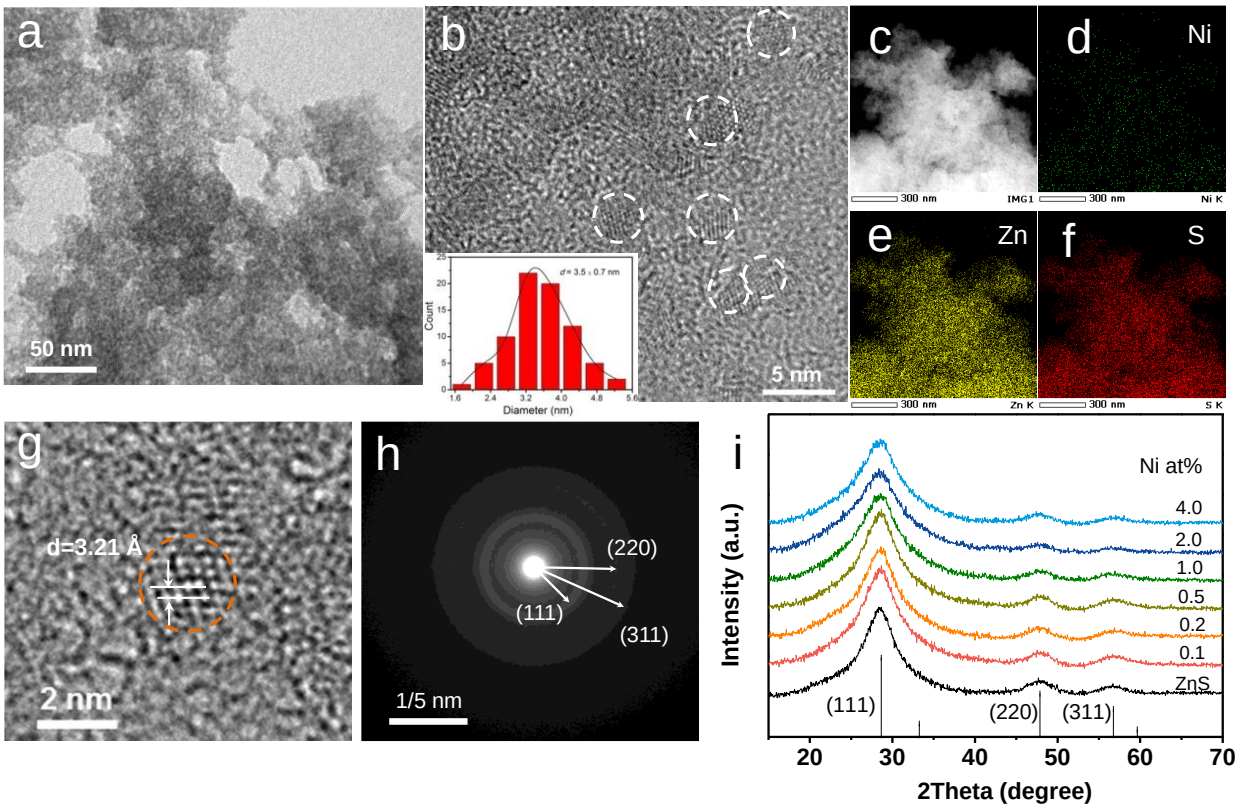

Figure 3.1 Morphological and structural characterization. (a) Bright-field TEM image, (b) HRTEM image (Inset: size distribution), (c) HAADF-STEM image, (d-f) elemental mapping of Ni, Zn, S, (g) HRTEM

image, (h) SAED pattern of the Ni-doped ZnS:Ni (2.0%) colloidal nanocrystals, (i) XRD pattern of the Ni-doped ZnS colloidal with doping amount from 0-4.0 %.

According to the size distribution in high-resolution TEM (HR-TEM) images (Inset of Figure 3.1b), the estimated average size of the colloidal ZnS:Ni nanocrystals is 3.5±0.7 nm, in accord with the derived result from Scherrer's equation based on the X-ray powder diffraction (XRD) spectra, which give an average particle size of *ca*. 3 nm. When dispersing the samples in the liquid phase, the small dimensions can furnish with more surfaces and active sites for the photocatalytic CO_2 reduction. This was testified through BET and volumetric CO_2 uptake measurement, which clarify the Ni doping effect on the surface area and CO_2 adsorption capacity. To diminish the temperature effect on the structure of the low-crystalline nanocrystals, the colloidal ZnS and the ZnS:Ni were dried by freeze-drying instead of heat treatment. As seen from Figure 3.2a, the surface area in the ZnS:Ni (0.2 %) are 145.83 m^2g^{-1}, slightly higher than that of the undoped ZnS (133.30 m^2g^{-1}) but nearly two times higher than that of the ZnS:Ni (2.0 %) samples (60.40 m^2g^{-1}). CO_2 uptake amount comparison also exhibits the same trend as exhibited in Figure 3.2b. However, when small amount of Ni (0.2 %) was doped into the colloidal ZnS, both the surface area and the CO_2 volumetric adsorption are maintained at same level. However, the heavy doping amount like 2.0 % caused an obvious decrease, indicating Ni may diminish the adsorption sites in the colloidal ZnS nanocrystals.

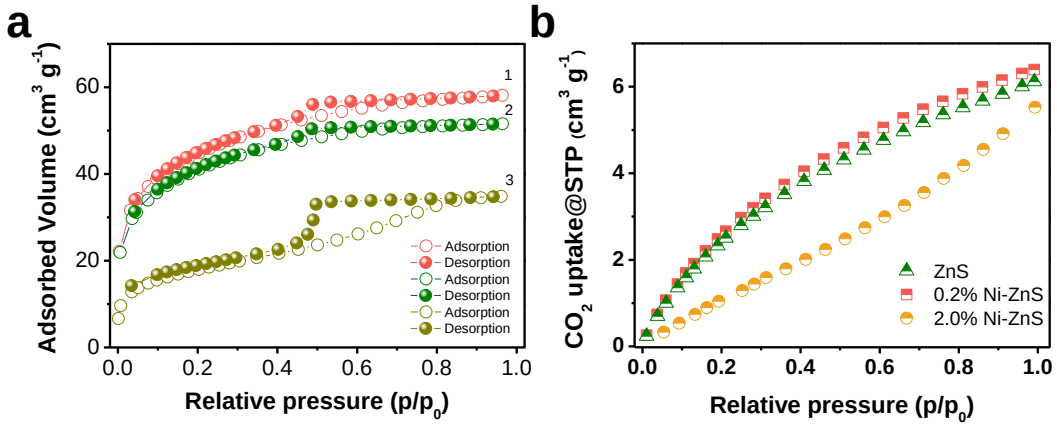

Figure 3.2 (a) BET nitrogen adsorption-desorption isotherms and (b) CO_2 adsorption isotherms for **1**: ZnS:Ni (0.2 %), **2**: undoped ZnS, **3**: ZnS:Ni (2.0 %)

3.3.2 Electronic structure and photophysical property

To gain insight into the electronic structure, we constructed the ZnS:Ni and perfect ZnS supercell slabs to implement the density functional theory (DFT) calculations. The theoretically calculated band structure and projected density of states (PDOS) are displayed in Figure 3.3. Ni dopant introduced an occupied state above the valence band of the pristine ZnS with an additional contribution from S orbitals. The created new energy level within the band gap extend the absorption to visible light range as the simulated optical absorbance spectrum predicts in Figure 3.4a. The UV−Vis absorption spectra (Figure 3.4b) of the ZnS:Ni colloidal crystallites transformed from the diffuse reflectance spectra (DRS) via K-M method possess an intrinsic absorption feature edged at 340 nm and enhanced photo-absorption in the visible light ranging from 340~470 nm, related to the transition from the occupied Ni 3d orbitals to the hybridization of Zn 4s-S 3p orbitals. The accordance of UV−Vis absorption spectra with the simulated optical absorption configuration derived from the electron structure, also testifies that Ni is successfully doped into ZnS crystal lattice. We can also observe from the optical photographs in Figure 3.4c, that the color of the as-synthesized ZnS:Ni colloidal varied from bright yellow to deep yellow as with the doping amount increment from 0.1% to 4.0%.

Herein we have conducted Mott-Schottky measurement and XPS valence band (VB) to roughly estimate the conduction band and valence band edges. From the Mott-Schottky measurement, we obtained the flatband potential for each representative samples. The intersection is the $E_{fb}+k_BT/e$ (V vs. Ag/AgCl), where E_{fb} is the flatband potential, k_b is the Boltzmann constant with the value of 1.380649×10^{-23} J/K, T is the absolute temperature with a value of 298, e is the electronic charge with a value of 1.6021892×10^{-19} C. The potential vs. Ag/AgCl is converted to that vs. NHE (pH=0) using the equation of $E_{NHE}= E(Ag/AgCl)+E^0(Ag/AgCl)$, where $E^0(Ag/AgCl)$ is equal to 0.197 V at 25℃. Therefore, the Fermi level of ZnS, ZnS:Ni (0.1%) and ZnS:Ni (2.0%) is -0.79 V, -0.77 V and -0.72V, respectively.

From XPS valence band spectra, we can roughly determine the distance between the valence band top to Fermi level from the rising edge. The bandgap between Fermi level to the VBM for ZnS, ZnS:Ni (0.1%) and ZnS:Ni (2.0%) is 3.47 eV, 3.13 eV and 2.60 eV, respectively. Therefore, the VB position of ZnS, ZnS:Ni (0.1%) and ZnS:Ni (2.0%) is 2.68 V, 2. 36V and 1.88 V, respectively. It is clear to see the Ni dopant created a new level at the position 0.8 eV above the VB of ZnS, well correlated with what the theoretical simulation predicts.

From the Tauc plots converted from the UV-Vis spectra, the dominant photon energy of the intrinsic transition and the transition from Ni level to CB is 3.59 eV and 2.74 eV, respectively. The CB position is determined at -0.91V and -0.86 V for ZnS and ZnS:Ni (2.0%), respectively. As the Ni effect is to level up the VBM but not impacts the CB, the CB position of ZnS:Ni (0.1%) is estimated at -0.9 V, similar to that of ZnS and ZnS:Ni (2.0%). It is clear to see the Ni dopant created a new level at a position of 0.8 eV above the VBM of ZnS, well correlated with what the theoretical simulation predicts.

It is worth mentioning that the longer wavelength absorption tails in the visible region is ascribed to V_S,[20] attributed to the transition from a newly created midgap state by S_v just below CB to the CB of ZnS, suggesting the abundant V_S within the as-prepared samples. In addition, the tails level off with an increase of the doping amount until the 4.0 % Ni-doped sample, indicating the Ni doping can modulate the mount of V_S within the ZnS:Ni colloidal nanocrystals.

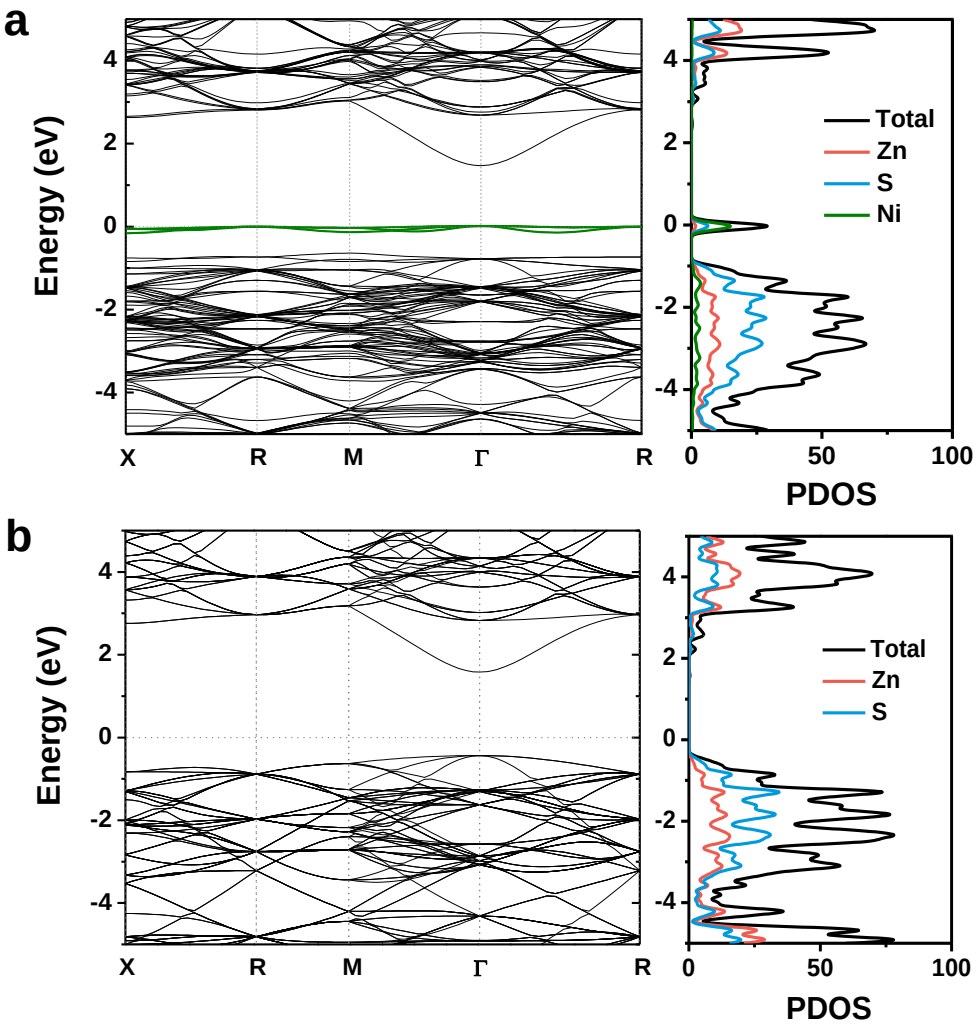

Figure 3.3 The electronic band structure and the decomposition of the total density of states (DOS) into PDOS of Ni, Zn and S orbitals of (a) ZnS:Ni (2.7%) and (b) undoped ZnS, respectively.

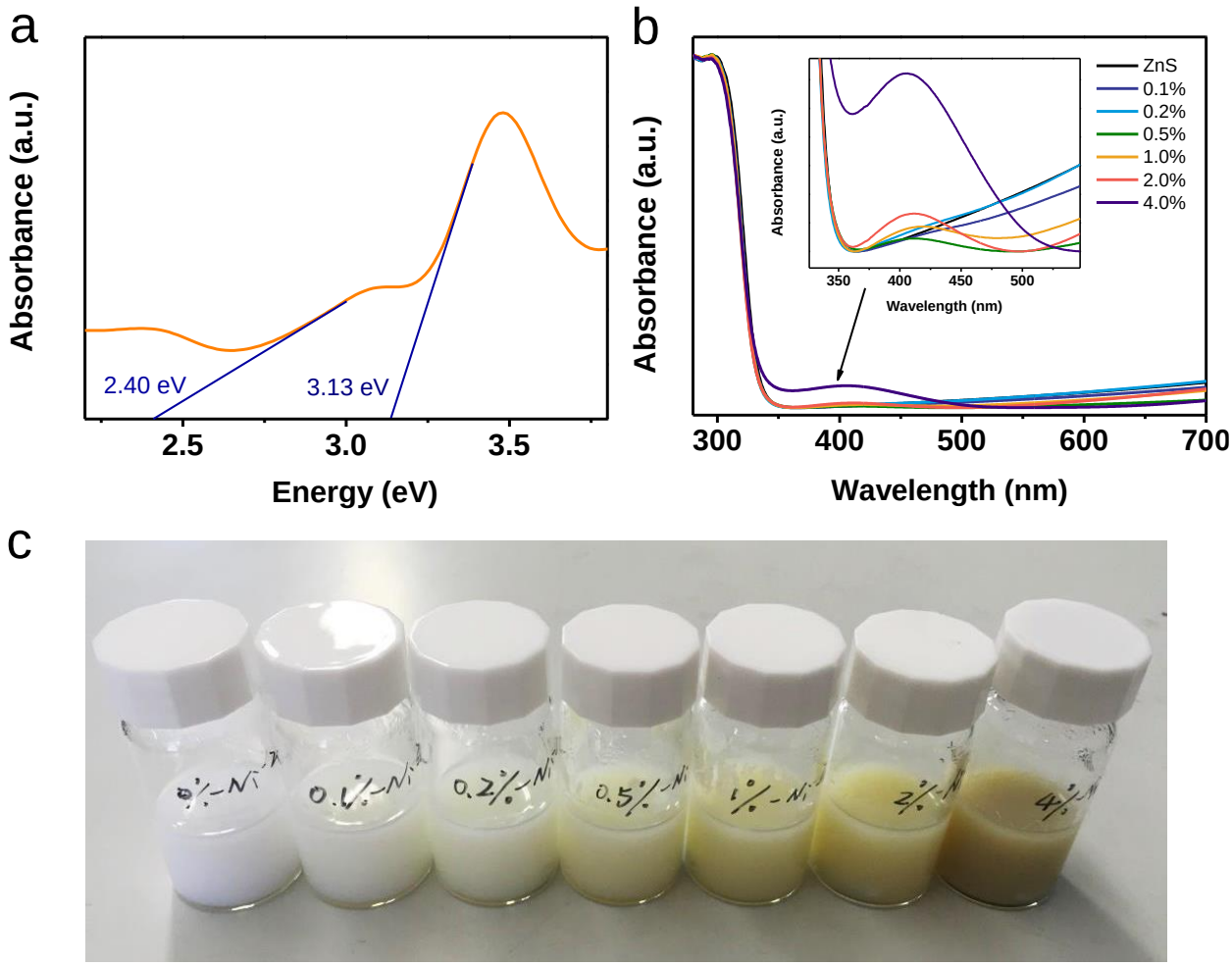

Figure 3.4 (a) Simulated UV-Vis spectrum of the ZnS:Ni (b) UV-Vis absorption spectra of ZnS:Ni colloidal nanocrystals (c) Optical photographs of the as-synthesized colloidal ZnS nanocrystals with different doping amount. From left to right: 0%, 0.1 %, 0.2 %, 0.5 %, 1.0 %, 2.0 % and 4.0 %.

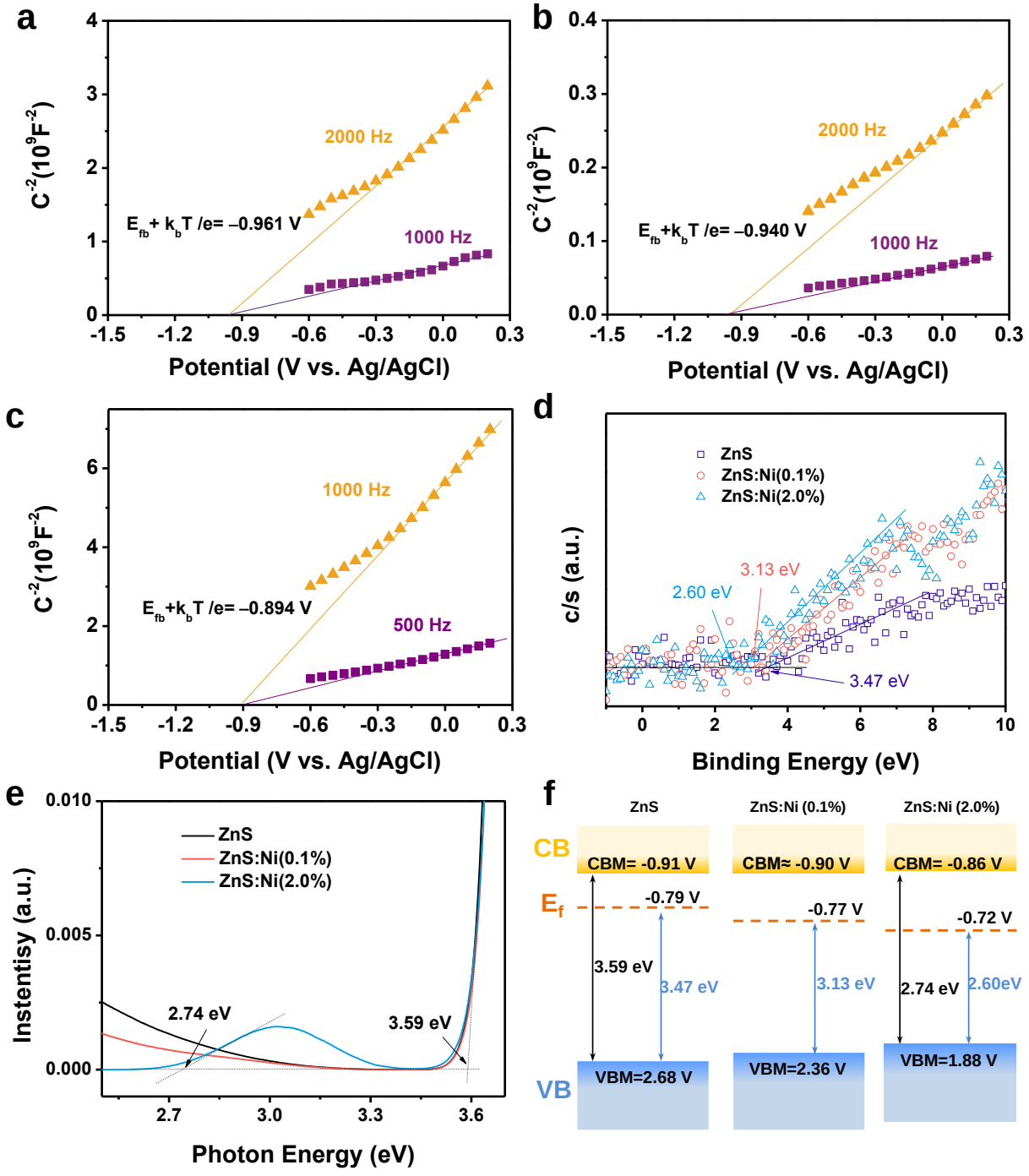

Figure 3.5 Mott-schottky curves of (a) undoped ZnS, (b) ZnS:Ni (0.1%), (c) ZnS:Ni (2.0%). (d) XPS valence band spectra of the undoped ZnS, ZnS:Ni (0.1%) and ZnS:Ni (2.0%) (e) Tauc plots of the undoped ZnS, ZnS:Ni (0.1%) and ZnS:Ni (2.0%) (f) Schematic band diagram of ZnS and ZnS:Ni (V vs. NHE, pH=0).

3.3.3 Photocatalytic CO_2 reduction activity

The CO_2 reduction reaction (CO_2RR) of the ZnS:Ni colloidal suspension was assessed over the CO_2-saturated $KHCO_3$ solvent with K_2SO_3 as the electron donors in the pyrex cell with a quartz lid. A 300W full arc Xe lamp with and with no cutoff filter (>420 nm) were first adopted as the outer irradiation source. As reported previously, Cd^{2+} can serve as an efficient cocatalyst for the highly selective formate production.[1, 21] Herein 2.0 % Cd^{2+} was added to promote the formate production. When the photocatalytic reaction was carried out, photogenerated holes were irreversibly consumed by the reducing reagent SO_3^{2-} and thereby boosting the photogenerated electrons in the conduction band transfer to chemisorbed CO_2 for the reduction. The evolved rates of H_2, CO and the liquid product, HCOOH under irradiance with wavelength > 420 nm are figured in Figure 3.6; H_2, CO and HCOOH were produced at a rate as high as 23.8 μmol h^{-1}, 0.18 μmol h^{-1} and 427.5 μmol h^{-1}, respectively, when full arc Xenon lamp was employed. As contrast, the undoped ZnS had no activity under the visible light irradiation. Then to simulate the photocatalytic CO_2 reduction under solar light, the reaction was carried out under an AM 1.5 G solar simulator. The time-conversion plot of the gaseous products, H_2 and CO over time course and the average production rate of formate were figured in Figure 3.7a, 3.7b and 3.7c. Even under the weak sunlight, the formate production can reach up to 137.9 μmol h^{-1} with a selectivity up to 99 % over ZnS:Ni (0.1 %) (Figure 3.6c). The apparent quantum efficiency (AQY) curve in Figure 3.7d clearly shows a wavelength-dependence tracking the absorption of the ZnS:Ni. In this experiment, the AQY is 59.1 % @ 339.3 nm and 5.6 % @ 417.9 nm, dominated by the intrinsic ultraviolet absorption and the Ni doping-induced visible light absorption, respectively. In addition, despite a negligible absorption induced by Ni doping at 480 nm, there is an obvious AQY at 480.4 nm with a value of 1.19 %, suggesting the abundant V_S also contributes to the visible-light-responsive activity over the ZnS:Ni.

The CO_2RR activity over the series of ZnS:Ni were also tested as shown under different light source in Figure 3.8-3.10 with a different optimal doping amount of Ni. It can be found the optimal doping amount of Ni shifts to larger when increasing the visible light component in the irradiation source, demonstrating

the Ni doping effect and existence of V_S successfully extends the CO_2RR activity of colloidal ZnS nanocrystals into visible light region.

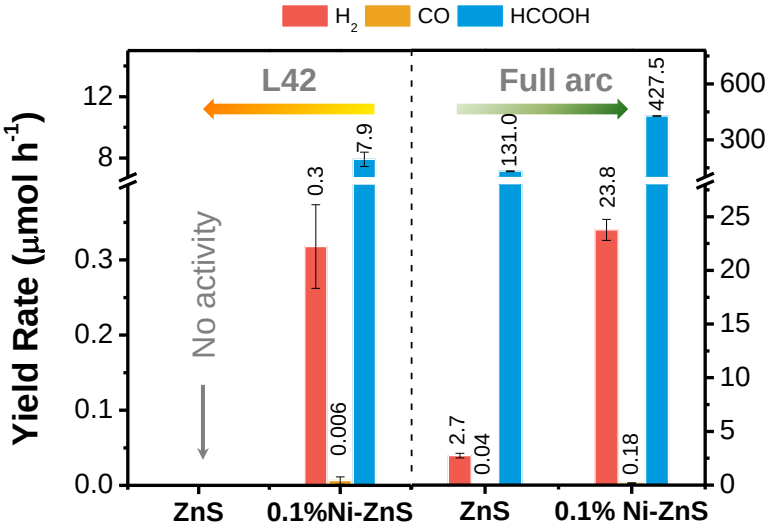

Figure 3.6 Evolution rates of H_2, CO and HCOOH under 300 W full arc Xenon lamp with a cutoff filter of 420 nm (left panel) and without any cutoff filter (right panel) over colloidal ZnS:Ni (0.1%) nanocrystals.

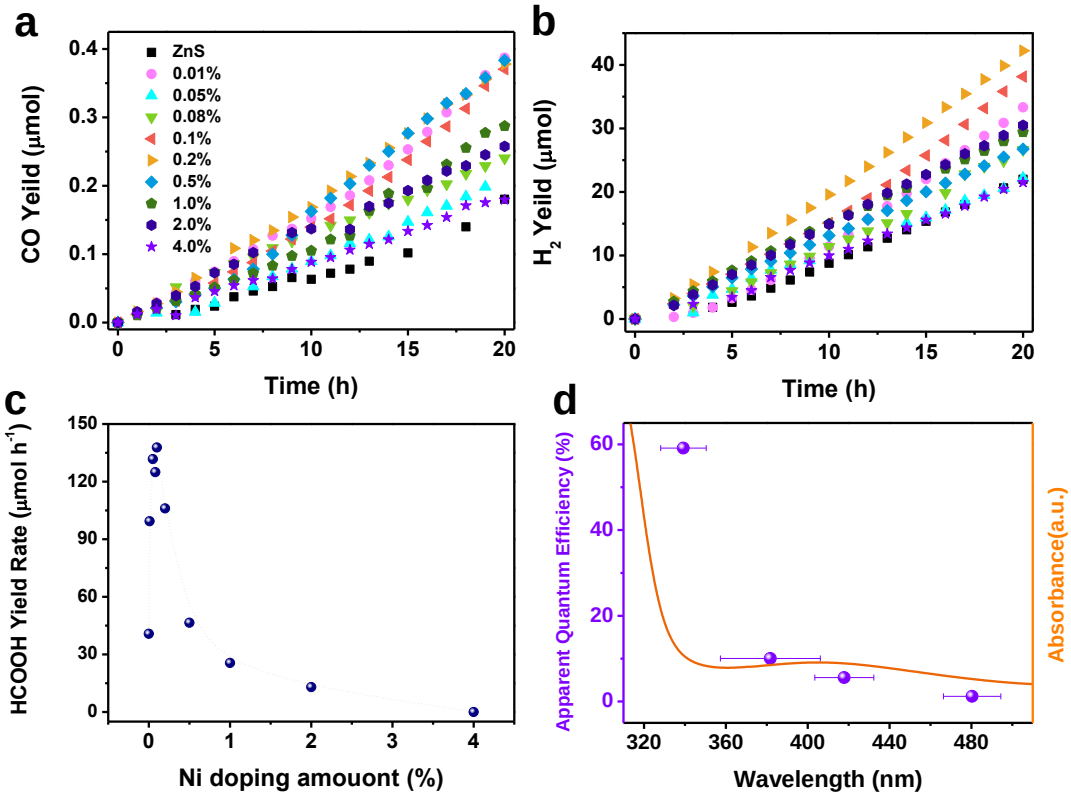

Figure 3.7 Time-conversion plot of the gaseous product under AM 1.5 simulator: (a) CO and (b) H_2. (c) HCOOH production rate of colloidal ZnS:Ni with different doping amount of Ni (d) The wavelength-dependent AQY of photocatalytic HCOOH production over colloidal ZnS:Ni (0.1%) nanocrystals.

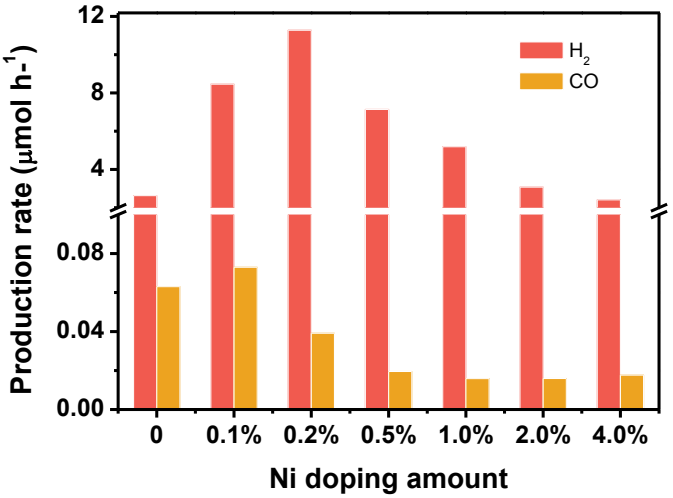

Figure 3.8 Photocatalytic CO_2RR activity over the colloidal ZnS nanocrystals with different doping amount under AM 1.5G simulator. With no cocatalyst of Cd^{2+}, the optimal activity was achieved at 0.2 %.

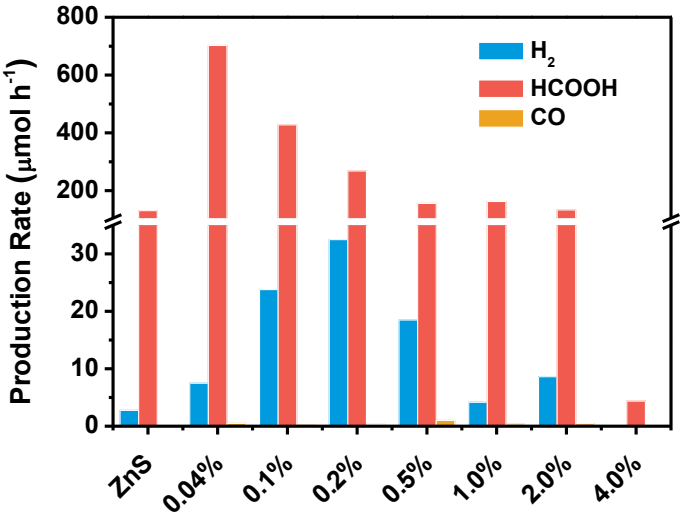

Figure 3.9 Photocatalytic CO_2RR activity over the colloidal ZnS nanocrystals loaded with Cd^{2+} with different doping amount under 300 W full arc Xe lamp. The optimal activity was achieved when Ni doping amount is 0.04 %.

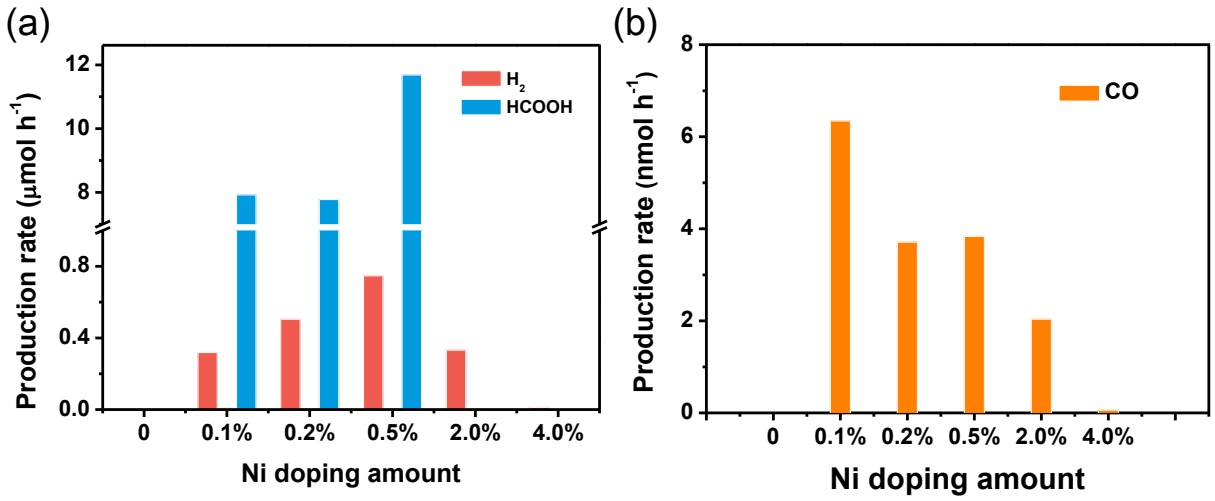

Figure 3.10 Photocatalytic CO_2RR activity over the colloidal ZnS nanocrystals with different doping amount in the presence of Cd^{2+} under 300 W Xe lamp (>420 nm). The optimal Ni doping amount is achieved at 0.5 %.

The isotope experiment using $^{13}CO_2$ under the similar reactant conditions excluding the utilization of $KHCO_3$ was carried out to validate the source of the produced CO and HCOOH. The GC-MS results in Figure 3.11 clearly demonstrate the production of ^{13}CO (m/z=29). The identification of liquid $H^{13}COO^-$ was performed on ^{13}C nuclear magnetic resonance (NMR). The peaks at d=170.5 ppm and 160.5 ppm assigned to $H^{13}COO^-$ and $H^{13}CO_3^-$ in ^{13}C NMR spectrum (Figure 3.12) and the doublet peak at 8.1 and 8.6 ppm in ^1H NMR spectrum (Figure 3.13) together confirmed the liquid product HCOOH all comes from the $^{13}CO_2$.

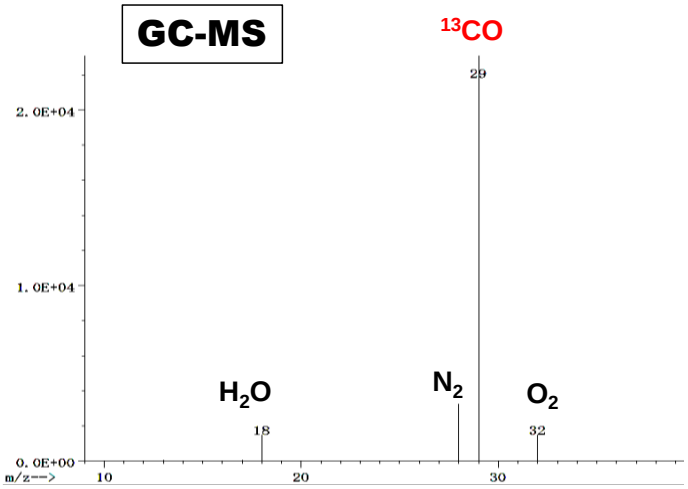

Figure 3.11 Representative GC-MS spectrum after photocatalytic CO_2 reduction using isotope $^{13}CO_2$ over the colloidal ZnS:Ni nanocrystals to confirm the carbon source in the gaseous products (CO).

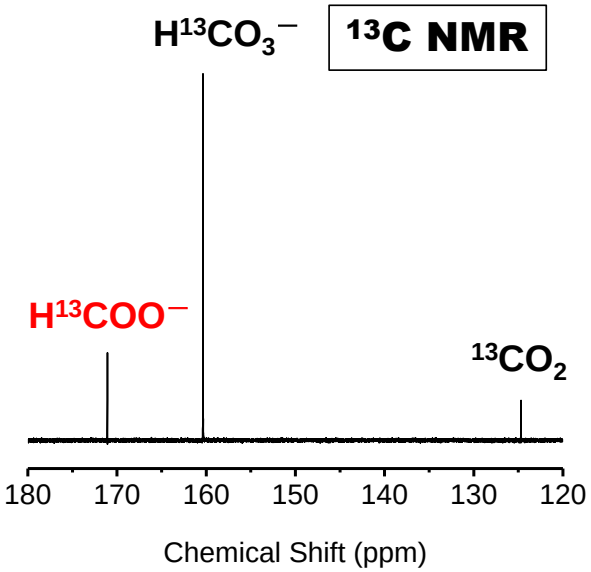

Figure 3.12 Representative ^{13}C NMR spectrum after photocatalytic CO_2 reduction using isotope $^{13}CO_2$ over the colloidal ZnS:Ni nanocrystals to confirm the carbon source in the liquid products (formate).

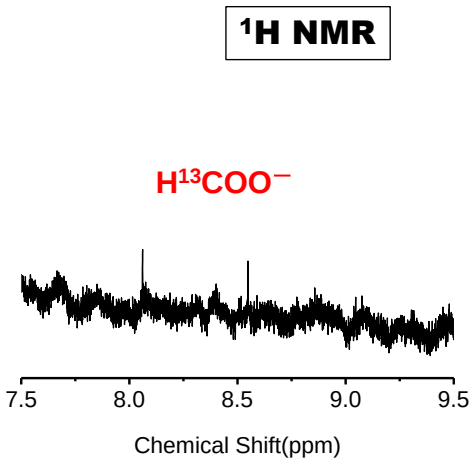

Figure 3.13 Representative ^{1}H NMR spectrum after photocatalytic CO_2 reduction using isotope $^{13}CO_2$ over the colloidal ZnS:Ni nanocrystals to confirm the carbon source in the liquid product (formate).

To test the ZnS:Ni photocatalysts' durability, long-term photochemical CO_2 reduction experiments were performed over 80 h. As displayed in the Figure 3.14, no obvious deactivation was observed in this long period, underlying the colloidal ZnS:Ni exhibits quite strong durability. Notably, the CO production rate were even slightly higher in the late stage as shown.

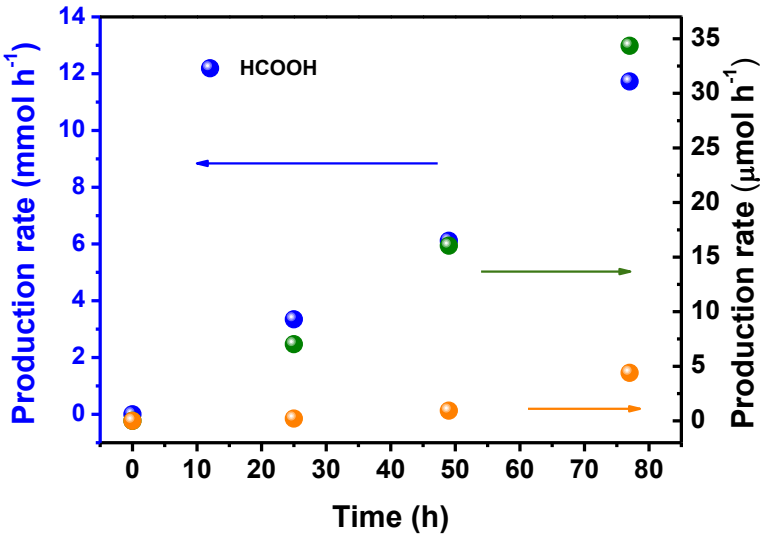

Figure 3.14 Long-term stability test of the colloidal ZnS:Ni nanocrystals over 80 h: time-dependent evolution plot of (a) H_2, (b) CO and (c) HCOOH.

3.3.4 The correlation between Ni dopant and sulfur vacancy

It has been already stated the abundant sulfur vacancies in such aqueous colloidal structure induce the excellent performance for CO_2RR and Ni doping increase the valence band position with respect to the band structure, improving the visible light utilization and hence the activity under solar light. But the fact that light doping increased the activity nearly three times and heavier doping of Ni leading to a decrease of CO_2RR production raise a question why the optimal activity is obtained at 0.1 % doping amount. We measured the photocurrents (in Figure 3.15) of the representative samples to describe the charge separation efficiency and carrier transport under irradiation but found that only slight discrepancies were presented, not sufficient to account for the large difference in activity. Then we turned to the surface sites indicated by the CO_2 uptake experiment for the reason. Our theoretical calculation predicts the sulfur vacancies formation increases 0.76 eV after incorporation of Ni, indicating the Ni doping is not beneficial for the formation of the V_S.

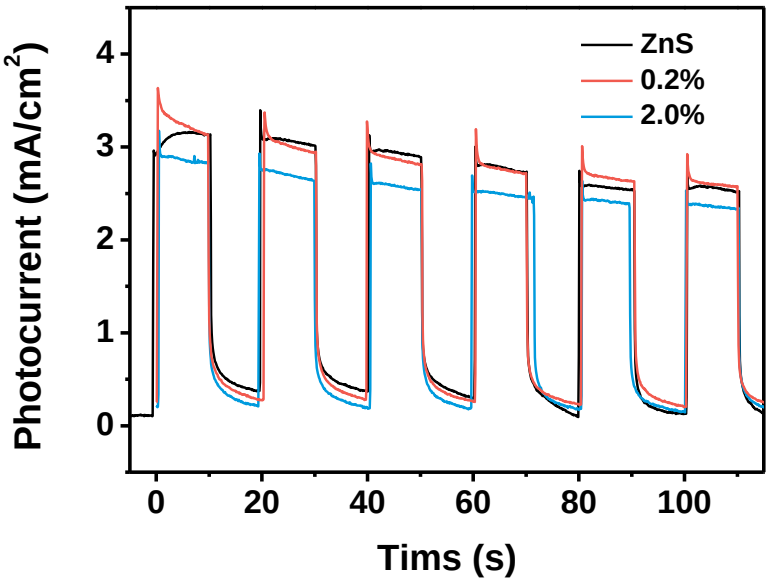

Figure 3.15 Photocurrents of pristine ZnS (black), ZnS:Ni (0.2 %) (red) and ZnS:Ni (2.0 %) (blue).

The factors of Ni dopants and V_S are actually complex and interrelated. To get a deeper insight into how the Ni doping affects the V_S and photocatalytic CO_2RR performance, the electron spin resonance (ESR) spectroscopy was further employed to observe the electron performance as shown in Figure 3.16a. It was clearly noted that a sharp signal at $g_1 = 1.999 \pm 0.004$ and a broad signal located at $g_2 = 2.007 \pm 0.004$ were detected both over the undoped and ZnS:Ni colloidal nanocrystals. According to the reference, the broad signal is the feature of the dipolar interaction between the physically absorbed molecular oxygen on the paramagnetic centers as we performed the ESR in air[22]; the sharp signal can be assigned to the F center, a singly negatively charged V_S in the cubic ZnS crystals, strongly supporting the existence of V_S [23]. No Ni-related signatures were observed in this range.[24] As the ESR signal is correlated with the density of paramagnetic electrons from V_S, it is concluded that the V_S amounts in the undoped ZnS is larger than that in the ZnS:Ni (0.2 %), and much larger than that in ZnS:Ni (2.0 %), consistent with the absorption observations stated above.

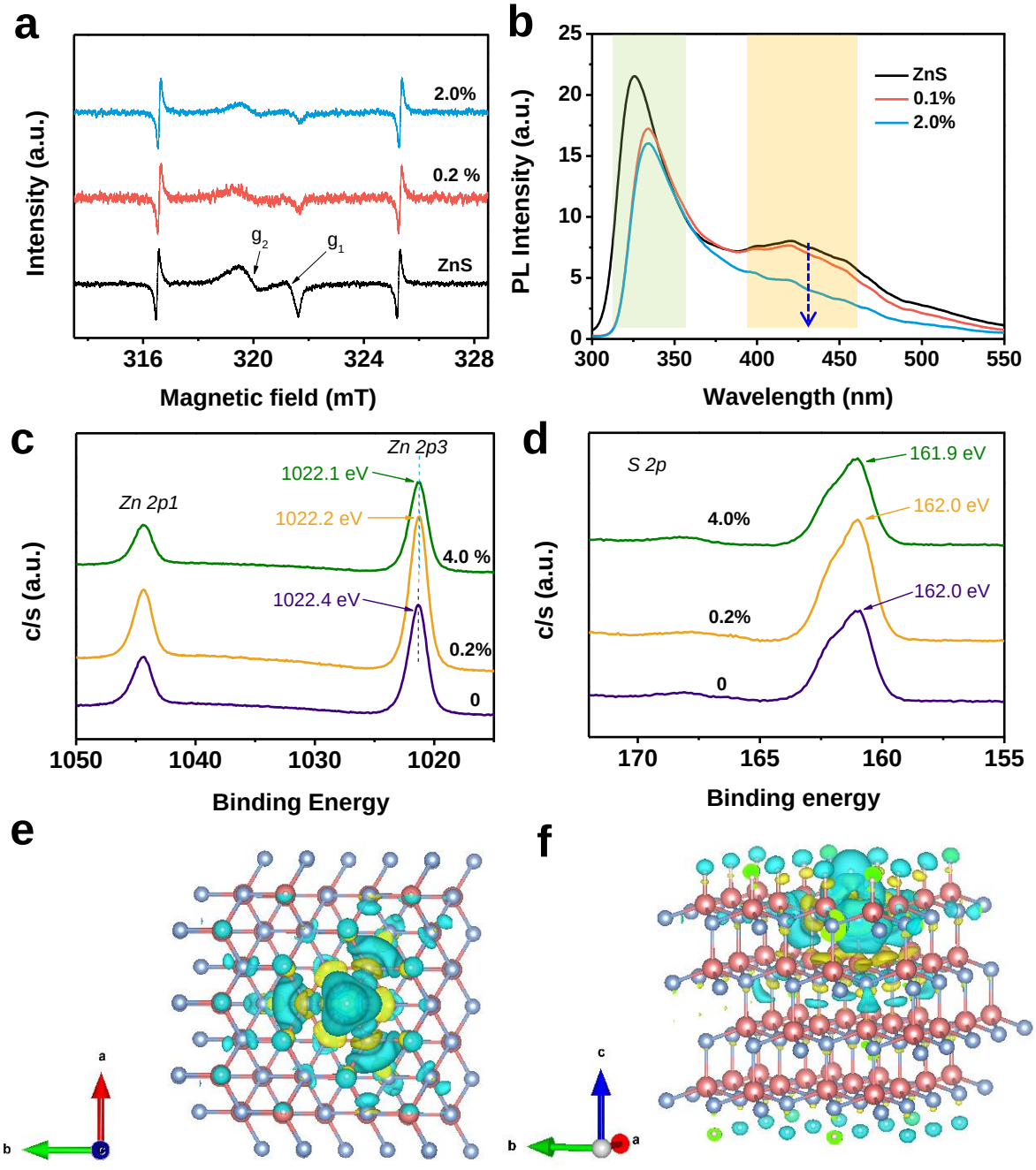

Figure 3.16 (a) ESR spectra and (b) PL spectra of undoped, 0.2 % doped and 2.0 % doped colloidal ZnS nanocrystals at room temperature. The 425 nm emission represents the sulfur vacancy signature. High-resolution XPS spectra of (c) Zn 3d and (d) S 2p, respectively of the undoped, 0.2 % doped and 4.0 % doped colloidal ZnS nanocrystals. (e) top view and (f) side view of the charge difference density distribution of ZnS:Ni (110).

Photoluminescence (PL) spectroscopy is another efficient and direct way to figure out the photogenerated charge carriers dynamics under a certain excitation wavelength. From the PL emission spectra in Figure 3.16b, we can have a clear view of the energy states within the bandgap. Under 280 nm excitation, there are two major emission peaks. The 320 nm emission peak (green area) is assigned to the intrinsic transition of photoelectrons and holes from conduction band to valence band. With the new states above the valence band maximum (VBM) created by Ni to trap the holes and promote the charge separation, the reduced intensity at 320 nm with the increasing Ni amount is easy to correlated with the suppressed recombination. The broad peak centered at 425 nm peak (yellow area) arising from the deep trap level near conduction band was reported from V_S in the previous literature.[25, 26] From the decreasing intensities of the blue emission at 425 nm, it is deduced Ni doping can curtail the excessive V_S in the undoped ZnS, in well accord with what we have observed in ESR spectra. The PL decay curves of the representative samples (undoped, light Ni-doped and heavy Ni-doped ZnS) and an estimation of the average fluorescence lifetime fitted with a second-exponential function over the undoped and doped colloidal suspensions are revealed in Figure 3.17 and Table 3.1. The ZnS:Ni (0.1%) nanocrystals shows the longest average lifetime of 30.2 ns as well as the optimal photocatalytic CO_2 reduction activity primarily to HCOOH. The overall trend of all the samples is almost consistent with the photocatalytic activity, strongly suggesting the activated states are longer-lived with the existence of abundant sulfur vacancies.

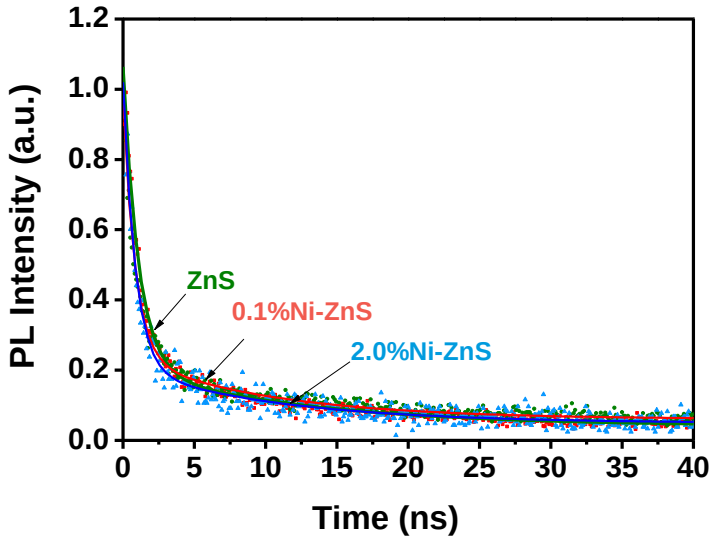

Figure 3.17 Photoluminescence decay curves of the representative colloidal ZnS:Ni nanocrystals

Table 3.1 The photoluminescence decay time of all the samples derived from the time-resolved photoluminescence spectra.

Sample	Decay time (ns)		Relative amplitude (%)		Average lifetime (τ,ns)[a]
	τ_1	τ_2	f_1	f_2	
0	1.273	27.587	0.849	0.14	21.83345
0.1	1.273	35.684	0.795	0.15	30.21234
0.2	1.136	30.787	1.035	0.121	23.67365
0.5	1.221	25.618	0.893	0.149	20.19738
1.0	1.057	23.652	1.031	0.138	17.99634
2.0	1.157	25.864	4.976	0.125	10.04195
4.0	1.049	25.864	7.692	0.111	7.56113

[a] The average lifetime was calculated using equation: $\tau = (f_1\tau_1^2+f_2\tau_2^2)/(f_1\tau_1+f_2\tau_2)$

Further chemical states analysis of the colloidal ZnS:Ni nanocrystals were conducted on X-ray photoelectron spectroscopy (XPS). The pristine ZnS, ZnS:Ni (0.2 %) and ZnS:Ni (4.0 %) were selected as the representative samples of the undoped, light doped and heavier doped one. As shown in Figure 3.16c, the high-resolution XPS spectrum of Zn 2p reveals that there is a pair of peaks located at 1022.4 eV and 1045.4 eV binding energy, which are assigned to Zn $2p_{3/2}$ and Zn $2p_{1/2}$ of undoped ZnS colloidal nanocrystals. When Ni was doped in the ZnS, the binding energy of the major Zn $2p_{3/2}$ peak shift to 1022.2 eV and to 1022.1 eV for ZnS:Ni (0.2 %) and ZnS:Ni (4.0 %), equivalent to a negative shift of ~0.2 eV and ~0.3 eV with respect to the undoped counterpart, respectively. It is reasonable to deduce that Ni doping lead to a decrease of the electron density of the positively charged Zn ion adjacent to the S_v and hence a lower binding energy. From Figure 3.16d, we can observe the S 2p peaks slightly shifted from 162.0 eV toward lower binding energy of 162.0 eV and 161.9 eV for ZnS:Ni (0.2 %) and ZnS:Ni (4.0 %), respectively. The lowering of S 2p binding energy also demonstrates the weakened Zn-S bonds near the dopant site caused by Ni-S bond formation.

From the discussion above, large amount of sulfur vacancies in the bulk within the pristine undoped ZnS nanocrystals will bring about the severe recombination of charge carriers and suppress the reduction activity. As Ni doping are apt to localize the electrons from sulfur vacancies and reduce the V_S, light doping can balance off the excessive V_S and induce a significant enhancement in activity; heavier doping leads to a great loss of V_S and a low performance adversely despite an extended light absorption in visible region.

3.4 Conclusion

Solar-driven CO_2 reduction was successfully realized over ZnS:Ni colloidal nanocrystals with an optimal doping amount of 0.1 %. Loading with Cd^{2+}, the HCOOH production over ZnS:Ni colloidal nanocrystals has reached up to 427 μmol h^{-1} under 300W Xe lamp and 138 μmol h^{-1} (selectivity ~99%) under 1 sun. The AQY at 340 nm in the UV region and at 420 nm in the visible light region are 59.1 % and 5.6 %, respectively, at the front ranks in the currently reported photocatalytic CO_2RR systems. The reason

why photoconversion of CO_2 is optimized at a small doping amount (0.1 %) of Ni was explained. Demonstrated by PL, ESR and XPS, it was found the Ni dopants can modulate the V_S amount in the loose structured ZnS:Ni colloidal architecture. Light doping of Ni curtails the excessive V_S, suppressing the charge recombination in the bulk; heavier doping of Ni will cause the diminishing of V_S, unfavorable for the CO_2RR. Thus, only appropriate doping amount can give rise to the optimal performance of the photocatalytic CO_2RR. The discovery offers a unique insight into the doping strategy and modulation of anion vacancies on the photocatalysts towards CO_2 reduction.

References

[1] X. Meng, Q. Yu, G. Liu, L. Shi, G. Zhao, H. Liu, P. Li, K. Chang, T. Kako, J. Ye, Nano Energy, 34 (2017) 524-532.

[2] M. Kanemoto, T. Shiragami, C. Pac, S. Yanagida, J. Phys. Chem., 96 (1992) 3521-3526.

[3] H. Pang, G. Zhao, G. Liu, H. Zhang, X. Hai, S. Wang, H. Song, J. Ye, Small, 14 (2018) e1800104.

[4] A. Kudo, Y. Miseki, Chem. Soc. Rev., 38 (2009) 253-278.

[5] G. Yang, D. Chen, H. Ding, J. Feng, J.Z. Zhang, Y. Zhu, S. Hamid, D.W. Bahnemann, Appl. Catal. B: Environ., 219 (2017) 611-618.

[6] Y. Ji, Y. Luo, J. Am. Chem. Soc., 138 (2016) 15896-15902.

[7] S. Gao, B. Gu, X. Jiao, Y. Sun, X. Zu, F. Yang, W. Zhu, C. Wang, Z. Feng, B. Ye, Y. Xie, J. Am. Chem. Soc., 139 (2017) 3438-3445.

[8] X. Jiao, Z. Chen, X. Li, Y. Sun, S. Gao, W. Yan, C. Wang, Q. Zhang, Y. Lin, Y. Luo, Y. Xie, J. Am. Chem. Soc., 139 (2017) 7586-7594.

[9] S. Gao, Y. Lin, X. Jiao, Y. Sun, Q. Luo, W. Zhang, D. Li, J. Yang, Y. Xie, Nature, 529 (2016) 68-71.

[10] W. Tu, Y. Xu, J. Wang, B. Zhang, T. Zhou, S. Yin, S. Wu, C. Li, Y. Huang, Y. Zhou, Z. Zou, J. Robertson, M. Kraft, R. Xu, ACS Sustain. Chem. Eng., 5 (2017) 7260-7268.

[11] B. Wang, X. Wang, L. Lu, C. Zhou, Z. Xin, J. Wang, X.-k. Ke, G. Sheng, S. Yan, Z. Zou, ACS Catal., 8 (2017) 516-525.

[12] Z. Geng, X. Kong, W. Chen, H. Su, Y. Liu, F. Cai, G. Wang, J. Zeng, Angew. Chem. Int. Ed., 57 (2018) 6054-6059.

[13] C. Li, T. Wang, Z.J. Zhao, W. Yang, J.F. Li, A. Li, Z. Yang, G.A. Ozin, J. Gong, Angew. Chem. Int. Ed., 57 (2018) 5278-5282.

[14] X. Chen, L. Liu, P.Y. Yu, S.S. Mao, Science, 331 (2011) 746.

[15] M. Wang, L. Cai, Y. Wang, F. Zhou, K. Xu, X. Tao, Y. Chai, J. Am. Chem. Soc., 139 (2017) 4144-4151.

[16] G. Li, G.R. Blake, T.T. Palstra, Chem. Soc. Rev., 46 (2017) 1693-1706.

[17] F. Wang, S. He, H. Chen, B. Wang, L. Zheng, M. Wei, D.G. Evans, X. Duan, J. Am. Chem. Soc., 138 (2016) 6298-6305.

[18] Z. Mei, B. Zhang, J. Zheng, S. Yuan, Z. Zhuo, X. Meng, Z. Chen, K. Amine, W. Yang, L.W. Wang, W. Wang, S. Wang, Q. Gong, J. Li, F.S. Liu, F. Pan, Nano Energy, 26 (2016) 405-416.

[19] G. Murugadoss, J. Lumin., 132 (2012) 2043-2048.

[20] G. Wang, B. Huang, Z. Li, Z. Lou, Z. Wang, Y. Dai, M.H. Whangbo, Sci. Rep., 5 (2015) 8544.

[21] X. Meng, G. Zuo, P. Zong, H. Pang, J. Ren, X. Zeng, S. Liu, Y. Shen, W. Zhou, J. Ye, Appl. Catal. B: Environ., 237 (2018) 68-73.

[22] A. Tetsuya, M. Teruyoshi, S. Koichi, Jpn. J. Appl. Phys., 8 (1969) 1411.

[23] Z. Fang, S. Weng, X. Ye, W. Feng, Z. Zheng, M. Lu, S. Lin, X. Fu, P. Liu, ACS Appl. Mater. Interfaces, 7 (2015) 13915-13924.

[24] M. Surma, A. Zakrzewski, M. Godlewski, T. Surkova, Acta Physica Polonica A, 1 (1995) 221-224.

[25] H. Tang, G. Xu, L. Weng, L. Pan, L. Wang, Acta Mater., 52 (2004) 1489-1494.

[26] N.D. P. H. Borse, R. F. Shinde, S. K. Date, S. K. Kulkarni, J. Mater. Sci., (1999) 6087-6093.

Chapter 4 Zinc-Cadmium Exchange Induced Isolated Sites for Efficient CO_2 Conversion in Aqueous Solution

4.1 Introduction

Carbonaceous fuels can be in principle produced effectively through solar-driven CO_2 reduction reaction (CO_2RR) coupled with water oxidation, resembling the plant photosynthesis.[1] Photocatalytic route to reduce CO_2 to carbon-neutral fuels would provide an ideal medium, where semiconductors are particularly well-suited to undertake the underlying reactions.[2] Impressive strides have been taken on TiO_2, CdS, g-C_3N_4, $ZnGaO_4$ and conjugated semiconductors, etc. but they work inefficiently despite a large extra energy added in.[3-5] To optimize the efficient and selective photocatalysts for CO_2RR, it is essential to understand the reaction mechanism behind artificial photosynthesis.

Thermodynamically, ZnS is an exceptional photocatalyst with a negative conduction band (CB) that can work for superior CO_2RR in all-inorganic system with carbon-free hole scavengers, making sure the reduction products come from the CO_2 instead of the carbon-containing photocatalysts or the decomposition from the organic solvents or hole scavengers.[6] In the previous chapters, over the colloidal ZnS nanocrystals suspensions loaded with $CdSO_4$, formic acid is dominantly produced with a selectivity close to unity and an appreciable apparent quantum efficiency (Table 4.1). However, the role of Cd^{2+} and the mechanism underpinning the remarkable performance still remained elusive. This opens up several questions which we answer in this chapter. What is the exact status of Cd and how it impacts the highly selective photocatalytic CO_2RR into formate?

Table 4.1 Photocatalytic CO_2RR activity with Cd loading

Samples	Light	Formate (μmol/h)	H_2 (μmol/h)	CO (μmol/h)	Formate selectivity
ZnS	AM 1.5	1.16	9.65	0.19	10.5 %
Cd-ZnS	AM 1.5	40.74	0.87	0.01	97.9 %
ZnS:Cu (0.2 %)	AM 1.5	3.18	19.91	0.38	13.6 %
Cd-ZnS:Cu(0.2 %)	AM 1.5	148.83	1.42	0.01	99.0 %
ZnS:Ni (0.1 %)	AM 1.5	0	2.63	0.06	0
Cd-ZnS:Ni (0.1 %)	AM 1.5	137.81	1.58	0.014	98.9 %
Cd-ZnS:Ni (0.1 %)	Xe lamp (>420 nm)	8.58	0.32	0.01	96.4 %
ZnS:Ni (0.1 %)	Xe lamp	6.63	128.11	0.42	4.9 %
Cd-ZnS:Ni (0.1 %)	Xe lamp	427.55	23.77	0.19	94.7 %

Herein, we present more spectroscopic evidence to push ahead a deeper understanding of the decisive role of Cd in this reaction. The surface oxidation state of Cd is exactly determined by X-ray absorption fine structure (XAFS). And we employed ultrafast transient absorption spectroscopy (TAS) and photoluminescence (PL) spectroscopy to probe the exciton dynamics in the photocatalytic CO_2RR over colloidal ZnS nanocrystals loaded with Cd^{2+}. Additionally, we figured out the pathways of CO_2RR into formate based on the *in situ* attenuated total reflectance-infrared (ATR-IR) spectroscopy. The Cd effect in the kinetics were also evaluated by the *ab initio* calculations. It is found that Cd exerts significant impact on band alignment, charge transfer and the free energy reaction coordination diagram. This work sheds light on both thermodynamic and kinetics issues in designing active and selective photocatalysts and offer an efficient strategy for the construction of isolated sites for catalytic reactions.

4.2 Experimental section

4.2.1 Photocatalytic reaction

The methods of photocatalyst preparation, photocatalytic reaction and the product analysis can be referred to our previous chapters.

4.2.2 Characterization

X-ray diffraction patterns (XRD) were collected on the X-ray diffractometer (X'pert powder, PANalytical B.V., Netherlands) with Cu-Kα radiation. The high-angle annular dark field (HAADF) images and elemental mapping were measured on the transmission electron microscopy (TEM, FEI Tecnai G2 F30) in a STEM mode. The absorption spectra were obtained from the diffuse reflectance spectra (DRS) via Kubelka-Munk method performed on a Shimadzu UV-2500 spectrophotometer. The CO_2 adsorption isotherms were obtained at room temperature over BELsorp II mini (BEL Japan Inc.). The *in situ* attenuated total reflection-Fourier transform infrared (ATR-FTIR) spectroscopy was obtained over JASCO FT/IR-6300 with specific time period, which employs a mercury-cadmium-telluride (MCT) detector and a Ge crystal substrate. The fluorescence (PL) spectra were measured using fluorescence spectrometer (JASCO FP-6500) with an excitation of 280 nm and emission of 420 nm over the catalyst suspensions (1.0 g L^{-1}). The time-resolved fluorescence decay curves were acquired with the colloidal precipitates over a home-made ps-time resolved luminescence spectroscopy (Marubun Corporation, Japan). The X-ray chemical status and valence band (VB) spectra were analysed on a photoelectron spectroscopy (XPS) (PHI Quantera SXM, ULVAC-PHI Inc., Japan). Electron spin resonance (ESR) spectra were obtained on JEOL JES-FA-200.

Transient absorption spectroscopy study in mid-IR region was done with the following experimental setup. A commercial Ti: sapphire laser (Spitfire Ace, Spectra Physics) centered at 800nm with a pulse duration of 35 fs working at a repetition rate of 1kHz was used as the light source. The 800 nm pulse was split into two beams. One beam was used to pump a commercial optical parametric amplifier (TOPAS, Spectra Physics) to generate the 350nm excitation pulse to excite the sample. The other beam was used to generate a broadband mid-IR source as probe light. At first, BBO crystal was used to generate the second harmonic (SHG) 400 nm laser pulse and then the SHG and the fundamental pulses were focused simultaneously by an aluminum concave mirror into the air. Finally the broad mid-IR covering 3000nm ~9000 nm was generated via four-wave mixing (FWM) through filamentation in air. After sample, the

transmitted mid-IR light was collected and sent into a 64-channel MCT array detector coupled spectrometer (FPAS-0144, Infrared Systems Development, iHR 320, HORIBA Jobin Yvon). During the experiment, the diameter of the pump spot at sample was about 0.2 cm. The sample was prepared as KBr pellet with 2% sample mixed into 55 mg potassium bromide powder.

4.2.3 X-ray absorption spectroscopy

Cd K-edge XAFS spectra were measured at room temperature for Cd metal foil, CdO, CdS and 2-mol% Cd-ZnS samples were measured in the transmission mode in the Photon Factory Advanced Ring at the High Energy Accelerator Research Organization on beamline NW10A in which the storage ring energy was 6.5 GeV, and the ring current was 50 mA. A Si (3 1 1) double-crystal monochromator and a Pt-coated focusing cylindrical mirror were inserted into the X-ray beam path. The X-ray intensity was maintained at 67 % of the maximum flux using a piezo-translator applied to the crystal to suppress higher harmonics. The slit in front of the I_0 ionization chamber had an opening size of 1 mm (vertical) and 2 mm (horizontal). Spectra for the CdO (4 mg) sample diluted by boron nitride were measured at the beamline. The obtained Cd K-edge XAFS data was analyzed using XDAP software package using modified Victoreen function, spline function, Fourier transform, and multiple-shell curve fitting. The pre-edge background was approximated by a modified Victoreen function $C_2/E^2 + C_1/E + C_0$. The background of the post-edge oscillation was approximated by a smoothing spline function and was calculated for the particular number of data points, using

$$\sum_{i=1}^{\text{Data Points}} \frac{(\chi_i - BG_i)^2}{\exp\left(-0.075k_i^2\right)} \leq \text{smoothing factor} \qquad (4\text{-}1)$$

where k is the angular wavenumber of the photoelectrons.

4.2.4 DFT calculations

The theoretical calculations are based on the density functional theory (DFT). All the calculations were performed within the CASTEP package of the Materials Studio at the generalized gradient approximation

(GGA) level. The ion-electron interaction and the exchange-correlation functional of electrons were described using the projector augmented wave (PAW) pseudopotential and the Perdew-Burke-Ernzerhof (PBE). The cubic ZnS (111) surface was present by a 3×3×3 supercell with a vacuum layer of 20 Å. The Cd-ZnS model was based on cubic ZnS model with a surface Zn atom replaced by a Cd atom. The plane-wave cut-off energy levels for geometry optimization and energy calculation were set as 480 eV and 590 eV. The SCF tolerance level was set as 1.0×10^{-5} eV/atom in geometry optimization, and 1.0×10^{-6} eV/atom for energy calculation.

To study the influence of Cd on the charge transfer, the adsorption energies of molecules involved in the reduction pathways, denoted as E_{ads} (X/surface) (X=H, CO_2, COO*, HCO_3^-, HCO_3*, HCOO*, HCOOH), on the surface were calculated using the following equation:

$$E_{ads}(\text{X/surface}) = E_{tot}(\text{X/surface}) - E_{tot}(\text{X}) - E_{tot}(\text{surface}) \quad (4\text{-}2)$$

, Where E_{tot}(X/surface) is the total energy of optimized X adsorption configuration on the specific surface, E_{tot}(X) and E_{tot}(surface) are the total energy of an isolated X molecule and the surface slab, respectively.

DOS Calculations for ZnS (111) and (110) surfaces with Cd modification

Both the (111) and (110) surfaces of ZnS with Cd modification were simulated using the slab models consisting of 5 atomic layers, as shown in Figure 4.1. To avoid the neighboring interaction between the periodic slab models, a 16 Å vacuum region was added in the above surface structures along the out-plane direction. 3×3×1 and 3×2×1 Monk-horst k-point meshes were used for the Brillouin-zone integrations of (111) and (110) surface models, respectively. The positions of all atoms were allowed to relax. In addition, the (111) surface is a polar one with a Cd/Zn-terminal and S-terminal, respectively, which may induce large dipole moments. Hence, a $H_{1.5}$ (H with 1.5 positive charge) was chosen to passivate the Cd/Zn-terminal, and $H_{0.5}$ (H with 0.5 positive charge) was used to passivate the S-terminal.

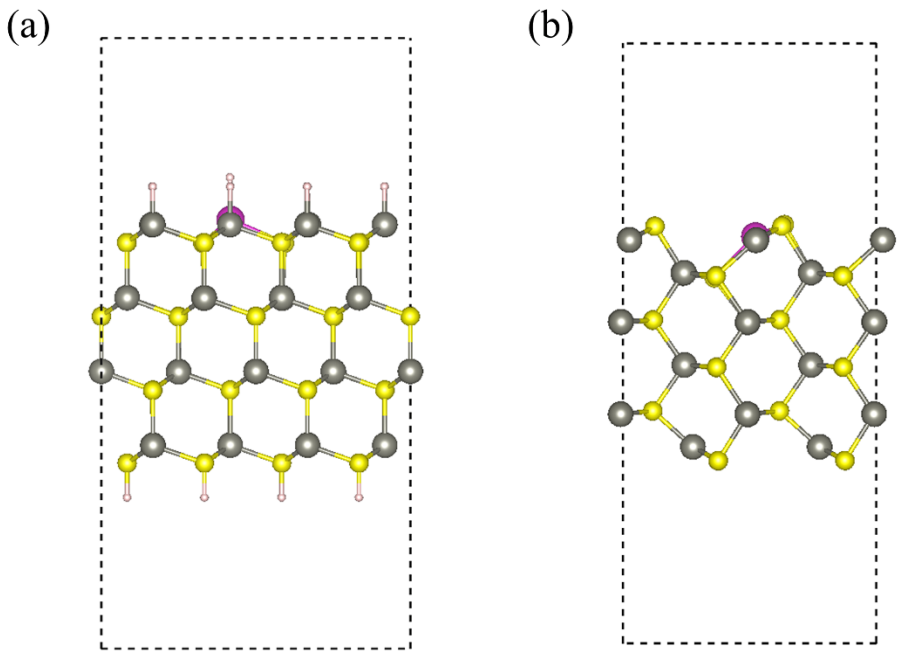

Figure 4.1 Slab models for (a) (111) and (b) (110) surfaces of ZnS, respectively. The gray, yellow, purple and pink balls indicate the Zn, S, Cd and H atoms.

4.3 Results and discussion

4.3.1 Characterization of Cd status on the surface of ZnS nanocrystals

According to our previous study, the ZnS nanocrystals loaded with Cd with a concentration of 2.0 % are adopted here for further studies. As displayed in the high-angle annular dark field scanning transmission electron microscopy (HAADF-STEM) image (Figure 4.2a) and STEM elemental mapping (Figure 4.2b-d), the Cd element is homogeneously distributed. To gain more accurate information of Cd state within the crystal structure, X-ray photoelectron spectroscopy (XPS) was performed and analyzed. Figure 4.3a depicts the Cd 3d XPS spectrum, which reveals two characteristic peaks at 404.9 eV and 411.6 eV, corresponding to Cd $3d_{5/2}$ and $3d_{3/2}$ of Cd^{2+}, testifying the oxidation state of Cd is in divalent state. Further, X-ray absorption near-edge structure (XANES) at the Cd K-edge helps get an insight into the local chemical environment around Cd and its electronic interaction with ZnS lattice. As shown in Figure 4.3b, Cd K-edge absorption

from 26.697 keV are consistent with that of the CdO and Cd, indicating the divalent oxidation status of Cd at the surface of colloidal ZnS nanocrystals. But the energy values at the tops and the bottoms of the post-edge oscillation for normalized intensity of Cd-ZnS were quite different from that of Cd metal and CdO. Instead, this absorption spectrum was characterized by an additional feature that showed a quite flat shape containing Cd bonding feature with S ligands.[7] The detailed coordination environment was probed from the extended X-ray absorption fine structure (EXAFS). As displayed in Figure 4.3c, the Cd atoms are coordinated by S nearest neighboring shell at 2.03 Å, while the Cd−O at 1.81 Å and Cd-(O)-Cd at 3.07 Å are almost out of phase, which is well consistent with the published data.[8, 9] It shows no sign of Cd-O or Cd-Cd bond in the EXAFS for the sample of Cd-ZnS. In total, we conclude that the Cd ions substitutes the Zn sites of the host ZnS lattices, rather than segregating out to form the Cd metal nanoparticles. Collectively, our XAFS results clearly demonstrate Cd is divalent and bound to S in the Cd-ZnS colloidal nanocrystal architectures by cation exchange.

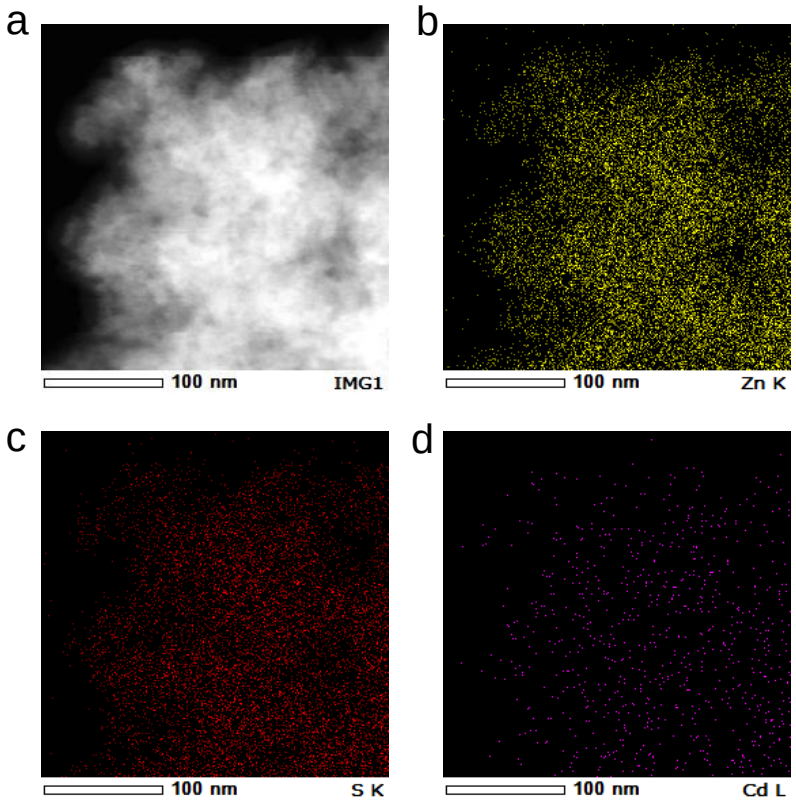

Figure 4.2 (a) HAADF-STEM image, (b-d) elemental mapping of Zn, S, Cd of the 2% Cd-ZnS.

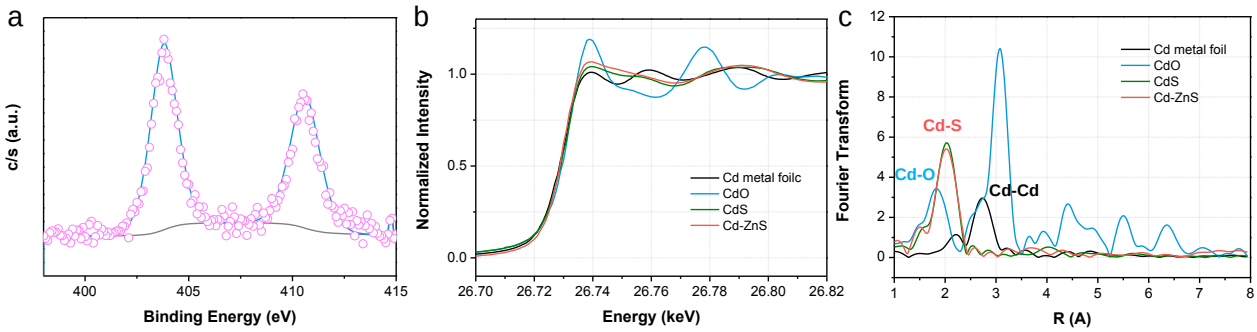

Figure 4.3 (a) High-resolution XPS spectrum of Cd 3d. Cd K-edge XANES (b) and its associated Fourier transform of angular wave number k^3-weighted EXAFS χ-function spectra (c) for Cd metal foil (thickness 5 μm, black line), CdO (4 mg, blue line), CdS (26 mg, green line) and fresh Cd-ZnS (50 mg, red line).

4.3.2 Cd effect on electronic structure and charge transfer

To examine whether Cd^{2+} helps to modify the band structure, we first compared the optical band gap derived from the UV-Visible absorption spectra and the room-temperature steady-state photoluminescence (PL) spectra shown in Figure 4.4a. The UV-Vis absorption spectra (blue and yellow curves) change in the wavelengths longer than 1S exciton after Cd^{2+} was loaded on the colloidal ZnS nanocrystals. Except for the subtle red-shift of the absorption edge, the levelling off long tails in the visible region, which is described as the charge transition from sulfur vacancies to CB, implies a quenching effect of sulfur vacancies after Cd^{2+} loading. Correspondingly, the emission peak centered at 425 nm assigned to sulfur vacancies[10] over the pristine ZnS nanocrystals are decreased after incorporation of Cd^{2+} (See green and purple curves in Figure 4.4). Taking into consideration of the intensity of electron spin resonance (ESR) signals associated with sulfur vacancies[11] (Figure 4.5) and the CO_2 uptake amount (Figure 4.6) remained same, it is reasonable to deduce the Cd substitution exerts impact on the electrons localized on the sulfur vacancies but not on the amount of the sulfur vacancies, leading to the diminished photophysical characteristic of the sulfur vacancies.

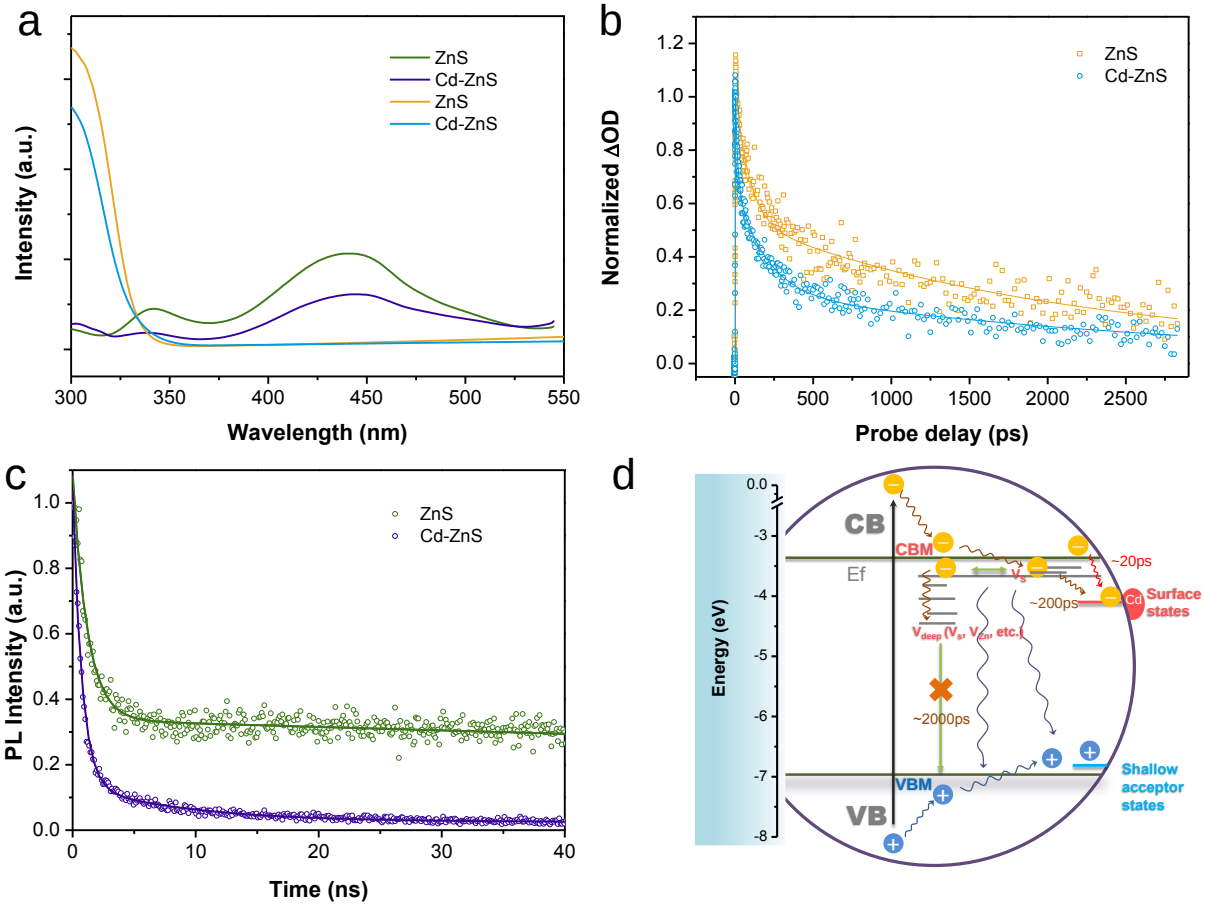

Figure 4.4 (a) PL (blue and yellow) and UV-vis absorption spectra (purple and green), (b) transient absorption kinetic profiles (c) time-resolved PL decay curves of the ZnS and Cd-ZnS. (d) The proposed band structure and charge carrier dynamics of Cd-ZnS.

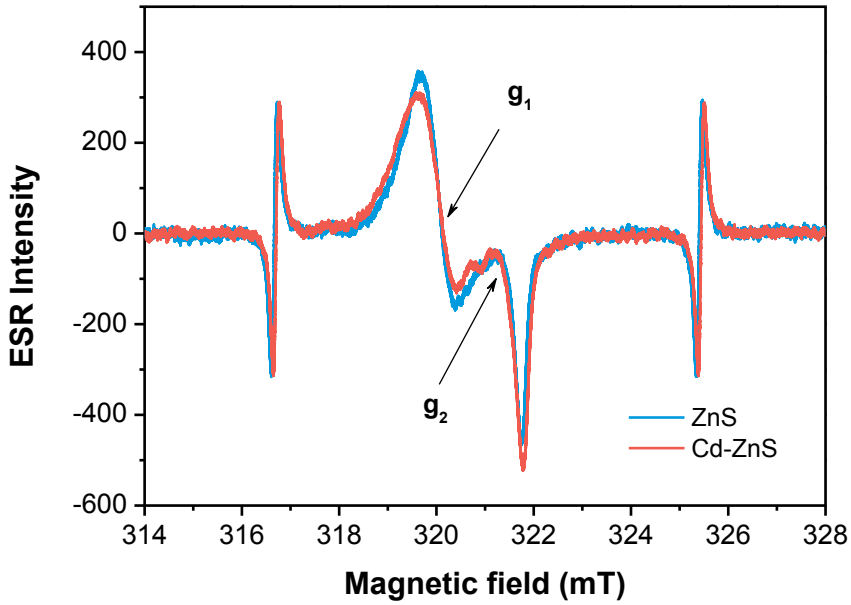

Figure 4.5 Electron spin resonance (ESR) of pristine ZnS and 2.0 % Cd-ZnS. The almost same intensity of the signal at g_1= 2.003 and g_2= 1.999, assigned to the signature of the chemisorbed oxygen molecules and sulfur vacancies, respectively, demonstrated the Cd impact is not the sulfur vacancies amount but the excited electrons behavior.

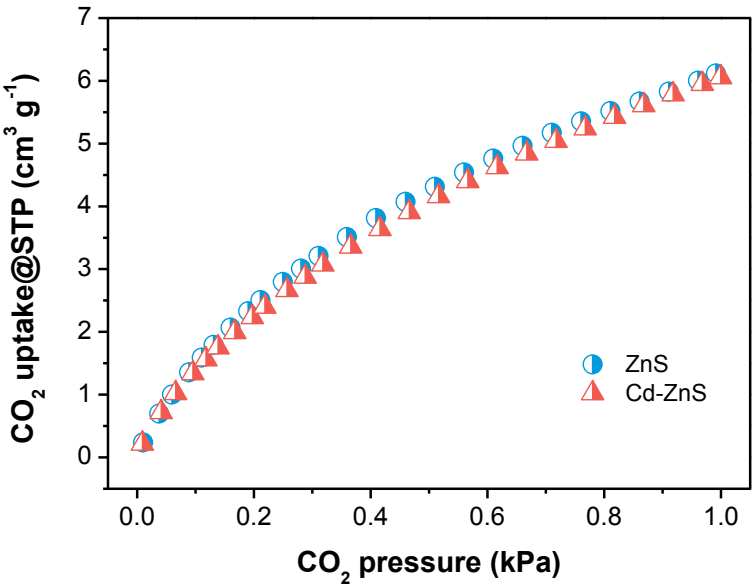

Figure 4.6 CO_2 uptake experiment over ZnS and Cd-ZnS at ambient pressure

As the favorable alignment of the conduction band between bulk and surface implicates readily electron transfer from CB to surface Cd sites and CB to sulfur vacancies as well as the transfer from sulfur vacancies to surface Cd sites, femtosecond transient absorption (fs-TA) spectroscopy was then employed to monitor the electron transfer within the Cd-ZnS on the picosecond scale. Figure 4.4b shows the TA spectra excited by a 350 nm pump wavelength with 90 nJ cm^{-2} and probed at a mid-infrared (MIR) wavelength 5000 nm to detect the states created by sulfur vacancies. The ultrafast charge transfer process was identified when we use a multi-exponential decay function to describe the charge carrier relaxation dynamics over the multiple time regimes. Generally, τ<20 ps is associated with the very fast decay process; τ in 20~500 ps represents the further relaxation between the deep trap states and shallow surface defects, usually dominating the general relaxation dynamics; τ >500 ps is related to the recombination to the deeper trapped states or the ground states of the longer-lived untrapped excitons.[12] The fitted time constants for pristine ZnS and Cd-ZnS are listed in Table 4.2. Compared with τ_1, the rapid depopulation of Cd-ZnS indicates a faster electron transfer from the conduction band of ZnS to the Cd sites rather than recombination into the deeper trapped states or ground states; the shortened τ_2 means that the electron transfer from sulfur vacancies to shallow surface states has been accelerated because of the Cd loading. As the instrumental window in this measurement is limited to 3 ns, the longer-lived components, which directly react with the adsorbates and are important to the effective photocatalytic performance, are usually identified using time-resolved photoluminescence (tr-PL) spectroscopy instead of the TAS.

Table 4.2 The fitting results of TAS kinetics for pristine ZnS and Cd/ZnS

samples	**τ_1 (ps)**	**τ_2 (ps)**	**τ_3 (ps)**	**A_1 (%)**	**A_2 (%)**	**A_3 (%)**
ZnS	90.3	1999	10000.0	47.5	45.4	7.1
Cd-ZnS	13.5	187.9	2996.2	36.4	38.1	25.5

The tr-PL spectra in Figure 4.4c shows the lifetime decay curve of Cd-ZnS and ZnS. Fitting with a biexponential function for the pristine ZnS and the Cd-ZnS, the fitted lifetime components are listed in the Table 4.3. The distinct order of fitting is indicative of the different relaxation pathways of the excitons within Cd-ZnS and ZnS. As with the smaller values of τ_1 and τ_2, both the relaxation processes on Cd-ZnS are remarkably faster than that of ZnS. The average effective minor carrier lifetime for ZnS and Cd-ZnS were estimated to be 21.83 ns and 16.94 ns, respectively. As a result, the Cd incorporation significantly shortens the excited states lifetimes. As we performed the tr-PL experiments in the reactant conditions with sacrificial reagent of SO_3^{2-} as the hole scavengers and weakly bound CO_2, bicarbonate as the electron acceptors, it is speculated that partly substitution of Cd with Zn atoms on the surface can improve the electric conductivity and the e^- - h^+ pairs separation, making charge recombination less likely. This is well consistent with the theoretical calculation that predicts in Figure 4.7. With Cd atoms exchanged with surface Zn atom, an internal electric field arised between surface and bulk.[13] Our results reveal a remarkably high charge density located at the Cd sites (Figure 4.7a-d), suggesting that the excited electrons in ZnS system prefer to be trapped by the surface state created by Cd^{2+}, as the reaction sites of photocatalytic CO_2 reduction. Next, we compared the projected density of states (PDOS) of the Zn atom and Cd atom at ZnS surface and analyzed the contributions from their electronic states of *s*, *p* and *d* orbitals to the photocatalytic CO_2 reduction (Figure 4.7e-j). The band-edge electronic states of these orbitals above Fermi level E_f, i.e., near the CB of ZnS (mainly composed of Zn *sp* orbitals), should be of particular interest for understanding the kinetic behavior of photoexcited electrons. The obtained data indicate that, compared with the *p* and *d* orbitals, the energy distribution of *s* orbitals for Zn and Cd at both crystal surfaces are closer to the E_f. Notably, the Cd *s* orbital above E_f displays obviously higher density of states near band-edge with a relatively lower lying band center than that of Zn *s* orbital (Figure 4.7 e,h). This reveals that Cd *s* orbital plays the key role in separating electrons from CB of ZnS and catalyzing CO_2 reduction successively. This can be also reasonably understood that the outmost *s* orbital of Cd^{2+} ions will supply electrons to the electrophilic CO_2 molecule in the reduction reaction. In this regard, the role of Cd^{2+} serves as cocatalyst by

Ohmic contact for reduction reaction. Accordingly, combined with the XPS (VB) spectrum in Figure 4.8, we figured out the band alignment and possible electron transfer pathways in Figure 4.4d.

Table 4.3 The photoluminescence decay time of pristine ZnS derived from the time-resolved photoluminescence spectroscopy

Sample	Decay time (ns)		Relative amplitude (%)		Average lifetime (τ,ns) [a]
	τ_1	τ_2	f_1	f_2	
ZnS	1.273	27.587	0.849	0.14	21.833
Cd-ZnS	0.982	24.389	1.02	0.088	16.941

[a] The average lifetime was calculated using equation: $\tau = (f_1\tau_1^2+f_2\tau_2^2)/(f_1\tau_1+f_2\tau_2)$

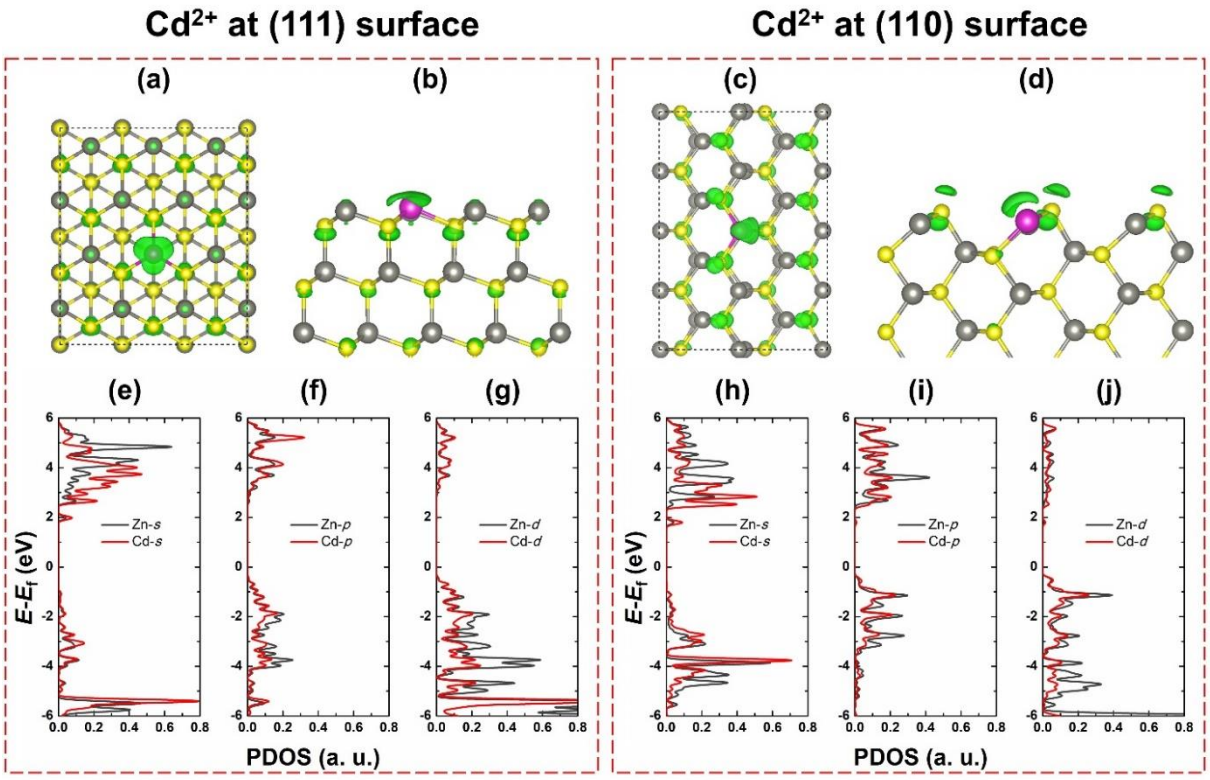

Figure 4.7 Charge density distribution of Cd^{2+} modified ZnS (111) and (110) planes from top view (a) and (c), and side view (b) and (d). The gray, yellow and purple balls indicate the Zn, S and Cd atoms, respectively. And the passive H atoms in (111) are not shown here. The green dot surface represents the isosurface of charge density with value of 4×10^{-3} e/Å. (e-j) show the PDOSs of *s*, *p*, and *d* orbitals for Cd^{2+} and Zn^{2+} at ZnS (111) and (110) planes, respectively.

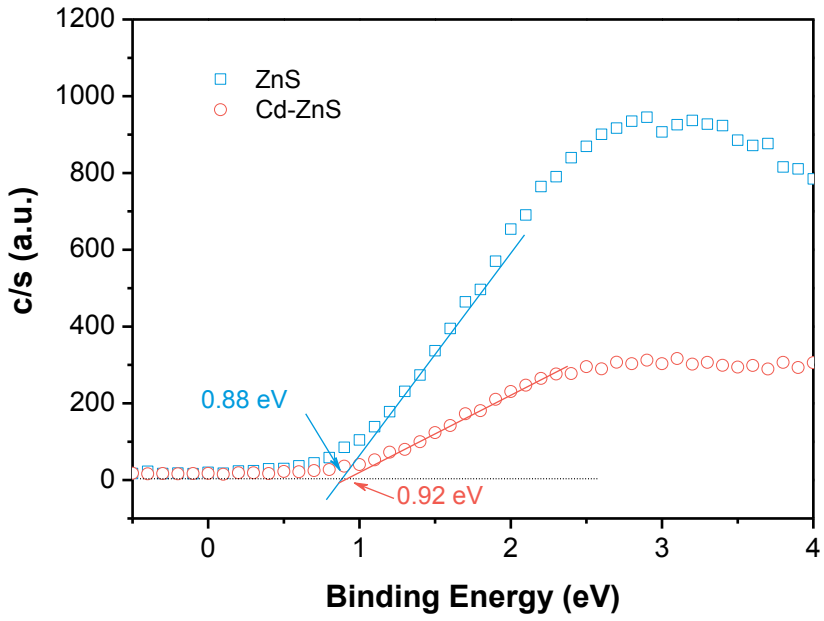

Figure 4.8 XPS valence band (VB) spectra clearly indicated a minor VB shift of 0.04 eV after loading with Cd (II) and forming a $Zn_{1-x}Cd_xS$ thin layer on the surface.

4.3.3 Mechanistic pathways analysis by *in situ* ATR-IR spectroscopy

In order to understand the ambiguous mechanistic pathways of the carbonaceous species transformation on the surface of the Cd-modified colloidal ZnS, *in situ* attenuated total reflectance-Fourier transform infrared (ATR-FTIR) spectroscopy was utilized to monitor the intermediates during the CO_2RR to the major product of formate. Figure 4.9 shows the ATR-IR transmission spectra. Apart from the doublet CO_2 signals with the band centered at around 2340 cm^{-1},[14] there are several peaks observed. At the initial stage of photoexcitation and CO_2 conversion, the most evident species of the bicarbonate species, characterized by the strong absorption at 3613 cm^{-1}, 1640 cm^{-1} and 1365 cm^{-1}, are assigned to the hydroxyl group vibration ν(OH), antisymmetric and symmetric stretching vibration of (CO_3), respectively.[15] Afterwards, the characteristic peaks at 1599 cm^{-1} and 1095 cm^{-1} arising from the ν(C=O) vibration and ν_s(C-O) stretching vibration in

carboxylate coupled with the asymmetric vibration ν(HCOO) at 977 cm^{-1} increases, indicating the formation of formate species ($HCOO_{ad}$*) on the surface of ZnS. The discernible small peak at 1410 cm^{-1} is at the similar position of symmetric stretching of CO_3 ν_s(C-O) in monodentate bicarbonate on Zn; the peak shift from 1410 cm^{-1} to 1400 cm^{-1} is a signature of monodentate formate species formation[16] as the latter belongs to the asymmetric vibration ν_{as}(C-O) in this intermediate towards formate. As the electronic interaction of metal-substrate causes a peak shift of carbonyl bond to lower wavenumber, it is reasonable to assign the three arising peaks at 2944 cm^{-1}, 1699 cm^{-1}, 1007 cm^{-1} to the δ(C-H) deformation[17], ν(C=O) stretching vibration, ν(HCOO) stretching vibration in formate desorbed from the catalyst surface, respectively; the increasing broad peak between 2500 cm^{-1} and 2700 cm^{-1} arising from the OH in carboxylic acid is increasing; 3569 cm^{-1} and 3677 cm^{-1} assigned to the H-bound OH or H-bound water in the vicinity of formate ion species also indicate the formate desorbed from the catalyst surface[18]; all the above demonstrate the formate acid generation. Simultaneously, the broad band between 3000 cm^{-1} and 3500 cm^{-1} derived from ν(OH) stretching decreasing with time under photoirradiation indicates the surface-bound water was consumed during the reaction.

As the interaction between Zn atoms and CO_2 is the Lewis acid-base interaction[19], it is more likely the carbon oxygen species attached the transition metal through oxygen atom instead of carbon atom. But as the CO was formed in the experiment except HCOOH, it was speculated the species are able to attach the transition metal sites through carbon atoms occasionally, which, however, is too negligible to detect in ATR-IR in this circumstance.

On the basis of the observations above, the speculated mechanism is proposed in the Scheme 4.1. Bicarbonate (HCO_3^-) or CO_2 initials with a nucleophilic attack on the surface of ZnS. In the case of HCO_3^-, after OH^- from the buffer solution reacting with CO_3^{2-},[6] the first intramolecular electron ($1H^+/1\ e^-$) transfer at metal site takes place to form the monodentate HCOO* species where the proton is provided by water instead of the bicarbonate. If starting from CO_2, $COO^{\bullet -}$ formed at

the first stage, followed by the protonation, also generating the monodentate HCOO* as the intermediate. Then the majority of HCOO* species are absorbed on the Zn through oxygen atoms while a minor proportion attached through carbon atoms, which subsequently accept one more electron to give out formate acid and CO, respectively. As the Zn is the *sp* metal with moderate strength of absorption and desorption[20], the formate is apt to detach from the catalyst surface.

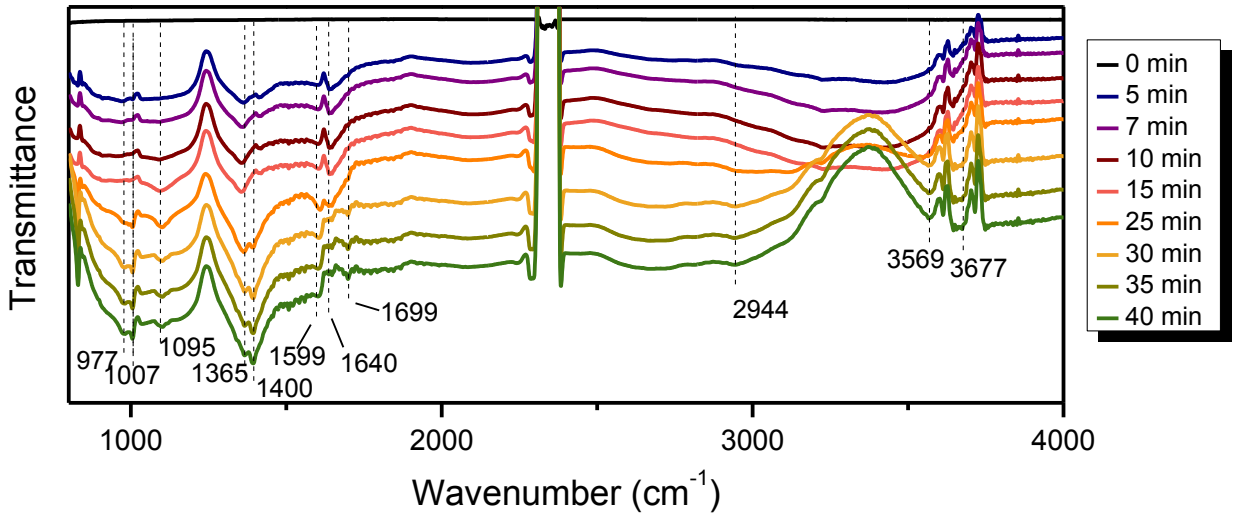

Figure 4.9 In situ ATR-IR spectra over Cd-ZnS under photo-irradiation

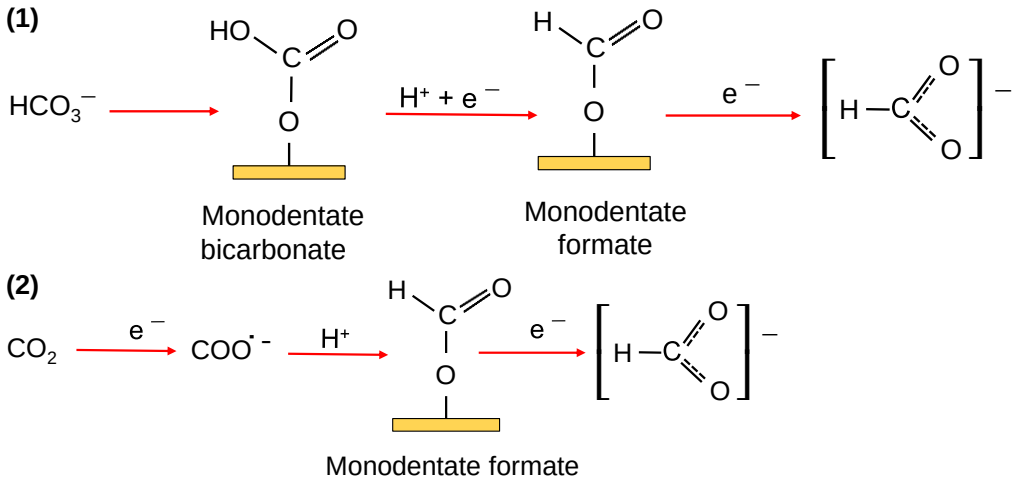

Scheme 4.1 Possible mechanistic pathways for CO_2RR over Cd-ZnS

4.3.4 CO_2 adsorption and activation

Based on the result of the *in situ* ATR-IR analysis, microkinetic modellings of the full path in terms of the most significant intermediate of HCOO* and the main product of $HCOO^-$ over Cd-ZnS were undertaken to further deconvolute the role of Cd^{2+} in kinetics. We first figured out the proton adsorption energy (ΔG_{ads}) coordination in Figure 4.10 to give the reason why Cd substitution suppressed the hydrogen evolution reaction. There is no difference on the proton adsorption for Zn and Cd atoms from the inset figure. However, compared with of the proton adsorption energy (ΔG_{ads}(H*)=-0.28 eV) of Cd-ZnS, the pristine ZnS surface without Cd substitution (ΔG_{ads}(H*)=-0.24 eV) is more close to the zero. HER is a classic two-electron transfer reaction following a Sabatier principle with one chemisorbed intermediate H*. Smaller thermodynamic overvoltage is more beneficial for HER. In a word, the pristine ZnS surface is more favorable for HER, accounting for the lower selectivity into H_2 after one Cd atom exchanged with Zn.

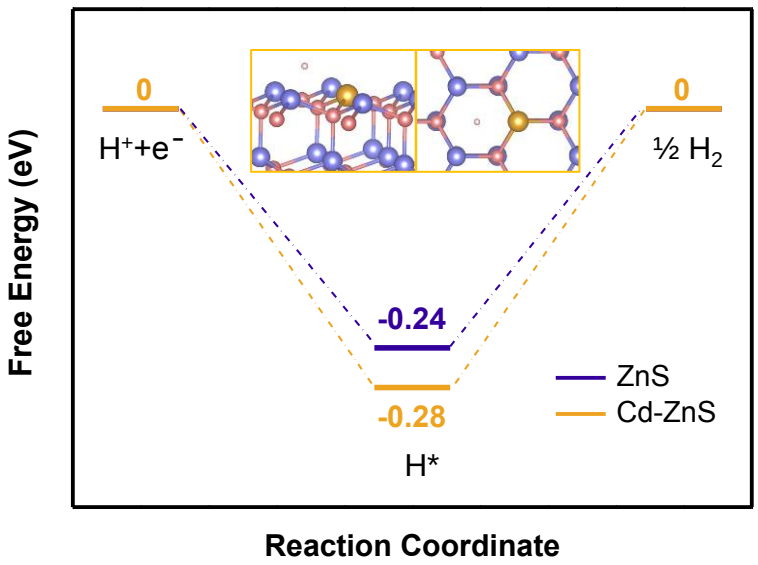

Figure 4.10 Hydrogen adsorption free energy versus the reaction coordinate of HER on ZnS surface. Inset: proton adsorption sites on Cd-ZnS surface (blue:Zn atom, red: S atom, yellow: Cd atom, pink: H atom).

Then we turn to the energetics of CO_2 conversion process. The free energy diagram coupled with the model of CO_2, COOH* and $HCOO^-$ on ZnS (111) surface with and without Cd substitution was figured out as displayed in Figure 4.11. Based on the ATR-IR observation, the pathway starting from bicarbonate ion (HCO_3^-) is considered dominant. However, as shown in Figure 4.11a, despite an exothermic adsorption of HCO_3^- on both surface to HCO_3*, the second step in which one proton and one electron coupled with HCO_3^- is highly endergonic with a free energy difference (ΔG) of 0.20 eV and 0.26 eV over Cd-ZnS surface and ZnS surface, respectively. The great barrier determines this step is difficult to occur in the whole process. When the experiment was devoid of $KHCO_3$, CO and HCOOH were still able to be identified, suggesting the pathway starts from CO_2 also existed in the reaction though no direct evidence was discernible in the *in situ* ATR-IR spectra. Also, it is suggested even starting from HCO_3^-, the OH^- from the buffer solution will convert it into CO_3^{2-}. Thus, the dominant process are initialized with the deformation of CO_2 derivatives. Displayed in Figure 4.11b, the nearly downstream route with large ΔG of -0.77 eV strongly suggests a fairly easy pathways over Cd-ZnS surface with exclusively a small barrier of 0.03 eV when first electron transfers and COO^-* is formed as the rate-determining step. The lower ΔG can accelerate the overall reduction rate, explaining the higher production of formate over Cd-ZnS surface. Compared with the pristine ZnS surface, the presence of Cd atom helps to stabilize COO*, COO^-*, HCOO* intermediates, responsible for the high efficiency of formate evolution. Moreover, the downhill desorption of $HCOO^-$ is more readily from the Cd-ZnS surface in terms of the larger ΔG at the second electron transfer step. However, the strong binding interaction of $HCOO^-$ with Cd-ZnS and ZnS surfaces indicated by the much negative ΔG_{ads} might be the reason why they are difficult to desorb from the catalyst and identify. The three steps from CO_2 and HCO_3^- are respectively summarized in the colorful frames at the bottom of each free energy diagram.

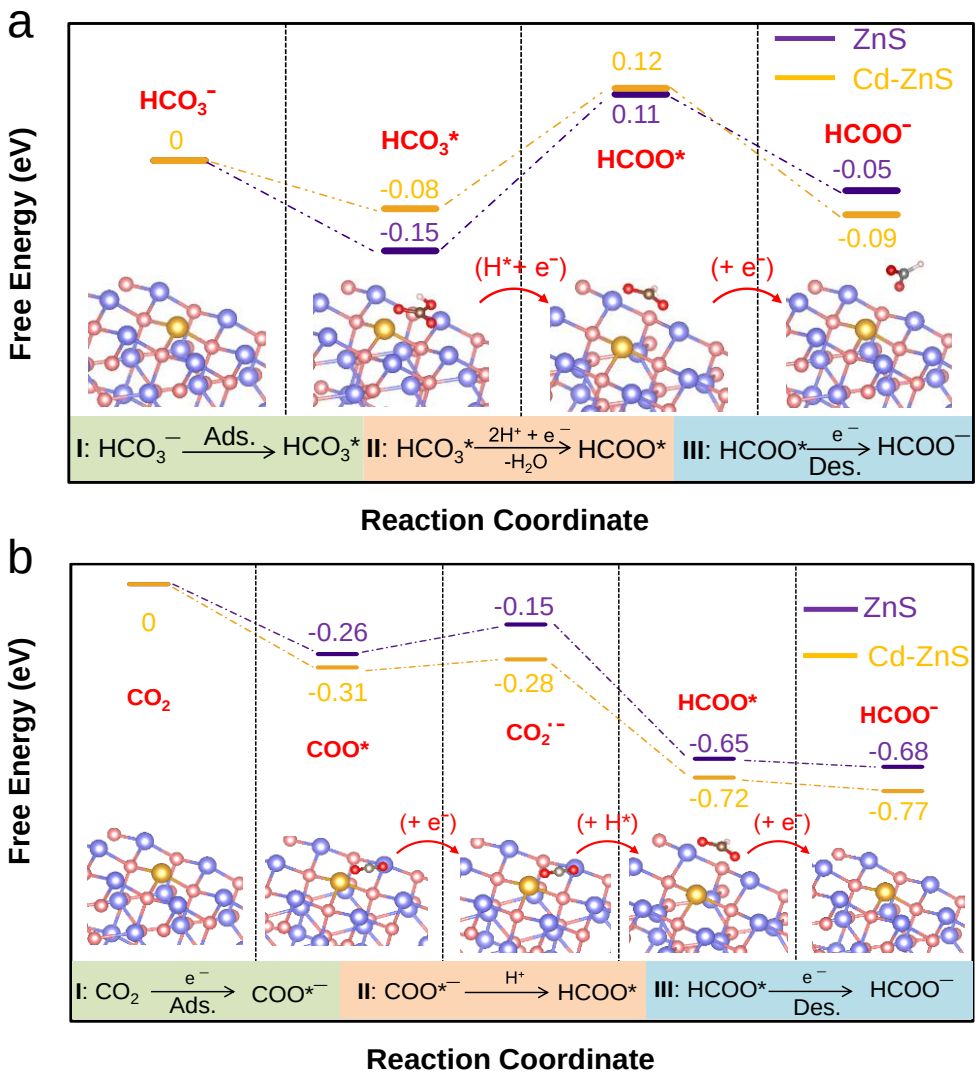

Figure 4.11 Calculated free energy diagram for the pathways of (a) bicarbonate (b) CO_2 molecule to formate. In each diagram, the pathway represents the free energy vs. SHE. The simplified surface structures correspond to the various species along the pathway, indicating the electron/proton transfer process at the (111) surface of Cd-ZnS.

4.4 Conclusion

In summary, the combined experimental and theoretical results well elucidate the exact reaction process over the ZnS catalyst surface at a molecular level and give out a reasonable explanation for the

favorable kinetics in the presence of Cd loading. The isolated sites of Cd atoms on the surface of ZnS nanocrystals enhance the charge and energy transfer and confers the CO_2RR kinetically. The cation exchange strategy and isolated sites construction open the new possible pathways to the fabrication of nanomaterials and efficient photocatalysts.

References

[1] W. Kim, B.A. McClure, E. Edri, H. Frei, Chem. Soc. Rev. 45 (2016) 3221-3243.

[2] H. Gerischer, Faraday Discuss. Chem. Soc. 70 (1980) 137-151.

[3] X. Meng, L. Liu, S. Ouyang, H. Xu, D. Wang, N. Zhao, J. Ye, Adv. Mater. 28 (2016) 6781-6803.

[4] K. Li, B. Peng, T. Peng, ACS Catal. 6 (2016) 7485-7527.

[5] Y. Fu, D. Sun, Y. Chen, R. Huang, Z. Ding, X. Fu, Z. Li, Angew. Chem. Int. Ed. 51 (2012) 3364-3367.

[6] X. Meng, Q. Yu, G. Liu, L. Shi, G. Zhao, H. Liu, P. Li, K. Chang, T. Kako, J. Ye, Nano Energy 34 (2017) 524-532.

[7] I. J. Pickering, R. C. Prince, G. N. George, W. E. Rauser, W.A. Wickramasinghe, A. A. Watson, C. T. Dameron, I. G. Dance, D. P. Fairlie, D. E. Salt, Biochim. Biophys. Acta 1429 (1999) 351-364

[8] N. Fukuda, A. Hokura, N. Kitajima, Y. Terada, H. Saito, T. Abe, I. Nakai, J. Anal. At. Spectrom. 23 (2008) 1068.

[9] Y. L. Soo, W. H. Sun, S. C. Weng, Y. S. Lin, S. L. Chang, L.Y. Jang, X. Wu, Y. Yan, Appl. Phys. Lett. 89 (2006) 131908.

[10] M. Piñero, R. Litrán, C. Fernández-Lorenzo, E. Blanco, M. Ramírez-Del-Solar, N. De La Rosa-Fox, L. Esquivias, A. Craievich, J. Zarzycki, J. Sol-Gel Sci. Technol. 2 (1994) 689-694.

[11] S. Kumar, C. L. Chen, C. L. Dong, Y. K. Ho, J. F. Lee, T. S. Chan, R. Thangavel, T. K. Chen, B. H. Mok, S. M. Rao, M. K. Wu, J. Alloy. Compd. 554 (2013) 357-362.

[12] Z. Fang, S. Weng, X. Ye, W. Feng, Z. Zheng, M. Lu, S. Lin, X. Fu, P. Liu, ACS Appl. Mater. Interfaces 7 (2015) 13915-13924.

[13] L.B. Hoch, P. Szymanski, K.K. Ghuman, L. He, K. Liao, Q. Qiao, L.M. Reyes, Y. Zhu, M.A. El-Sayed, C.V.

Singh, G.A. Ozin, Proc. Natl. Acad. Sci. 113 (2016) E8011-E8020.

[14] M.F. Baruch, J.E. Pander, J.L. White, A.B. Bocarsly, ACS Catal. 5 (2015) 3148-3156.

[15] M.C. Figueiredo, I. Ledezma-Yanez, M.T.M. Koper, ACS Catal. 6 (2016) 2382-2392.

[16] K. Teramura, K. Hori, Y. Terao, Z. Huang, S. Iguchi, Z. Wang, H. Asakura, S. Hosokawa, T. Tanaka, J. Phys. Chem. C 121 (2017) 8711-8721.

[17] E.M. Kock, M. Kogler, T. Bielz, B. Klotzer, S. Penner, J. Phys. Chem. C Nanomater Interfaces 117 (2013) 17666-17673.

[18] H. Zhang, S. Kawamura, M. Tamba, T. Kojima, M. Yoshiba, Y. Izumi, J. Catal. 352 (2017) 452-465.

[19] K. Bhattacharyya, A. Danon, B. K.Vijayan, K.A. Gray, P.C. Stair, E. Weitz, J. Phys. Chem. C 117 (2013) 12661-12678.

[20] H. K. Kita, Takao, J. Res. Inst. Catal. Hokkaido Univ. 21 (1973) 200-246.

Chapter 5 Cation Vacancy-Initiated CO_2 Photoactivation over the Well-Crystalline ZnS for Efficient Formate Production

5.1 Introduction

Massive carbon dioxide (CO_2) emissions resulted from the anthropogenic activity and combustion of petroleum and gases have endangered our living environment and the earth's atmospheric layer.[1-4] The diminishing reserve of carbonaceous fuels necessitates our development of clean and renewable alternative energy resources.[5-7] With infinite solar energy, photocatalytic carbon dioxide reduction reaction (CO_2RR) towards chemical feedstocks pivot on sunlight and suitable catalysts stand out as an attractive approach to address the problem.[8,9] To date, despite the endeavor in such field and the discovery of a variety of photocatalysts, the efficiency and selectivity are still far behind the break-even point taking the cost into consideration.[10,11]

Nowadays, a problem worth noting in the research of photocatalytic CO_2RR is that the abuse of the carbon-containing photocatalysts, organic hole scavengers (methanol, triethanolamine, etc.), and even the organic chemicals used for synthesis makes it ambiguous to tell whether the seemingly identified products come from the CO_2RR or the decomposition of the involved carbonaceous materials, hindering the investigation of such reaction and the corresponding mechanism. In particular, ZnS, with a sufficiently negative conduction band situated at –1.04 V vs. NHE (pH=0),[12] is an excellent host material for CO_2RR that can work in all-inorganic reactant environment.[13] Nonetheless, the commercial ZnS with high crystallinity is rarely capable to show CO_2RR performance due to lack of active sites for activation of the stable CO_2 molecules.[13] Hence, the development of simple and effective approaches for endowing the photocatalysts with more reactive sites is urgently needed.

It is no wonder that utilizing a small stoichiometric deviation can alter the physicochemical properties of materials significantly.[14-16] The critical role of vacancies is worth noting as they always plays a decisive role in the photocatalytic chemistry.[9,17] Generally speaking, the advent of the vacancies brings about energetic and electronic disorder on the surface of catalyst, which allows for a higher possibility to activate the adsorbed species[18]; their involvement in trapping the photogenerated charge carrier affects charge separation and hence the photocatalytic efficiency.

In the past, numerous studies engineered the materials using anion vacancies for water splitting[19-24], nitrogen fixation[25-28], and CO_2 conversion[29-31]. However, anion vacancies are susceptibly deactivated by the oxygen species from the reaction environment. Though the sulfur vacancies have been demonstrated effective in chapter 2 and chapter 3. The deactivation of sulfur vacancy arouse us to seek for another more sustainable active site on ZnS. In addtion, as the Cd is a toxic element, the use of Cd is actually not expected. But the prounounced selectivity induced by Cd is obvious, which also encourages us to find an active site with high selectivity for CO_2 coversion.

Very recently, cation vacancy has intrigued scientists to open an alternative avenue to optimize the catalysts[32-35], but few researchers have touched the challenging CO_2RR in photocatalysis, especially a full understanding of the exact nature of cation defects on the surface and their impacts on the photocatalytic activity of CO_2RR at current stage.

In this chapter, cation vacancy-rich ZnS has been developed by an acid etching method, which can introduce imperfections on the outmost layers of ZnS but avoid the detrimental effect of the bulk defects within the photocatalyst. As a consequence, the photocatalytic CO_2RR behavior was boosted with a high production and selectivity to formate (> 85 %) in the absence of any rare, expensive and toxic elements and co-catalyst. Herein, a further step was taken to unravel the role of surface cation vacancies on photocatalyst in CO_2RR. *In situ* attenuated total reflection infrared (ATR-IR) spectroscopy was performed to substantiate that CO_2RR underwent a formate route via HCOO*. Structures of CO_2 molecules and their variant absorbed on the defective ZnS slabs were simulated using density functional theory (DFT) calculations to elucidate

the high selectivity and favorable kinetics for CO_2 conversion into formate with the presence of V_{Zn}. This work discloses the importance of cation vacancies on the surface and offers an inspiration for promoting the CO_2 reduction performance of the existing photocatalysts.

5.2 Experimental section

5.2.1 Preparation of photocatalysts

Acid etching was carried out directly over the commercial ZnS powders (95.0+ %, Wako Pure Chemical Industries, Ltd.). Firstly, 50 mL H_2O with different pH values (0.2, 0.7, 1.2, 1.8, 2.5) were prepared by carefully adding the concentrated sulfuric acid (H_2SO_4, 96.0~98.0 %, Wako Pure Chemical Industries, Ltd.) dropwise into the solutions. Then 1.0 g of the commercial ZnS powders were suspended in the as-prepared acidic solutions. The flasks were positioned at the magnetic stirrer and kept constant stirring over the course of 5 h. After etching, the resulting samples were washed and dried overnight in the vacuum oven at 80 ℃.

5.2.2 Characterization

X-ray diffraction patterns (XRD) were recorded on an X-ray diffractometer (X'pert powder, PANalytical B.V., Netherlands) with Cu-Kα radiation. The scanning electron microscopy (SEM) and transmission electron microscopy (TEM) images were acquired on a field emission- SEM (FE-SEM) (Hitachi, S-4800) and FEI Tecnai G2 F30 TEM (300 kV), respectively. UV−Visible (UV−Vis) absorption spectra were obtained via the Kubelka−Munk transformation from the diffuse reflectance spectra (DRS) measured on an UV−Vis spectrophotometer (UV-2500, Shimadzu, Japan) equipped with an integrating sphere. The Brunauer–Emmett–Teller surface area and CO_2 adsorption isotherms were acquired at 77K and room temperature, respectively, on BELsorp II mini (BEL Japan Inc.). The *in situ* attenuated total reflection-infrared (ATR-IR) spectroscopy was carried out by 45° IR incidence in CO_2 atmosphere on JASCO FT-IR-6300h. Samples were spread on the Ge crystal substrate irradiated by a 300 W Xe-lamp.

The fluorescence (PL) measurements were performed on a fluorescence spectrometer (JASCO FP-6500) with excitation wavelength of 320 nm. Time-resolved fluorescence measurements were carried out with the Fluorolog (Horiba Jobin Yvon, USA) using a 330 nm line of a NanoLED operating at room temperature. Raman measurement was performed on a Horiba Jobin Yvon Xplora-plus spectroscopy in air. X-ray photoelectron spectroscopy (XPS) was performed on PHI Quantera SXM (ULVAC-PHI Inc., Japan) to analyze the compositions and valence states of the samples. Electron spin resonance (ESR) measurements were performed with JEOL JES-FA-200 at room temperature.

5.2.3 Photocatalytic CO_2 reduction reaction

The photocatalytic CO_2RR over ZnS were carried out in a Pyrex glass reaction cell linked to a gas-closed circulation system connected to a gas-chromatography (GC) (GC-8A, Shimadzu Co., Japan, Carrier gas: Ar) with a thermal conductivity detector (TCD) for H_2 analysis. For each sample, 0.1 g photocatalyst was suspended in 50 mL aqueous solution containing 1.0 M $KHCO_3$ and 0.2 M K_2SO_3 sacrificial reagent. Before photo-reaction, the solution was evacuated until there were no O_2 and N_2 peak on GC analysis spectrum. High-purity CO_2 (99.999%) was purged into the system for several times until the CO_2 adsorption was fully saturated. A 300 W Xe lamp was used as the light source.

5.2.4 Carbonaceous species analysis and isotope tracer

The evolved gaseous carbon-species product was sampled and analyzed by a GC (GC-14B, Shimadzu Co., Japan) with a flame ionization detector (FID). For isotope tracer, $^{13}CO_2$ was purged in the system instead of the high-purity $^{12}CO_2$. $KHCO_3$ was not added to avoid the confusion of carbon source in this experiment. ^{13}CO was identified on a gas chromatography-mass spectrometry (GC-MS, JMS-K9, JEOL Co. Japan). The proton (^1H) spectra were recorded to determine the formate ions concentration on a 400 MHz nuclear magnetic resonance (NMR) spectrometer using deuterated water (D_2O) as solvent and dimethyl sulfoxide (DMSO, Sigma, 99.99%) as internal standard reference. $H^{13}COOH$ was identified by both ^1H spectrum and carbon (^{13}C) spectrum on the NMR.

5.2.5 Theoretical calculations

The theoretical method employed here was based on density functional theory (DFT). All the calculations were performed by CASTEP package within the Materials Studio at the generalized gradient approximation (GGA) level. The projector augmented wave (PAW) pseudopotential and the Perdew-Burke-Ernzerhof (PBE) was used to describe the ion-electron interaction and the exchange-correlation functional of electrons. The semi-empirical London dispersion corrections of Grimme were conducted to calculate the interactions between absorbers and samples.[35] The wurtzite ZnS (001) surface was present by a 3×3×3 supercell with a vacuum layer of 20 Å. The ZnS with V_{Zn} model were based on wurtzite ZnS model with a surface Zn atom replaced by a vacancy. The plane-wave cut-off energy level for geometry optimization and energy calculation were set as 480 eV and 590 eV, while the SCF tolerance level was set as 1.0×10^{-5} eV/atom in geometry optimization, and 1.0×10^{-6} eV/atom for energy calculation.

To study the influence of V_{Zn} on the kinetics, the adsorption energies of molecules involved in the CO_2RR pathways, denoted as E_{ads} (X/surface) (X=CO_2, COO*, HCO_3^-, HCO_3*, HCOO*, HCOOH), were calculated on the vacancy-present surface and well-crystalline surface, respectively, using the following equation:

$$E_{ads}\text{ (X/surface)} = E_{tot}\text{(X/surface)}-E_{tot}\text{(X)}-E_{tot}\text{(surface)} \quad (5\text{-}1)$$

, where E_{tot}(X/surface) is the total energy of optimized configuration of X adsorbed on the specific surface, E_{tot}(X) and E_{tot}(surface) is the total energy of an isolated X molecule and the surface slab, respectively.

The surface energy (γ) was calculated using the formula[36]:

$$\gamma = \frac{E_{slab}-nE_{bulk}}{2A} \quad (5\text{-}2)$$

, where E_{slab} is the total energy of the slab, E_{bulk} is the total energy of the bulk per unit cell, n is the number of bulk unit cells contained in the slab, and A is the surface area of the slab.

5.3 Results and discussion

5.3.1 Photocatalytic CO_2 reduction performance

Figure 1 depicts the production rate over the ZnS samples etched with sulfuric acid of different pH values under the Xenon lamp. When the catalyst was the pristine commercial ZnS, only H_2 and a small amount of CO could be detected. No detectable liquid product was identified by NMR even after 100 h irradiation. With the irradiation time prolonged, H_2 and CO were continuously produced with average rates displayed in Figure 5.1. In contrast, the ZnS samples after acid etching all showed markedly enhanced activity (Figure 5.2a) with a paramount production of 8.41 μmol h HCOOH when the acid solution pH reached to 1.2. The selectivity of HCOOH, CO, H_2 is shown as a column graph in Figure 5.2b. It was obvious that the main product of HCOOH over the acid-etched ZnS nanoparticles attained a selectivity up to 86.6 % in the absence of any rare, toxic and expensive elements and cocatalysts. Under a long-term irradiation of 60 h, it was seen that both H_2 and CO were generated in a linear manner (Figure 5.3) without any deactivation, indicating the V_{Zn}-contained samples are fairly stable during CO_2RR.

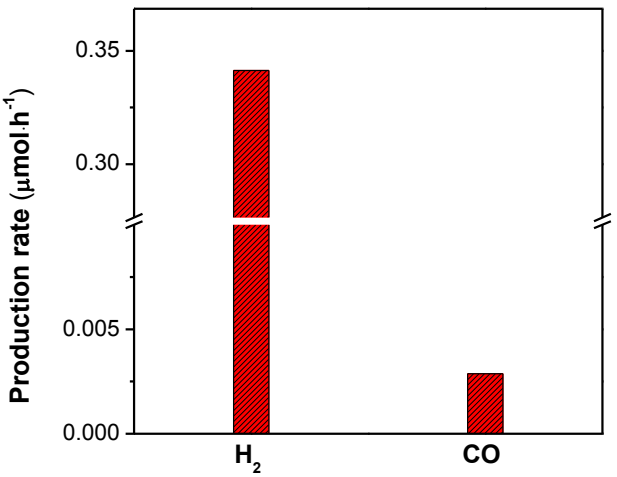

Figure 5.1 H_2 and CO evolution rate over pristine commercial ZnS nanoparticles.

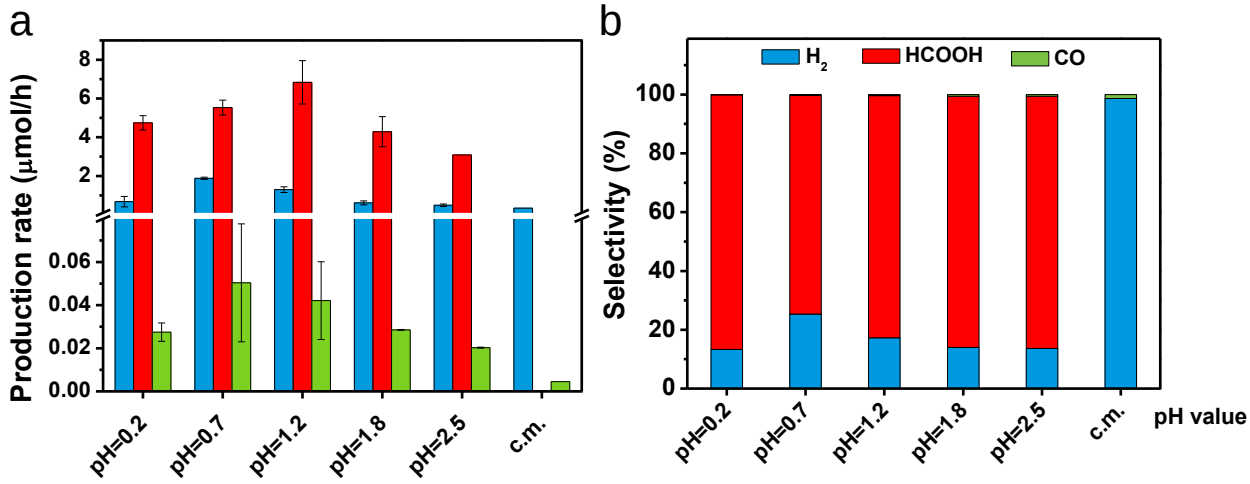

Figure 5.2 (a) Products (HCOOH, CO, H_2) evolution rates and (b) selectivity over the as-prepared ZnS samples etched with sulfuric acid of different pH values.

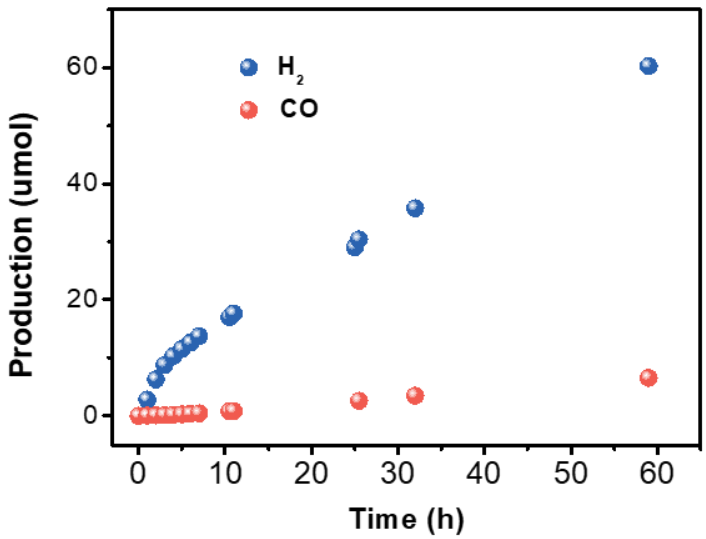

Figure 5.3 Long-term stability test of the representative sample in photocatalytic CO_2RR.

The isotope experiment using $^{13}CO_2$ as the carbon source confirmed that the gaseous product of CO originated from CO_2 instead of other carbon source on GC-MS with the peak at m/z=29 assigned to ^{13}CO (Figure 5.4). The liquid product (HCOOH) was validated both by ^{1}H and ^{13}C NMR spectra. As displayed in Figure 5.5, the peaks with chemical shift at 8.1 ppm and 8.6 ppm in the ^{1}H spectrum as well as the peak

at 170.5 ppm in the ^{13}C spectrum (Figure 5.6) indicate that the main liquid product formate stemmed from the starting $^{13}CO_2$ source.

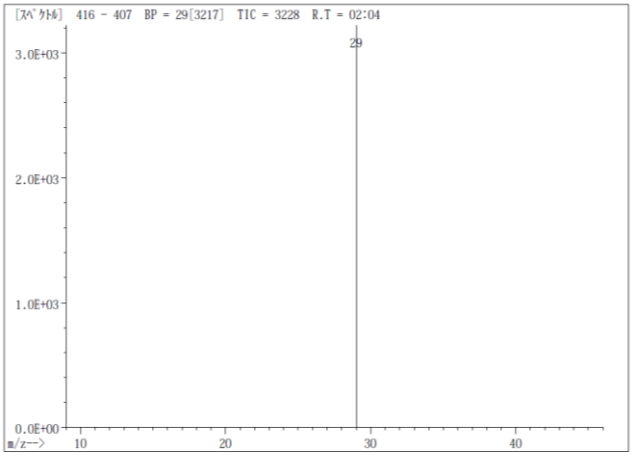

Figure 5.4 GC-MS spectrum of the gaseous product (CO) using isotope $^{13}CO_2$ over the representative acid-etched ZnS (pH=1.2).

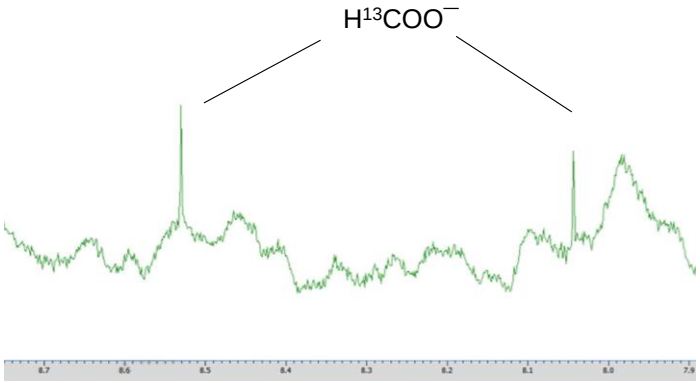

Figure 5.5 ^{1}H NMR spectrum of the liquid product (formate) using isotope $^{13}CO_2$ over the representative acid-etched ZnS (pH=1.2).

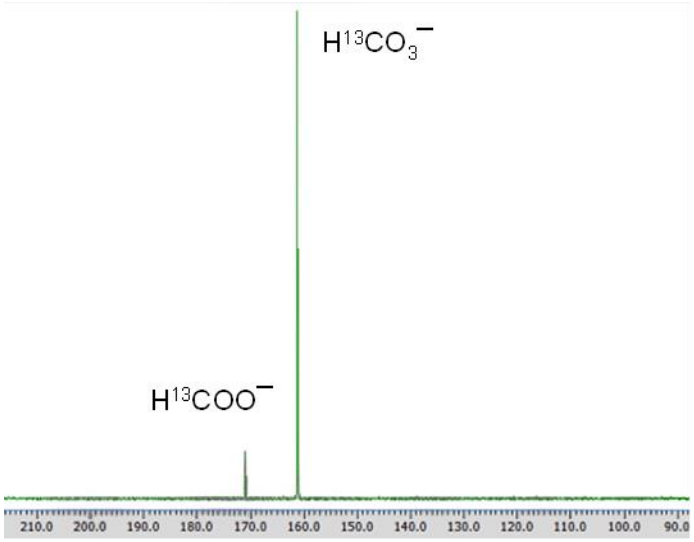

Figure 5.6 ^{13}C NMR spectrum of the liquid product (formate) using isotope $^{13}CO_2$ over the representative acid-etched ZnS (pH=1.2).

5.3.2 Crystal structure of acid-etched crystalline ZnS

To understand the origin of the pronounced photocatalytic performance behind the acid-etched samples, we begin with analyzing the morphology and structure. Etched by acid with different pH values, ZnS well maintained a typical wurtzite structure with *z*=2 (2H phase) that can be indexed to JCPDS No. 01-075-1547. There is no distinction of the crystallographic structure and morphology after acid etching as the surface composition change is too minor to be reflected on the XRD patterns and morphology (Figure 5.7a, 5.7b and 5.8). The most intensive peak at 28.4 °, indexed to 002 diffraction, is in agreement with our interpreted results from the high-resolution transmission electron microscopy (HRTEM) image in Figure 5.7c. The interplanar distance of the major exposed surface is 0.322 nm, in accord with the (002) crystal planes. Based on these results, we construct our surface slab as the model in the theoretical calculation.

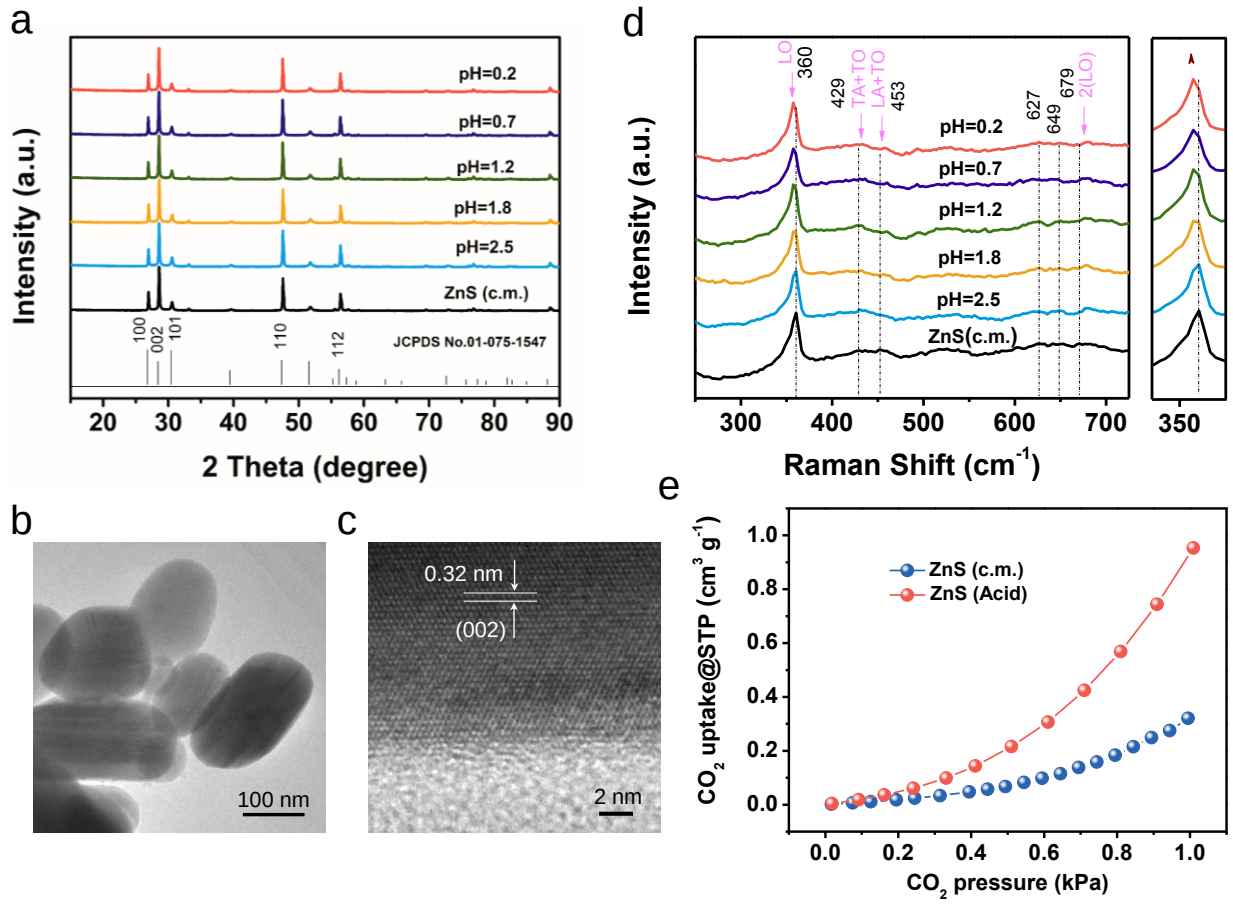

Figure 5.7 (a) XRD patterns of ZnS particles after etching with acid of different pH values. (b) TEM and (c) HRTEM images of the representative acid-etched ZnS sample (d) Raman spectra of ZnS particles after acid etching with different pH values (e) CO_2 adsorption isotherms for the pristine and the representative acid-etched ZnS sample.

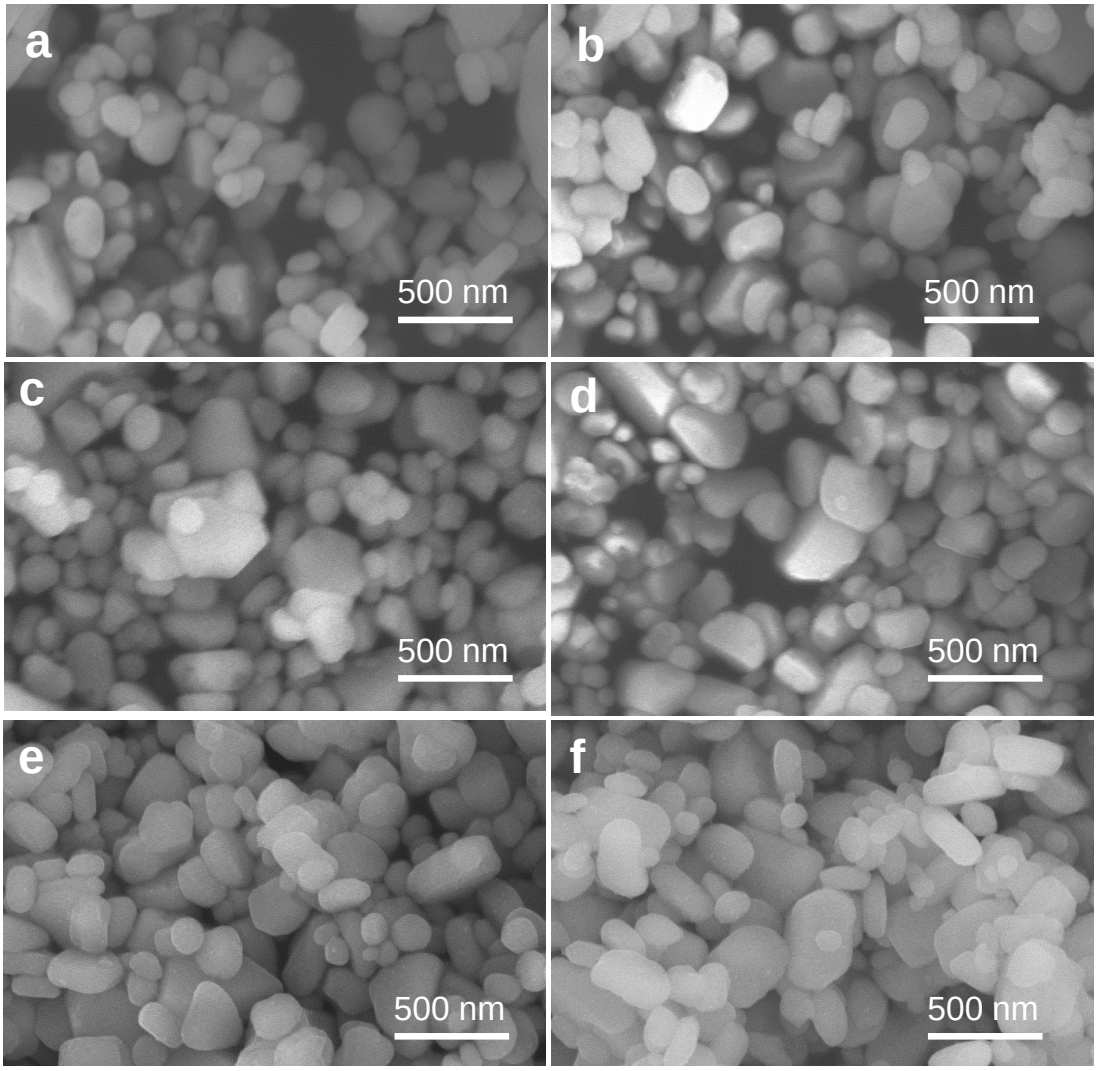

Figure 5.8 SEM images of the ZnS samples treated with acid (a) pristine (b) pH=2.5 (c) pH=1.8 (d) pH=1.2 (e) pH=0.7 (f) pH=0.2.

Probing the subtle information of the crystallinity and disorder on the surface, Raman scattering (Figure 5.7d) spectra clearly show a blue shift which occurs on the strong unresolved doublet peak at 360 cm^{-1}, which can be attributed to the first-ordering scattering longitudinal-optic A_1(LO) and E_1(LO) phonon modes.[38-40] In the intermediate region, the peaks at 429 cm^{-1} and 453 cm^{-1} are assigned to the transverse acoustic and optical modes (TA+TO) and transverse optical and longitudinal acoustic mode (TO+LA), respectively. In the high frequency region, our assignment of the 627 cm^{-1} to 2 (TO) overtones, 649 cm^{-1} to

(TO + LA) and 679 cm^{-1} to 2 (LO) are consistent with the ref[39]. As the LO and TO Raman bands are well known sensitive to the crystalline order of the material[38], the shift of peaks originally at 360 cm^{-1}, 429 cm^{-1}, 453 cm^{-1} and 679 cm^{-1} (marked by the pink arrows) found on the acid-etched samples with respect to the pristine ZnS might be caused by the structural distortion or the surface tensile stress.

The surface area and CO_2 adsorption capacity are of vital importance to the photocatalytic properties of the materials. Illustrated in Figure 5.9, the N_2 adsorption-desorption isotherms suggest that the pristine and acid-etched ZnS have the similar surface area, indicating that the acid etching on the commercial ZnS samples had no substantial effect on the surface area, in well accordance with the previous observations of SEM/TEM results. However, the acid-etched sample possesses almost three times higher CO_2 adsorption capacity than the pristine counterpart as shown in Figure 5.7e, partly accounting for the enhanced catalytic activity in terms of the increased interaction between the adsorbates and the active sites at the initial stage of CO_2RR.

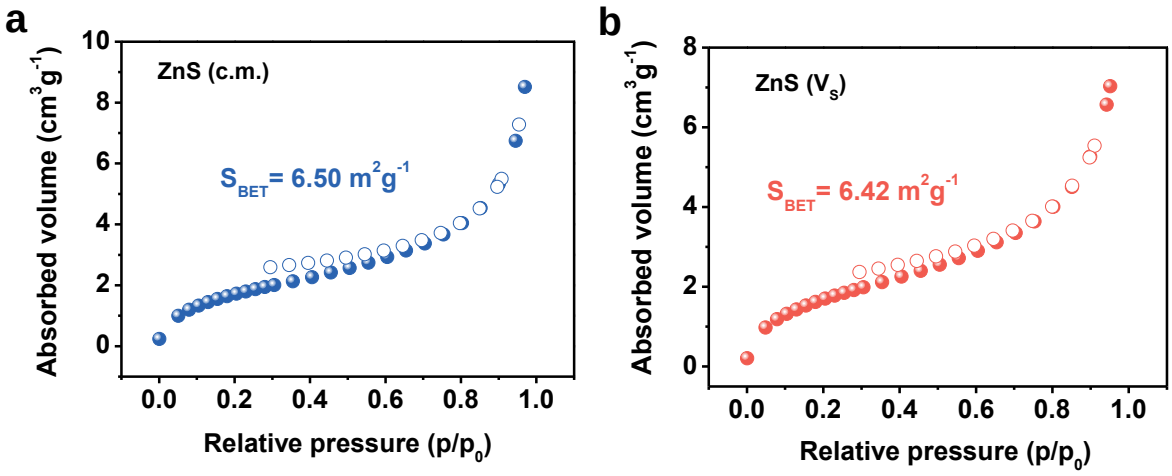

Figure 5.9 BET N_2 adsorption-desorption isotherms of (a) ZnS (c.m.) and (b) acid-etched ZnS (pH=1.2).

5.3.3 Zn vacancies in acid-etched crystalline ZnS

To determine the type of vacancy species existing on the surface, the bulk and near-surface Zn/S ratios of acid-etched ZnS samples were roughly determined by semi-quantification via the energy disperse

spectroscopy (EDS) and X-ray photoelectron spectroscopy (XPS), respectively. The molar ratios of Zn and S elements are shown in Table 5.1, indicating a stoichiometric excess of sulfur in the acid-etched samples compared with the pristine commercial counterpart. Therefore, we deduce that the acid etching promoted the Zn deficiency on the surface.

Table 5.1. Composition molar ratio (Zn/S) of pristine and acid-treated ZnS

Sample	**Bulk Zn/S ratio (EDX)**	**Surface Zn/S ratio (XPS)**
commercial	50.05/49.95=1.00	9.788/9.255=0.95
pH=1.8	49.64/50.36=0.99	24.776/28.529=0.87
pH=1.2	49.5/50.5=0.98	15.2/18.0=0.84
pH=0.7	49.3/50.67=0.97	29.676/37.677=0.79
pH=0.2	48.92/51.08=0.96	--

To detect the performance of the trapped electron and further verify the defect species of the acid-etched samples, ESR was further employed to gain a more direct evidence for the vacancies. The signals originated from the non-axial singly ionized V_{Zn} site with one hole localized on the three S neighbors in a trigonal symmetry split into six hyperfine lines in ZnS polycrystalline form[41-47]. Exhibited in Figure 5.10a, two discernible lines with g-factor value located at 2.021 and 1.978 belong to the reported six hyperfine lines of ZnS while the other four fall beyond the measured range (313.5-328.5 mT) and the other two symmetric peaks in the spectra are the reference lines of Mn markers (3rd and 4th).[47] Furthermore, the absence of the ESR peak at g=2.003, which is usually observed in the middle of the Mn 3rd and 4th makers and considered as the signature of sulfur vacancy (F center)[48], also indicate that the vacancy species is V_{Zn} instead of S vacancy (V_S) herein. Since the ESR signal intensity is correlated to the density of vacancies in the ZnS,[49] the enhanced intensity of ZnS (pH=0.7) and ZnS (pH=1.8) in contrast with the pristine ZnS can give a rough estimation of V_{Zn} amount tendency as displayed in Figure 5.10b.

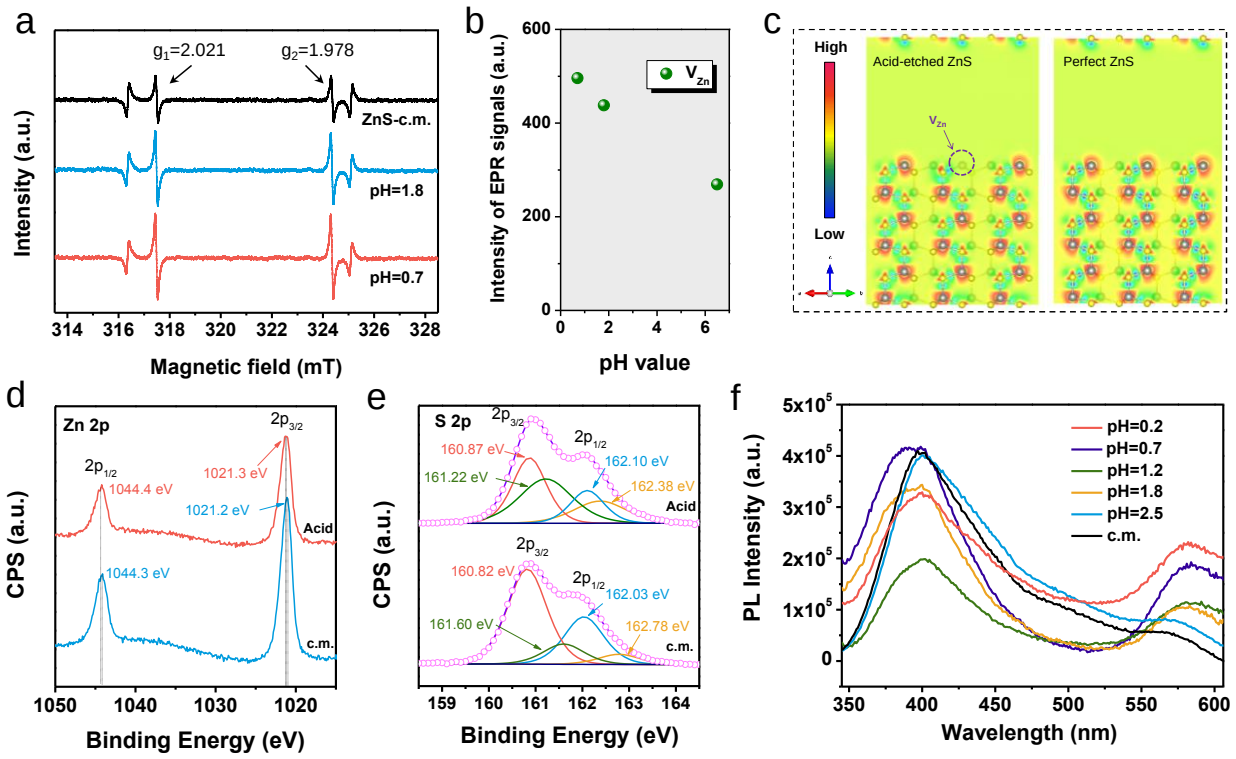

Figure 5.10 (a) Room-temperature ESR spectra (b) Calculated intensity of ESR signals at g_2=1.978 for the estimated relationship between V_{Zn} and pH value of the treated acid solution (c) Optimal cell structures of acid-etched ZnS ($Zn_{53}S_{54}$) and perfect ZnS ($Zn_{54}S_{54}$) with charge density. High-resolution XPS spectra of (d) Zn 2p and (e) S 2p of the pristine ZnS and the representative sample etched by sulfuric acid (f) PL spectra of the pristine ZnS and the acid-etched ZnS samples.

In Figure 5.10c, DFT calculations on (001) surface slabs of pristine and defective ZnS predict that the charge density of S atoms in the vicinity of V_{Zn} is less than that of the normal site, which is confirmed by the X-ray photoelectron spectroscopy (XPS). Compared with the high-resolution spectra of Zn 2p from the pristine ZnS, the binding energy of Zn $2p_{1/2}$ and Zn $2p_{3/2}$ in Figure 5.10d at 1021.3 eV and 1044.4 eV shift about 0.1 eV towards the higher binding energy, suggesting an increase of the Zn valence in the acid-etched samples. As single negative charged V_{Zn} decreases the electron density at the neighboring S sites, the binding energy of S is supposed to decrease concomitantly. In the spectra, the deconvoluted peaks at the

binding energy of 162.82 eV and 162.03 eV, assigned to S $2p_{3/2}$ and S $2p_{1/2}$ of the normal S atoms, respectively, almost remain at the same position but with a less proportion ratio. The peaks at 161.60 eV and 162.78 eV, representing the disordered S, shift toward lower binding energy to 161.22 eV and 162.38 eV, further validates the decreased electron density of the dangling S atoms due to the formation of V_{Zn} after acid etching (Figure 5.10e).

The V_{Zn} has been long accompanied with the self-activated luminescent centers.[50] To examine the luminescent property and the electron transfer behavior in the ZnS with the vacancy species, the steady-state photoluminescence (PL) spectroscopy over the ZnS samples was performed. As shown in Figure 5.10f, the excitation of 320 nm induces two major emission peaks at 390 nm and 580 nm. The blue emission peak near 390 nm lies close to the bandgap while the lower energy peak at 580 nm is consistent with the reported donor-acceptor luminescence band associated with V_{Zn}, which is another evidence of V_{Zn} formation on the surface.[51] PL studies also reveal that the intensities of the 580 nm peak increase with the pH value of acid decreasing, indicating more defective sites were generated by more acidic solution etching. It is also found that the most significant quenching of the blue emission occurs over ZnS (pH=1.2), reflecting its suppressed recombination of photocharged carriers and highest charge separation efficiency of the induced electron-hole pairs. When the time-resolved photoluminescence spectroscopy (tr-PL) was performed and the fluorescence decay curves were fitted by a bi-exponential function (Figure 5.11 and Table 5.2), the average lifetime of the ZnS (pH=1.2) also showed the longest lifetime up to 33.7 ns, accounting for the most effective charge separation and optimal formate production performance via supplying longer-lived electrons to the adsorbed CO_2.

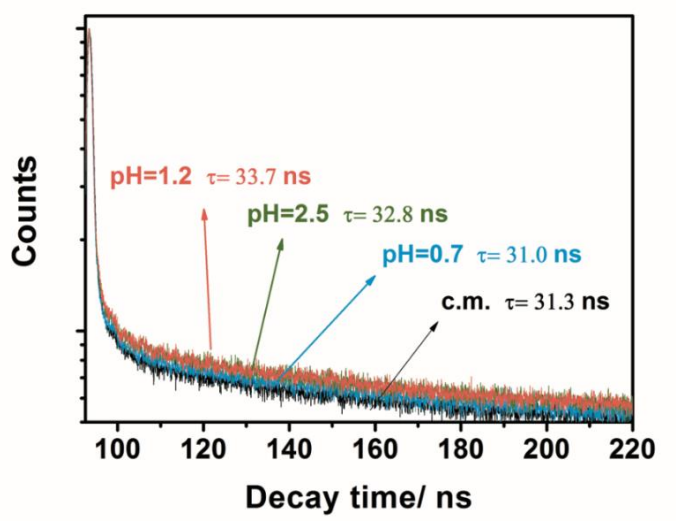

Figure 5.11. Photoluminescence decay curves of the representative ZnS nanoparticles with different acid etching conditions.

Table 5.2 Photoluminescence decay time of all the samples derived from the time-resolved photoluminescence spectra

Sample (acid pH value)	τ_1/ns	τ_2/ns	f_1	f_2	τ_{avg}
c.m.	0.113	31.4	0.5578	0.4422	31.3
0.2	0.003	28.5	0	1	28.5
0.7	0.265	31.2	0.4942	0.5058	31.0
1.2	0.267	33.9	0.4858	0.5142	33.7
1.8	0.211	33.4	0.4895	0.5105	33.2
2.5	0.142	32.9	0.5132	0.4868	32.8

*The average lifetime was calculated using the following equation: $\tau = (f_1\tau_1^2+f_2\tau_2^2)/(f_1\tau_1+f_2\tau_2)$

To disclose the correlation between surface V_{Zn} and electronic structure, DFT calculation was employed to calculate the band structure in the presence of V_{Zn}. As shown in Figure 5.12, after incorporation with a V_{Zn}, the bandgap of the ZnS is narrowed down, consistent with the slight red-shift of the absorption edge in the UV-Vis spectra (Figure 5.13). Noting that the electronic states of the V_{Zn}-contained ZnS above

Fermi level displays a higher density than that of the well-crystalline ZnS, it is reasonable to deduce that the defective ZnS can supply photo-excited electrons to the adsorbates in a more kinetically favorable manner, beneficial for the CO_2RR. Furthermore, as the electronic states of density increases in the vicinity of Fermi level of the defective ZnS, marked by the blue ribbon in Figure 5.12b, the defective ZnS possesses better conductivity, facilitating the electron transportation and charge separation as suggested before. In addition, the atomic and energetic disorder around V_{Zn} may provide a possible reactive site for the interaction between CO_2 molecules and the photocatalyst. The higher surface energy (γ) of 1.93 J/m^2 for V_{Zn}-contained (001) surface than that of the perfect *w*-ZnS surface, which is 1.12 J/m^2, also testifies that the defective ZnS is more reactive than the pure ZnS.

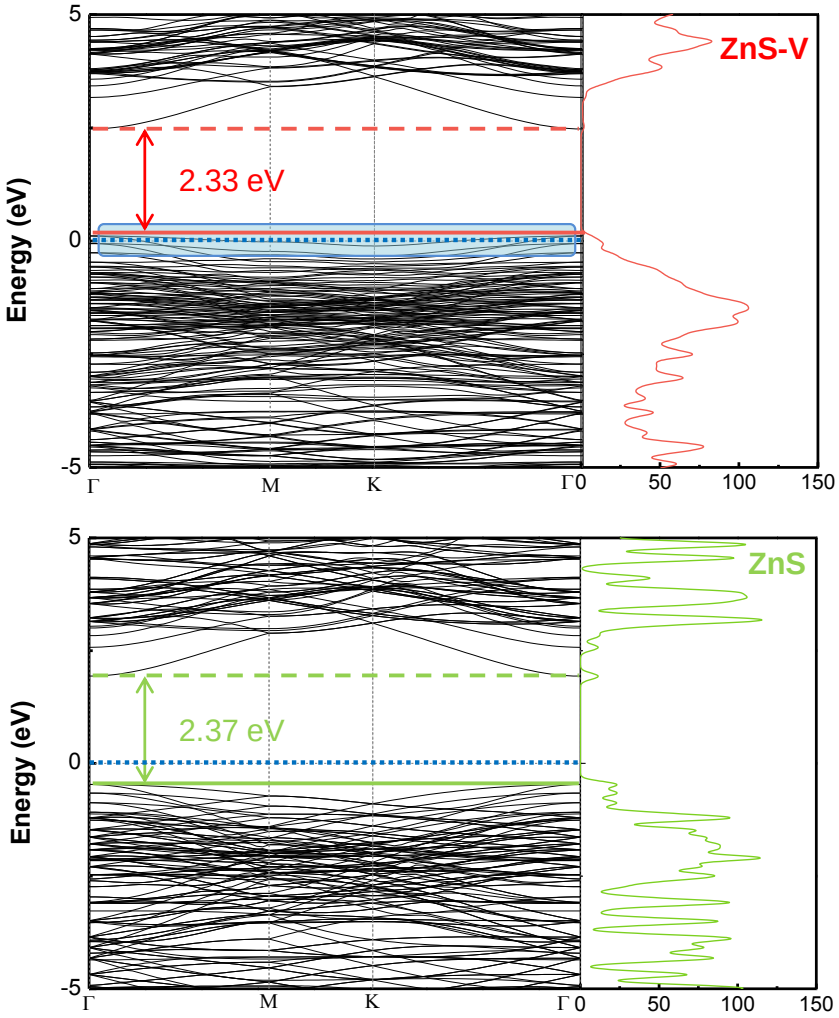

Figure 5.12 Band structure of pristine $Zn_{54}S_{54}$ (top panel) and V_{Zn}-contained $Zn_{53}S_{54}$ (bottom panel). The lines indicate different position: Fermi level (blue dot); CBM of $Zn_{54}S_{54}$ (green dot); VBM of $Zn_{54}S_{54}$ (green solid); CBM of $Zn_{53}S_{54}$ (red dot); VBM of $Zn_{53}S_{54}$ (red solid). The blue ribbon marked the mentioned electronic states near Fermi level.

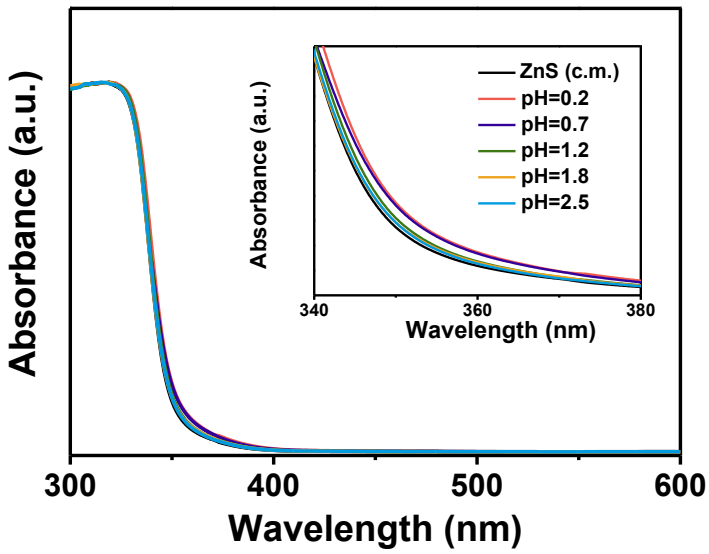

Figure 5.13 UV-Vis spectra of the acid-etched ZnS. Inset: enlarged absorption edge region (340-380 nm).

5.3.4 *In situ* ATR-IR observation during CO_2 reduction

The transformation of C1 molecules on solid surface is necessary for understanding the mechanism of the heterogeneous catalytic reaction. Nowadays, *in situ* techniques and theoretical calculations afford direct and powerful avenues to better understand the detailed catalytic transformation process.[52-55] In order to probe the catalytic transformation process over the V_{Zn}-contained ZnS in CO_2-saturated aqueous $KHCO_3$ solution, the *in situ* attenuated total reflection-Infrared (ATR-IR) spectra were collected in the atmosphere of CO_2. Herein the wet precipitate was spread directly on the Ge substrate after centrifugation of the reactant suspension containing the catalyst, K_2SO_3 and $KHCO_3$ saturated with CO_2.

As shown in Figure 5.14, the FTIR spectra after a period of illumination allow the monitoring of peaks in the range of 800-4000 cm^{-1} for the carbonaceous species transformation. The doublet bands centered at 2340 cm^{-1} indicate the chemisorbed gaseous CO_2 molecules.[54] As the range from 1000 cm^{-1} to 1750 cm^{-1} contains a lot of carbonaceous species information, a zoomed-in perspective of this region is shown in Figure 5.15. Peaks at 1684 cm^{-1}, 1637 cm^{-1}, 1386 cm^{-1}, and 1018 cm^{-1} originate from the stretching vibration of C=O [ν(C=O)], asymmetric and symmetric vibration of CO_3 stretching [$\nu_{as}(CO_3)$ and $\nu_s(CO_3)$] as well as the stretching vibration of C-O [ν(C-O)] of bicarbonate at the initial stage, indicating the reactant species are mainly bicarbonate except CO_2. Then, the shift of 1637 cm^{-1} to 1652 cm^{-1} indicates that the one electron transfer step occurs, generating the monodentate bicarbonate (*m*-HCO_3*) intermediate. The discernible peak at 1437 cm^{-1} with a shoulder peak at 1416 cm^{-1} is another signature of *m*-HCO_3.[56]

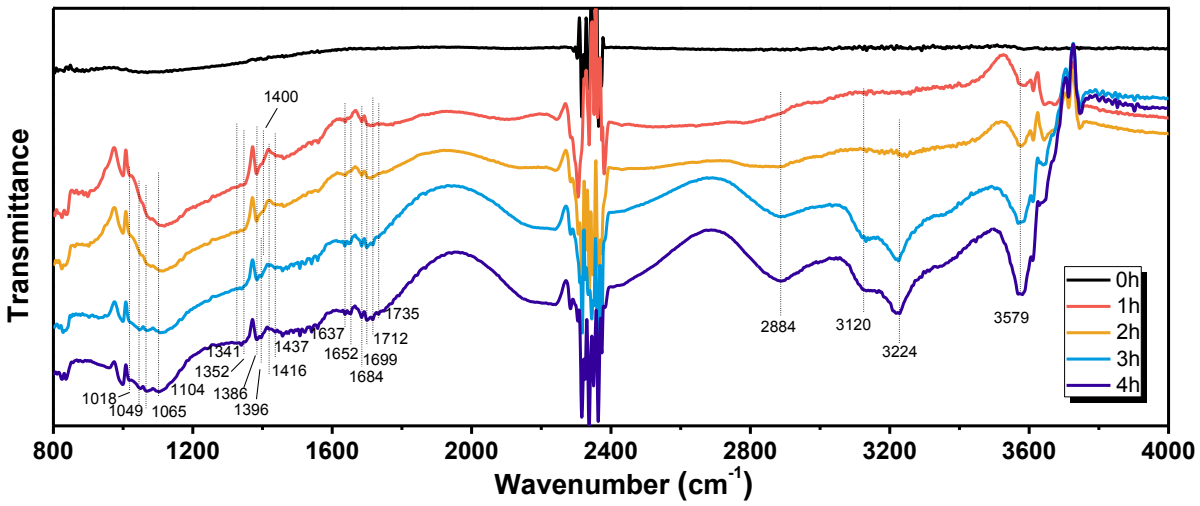

Figure 5.14 Time-dependent *in situ* ATR-IR spectra of V_{Zn}-contained ZnS under photo-irradiation in CO_2 atmosphere in the range of 800-4000 cm^{-1}.

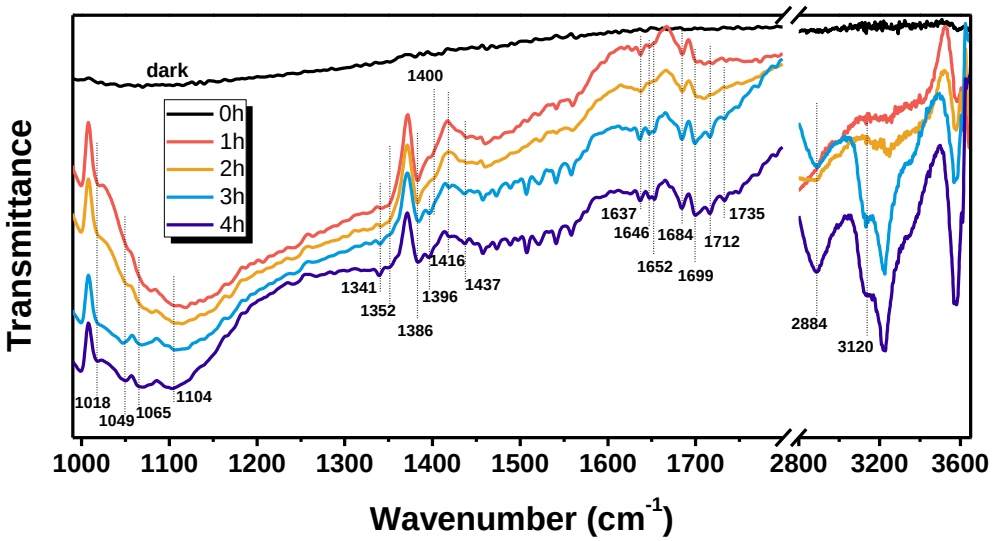

Figure 5.15 Zoomed-in time-dependent *in situ* ATR-IR spectra of V_{Zn}-contained ZnS under photo-irradiation in CO_2 atmosphere in the range of 1000-1800 cm^{-1} and 2800-3600 cm^{-1}.

It is generally accepted that the chemically adsorbed CO_2* initially accepts one electron to form the $CO_2^{\bullet -}$ intermediate. However, as the vibrational modes of such intermediate is in the same region with carbonate or bicarbonate species, it is difficult to identify its adsorbed configuration in the ATR-IR spectra.[57-59] From our observation and literature, the 1396 cm^{-1} contains the symmetric vibration of the intermediate COO^{-}*, which is considered visible within the spectra.

The peak alteration at 1712 cm^{-1}, 1341 cm^{-1}, and 1049 cm^{-1}, assigned to ν(C=O), ν(COO), ν(C-O), together with the peak at 2884 cm^{-1} assigned to C-H deformation [δ(C-H)], respectively, indicate the formate species formation. The shifted peak from 1400 cm^{-1} to 1396 cm^{-1} represents the formation of intermediate monodentate formate (*m*-HCOO*).[56] Closer examination reveals that there are two types of formate intermediate generated during the reaction. Careful comparison with the previous literature attributes the peak at 1646 cm^{-1} between 1637 and 1652 cm^{-1} as the characteristic of O-C-O stretching of bidentate bicarbonate (*b*-HCO_3*).[60] Accordingly, in addition to the *m*-HCOO*, bidentate formate (*b*-HCOO*) existed in the reaction. The growth bands at 1735 cm^{-1}, 1352 cm^{-1} and 1065 cm^{-1} which are attributed to ν(C=O), ν_s(COO) and ν(C-O), respectively, also demonstrate the generation of *b*-HCOO*.

With the prolongation of photoirradiation time, the peak at 1699 cm^{-1} associated with the *v*(C-O) at 1104 cm^{-1} and the broad peak 2700-3000 cm^{-1} arising from carboxylic acid hydroxide becoming stronger confirm the formate generation. The characteristic peak at 3120 cm^{-1} suggests that the final product is the stable conformer *trans*-HCOOH.[61] Compared with the production of HCOOH, CO is negligible as configured as the minor pathways in the CO_2 conversion.

A combination thereof figured out a plausible major pathway for CO_2 reduction on the surface of ZnS. The reaction path ways over the ZnS surface were most likely consisted of three elementary steps. In the first step, the chemisorbed CO_2 or HCO_3^- attached to the metal surface. When the semiconductor was excited and electron transfer occured, HCOO* was generated and linked to the ZnS surface. Then the second electron transfer to form $HCOO^-$, which were subsequently desorbed from the catalyst surface.

5.3.5 CO_2 activation and reduction

To clarify the impact of V_{Zn} on the kinetics and more details of the major pathways of CO_2RR over the defective ZnS surface, density functional theory (DFT) method was then performed to calculate the adsorption energy of the intermediates based on the experimental observations. According to the TEM and XRD results, the well-defined and defective (001) surface of wurtzite ZnS were adopted to simulate the reaction process.

First, we optimized the proton (H) adsorption to elucidate why the defective ZnS could give a high selectivity to the CO_2RR. Shown in the Figure 5.16, it is found that the H is simultaneously bound to the middle site of three Zn atoms, far away from the V_{Zn}. And the proton adsorption energy of -0.24 eV indicates the V_{Zn}-present ZnS surface is not favorable compared with the perfect ZnS from the energy configuration. Both the active site and thermodynamics suggest the V_{Zn} is not favorable for HER. However, the adsorption energy of CO_2 is -0.53 eV, lower than that of the H adsorption energy of -0.41 eV (See Figure 5.17) over the V_{Zn}-present surface, suggesting CO_2 stabilization is favored than proton on the V_{Zn}-present surface, when both reduction reactions exist. Thus, CO_2RR preferentially take places on the V_{Zn}-present ZnS,

accounting for the high selectivity of CO_2RR in the presence of competitive HER. Then, we throw the observed intermediate species of CO_2RR on the surface with and without V_{Zn}. The free energy diagram coupled with the model of CO_2, HCOO* and HCOOH on *w*-ZnS (100) surface was figured out in Figure 5.18.

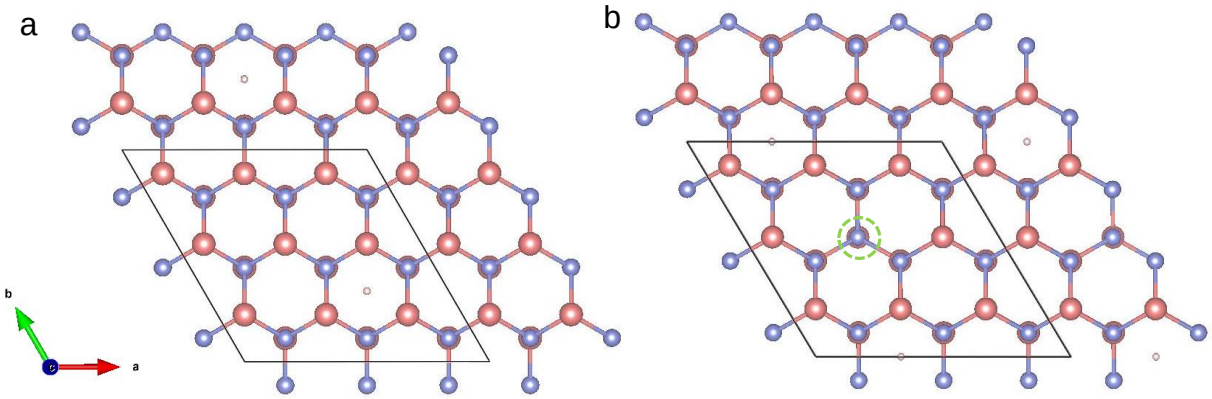

Figure 5.16 Illustration of the proton adsorption site over (a) perfect and (b) V_{Zn}-contained (001) ZnS surface. H: pink sphere, V_{Zn}: green circle.

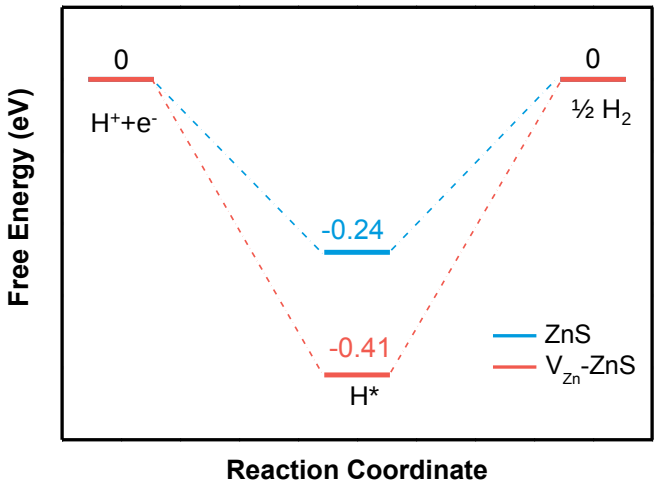

Figure 5.17 Hydrogen adsorption free energy versus the reaction coordinate of HER on perfect ZnS surface (blue) and V_{Zn}-contained ZnS surface.

When the reaction starts from CO_2 (Figure 5.18a), the free energy of adsorption on both surface with and without V_{Zn} is exothermic, indicating the adsorption of CO_2 is fairly easy. In this step, the free energy changed from -0.26 eV on the V_{Zn}-free surface to -0.53 eV on V_{Zn}-contained surface, indicating a much stronger capacity of the CO_2, consistent with the CO_2 uptake experiment stated above. When CO_2 accepts one electron to form COO^-*, the free energy increases, suggesting that the first electron transfer from ZnS surface to CO_2 is the rate-determining step. The energy barrier of 0.11 eV on perfect ZnS is reduced to 0.06 eV on the V_{Zn}-contained surface. Compared with the defect-free surface, the presence of V_{Zn} helps to stabilize the COO^-*, and thus accelerating the overall catalytic reduction rate. Since the conversion of COO^-* to HCOO* is exergonic (downhill in free energy) along the pathway, the protonation is easily surmountable. The intermediate HCOO* finds its optimized position attached to the ZnS surface with an O bridging between the intermediate species and V_{Zn}, in well accordance with our former interpretation of the *in situ* ATR-IR results, implying the pathway through *m*-HCOO* is dominant. In this step, more negative adsorption energy (-0.94 eV) is observed on the V_{Zn}-contained surface, signifying that the stability of *m*-HCOO* species is encouraged on the V_{Zn}-contained surface. The phenomenon may be responsible for the higher production of formic acid. In the next step, proton transfers to form the $HCOO^-$ which subsequently desorbed from the surface. On either defective or perfect surface, this reaction barrier is much small, suggesting the weakly bound conditions of $HCOO^-$ to the reactive sites in both cases, which enables the desorption of $HCOO^-$ from the active sites.

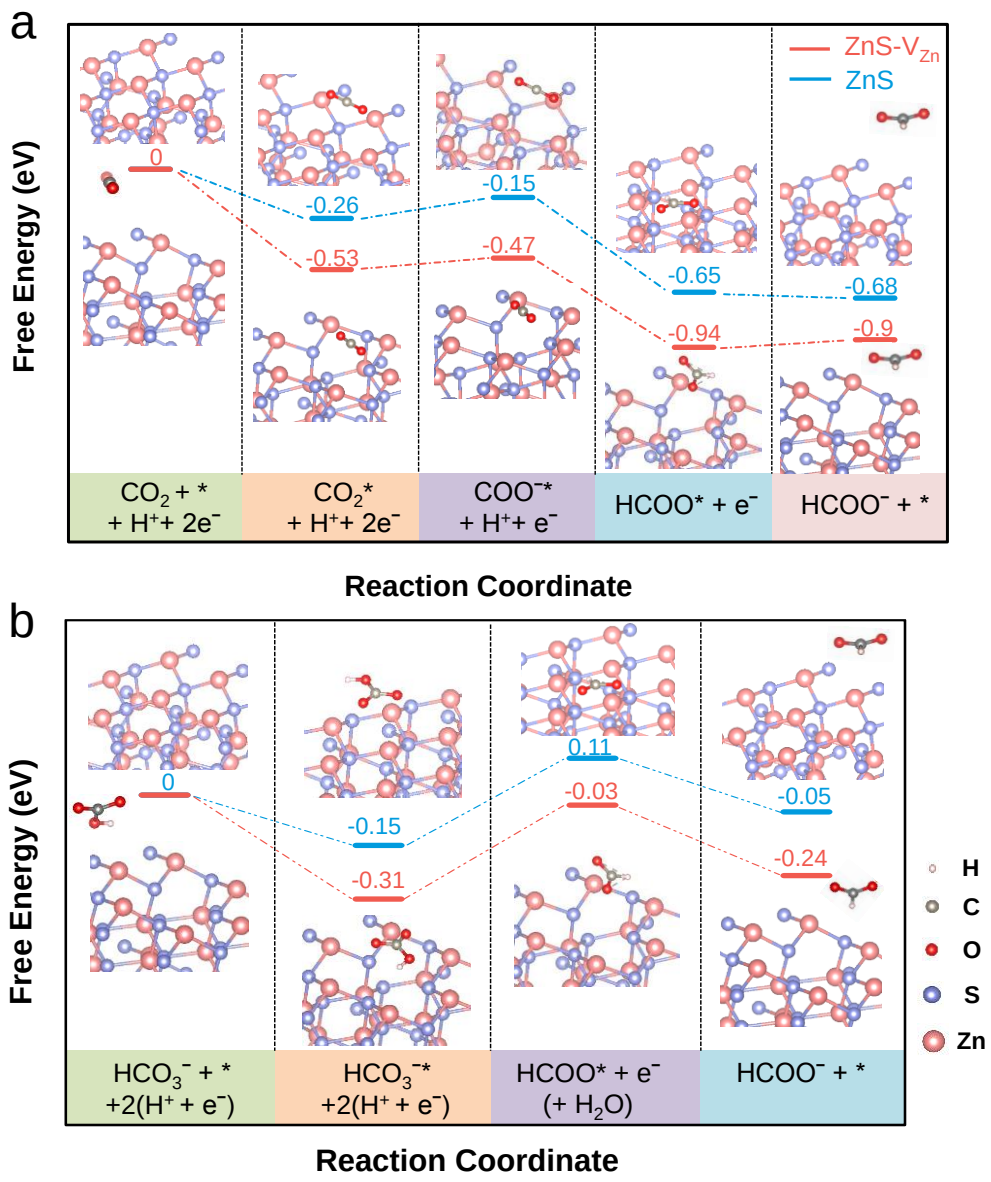

Figure 5.18 Calculated free energy diagram for the pathways of (a) CO_2 molecule (b) bicarbonate to formate. In each diagram, the pathway represents the free energy *vs.* SHE. The simplified surface structures correspond to the various species along the pathway, indicating the electron/proton transfer process at the (001) surface of *w*-ZnS.

In the case of bicarbonate (Figure 5.18b), the adsorption of HCO_3^- is also exothermic, indicating that the adsorption of CO_2 proceeds readily. The rate-determining step takes place where a proton-electron pair

couples with bicarbonate to form the bicarbonate species when the free energy is uphill along the pathway. The positive energy barrier from *m*-HCO_3 to *m*-HCOO* may prevent the conversion process.[10] Thus, the bicarbonate serves to enhance the concentration of effective CO_2 instead of the starting reactants.

Through computational calculations, we provide a possible explanation for the facile kinetic pathways of CO_2RR into the major product (formate) over the defective ZnS surface. The key holding for the efficient CO_2RR to formic acid over ZnS lies in the formation of intermediate COO^-* and HCOO* from CO_2. With V_{Zn} being exposed on the surface, the surmountable activation barriers can be significantly reduced. The combination of experiment and theory affords a more complete story to understand the importance of active sites in CO_2RR.

5.4 Conclusion

In summary, appropriate acid etching gave rise to V_{Zn} on the surface of well-crystalline ZnS nanoparticles and a significant enhancement of photocatalytic CO_2 conversion into formate occured. The high surface energy, the lower adsorption energy, and the enhanced charge separation, caused by the V_{Zn} contribute to the pronounced efficiency of the CO_2RR over the defective surface of ZnS. *In situ* ATR-IR and DFT calculations were adopted to elucidate the process of CO_2RR over ZnS via HCOO* and the high selectivity in the presence of HER. The current work gives a deep insight into the influence of cation vacancies on CO_2RR and inspires the exploration for efficient photocatalysts. For a broad perspective, our method should be applicable to the other photocatalysts designed thourgh band engineering towards visible light. In future, the strategy on the basis of surface cation vacancy are highly expected to develop the efficient photocatalysts for CO_2RR.

References

[1] C. Mesters, Annu. Rev. Chem. Biomol. Eng., 7 (2016) 223-38.

[2] W. Kim, B. A. McClure, E. Edri, H. Frei, Chem. Soc. Rev., 45 (2016) 3221-43.

[3] W.-H. Wang, Y. Himeda, J. T. Muckerman, G. F. Manbeck, E. Fujita, Chem. Rev., 115 (2015)12936-12973.

[4] G. A. Olah, G. K. S. Prakash, A. Goeppert, J. Am. Chem. Soc., 133 (2011)12881-12898.

[5] D. Kim, K. K. Sakimoto, D. Hong, P. Yang, Angew. Chem. Int. Ed., 54 (2015) 3259-3266.

[6] E. V. Kondratenko, G. Mul, J. Baltrusaitis, G. O. Larrazabal, J. Perez-Ramirez, Energ. Environ. Sci., 6 (2013) 3112-3135.

[7] S. C. Roy, O. K. Varghese, M. Paulose, C. A. Grimes, ACS Nano, 4 (2010) 1259-1278.

[8] H. Tong, S. Ouyang, Y. Bi, N. Umezawa, M. Oshikiri, J. Ye, Adv. Mater., 24 (2012) 229-251.

[9] X. Chang, T. Wang, J. Gong, Energ. Environ. Sci., 9 (2016) 2177-2196.

[10] M. I. Guzman, R. Zhou, J. Phys. Chem. C, 118 (2014) 11649-11656.

[11] K. S. Joya, Y. F. Joya, K. Ocakoglu, R. van de Krol, Angew. Chem. Int. Ed., 52 (2013) 10426-10437.

[12] D. Guzmán, M. Isaacs, I. Osorio-Román, M. Garcá, J. Astudillo, M. Ohlbaum, ACS Appl. Mater. Interfaces, 7 (2015) 19865-19869.

[13] X. Meng, Q. Yu, G. Liu, L. Shi, G. Zhao, H. Liu, P. Li, K. Chang, T. Kako, J. Ye, Nano Energy, 34 (2017) 524-532.

[14] L. Pan, S. Wang, W. Mi, J. Song, J.-J. Zou, L. Wang, X. Zhang, Nano Energy, 9 (2014) 71-79.

[15] G. Pacchioni, ChemPhysChem, 4 (2003) 1041-7.

[16] G. Li, G. R. Blake, T. T. Palstra, Chem. Soc. Rev., 46 (2017) 1693-1706.

[17] X. Meng, L. Liu, S. Ouyang, H. Xu, D. Wang, N. Zhao, J. Ye, Adv. Mater., 28 (2016) 6781-803.

[18] B. Hammer, J. K. Norskov, Nature, 376 (1995) 238-240.

[19] X. Chen, L. Liu, P. Y. Yu, S. S. Mao, Science, 331 (2011) 746.

[20] G. Ou, Y. Xu, B. Wen, R. Lin, B. Ge, Y. Tang, Y. Liang, C. Yang, K. Huang, D. Zu, R. Yu, W. Chen, J. Li, H. Wu, L. M. Liu, Y. Li, Nat. Commun., 9 (2018) 1302.

[21] N. Wang, M. Liu, H. Tan, J. Liang, Q. Zhang, C. Wei, Y. Zhao, E. H. Sargent, X. Zhang, Small, 13 (2017) 1603527.

[22] S. Wang, P. Chen, Y. Bai, J.-H. Yun, G. Liu, L. Wang, Adv. Mater. 2018, 30, 1800486.

[23] B. Zhang, L. Wang, Y. Zhang, Y. Ding, Y. Bi, Angew. Chem. Int. Ed., 57 (2018) 2248-2252.

[24] D. Chen, M. Qiao, Y. Lu, L. Hao, D. Liu, C. Dong, Y. Li, S. Wang, Angew. Chem. Int. Ed., 57 (2018) 8691-8696.

[25] Q. Wu, R. van de Krol, J. Am. Chem. Soc., 134 (2012) 9369-75.

[26] C. Li, T. Wang, Z. J. Zhao, W. Yang, J. F. Li, A. Li, Z. Yang, G. A. Ozin, J. Gong, Angew. Chem. Int. Ed., 57 (2018) 5278-5282.

[27] S. Wang, X. Hai, X. Ding, K. Chang, Y. Xiang, X. Meng, Z. Yang, H. Chen, J. Ye, Adv. Mater., 29 (2017) 1701774.

[28] N. Zhang, A. Jalil, D. Wu, S. Chen, Y. Liu, C. Gao, W. Ye, Z. Qi, H. Ju, C. Wang, X. Wu, L. Song, J. Zhu, Y. Xiong, J. Am. Chem. Soc., 140 (2018) 9434-9443.

[29] F. Wang, S. He, H. Chen, B. Wang, L. Zheng, M. Wei, D. G. Evans, X. Duan, J. Am. Chem. Soc., 138 (2016) 6298-305.

[30] L. Liu, Y. Jiang, H. Zhao, J. Chen, J. Cheng, K. Yang, Y. Li, ACS Catal., 6 (2016) 1097-1108.

[31] K. Xie, N. Umezawa, N. Zhang, P. Reunchan, Y. Zhang, J. Ye, Energ. Environ. Sci., 4 (2011) 4211-4219.

[32] M. Guan, C. Xiao, J. Zhang, S. Fan, R. An, Q. Cheng, J. Xie, M. Zhou, B. Ye, Y. Xie, J. Am. Chem. Soc., 135 (2013) 10411-7.

[33] X. Jiao, Z. Chen, X. Li, Y. Sun, S. Gao, W. Yan, C. Wang, Q. Zhang, Y. Lin, Y. Luo, Y. Xie, J. Am. Chem. Soc., 139 (2017) 7586-7594.

[34] S. Wang, L. Pan, J. J. Song, W. Mi, J. J. Zou, L. Wang, X. Zhang, J. Am. Chem. Soc., 137 (2015) 2975-83.

[35] X. Hao, Y. Wang, J. Zhou, Z. Cui, Y. Wang, Z. Zou, Appl. Catal. B: Environ., 221 (2018) 302-311.

[36] S. Grimme, J. Comput. Chem., 27 (2006) 1787-99.

[37] Y. Bi, S. Ouyang, N. Umezawa, J. Cao, J. Ye, J. Am. Chem. Soc., 133 (2011) 6490-2.

[38] Q. Xiong, J. Wang, O. Reese, L. C. Lew Yan Voon, P. C. Eklund, Nano Lett., 4 (2004) 1991-1996.

[39] Y. C. Cheng, C. Q. Jin, F. Gao, X. L. Wu, W. Zhong, S. H. Li, P. K. Chu, J. Appl. Phys., 106 (2009) 123505.

[40] J. Diaz-Reyes, R. Castillo-Ojeda, J. Mart ínez-Ju árez, O. Zaca-Moran, J. Flores-Mena, M. Galvan-Arellano, Int. J. Circuits Syst. Signal Process, 8 (2014) 15-21.

[41] P. H. Kasai, Y. Otomo, J. Chem. Phys., 37 (1962) 1263-1275.

[42] J. Schneider, A. Räuber, B. Dischler, T. L. Estle, W. C. Holton, J. Chem. Phy., 42 (1965) 1839-1841.

[43] J. Schneider, A. Räuber, Solid State Commun., 5 (1967) 779-781.

[44] H. Li, J. L. Bredas, Adv. Mater., 28 (2016) 3928-36.

[45] A. B. Djurišić, W. C. H. Choy, V. A. L. Roy, Y. H. Leung, C. Y. Kwong, K. W. Cheah, T. K. Gundu Rao, W. K. Chan, H. Fei Lui, C. Surya, Adv. Funct. Mater., 14 (2004) 856-864.

[46] N. T. Son, J. Isoya, I. G. Ivanov, T. Ohshima, E. Janzén, AIP Conf. Proc. 2014, 341-344.

[47] J. Schneider, B. Dischler, A. Räuber, J. Phys. Chem. Solids, 31 (1970) 337-353.

[48] Z. Fang, S. Weng, X. Ye, W. Feng, Z. Zheng, M. Lu, S. Lin, X. Fu, P. Liu, ACS Appl. Mater. Interfaces, 7 (2015) 13915-24.

[49] Y. Shono, T. Oka, J. Cryst. Growth, 210 (2000) 278-282.

[50] N. Riehl, J. Luminescence, 24-25 (1981) 335-342.

[51] K. M. Lee, K. P. O'Donnell, G. D. Watkins, Solid State Commun., 41 (1982) 881-883.

[52] N. J. Firet, W. A. Smith, ACS Catal., 7 (2016) 606-612.

[53] M. C. Figueiredo, I. Ledezma-Yanez, M. T. M. Koper, ACS Catal., 6 (2016) 2382-2392.

[54] M. F. Baruch, J. E. Pander, J. L. White, A. B. Bocarsly, ACS Catal., 5 (2015) 3148-3156.

[55] J. E. Pander, M. F. Baruch, A. B. Bocarsly, ACS Catal., 6 (2016) 7824-7833.

[56] K. Teramura, K. Hori, Y. Terao, Z. Huang, S. Iguchi, Z. Wang, H. Asakura, S. Hosokawa, T. Tanaka, J. Phys. Chem. C, 121 (2017) 8711-8721.

[57] M. Dunwell, Q. Lu, J. M. Heyes, J. Rosen, J. G. Chen, Y. Yan, F. Jiao, B. Xu, J. Am. Chem. Soc., 139 (2017) 3774-3783.

[58] H. Sheng, M. H. Oh, W. T. Osowiecki, W. Kim, A. P. Alivisatos, H. Frei, J. Am. Chem. Soc., 140 (2018) 4363-4371.

[59] C. Amatore, J. M. Saveant, J. Am. Chem. Soc., 103 (1981) 5021-5023.

[60] E. M. Kock, M. Kogler, T. Bielz, B. Klotzer, S. Penner, J. Phys. Chem. C, 117 (2013) 17666-17673.

[61] F. Richter, P. Carbonniere, J. Chem. Phys., 148 (2018) 064303.

Chapter 6 Interfacing Photosynthetic Membrane Protein with Mesoporous WO_3 Photoelectrode for Solar Water Oxidation

6.1 Introduction

Driven by the environmental concerns and the fossil fuels deficiency, the demand for clean and renewable energy resources has stimulated the development of highly efficient solar-to-fuel conversion innovations.[1-3] Recently, artificial photosynthesis based on inorganic solid-state semiconductors represents a sustainable route to generate alternative emission-free energy making use of solar light through photocatalytic or photoelectrochemical approaches.[4-11] However, artificial photosynthesis with conventional inorgnaic materials seems poised to realize sufficient supply of chemical feedstocks despite the extensive research on the exploitation of new materials[12-17] as most semiconductors are limited to absorb ultraviolet wavelengths, which only account for 4 % of the total solar energy (Figure 6.1).[18] Hundreds of individual light-harvesting complex aroused the interest of researchers. The bio-organism catalysts are profusely available and easily extracted from the photosynthetic organisms, even sometimes with self-repairing and self-replicating abilities.

As suggested in Chapter 1, with intricate and sophisticated light-harvesting and energy transduction systems, *Photosystem II* (PS II), a transparent protein, found in the thylakoid membrane of higher plants, algae and cyanobacteria, is the only nature-designed oxygenic phototroph responsible for oxygen evolution reaction (OER) with a high turnover frequency up to 1000 s^{-1} and a small overpotential.[19, 20] Since perfectly emulating the nature architecture is a mammoth task, it is more propitious to interface the natural proteins with conventional solid-state materials to carry out solar-to-fuel conversion.[12, 21]

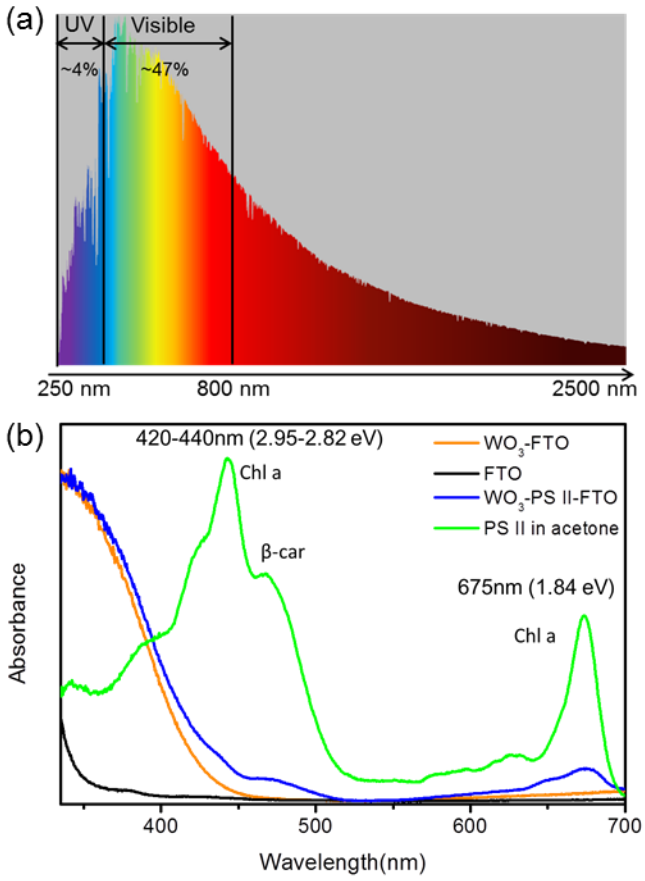

Figure 6.1 (a) Solar light spectrum (ASTM E-490) (b) UV-Vis spectra of the WO_3 film (orange), PS II-WO_3 on FTO (blue), PS II in acetone (green) and FTO glass (black).

In previous studies, the majority photoanodes hybridized with PS II focused on gold electrodes[22, 23] or carbon nanomaterials[24-26] as the substrates. Also, the redox mediators are usually involved to fulfill the cyclic electron flow to overcome the poor electron trasfer. Although the modification or hybridization can improve the photoresponse of PS II by promoting the electron transfer between the proteins and electrodes, the non-responsive Au electrodes or nanotubes/graphene made no contribution to the photocurrents under illumination, and prevented the affinity of protein coverage. Until now, only a few published reports have engaged semiconductors to enhance the photocurrent of PS II- based photoanodes.[27-30] Kato *et al* ever fabricated mesoporous ITO to allow for a dense coverage of PS II on

the electrode, obtaining a turnover frequency (TOF) of about 0.18 (mol O_2) (mol PS II)$^{-1}$ s^{-1} under monochromatic red illumination.[27] Even though there is a couple of studies involved with hematite[30] or TiO_2[29, 31, 32], the reported photocurrents under solar light are in the scale of nanoampere. Very recently, Rutherford *et al* suggested tungsten oxide (WO_3) might be a better candidate with the conduction band edge at least 0.2 V more positive than the reduction potential of Q_A and moderate charge mobility.[33] Thus, even devoid of the electron-transfer redox mediators, the electrons are facile to flow along the energy cascade from PS II to WO_3. In addition, to our knowledge, WO_3 is a visible-light responsive and uncostly semiconductor with chemical durablity and biocompatibility in photocatalysis,[33-39] extending the light absorbance to larger proportion of the solar spectrum than the previous ITO or TiO_2. Furthermore, the absorption region of the PS II-WO_3 assembly encompassed the most intense region of the solar spectrum (400~ 700 nm) as seen in Figure 6.1b. Thus, the bio-inorganic interaction between a visible semiconductor and photosynthetic protein may expand the light utility and increase the activity of the protein-inorganic hybrid.

In this chapter, a bio-conjugated hybrid of PS II with modified tungsten oxide (WO_3) mesoporous matrix is constructed for the first time and the photoanodic performance is evaluated. Direct assembly was investigated to simplify the process of the electron transfer and avoid the undesirable use of the mediators. Once irradiated, electrons released from PS II provoked by light inject into the conduction band of WO_3 following the possible pathways illustrated in Scheme 6.1. The bio-hybrid photoanode shows better photoelectrochemical performace than either WO_3 or PS II itself in the absence of redox mediators. Our work reported herein may provide insights both in artificial photosynthetic and biological research to explore the interdisciplinary possibilities and mechanism behind the construction of bio-conjugated inorganic architecture for future energy conversion.

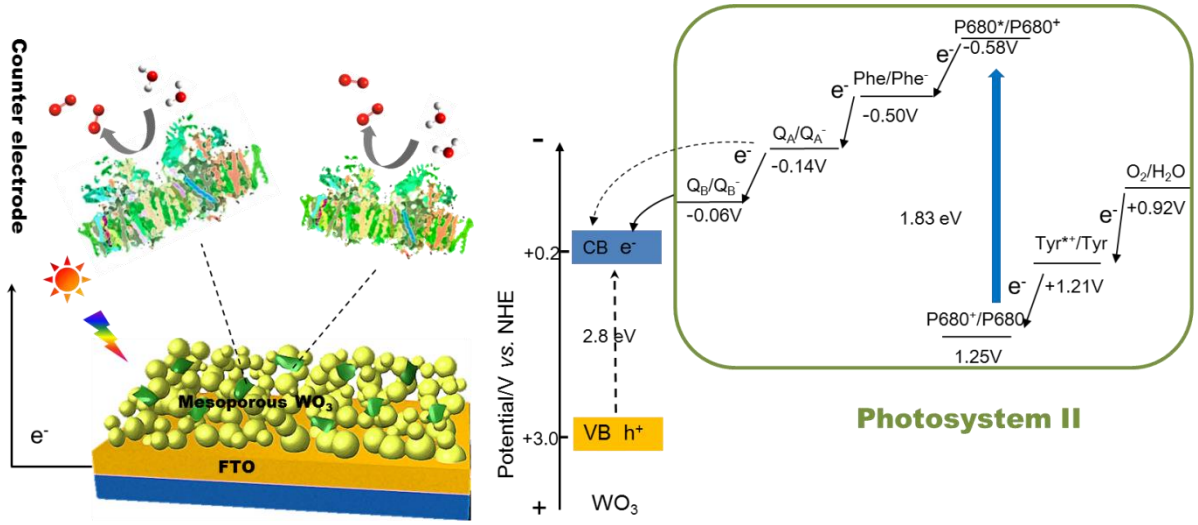

Scheme 6.1 Schematic illustration of the bio-hybrid photoanode consisted of mesoporous WO_3 and *Photosystem II* (PS II) on FTO substrate and the possible electron transfer pathways of the main cofactors in the bio-semiconductor assembly.

6.2 Experimental section

6.2.1 Fabrication of mesoporous WO_3 electrode

The fabrication of colloidal WO_3 solution was according to a sol-gel method with modification.[40] In details, tungstic acid was achieved from the aqueous Na_2WO_4 solution (0.1 M) passing through a ion exchange resin (Dowex 50 WX2-200 (H)). The elution was collected in ethanol and concentrated overnight to *ca.* 0.5 mol^{-1} L under continuous stirring. 4.1 mL poly(ethylene glycol) (PEG) 300 was added as a stabilizer to the freshly concentrated tungstic acid alcohol solution. The obtained viscous and yellow solution was maintained under stirring for subsequent spin coating of WO_3 film.

The WO_3 film was spread onto the conducting glass substrate of F-doped SnO_2 (Sigma-Aldrich, surface resistivity~7 Ω/square) by spin-coating. 20 μL was dropped at one time onto the substrate followed by first spin coating at a low rate of 500 rpm for 20 sec and second spin coating at 2,000 rpm for 50 sec. The deposited layer was then dried at room temperature and annealed at 500 ℃ for 30 min.

6.2.2 Extraction of *photosystem II* (PS II) from *Spinach*

PS II in this experiment was extracted from *Spinach* purchased from a local market by a developed method.[26] All the reagents and operation was under 4 ℃ in the dark. Fresh spinach leaf without any stems and stalks were selected and washed with ultrapure water (Direct-Q® 3UV), cut into small pieces and grinded in a precooled mortar using Buffer A (20 mM Tricine-NaOH pH 7.8, 0.4 M sucrose, 2 mM $MgCl_2$, 40 mM NaCl, 2 mM Vitamin C, 0.2% bovine serum albumin (BSA)). Then the mud was immersed in the Buffer A to dissolve the chloroplasts and filtered with eight layers of cotton gauze. The filtrate was centrifuged at 400 g for 1 min and the supernatant was centrifuged at 6000 rpm (Beckman F0630 Rotor) for 15 min. The precipitant was suspended in the Buffer B (20 mM Tricine-NaOH pH 7.8, 5 mM $MgCl_2$, 10 mM NaCl, 0.2% BSA) and stirred for 15 min in an ice bath, followed by 2 min centrifugation at 250 g. The supernatant was then centrifuged at 7,000 g for 15 min to get the thylakoid membranes. The precipitant was suspended in 40 mL Buffer C (20 mM MES-NaOH pH 6.5, 0.4 M sucrose, 15 mM NaCl, 5 mM $MgCl_2$). The chlorophyll (Chl) concentration was determined by adding 10 μL suspension into 3 mL acetone (20 % vol). UV-Vis spectrum was measured over the obtained solution and the Chl concentration was determined as 2.3 mg mL^{-1} from the fomula: Chl = 7.15*A663.2+18.71*A646.8 (mg mL^{-1}). A663.2 and A646.8 was the absorption value at the wavelength of 663.2 nm and 646.8 nm. 7.65 mL 20 wt% TX-100 was added into Buffer C to obtain the Buffer D. Afterwards, the Buffer D was slowly added to the suspension with gently stirring to avoid foaming until the ratio of TX-100 to Chl (w/w) is 20:1. After stirring for 10 min in ice bath, the solution was centrifuged at 10,000 g (6000 rpm) for 1 min to remove the debris and then high-speed centrifuged at 35,000 g for 30 min. The obtained precipitated pellet was again suspended in the Buffer C and washed by centrifugation for three times until the suspension was colorless. The final obtained pellets was then suspended in 5 mL Buffer E (4.5 mL Buffer C+ 0.5 mL 0.5 M Betaine). For convenience, the final suspension was divided in ten 0.5 mL aliquots and stored in −80 ℃ frozen refrigerator for further use.

6.2.3 Assembly of PS II and mesoporous WO_3 (meso WO_3) electrode

Positive charged PEI molecules were used to anchor the PS II onto the mesoporous WO_3 substrate by electrostatic interaction. To achieve the assembled electrode, the as-prepared WO_3 substrate was immersed in PEI solution (2.0 mg mL^{-1}, 0.2 M NaCl, 20 mM MES, pH 6.5) for 30 min at 4 ℃. Then the substrate was washed by MES buffer (20 mM, pH 6.5) to remove the unattached molecules. After dried by a mild stream of Ar, the PEI-WO_3 substrate were immersed into 5 mL PS II solution (~ 0.5 mg Chl mL^{-1}, 20 mM MES) for self-assembly. After specific period, the substrate was rinsed with MES buffer solution to remove the excessive unbounded PS II proteins and dried by a mild Ar stream before characterization and photoelectrochemical measurements. The preparation of PS II directly assembled on FTO substrate underwent the same process.

6.2.4 Characterization

The XRD patterns of the prepared samples were recorded on an X-ray diffractometer (XRD, RINT 2000; Rigaku Corp.) with monochromatized Cu K*a* radiation (λ = 1.54178 Å), under 40 kV and 30 mA. Optical absorption properties of the WO_3 and composite electrode were measured over an UV–Vis spectrophotometer (UV–2500PC; Shimadzu Co., Japan). The concentration of Chl during the purification of PS II were determined by another UV–Vis spectrophotometer (Hitachi U–3900). The morphologies of the mesoporous WO_3 substrate was studied by scanning electron microscopy (SEM, S4800, Hitachi Co., Japan) and transmission electron microscopy (TEM, 2100F, JEOL Co., Japan). The fluorescence images were visualized by an Leica DM 2500 upright fluorescence microscope (Leica Microsystems, Wetzlar, Germany) with equipped L5 band-pass (BP) 480/40 nm excitation filter and attached to a Leica DFC 300 FX camera.

6.2.5 Photoelectrochemical measurements

The photoelectrochemical performance were measured in a three-electrode system with a CHI electrochemical analyzer (ALS/CH model 650A). The prepared electrode was set as the working electrode

with a Pt sheet counter and saturated calomel electrode (SCE) (RE-2BP; BAS Inc.) as reference electrode. To maintain the activity of the used protein, a buffer (20 mM MES, 50 mM KCl, 5 mM $MgCl_2$ and 3 mM $CaCl_2$) with pH value of 6.5 was used as the electrolyte and precooled at 4 ℃. Before carrying on the PEC measurements, the solution was bubbled with Ar for at least 15 min to purge the dissolved O_2. A 500 W Xe lamp (Optical ModuleX; Ushio Inc., 0.6 W cm^{-2}) and an AM 1.5 solar simulator (WXS−80C−3 AM 1.5G, 87 mW cm^{-2}) were used as the light source using a spectroradiometer (USR−40; Ushio Inc.). All the potentials in PEC performance vs. SCE were converted to the reversible hydrogen electrode (RHE) scale via the Nernst equation:

$$E_{RHE} = E_{SCE} + 0.059\ pH + E^{o}_{SCE} \quad (6\text{-}1)$$

, where E_{RHE} is the converted potential vs. RHE, E_{SCE} is the experimental potential measured against SCE reference electrode, E^{o}_{SCE} is 0.2415 V (25 ℃). The incident photon to electron conversion efficiency (IPCE) was measured using a motorized monochrometer (M10; Jasco Corp.). IPCE can be calculated as

$$IPCE = 1240\, j_p(\lambda) / \lambda E_\lambda(\lambda) \quad (6\text{-}2)$$

, where $j_p(\lambda)$ is the measured photocurrent density (mA cm^{-2}), λ is the incident light wavelength (nm) and $E_\lambda(\lambda)$ is the incident monochromatic light power density (mW cm^{-2}) at a certain wavelength.

The half-cell power conversion efficiency (η) is calculated following the equation[41]

$$\eta = \frac{|J_{light} - J_{dark}|(mA \times cm^{-2}) \times (1.23 - E_{RHE})(V)}{P_{sun}(mW \times cm^{-2})} \quad (6\text{-}3)$$

, where J_{light} and J_{dark} are the measured current density under illumination of AM 1.5 and in the dark, respectively; E_{RHE} is the potential of the working electrode versus RHE, P_{sun} is the incident of AM 1.5 irradiance.

To test the electron pathway in the presence of DCMU, a solution of DCMU in DMSO was added to the electrolyte with the final concentrations of DCMU and DMSO were 1 mM and 1% (v/v), respectively.[38] We calculated the flatband potential (E_{fb}) of the pristine WO_3 from the following Mott–Schottky equation [42]:

$$1/C^2 = (2/ee_0\varepsilon\varepsilon_0 N_d)(E - E_{fb} - kT/e_0) \quad (6\text{-}4)$$

, where C is the differential capacitance of the Helmholtz layer, e_0 is the electron charge, ε the dielectric constant of WO_3, ε_0 the permittivity of vacuum, N_d the donor density, and E the applied bias at the electrode. The measured flatband potential vs. Ag/AgCl can be converted to the potential vs. NHE following the next equation:

$$E_{NHE} = E_{Ag/AgCl} + 0.197 \quad (6\text{-}5)$$

, where E_{NHE} is the potential with respect to NHE and the $E_{Ag/AgCl}$ is the measured potential with reference electrode of Ag/AgCl.

6.3 Results and discussion

6.3.1 Characterization of the PS II| meso WO_3 photoelectrode

In order to enlarge the surface active sites to immobilize PS II segments, mesoporous WO_3 substrates were fabricated by a sol-gel process onto the FTO glass. The crystalline WO_3 film has a monoclinic phase as tested by X-ray diffraction (XRD) pattern in Figure 6.2a. The WO_3 film was prepared on a surface of 1.0 cm^2 by annealing WO_3 nanoparticles with diameters ranging from 20 to 100 nm at 500 ℃ as seen from the SEM images in Figure 6.3a and TEM images in Figure 6.2b and c. The resulting porous morphology is obtained with gully distributed and interconnected on FTO-coated glass slides. As seen from Figure 6.2d, Brunauer–Emmet–Teller (BET) analysis of the scraped WO_3 film debris gave a surface area value of 39 m^2 g^{-1}, confirming the high porosity determined by the interconnected network of the WO_3 gullies. From the inset of pore-size distribution, it is observed except for the pores around approximately 4 nm in the mesoporous region, the interparticle macroporous pores diameters ranged from 10 nm to 35 nm. The film has a thickness of approximately 1.3 μm (Figure 6.3b) and gully morphology with opening size up to 200 nm. Such porous structure could provide with channels for the PS II to diffuse into the pores, enabling the successful anchoring of PS II on WO_3 film. In addition, the better hydrophilic property of the porous WO_3, based on the phenomena that the water droplet instantly immersed into the film with a contact angle close

to 0 ° (Figure 6.2e), would promote the entrapment of the enzymes which typically include a variety of functional groups such as hydroxyl group and sulfonate group like that in water. Thus, it is potentially capable of supporting the PS II with a dimension of $20.5 \times 10.5 \times 11.0$ nm^3 that is well-matching to the pore size.[43] The biocatalyst, PS II in this work, are isolated and purified from fresh spinach. The electrophoresis result shows that the sodium dodecyl sulfate polyacrylamide gel electrophoresis (SDS-PAGE) patterns are well consistent with that in previous reference[26] (Figure 6.4). Together with the UV-Visi spectrum of PS II in acetone (Figure 6.1b), which shows two major peaks at 450 nm and 675 nm, corresponding to Chlorophyll *a* (Chl *a*), we can confirm that the isolated part indeed includes the intact reaction complex of PS II. A branched polymer, polyethylenimine (PEI), with an amino group at the end, was grafted on the WO_3 substrates as a cationic polymer ligand to couple the PS II stromal side by electrostatic attachment, confirmed by the measured zeta potential of the PEI and PS II, which are 1.19 mV and −0.93 mV, respectively. The optimized loading amount of PS II was achieved after immersion in 0.12 mg mL^{-1} Chl *a* solution (details of the optimization are seen in the Figure 6.5). The final maximum amount of multilayered PS II on electrode was quantified as *ca.* 0.27 ± 0.01 pmol by calculating the Chl *a* amount. The successful assembly of PS II on the WO_3 electrode was validated from the bright-field optical microscope images (Figure 6.3c) and the corresponding fluorescence intensity image (excitation wavelength: 480 nm) (Figure 6.3d) as there are strong emission fluorescence on PS II| meso WO_3 stemming from the chlorophylls while no fluorescence imaging were present on bare WO_3 (Figure 6.6) on the FTO glass slide. To evaluate the elemental composition and distribution, we also conducted the EDS mapping over the pure WO_3 and PS II-WO_3 on FTO, respectively. As the *Spinach* protein are mainly built with the elements of carbon (C), nitrogen (N), sulfide (S) and Phosphorus (P), etc., the four elements are selected to determine the composition ratio semi-quantitatively and the data are summarized in Table 6.1. From Table 6.1, the higher content of C and the appearance of N, P, S also suggested the existence of PS II on the WO_3 substrate after modification with PS II. The UV-visible absorption spectra in Figure 6.1b also demonstrate the PS II has been evenly anchored on the WO_3 substrate. No distinct change was seen in the two spectra

of PS II in solution and as modification on WO_3 substrate, which indicate reaction center segments remains unaltered after assembly.

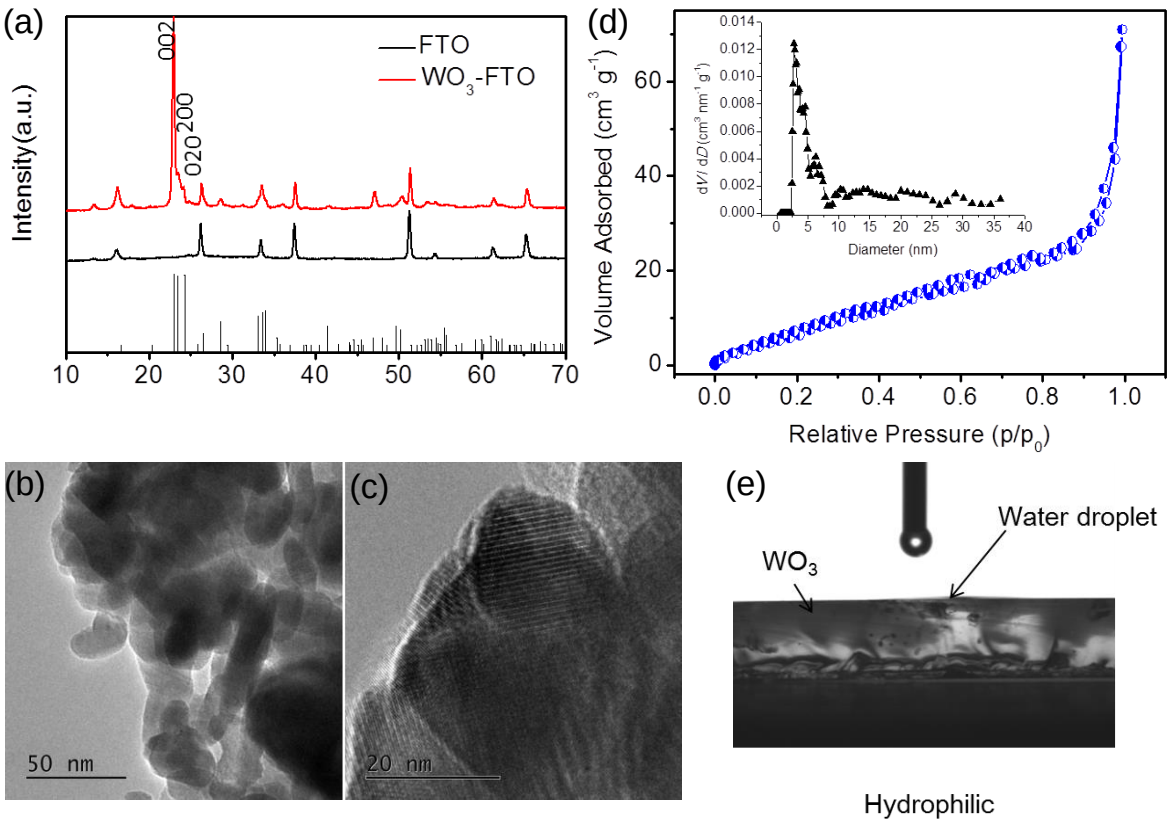

Figure 6.2 (a) X-ray diffraction patterns of the FTO substrate (black) and the mesoporous WO_3 film on FTO substrate (red). (Crystal phase: Orthohombic; ICSD code: #01-089-4477) (b and c) High-resolution TEM images of mesoporous WO_3 film (d) N_2 adsorption–desorption isotherms of mesoporous WO_3. Inset is the diameter distribution of pores. (e) Contact angle measurement of the mesoporous WO_3 substrate. The contact angle close to 0 ºindicates the hydrophilic nature of the WO_3 surface, beneficial for water oxidation.

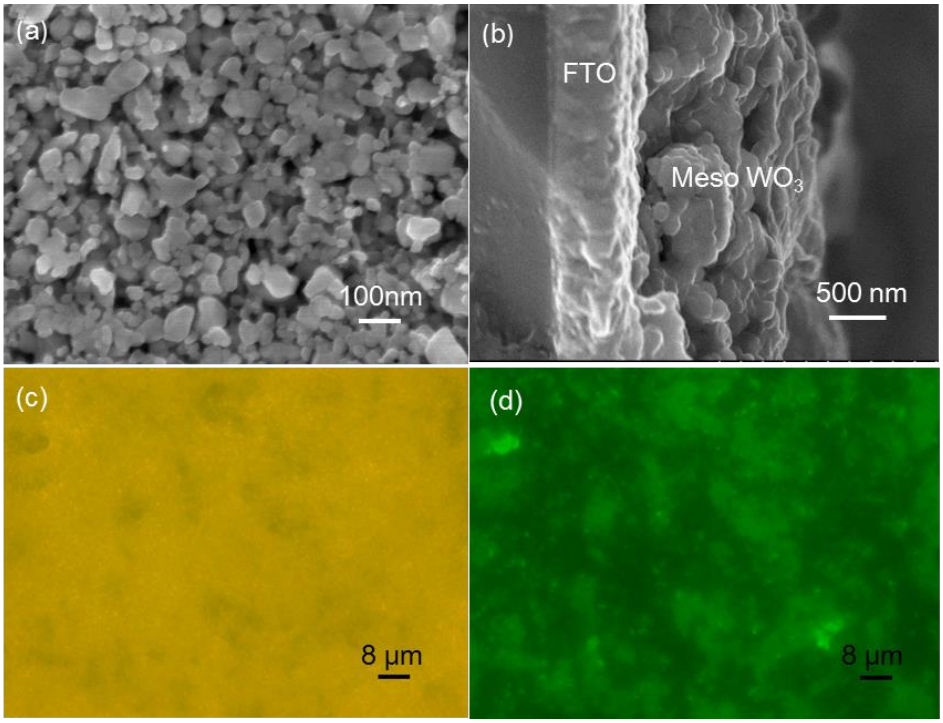

Figure 6.3 SEM images of the mesoporous WO_3 film on FTO substrate: (a) top view (b) side view; optical microscopic bright-filed (c) and fluorescence intensity images (d) of the PS II| meso WO_3 on FTO substrate.

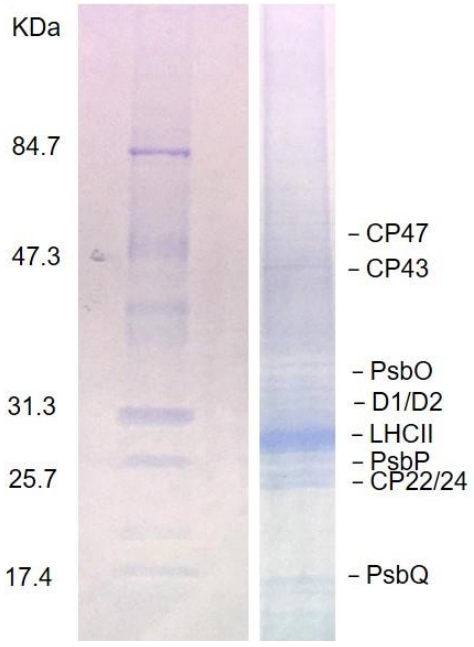

Figure 6.4 SDS-PAGE patterns of PS II by electrophoresis

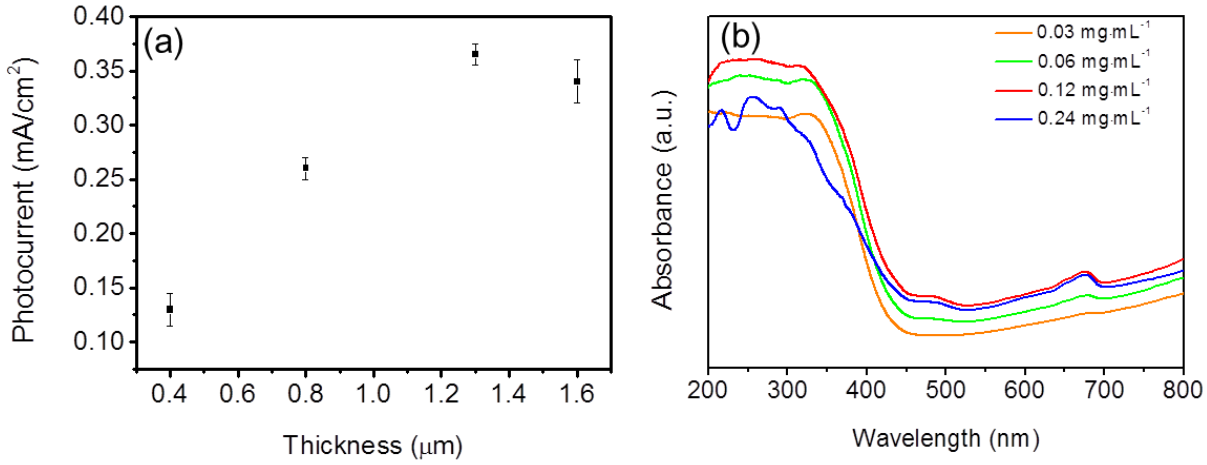

Figure 6.5 Optimization of the electrode: (a) the photocurrent densities of bare WO_3 substrate with repect to the thickness (b) the UV-Vis spectra of the hybrid PS II| WO_3 electrode after immersion in different Chl *a* concentration of the diluted PS II solution

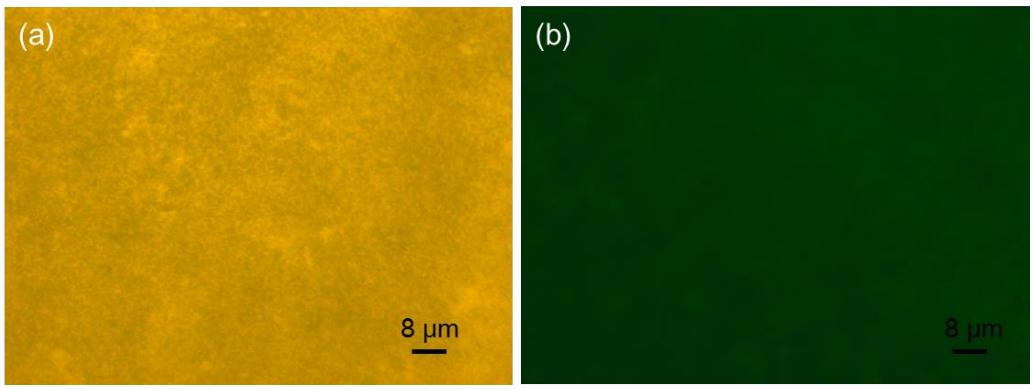

Figure 6.6 Bright-field (a) and the corresponding fluorescence intensity image (b) (excitation wavelength: 480 nm) of mesoporous WO_3 on FTO under optical microscope

Table 6.1 The semi-quantification results of WO_3 and PS II-WO_3 photoelectrode

electrode	**Composition ratio of each element (Atomic %)**						
	C	O	Sn	W	N	S	P
WO_3	8.21	73.11	4.46	15.36	0	0	0
PS II-WO_3	25.81	57.06	3.59	12.37	0.84	0.13	0.42

6.3.2 PEC performance of the PS II| meso WO_3 photoelectrode

The photoelectrochemical activity was evaluated starting from the open circuit potential (OCP) without mediators. After the electrodes immersed into the electrolyte buffer and reached to equilibrium, the OCP of PSII, unmodified and PS II| meso WO_3 electrodes stabilized at −0.10 V,− 0.037 V and − 0.080 V, respectively. As the OCP is related to the mixed potentials of a variety of redox components in electrode, PS II evolvement indeed caused a decrease of OCP of the WO_3 substrate, in agreement with the reported decrease [24] as the individual components of the PS II protein range from −1.3 V to 1.0 V.[44] Upon illumination of the AM 1.5 G simulator, an obvious variation was observed on OCP of the composite PS II| meso WO_3 which eventually stabilized at 0.204 V. As high as 212 mV photovoltage was achieved over the PSII| meso electrode, indicating the high photoelectrochemical activity of the hybrid electrode.

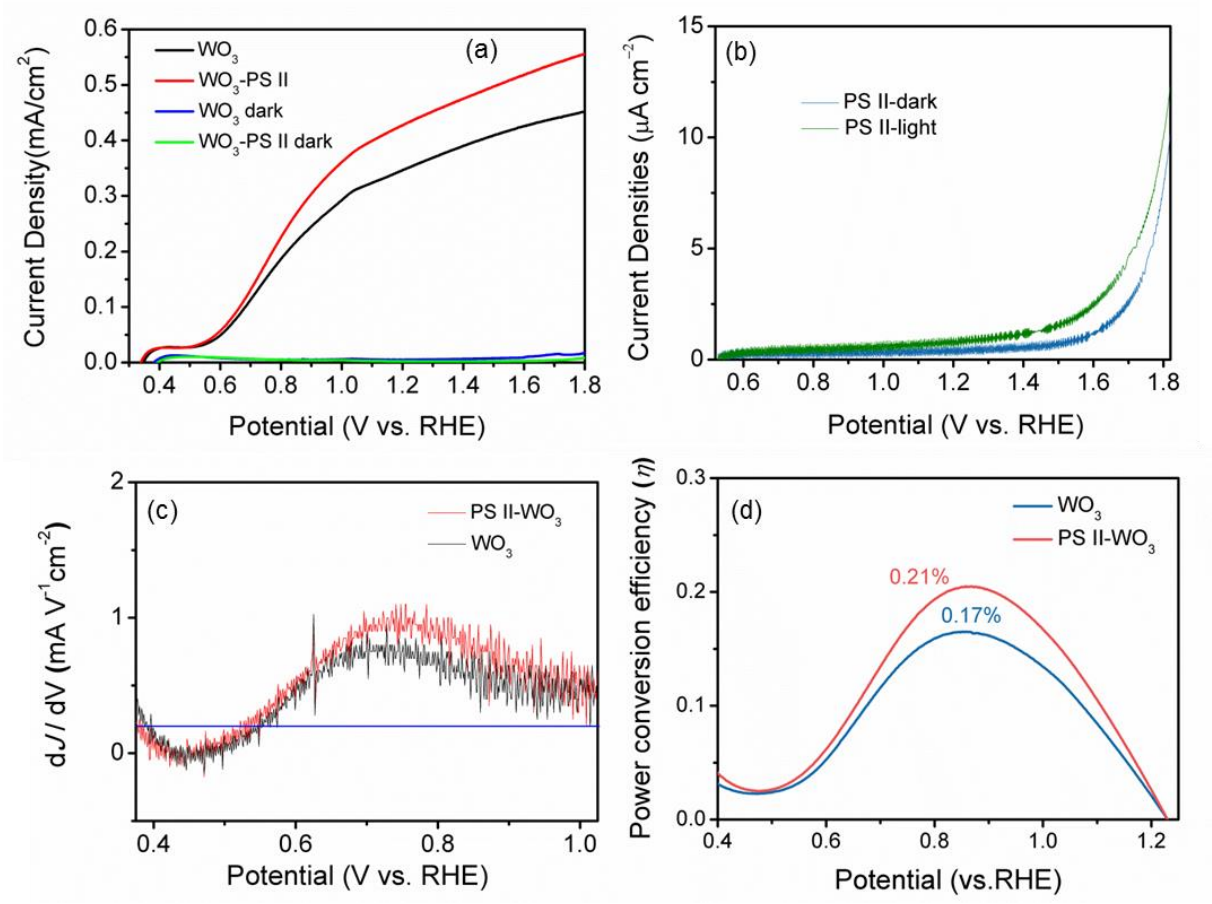

Figure 6.7 (a) Linear sweep voltammetry (LSV) curves of the WO_3 film as prepared and after PS II modification in the dark and under AM 1.5 G simulator irradiation (b) LSV curves of PS II on FTO substrate in the dark and under AM 1.5 G simulator irradiation (c) First-order derivative of the photocurrent densities as a function of voltage. Onset potential is defined as the value where $dJ/dV > 0.2$ mA cm^{-2} V^{-1} (d) Half-cell power conversion efficiencies calculated from LSV curves of WO_3 and PS II| meso WO_3 photoelectrodes.

Photoelectrochemical performances of the as-prepared hybrid PS II| meso WO_3 were first measured by linear sweep voltammetry (LSV) in the Figure 6.7. LSV curves in Figure 6.7a clearly show an enhancement of photocurrent density of the WO_3 electrode with PS II modification. The photocurrent density of the bio-hybrid photoelectrode is higher than that of either WO_3 electrode (Figure 6.7a) or PS II electrode (Figure 6.7b). The onset potential of the hybrid electrode is defined according to the formalism proposed by Grätzel.[45, 47] The deferential curve of the current-potential curve was obtained and the onset potential was the potential where dJ/dV attained a value of 0.20 mA cm^{-2} V^{-1} which were 533 mV and 551 mV of the PS II-modified and unmodified WO_3 electrode in this work (Figure 6.7c). Compared with the pristine WO_3, the onset potential was negatively shifted about 18 mV, suggesting the overpotential of water oxidation over WO_3 was decreased after hybridizing with PS II. According to the LSV curves, we also calculated the half-cell power conversion efficiency (PCE) of the PS II-modified WO_3 photoelectrode, which can reach 0.21 % as seen in Figure 6.7d. The potentiostatic polarization was evaluated at a constant anode potential of 1.23 V vs. RHE during light on-light off cycles under manually chopped AM 1.5 G simulator in a three-electrode system with a Pt counter and SCE reference electrode. We first tested the amperometric *I*-t curve under AM 1.5 G without any cutoff filter to simulate the performance under sunlight. The photocurrent density varied from 0.36 mA cm^{-2} to 0.45 mA cm^{-2} after modification during the light on-off cycles (see Figure 6.8a), showing a pronounced anodic photocurrent enhancement up to 0.09 mA cm^{-2} among PS II-based bio-photoelectrochemical conversion systems. The PSII| meso WO_3 hybrid

electrode performance was found to depend on the light wavelength. Amperometric *I*-t curve measured in Figure 6.8b shows a photocurrent of 0.07 mA cm^{-2} under incident light with wavelength longer than 420 nm, exhibiting a 16 % increase than that of the pristine WO_3 photoanode. An obvious and reproducible photocurrent of 0.17 μA cm^{-2} was observed on interval illumination with wavelength longer than 580 nm (Figure 6.8c), while no obvious photocurrent was observed over PS II-free WO_3 electrode and only 0.05 μA cm^{-2} over the pure PS II photoelectrode under the same incident light (See Figure 6.8d), which strongly suggests the photocurrent in the red region was dominated by PS II and enhanced by WO_3. Furthermore, based on the *I*-t curves measured under monochromatic illumination in the red irradiance region (Figure 6.9), we figured the action spectrum as shown in Figure 6.10a. The photocurrent action spectrum in this region almost overlays the PS II absorption spectrum, also confirming that PS II does make contribution to the photoactivity of the composite electrode in the red region. Monochromatic incident photon-to-current conversion efficiency (IPCE) value of the as-prepared PS II| meso WO_3 electrode was measured in the same electrolyte buffer which was displayed in Figure 6.10b. The maximum IPCE of PS II| meso WO_3 electrode reaches 15.24% at 400 nm in the visible light region and 2.74 % at 640 nm in red light region, both higher than the IPCE of WO_3 electrode. Therefore, the hybrid PSII| meso WO_3 electrode is an effective working electrode whether under visible light or solar light, even extending its application in red region.

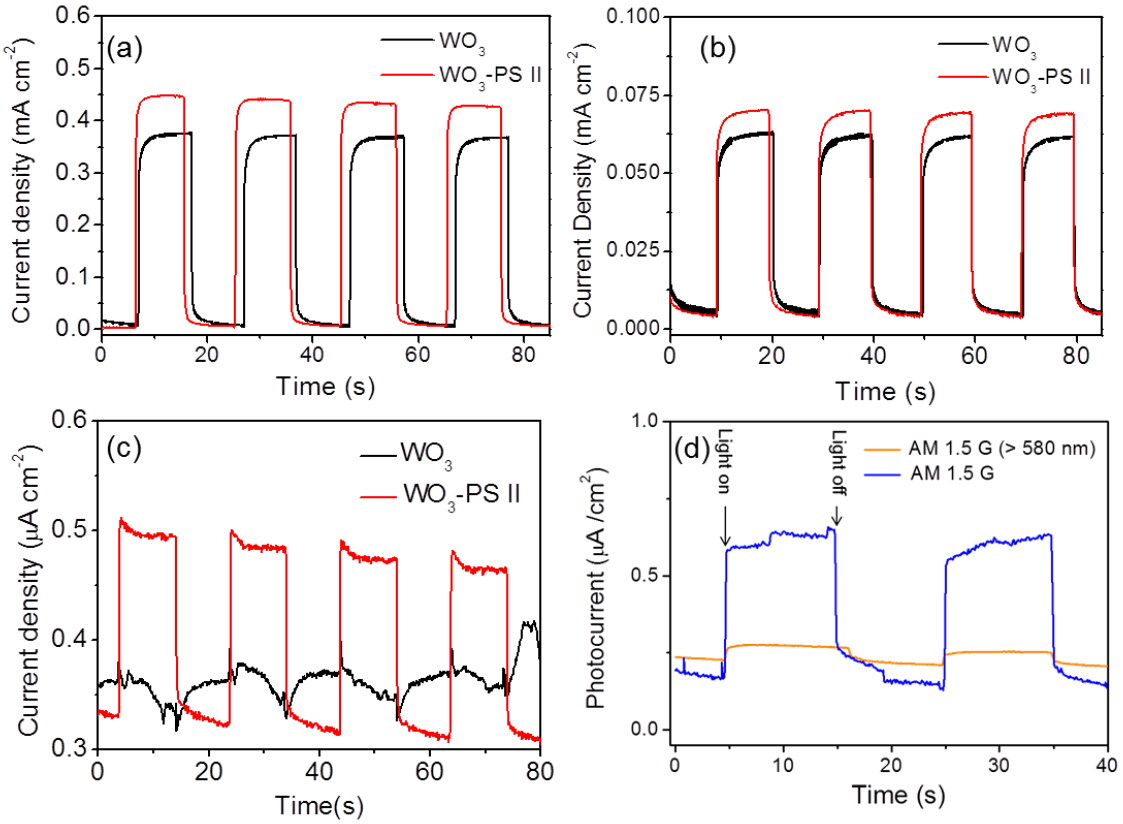

Figure 6.8 Photocurrent densities of the unmodified and PS II-modified WO_3 electrode at a fixed potential of 1.23 V vs. RHE under chopped light from AM 1.5 G lamp (a) without cutoff (b) with cutoff filter of 420 nm and (c) with cutoff filter of 580 nm (d) Photocurrent densities of PS II individually on FTO under different irradiation.

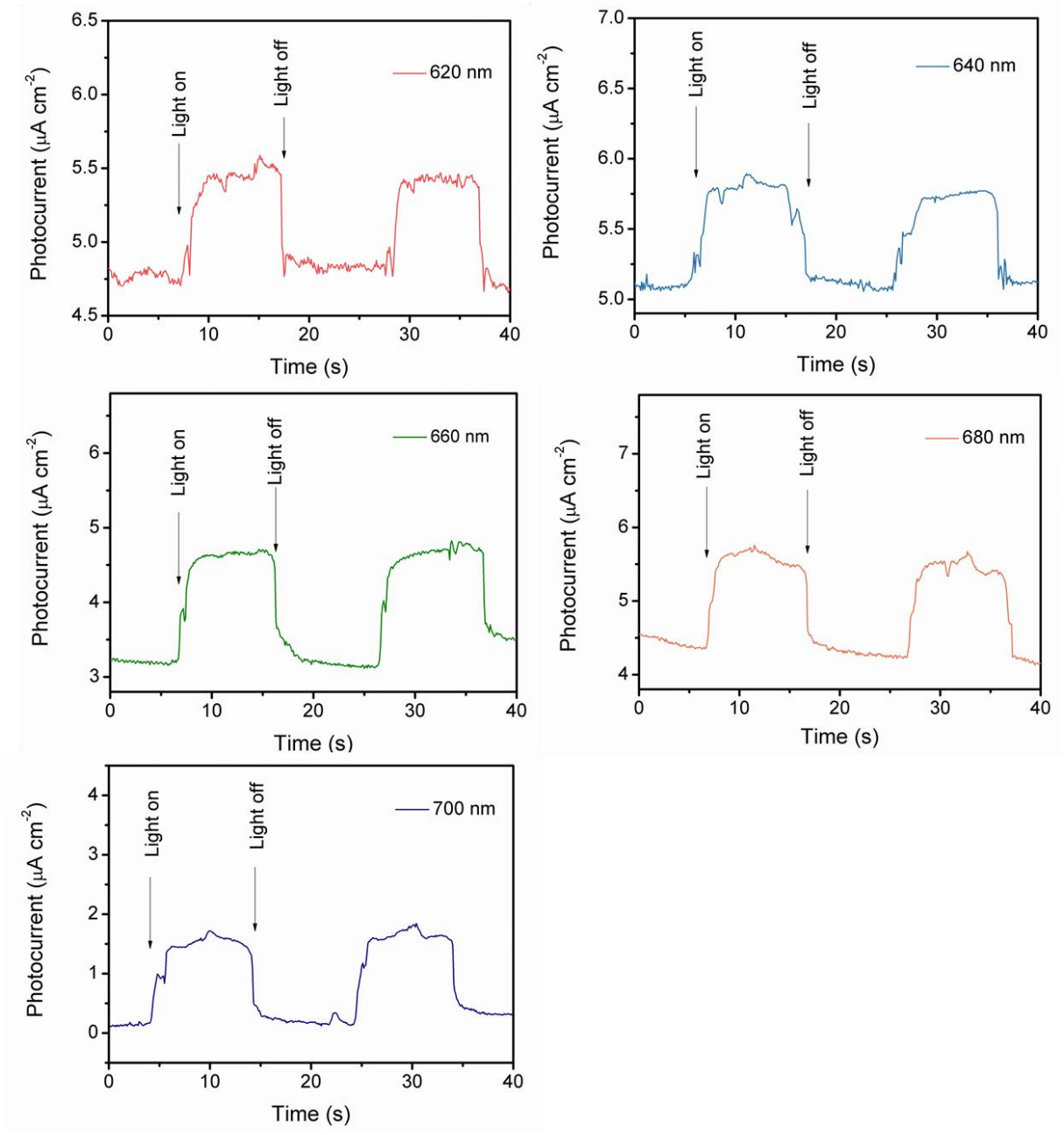

Figure 6.9 *I*-t curves under different monochromatic wavelength irradiation corresponding to the photocurrent action spectrum: (a) 620 nm (b) 640 nm (c) 660 nm (d) 680 nm (e) 700 nm

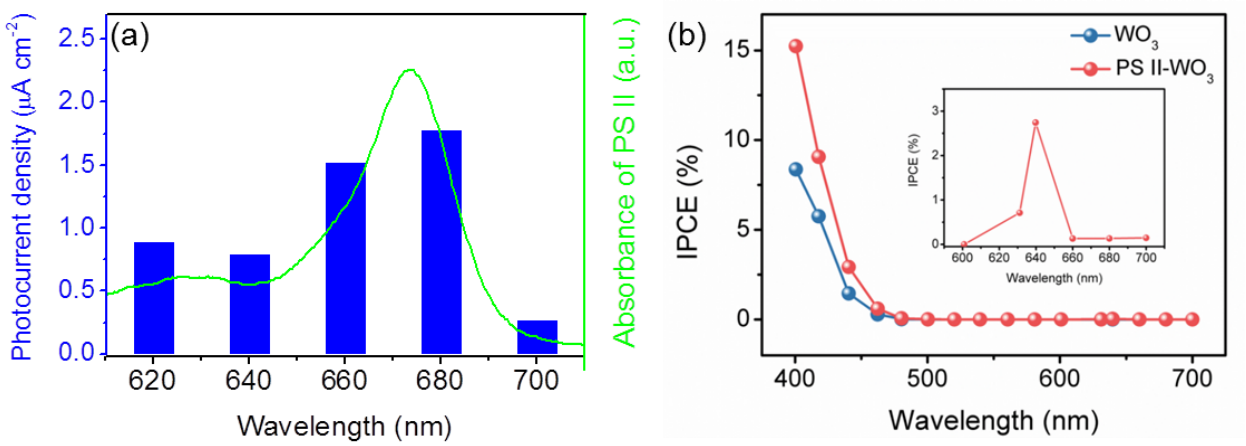

Figure 6.10 (a) Photocurrent action spectrum of the PS II| meso WO_3 film electrode in the red region from 620 nm to 700 nm (b) IPCE curves of the PS II| meso WO_3 and WO_3 photoelectrode at 1.23 V vs. RHE. Inset is the amplified curve of the 600-700 nm range.

In the stability test, a drastic reduction of the photocurrent was seen over the electrode of PS II directly tethered on the FTO substrate under continuous illumination (Figure 6.11), mainly arising from the slow kinetics of electron transfer and the accumulation of superoxide radicals that leads to deactivation of proteins under lasting light exposure, an inherent disadvantage of the natural organs in plants or other biological systems. However, only a slight decrease of the amplitude of photocurrent densities was observed from the cycled *I*-t curve (Figure 6.12a) over the PSII-modified WO_3 electrode. This is attributed to the faster electrons transfer rate when PS II was combined with a semiconductor electrode and hence free from the accumulation of the radicals.

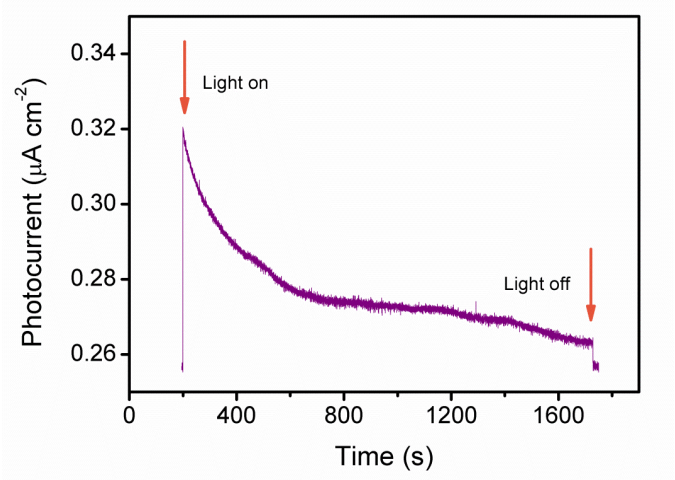

Figure 6.11 Photocurrent stability of PS II tethered onto FTO directly under continuous light irradiation of AM1.5 G at 1.23 V vs. RHE.

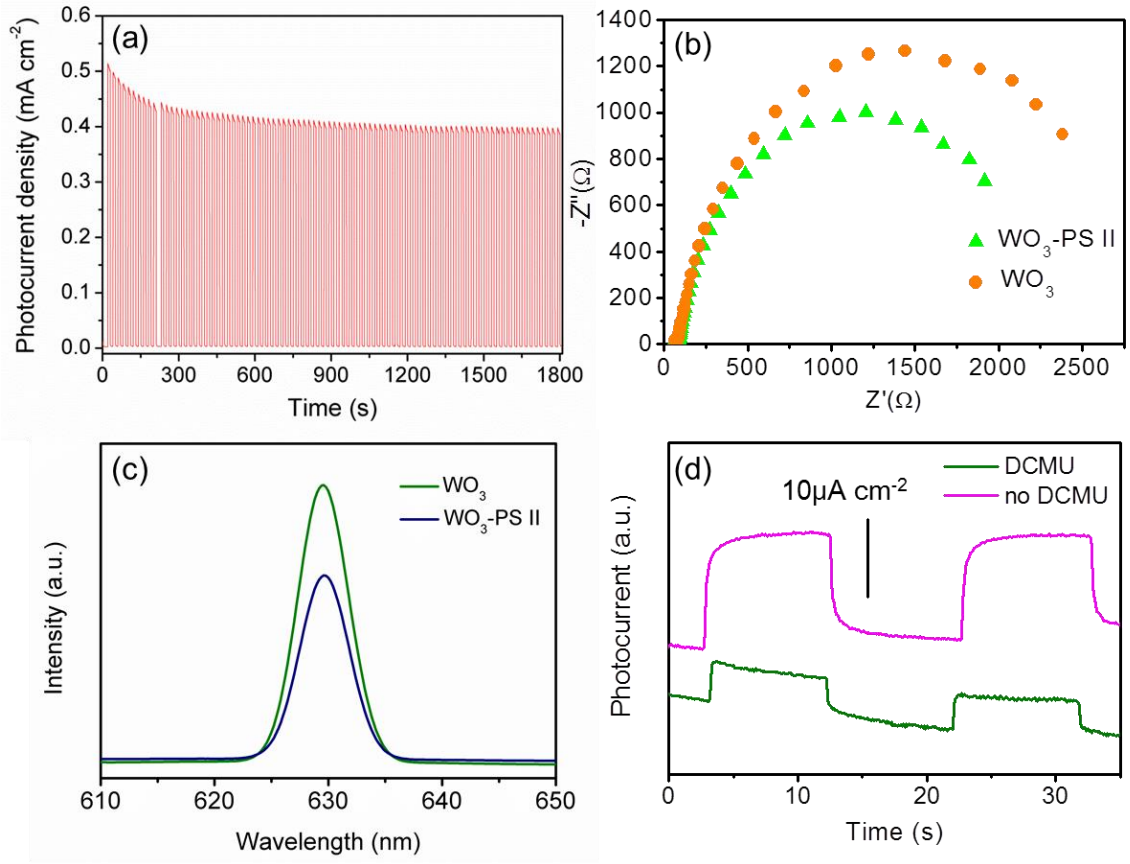

Figure 6.12 (a) Photocurrent stability of the PS II-modified WO_3 electrode under continuous irradiation of AM1.5 G at 1.23 V vs. RHE (b) Nyquist plots (-Z″ vs. Z′) for unmodified and PS II-modified WO_3

electrode under light conditions (c) Photoluminescence (PL) spectra of the PS II-modified WO_3 photoanode (purple) and the pure WO_3 photoanode (green) (Excitation: 400 nm) (d) Comparison of the photocurrent response of unexposed and DCMU exposed PS II-modified WO_3.

The electrochemical impedance spectroscopy (EIS) was measured under light to clarify the electron transfer resistance on photocurrent generation. Figure 6.12b shows the fitted Nyquist plots of the AC impedance data of the unmodified and PS II-modified WO_3 electrodes at the applied potential of 1.12 vs. RHE. The smaller diameter of the EIS spectrum of the PS II-modified WO_3 electrode means the resistance between the composite electrode/electrolyte interface is smaller than WO_3/electrolyte interface. With the PS II modification, the charge transfer barriers were decreased at the electrode surface. Figure 6.13 is the fitted equivalent electrical circuit from the Nyquist plots. Rs means resistance of the electrolyte between working electrode and reference; CPE1 can be envisaged as the capacitor between PS II and WO_3, R_t is the resistance between PSII and WO_3, Z_w means the Warburg resistance resulted from the mass transport of the electron mediators at the interface between PS II and WO_3; CPE2 is the capacitor between PS II| meso WO_3 electrode and electrolyte, R_{ct} is the charge transfer impedance in the composite electrode. Although there was no obvious diffusion limitation in both system and no bio-inorganic interface on pure WO_3 electrode, Z_w and R_t are included to ensure the perfect fit of the electrical circuit. The fitted Nyquist plots ($-Z''$ vs. Z') exhibit a clear decrease of the impedance on hybrid electrode under illumination, in agreement with the fitted values of R_{ct} were 2155 Ω and 2001 Ω for unmodified and PS II-modified WO_3 in the absence of mediators. Meantime, R_t increase on the PS II| meso WO_3 electrode with a new interface between PS II and WO_3 produced.

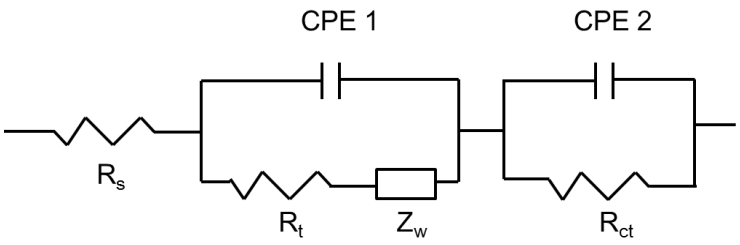

Figure 6.13 Equivalent electrical circuit of the Nyquist plots in impedance measurements.

In order to investigate the electron transfer process of the PS II| meso electrode, we first observed the photoluminescence (PL) quenching effect by PS II. From Figure 6.12c, we can observe that the intensity of intrinsic PL peak of WO_3 at 620-640 nm is decreased over the PS II| meso WO_3 bio-hybrid in contrast with that of the pure WO_3, suggesting PS II modification supressed the recombination of photogenerated charge carriers by extracting the holes from WO_3.[47] Secondly, 3′-(3,4-dichlorophenyl)-1,1′-dimethylurea (DCMU), a widely utilized herbicide to interrupt the electron flow pathways by specifically blocking the Quinone B (Q_B) site at the terminal of PS II, was engaged to observe the vibration of the anodic photocurrent under wavelength larger than 580 nm. As shown in Figure 6.12d, potentiostatic test under 1.23 V vs. RHE and the corresponding *I*-t curve suggests the photocurrent reduced from 0.17 μA to 0.04 μA after the addition of a plethora of DCMU in the electrolyte. The severe decrease was caused by the inhibition effect of DCMU on the Q_B sites of PS II, indicating the majority of electrons transfer from the Q_B sites of PS II to the electrode, dominating the direct electron transfer from PS II to WO_3 electrode. The small residual photocurrent was still observed after the addition of DCMU. The phenomenon was also reported by Kato *et al* and Katharina *et al* on meso ITO and TiO_2 respectively, which was attributed to the direct electron transfer from Q_A sites to the metal oxide electrode surface. [26, 31]

In the dye-molecule optoelectronic system, it was suggested a driving force (ΔG) of at least −0.2 eV for effective injection of the electrons from the excited states to the conduction band of a semiconductor.[48] It was reported the reduction potential of Q_A/ $Q_A^{-\bullet}$ and Q_B/ $Q_B^{-\bullet}$ were previously determined to be −60 mV and −140 mV vs. NHE.[49] We calculated the flatband potential (E_{fb}) of the pristine WO_3 from the Mott–Schottky configuration (in the Figure 6.14a) of the WO_3 electrode at frequency of 500 Hz, 1000 Hz and 1500 Hz. The flat band potential was estimated at 0.36 V vs. NHE (pH=6.5). Combined with the XPS Valence Band (VB) spectrum in the Figure 6.14b and UV-Vis spectrum (Figure 6.1b) of the as-prepared WO_3, the potentials of the bottom of the conduction band and the top of the valence band was located at 0.22 V vs. NHE and 3.02 V vs. NHE at this circumstance (Figure 6.14c). For n-type WO_3, the Fermi level lies deeply within the band gap near the bottom of the conduction band and far below

the reduction potential of Q_B in PS II. Given this values, the electron injection from the Q_A and Q_B sites of the PS II to WO_3 electrode is energetically favorable. As for the increase of the photocurrent under red light region where WO_3 exhibit no photoresponse, it can be explained from the morphology and quality of the WO_3 electrode substrate. WO_3 porous morphology allows for a higher coverage and comparable conductivity with FTO. The rate-limiting step of the protein-bound metal oxide electrode usually exists in the slow transfer of electrons through the metal oxide layer. In the present work, however, the resulting film of the tungsten oxide layer calcined at 500 ℃ on the FTO substrate had a resistance of 7.7 ± 1.3 kΩ sq^{-1}, comparable to that of the mesoporous ITO susbstrate, which increased the conductivity and promoted the electron transfer reflux for photocurrent generation, making WO_3 a favourable support compared with other water oxidizing metal oxide like TiO_2 or Fe_2O_3.[29, 30] According to the analysis above, the energy diagram and the electron transfer pathway was proposed as the cascade in scheme 6.1. Once under light irradiation, excited state of P680 chromophore ($P680^*$) takes place in the PS II dimer, which generate primary impetus to donate holes to Tyr_z and electrons to Pheophytins (Phe_{D1}) then to the two plastoquinone (Q_A and Q_B) for the subsequent injection to the conduction band of WO_3 while the holes are initiated to migrate from Tyr^+ towards the manganese-calcium (Mn_4Ca) clusters for water oxidation. Taken together, WO_3 serves as an excellent electron acceptor in the bio-hybrid photoanode.

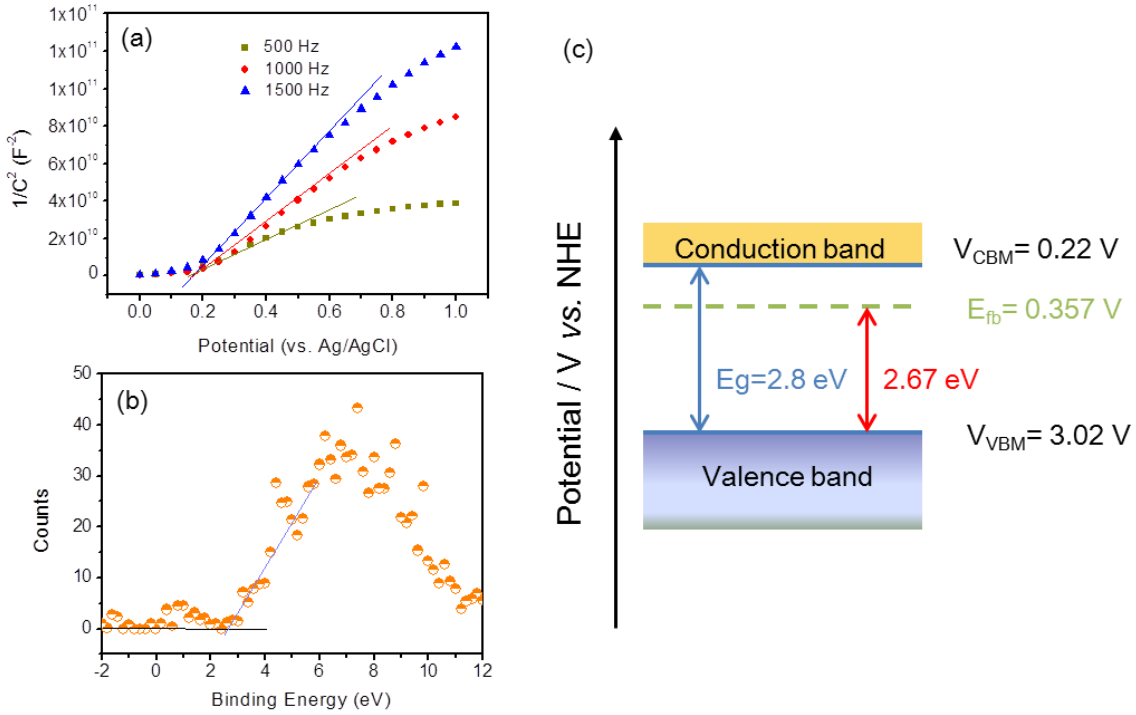

Figure 6.14 (a) Mott-Schottky curves of pristine WO_3 electrode at three frequencies of 500 Hz, 1000 Hz and 1500 Hz measured in 0.5 M Na_2SO_4 solution (b) XPS valence band spectrum of pristine WO_3 (c) Schematic band diagram of the pristine WO_3 at pH=0.

6.4 Conclusion

In conclusion, a photo-responsive semiconductor, WO_3 photoanode, was first assembled with PS II. Mesoporous structure of WO_3 that allows for the high protein coverage and direct electron transfer from PS II to WO_3 was introduced to amplify the PS II-based photoelectrode's solar water oxidation activity. Significant enhancement of the photocurrent and IPCE over PSII| meso WO_3| FTO with respect to WO_3| FTO and PS II| FTO were observed. The mesoporous WO_3 photoanode serves as an excellent support for immobilizing the biological catalysts for photoelectrochemical water splitting applications. This work demonstrated that co-assembly with highly efficient solar-responsive semiconductor may provide an effective approach to bring biology to photosynthetic conversion system, broadening the scope of support

for enzymes from thermodynamic and kinetic perspectives. Using band engineering to flexibly control the band structure of the light-responsive semiconductors and the interface of two components for the protein-based electrode is another superiority of such bio-hybrid electrode that may allow for more effective electron commuting between PS II and electrodes, which is another topic and target in the next stage of the application of the native photosynthetic biocatalysts.

References

[1] N. S. Lewis, D. G. Nocera, Proc. Natl. Acad. Sci., 103 (2006) 15729.

[2] D. Kim, K. K. Sakimoto, D. Hong, P. Yang, Angew. Chem. Int. Ed., 54 (2015) 3259.

[3] P. Kuang, L. Zhang, B. Cheng, J. Yu, Appl. Catal. B- Environ., 218 (2017) 570.

[4] A. Fujishima, K. Honda, Nature, 238 (1972) 37.

[5] H. Tong, S. Ouyang, Y. Bi, N. Umezawa, M. Oshikiri, J. Ye, Adv. Mater., 24 (2012) 229.

[6] A. Kudo, Y. Miseki, Chem. Soc. Rev., 38 (2009) 253.

[7] Z. Zou, J. Ye, K. Sayama, H. Arakawa, Nature, 414 (2001) 625.

[8] Y. Wei, X. Chang, T. Wang, C. Li, J. Gong, Small, 13 (2017) 1702007.

[9] Y. Wang, X. Liu, Z. Li, Y. Cao, Y. Li, X. Liu, S. Jia, Y. Zhao, Small, 13 (2017) 1700793.

[10] Y. Li, H. Zhang, P. Liu, D. Wang, Y. Li, H. Zhao, Small, 9 (2013) 3336.

[11] S. Wang, L. Yi, J. E. Halpert, X. Lai, Y. Liu, H. Cao, R. Yu, D. Wang, Y. Li, Small, 8 (2012) 265.

[12] K. K. Sakimoto, A. B. Wong, P. Yang, Science, 351 (2015) 74.

[13] C. Liu, J. J. Gallagher, K. K. Sakimoto, E. M. Nichols, C. J. Chang, M. C. Chang, P. Yang, Nano. Lett., 15 (2015) 3634.

[14] E. M. Nichols, J. J. Gallagher, C. Liu, Y. Su, J. Resasco, Y. Yu, Y. Sun, P. Yang, M. C. Y. Chang, C. J. Chang, Proc. Natl. Acad. Sci., 112 (2015) 11461.

[15] J. Qi, X. Lai, J. Wang, H. Tang, H. Ren, Y. Yang, Q. Jin, L. Zhang, R. Yu, G. Ma, Z. Su, H. Zhao, D. Wang, Chem. Soc. Rev., 44 (2015) 6749.

[16] H. Tang, C. M. Hessel, J. Wang, N. Yang, R. Yu, H. Zhao, D. Wang, Chem. Soc. Rev., 43 (2014) 4281.

[17] X. Lai, J. E. Halpert, D. Wang, Energy Environ. Sci., 5(2012) 5604.

[18] T. Hisatomi, J. Kubota, K. Domen, Chem. Soc. Rev., 43 (2014) 7520.

[19] M. Kato, J. Z. Zhang, N. Paul, E. Reisner, Chem. Soc. Rev., 43 (2014) 6485.

[20] Y. Umena, K. Kawakami, J.-R. Shen, N. Kamiya, Nature, 473 (2011) 55.

[21] R. E. Blankenship, D. M. Tiede, J. Barber, G. W. Brudvig, G. Fleming, M. Ghirardi, M. R. Gunner, W. Junge, D. M. Kramer, A. Melis, T. A. Moore, C. C. Moser, D. G. Nocera, A. J. Nozik, D. R. Ort, W. W. Parson, R. C. Prince, R. T. Sayre, Science, 332 (2011) 805.

[22] J. Maly, J. Masojidek, A. Masci, M. Ilie, E. Cianci, E. Foglietti, W. Vastarella, R. Pilloton, Biosens. Bioelectron., 21 (2005) 923.

[23] T. Noji, H. Suzuki, T. Gotoh, M. Iwai, M. Ikeuchi, T. Tomo, T. Noguchi, J Phys. Chem. Lett., 2 (2011) 2448.

[24] J. O. Calkins, Y. Umasankar, H. O'Neill, R. P. Ramasamy, Energy Environ. Sci. (6) 2013, 1891.

[25] H. A. Dewi, G. Sun, L. Zheng, S. Lim, Phys. Chem. Chem. Phys., (17) 2015, 3435.

[26] P. Cai, X. Feng, J. Fei, G. Li, J. Li, J. Huang, J. Li, Nanoscale,7 (2015) 10908.

[27] M. Kato, T. Cardona, A. W. Rutherford, E. Reisner, J. Am. Chem. Soc., 134 (2012) 8332.

[28] M. Kato, T. Cardona, A. W. Rutherford, E. Reisner, J. Am. Chem. Soc., 135 (2013) 10610.

[29] J. Li, X. Feng, J. Fei, P. Cai, J. Huang, J. Li, J. Mater. Chem. A, 4 (2016) 12197.

[30] W. Wang, Z. Wang, Q. Zhu, G. Han, C. Ding, J. Chen, J. R. Shen, C. Li, Chem. Commun., 51 (2015) 16952.

[31] K. Brinkert, F. Le Formal, X. Li, J. Durrant, A. W. Rutherford, A. Fantuzzi, Biochim. Biophys. Acta, 1857 (2016) 1497.

[32] S. Kavadiya, T. S. Chadha, H. Liu, V. B. Shah, R. E. Blankenship, P. Biswas, Nanoscale, 8 (2016) 868.

[33] H. Ma, J. Zhang, Z. Liu, Appl. Surf. Sci., 423 (2017) 63.

[34] J. Yu, H. Yu, H. Guo, M. Li, S. Mann, Small, 4 (2008) 87.

[35] J. Jin, J. Yu, D. Guo, C. Cui, W. Ho, Small, 11 (2015) 5262.

[36] H. Zhang, W. Zhou, Y. Yang, C. Cheng, Small, 13 (2017) 1603840.

[37] Y. M. Hunge, M. A. Mahadik, A. V. Moholkar, C. H. Bhosale, Appl. Surf. Sci., 420 (2017) 764.

[38] J. Zhou, S. Lin, Y. Chen, A. M. Gaskov, Appl. Surf. Sci., 403 (2017) 274.

[39] Y. Ma, Y. Jia, L. Wang, M. Yang, Y. Bi, Y. Qi, Appl. Surf. Sci., 390 (2016) 399.

[40] T. Shibamoto, Y. Kato, M. Sugiura, T. Watanabe, Biochemistry, 48 (2009) 10682.

[41] M. Zhong, T. Hisatomi, Y. Kuang, J. Zhao, M. Liu, A. Iwase, Q. Jia, H. Nishiyama, T. Minegishi, M. Nakabayashi, N. Shibata, R. Niishiro, C. Katayama, H. Shibano, M. Katayama, A. Kudo, T. Yamada, K. Domen, J. Am. Chem. Soc., 137 (2015) 5053.

[42] Q. Kang, J. Cao, Y. Zhang, L. Liu, H. Xu, J. Ye, J.Mater. Chem. A, 1 (2013) 5766.

[43] K. N. Ferreira, T. M. Iverson, K. Maghlaoui, J. Barber, S. Iwata, Science, 303 (2004) 1831.

[44] P. N. Bartlett, C. S. Toh, E. J. Calvo, V. Flexer, Modelling Biosensor Responses. In Bioelectrochemistry, John Wiley & Sons, Ltd: 2008; pp 267.

[45] Q. Yu, X. Meng, T. Wang, P. Li, J. Ye, Adv. Funct. Mater., 25 (2015) 2686.

[46] F. Le Formal, M. Grätzel, K. Sivula, Adv. Funct. Mater., 20 (2010) 1099.

[47] Y. Kim, D. Shin, W. J. Chang, H. L. Jang, C. W. Lee, H. Lee, K. T. Nam, Adv. Funct. Mater., 25 (2015) 2369.

[48] K. Kalyanasundaram, M. Grätzel, Coord. Chem. Rev., 177 (1998) 347.

[49] C. Santato, M. Odziemkowski, M. Ulmann, J. Augustynski, J. Am. Chem. Soc., 123 (2001) 10639.

Chapter 7 General Conclusion and Future Prospects

7.1 General conclusion

In this thesis, a systematic study was carried out on the half reactions of CO_2 reduction and water oxidation over "Photosystem I" and "Photosystem II", respectively for constructing artificial photosynthetic systems. Doping effect, surface vacancies and isolated co-catalyst were demonstrated of great significance on the photocatalytic CO_2 reduction activity over ZnS photocatalyst; their impacts are disclosed experimentally and theoretically, deepening the understanding of the CO_2 reduction pathways. Initial efforts were also paid on constructing *Photosystem II*| mesoporous WO_3 film as the other segment of the monoclinic artificial leaf. The detaild study could be concluded in the following parts.

1. Fabricating colloidal ZnS:Cu nanocrystal photocatalyst for highly efficient solar-light-powered CO_2 reduction

Colloidal Cu-doped ZnS (ZnS:Cu) nanocrystals were constructed in the aqueous solution and performed as an excellent visible-light-responsive photocatalyst. In the presence of $CdSO_4$, the ZnS:Cu obtained a remarkable quantum efficiency of 5.8 % at 420 nm with the optimal doping amount of 0.2 %. With surface area and large amount of sulfur vacancies, CO_2 was successfully photocatalytically converted into formic acid (HCOOH) over the ZnS:Cu nanocrystals in all-inorganic reactant environment under solar irradiation.

2. Probing the role of nickel dopant in aqueous colloidal ZnS nanocrystals for efficient solar-driven CO_2 reduction

A newly aqueous colloidal comprised of monodispersed Ni-doped ZnS (ZnS:Ni) nanocrystals were constructed as excellent visible-light-responsive photocatalysts for CO_2 reduction into formate. The wavelength-dependent apparent quantum yield (AQY) showed a significant contribution of Ni doping for

visible light absorption. A high selectivity (>95%) of HCOOH production and an AQY of 59.1% at 340 nm and 5.6 % at 420 nm were obtained over ZnS:Ni (0.1 %) colloidal nanocrystals modified by Cd^{2+}. The regulation of sulfur vacancies by Ni doping and their interplay on photocatalytic CO_2 reduction activity were presented and discussed. The abundant sulfur vacancies and extended visible light absorption of the constructed colloidal ZnS:Ni nanocrystals contribute to the prominent performance for CO_2RR; excessive doping of Ni does not guarantee an increase of photocatalytic CO_2RR due to a diminish of sulfur vacancy.

3. Zinc-cadmium exchange induced isolated sites for efficient photocatalytic CO_2 conversion in aqueous solution

The mechanism by which the colloidal ZnS nanocrystals loaded with Cd^{2+} induced a remarkable enhancement in the selective production of formate was investigated by spectroscopic observations and *ab initio* calculations. By clarifying the charge carrier dynamics associated with the electronic structures and free energy configurations of the CO_2 reduction pathways, it was found that the increased electron transfer rate due to the band offset and the facilitated kinetics by the cation exchange induced isolated Cd sites exposed on the surface contribute to the significant promotion of CO_2 conversion into formate.

4. Cation vacancy-initiated CO_2 photoactivation over the well- crystalline ZnS for efficient formate production

Zn vacancies (V_{Zn}) was proposed and created on the surface of well-crystalline ZnS as new active sites for CO_2 reduction while reserving the charge transport capability in the bulk. With no cocatalyst, the cation vacancy-rich ZnS acquired a high selectivity of formate production (> 85%). *In situ* attenuated total reflection-infrared (ATR-IR) spectroscopy and first-principle calculations were used to elucidate the pathways of CO_2 reduction and prove the surface V_{Zn} favorable by greatly lowering the barrier of the CO_2 reduction pathway and precluding the proton adsorption, clarifying the origin of the highly selective CO_2 reduction into formate in the presence of competitive hydrogen evolution reaction (HER).

5. Interfacing photosynthetic membrane protein with mesoporous WO_3 photoelectrode for solar water oxidation

A bio-hybrid photoanode of a photosynthetic membrane protein (*Photosystem II*, PS II) extracted from fresh *Spinach* was fabricated on mesoporous WO_3 film for water oxidation. The PS II could communicate with the WO_3 electrode in the absence of any soluble redox mediators and sacrificial reagent and extend the light absorption to 700 nm of the solar spectrum. The maximum incident photon-to-current conversion efficiency (IPCE) reached 15.24% at 400 nm in the visible light region. The bio-hybrid electrode generated a significantly enhanced photocurrent than the previously reported PS II-based photoanodes for solar water oxidation to potentially couple the CO_2 reduction and close the artificial carbon cycle. This work also provides some insights and possibilities into the assembly of the visible-light-responsive semiconductors and photosynthetic proteins for solar energy conversion system.

7.2 Future prospects

Although a great number of benchmark achievements have been accomplished in developing "Photosystems" ("Photosystem I" or "Photosystem II") towards artificial leaf, research either in the laboratories or in the industrial scale-up applications is still infant. There are many challenges, such as the low efficiency to utilizing the sunlight, instability of the catalysts and the catalytic activity, the high cost of materials as well as the unclear mechanism of the half reactions. In the future, sustainable and cost-effective photocatalysts for CO_2 reduction and water oxidation are still worth exploration and fabrication.

For the CO_2 reduction over ZnS, it still remains several questions to answer in the future. How the presence of the dopants alters the electronic structure of the defect states? What is the microscopic surface structure of the colloidal nanocrystals? What will happen if we use the ligand modulation to control the size of the colloidal nanocrystals and how the ligands play the synergetic effect with the reactant environment? All the questions are worth deep investigation as a key step to improve the photocatalytic properties of ZnS. In addition, except Cd, more cocatalysts are worth exploitation including the metals and the metal complex to expect a diversity of the products; other ion exchange possibilities are worth trial; more efficient catalysts with isolated sites are expected to synthesize through the approach. The cation vacancy-modulation method

could be extended to other materials with various nanostructures and morphologies. Higher carbonaceous products, for example, alcohols (methanol, ethanol, etc.) or alkenes (C_2H_6, C_3H_8, etc.) are expected to produce through the photocatalytic conversion.

Current studies on artificial photosynthesis are mainly focused on the half-reactions. As an ultimate goal of artificial photosynthesis, the standalone artificial leaf is worth constructing towards the sustainable overall process, devoid of sacrificial reagents and with solar energy as the sole input. The electrochemical efforts could be made over ZnS as the photocathode to couple with the *Photosystem II*- or semiconductor-based photoanodes to close the photosynthetic carbon cycle. Further, the non-bias photoelectrochemical cell are expected to realize the solar-powered CO_2 conversion and water oxidation simultaneously.

Acknowledgements

Most of my deep and sincere gratitude goes to my supervisor, Prof. Jinhua Ye for her constant support throughout my Ph.D stage. Her caring, understanding, encouragement and personal guidance support me to continue my Ph.D study every time I faced with difficulties. She is not only a mentor but also a virtue model of my future career. Thanks also have to go to my co-supervisors, Prof. Takuya Masuda and Prof. Kiyoharu Tadanaga. Their warm care and kind suggestions always remind me to keep an eye on the different aspects of research.

I would like to express my special thanks to Dr. Xianguang Meng, Dr. Peng Li, Dr. Kun Chang, Dr. Guigao Liu, Dr. Guixia Zhao, Dr. Huabin Zhang, Dr. Xiao Hai, Mr. Fumihiko Ichihara, Mr. Hui Song for their cooperation and advices. Thanks to all the members in Photocatalytic Materials Group in National Institute for Materials Science (NIMS) over the years: Dr. Kako Tetsuya, Dr. Qing Yu, Dr. Li Shi, Dr. Dong Hao, Dr. Arini Nuran, Dr. Zhou-jun Wang, Mr. Davin Philo, Mr. Gaoliang Yang, Ms. Samantha Kang, etc. for the fruitful discussion and happy time we stay together. My thanks also extend to Dr. Huiwen Lin, Dr. Jing Tang, Dr. Jie Li, Dr. Xianglan Li, Dr. Wipakorn Jewasuwan, Prof. Naoki Fukata, Mr. Toshiaki Takei, Mr. Hongwei Zhang, Prof. Yasuo Izumi for their assistance in experiment to complete my Ph.D course.

I also take this opportunity to express my sincere gratitude to NIMS for offering me the NIMS Junior Researcher fellowship and Hokkaido University for offering the Ph.D position.

Last but no means least, I must thank my parents for their selfless loves, support and encouragement throughout my life in Japan.

Publications & conferences

Publications

1. **Hong Pang**, Xianguang Meng, Hui Song, Wei Zhou, Gaoliang Yang, Hongwei Zhang, Yasuo Izumi, Toshiaki Takei, Wipakorn Jewasuwan, Naoki Fukata, and Jinhua Ye. Probing the role of nickel dopant in aqueous colloidal ZnS nanocrystals for efficient solar-driven CO_2 reduction, *Applied Catalysis B: Environmental* 2019, *244*, 1013-1020.

2. **Hong Pang**, Guixia Zhao, Guigao Liu, Huabin Zhang, Xiao Hai, Shengyao Wang, Hui Song, Jinhua Ye. Interfacing photosynthetic membrane protein with mesoporous WO_3 photoelectrode for solar water oxidation. *Small* 2018, *14*(19), 1800104.

3. **Hong Pang**, Takuya Masuda, Jinhua Ye. Semiconductor- based photoelectrochemical conversion of carbon dioxide: stepping towards artificial photosynthesis, *Chemistry–An Asian Journal* 2018, *2*(13), 127-142.

4. Xiao Hai, Kun Chang, **Hong Pang**, Mu Li, Peng Li, Huimin Liu, Li Shi, Jinhua Ye. Engineering the edges of MoS_2 (WS_2) crystals for direct exfoliation into monolayers in polar micromolecular solvents. *Journal of the American Chemical Society* 2016, *138*(45), 14962-14969.

5. Kun Chang, Xiao Hai, **Hong Pang**, Huabin Zhang, Li Shi, Guigao Liu, Guixia Zhao, Mu Li, Jinhua Ye. Targeted synthesis of 2H- and 1T- phase MoS_2 monolayers for catalytic hydrogen evolution. *Advanced Materials* 2016, *28*(45), 10033-10041.

6. Guigao Liu, Xianguang Meng, Huabin Zhang, Guixia Zhao, **Hong Pang**, Tao Wang, Peng Li, Tetsuya Kako, Jinhua Ye. Elemental boron for efficient carbon dioxide reduction under light irradiation, *Angewandte Chemie International Edition* 2017, *56(20)*, 5570-5574.

7. Shengyao Wang, Fumihiko Ichihara, **Hong Pang**, Hao Chen, Jinhua Ye. Nitrogen fixation reaction derived from nanostructured catalytic materials, *Advanced Functional Materials* 2018, *28*(50), 1803309.

8. Kun Chang, **Hong Pang**, Xiao Hai, Guixia Zhao, Huabin Zhang, Li Shi, Fumihiko Ichihara, Jinhua Ye. Ultra-small freestanding amorphous molybdenum sulfide colloidal nanodots for highly efficient photocatalytic hydrogen evolution reaction. *Applied Catalysis B: Environmental* 2018, *232*, 446-453.

9. Xianguang Meng, Guifu Zuo, Peixiao Zong, **Hong Pang**, Jian Ren, Xiongfeng Zeng, Shanshan Liu, Yi Shen, Wei Zhou, Jinhua Ye. A rapidly room-temperature-synthesized Cd/ZnS:Cu nanocrystal photocatalyst for highly efficient solar-light-powered CO_2 reduction, *Applied Catalysis B: Environmental* 2018, *237*, 68-73.

10. Guixia Zhao, **Hong Pang**, Guigao Liu, Peng Li, Huimin Liu, Huabin Zhang, Li Shi, Jinhua Ye. Co-porphyrin/carbon nitride hybrids for improved photocatalytic CO_2 reduction under visible light. *Applied Catalysis B: Environmental* 2017, *200*, 141-149.

11. Shengyao Wang, Xing Ding, Xuehao Zhang, **Hong Pang**, Xiao Hai, Guangming Zhan, Wei Zhou, Hui Song, Lizhi Zhang, Hao Chen, Jinhua Ye. In situ carbon homogeneous doping on ultrathin bismuth molybdate: a dual-purpose strategy for efficient molecular oxygen activation, *Advanced Functional Materials* 2017, *27(47),* doi.org/10.1002/adfm.201703923.

12. Xiao Hai, Wei Zhou, Shengyao Wang, **Hong Pang**, Kun Chang, Fumihiko Ichihara, Jinhua Ye. Rational design of freestanding MoS_2 monolayers for hydrogen evolution reaction, *Nano Energy* 2017, *39*, 409-417.

13. Guigao Liu, Guixia Zhao, Wei Zhou, Yanyu Liu, **Hong Pang**, Huabin Zhang, Dong Hao, Xianguang Meng, Peng Li, Tetsuya Kako, Jinhua Ye. In situ bond modulation of graphitic carbon nitride to construct p–n homojunctions for enhanced photocatalytic hydrogen production. *Advanced Functional Materials* 2016, *26*(37), 6822-6829.

14. Xiao Hai, Wei Zhou, Kun Chang, **Hong Pang**, Huimin Liu, Li Shi, Fumihiko Ichihara, Jinhua Ye. Engineering the crystallinity of MoS_2 monolayers for highly efficient solar hydrogen production, *Journal of Materials Chemistry A* 2017, *5*(18), 8591-8598.

15. Guixia Zhao, Guigao Liu, **Hong Pang**, Huimin Liu, Huabin Zhang, Kun Chang, Xianguang Meng, Xiangke Wang, Jinhua Ye. Improved photocatalytic H_2 evolution over g□carbon nitride with enhanced in- plane ordering.

Small 2016, *12*(44), 6160-6166.

16. Huabin Zhang, Zuju Ma, Guigao Liu, Li Shi, Jing Tang, **Hong Pang**, Kechen Wu, Toshiaki Takei, Jian Zhang, Yusuke Yamauchi, Jinhua Ye. Highly active nonprecious metal hydrogen evolution electrocatalyst: ultrafine molybdenum carbide nanoparticles embedded into a 3D nitrogen-implanted carbon matrix. *NPG Asia Materials* 2016, *8*(7), e293.

Conferences

1. **Hong Pang**, Xianguang Meng, Jinhua Ye: "Constructing zinc sulfide photocatalysts for carbon dioxide reduction" 24 回光触媒シンポジウム. (Nov. 2018, Tokyo, Japan).

2. **Hong Pang**, Xianguang Meng, Jinhua Ye: "Anion vacancy modulation of colloidal ZnS quantum dots by Ni incorporation for highly efficient solar-driven CO_2 reduction" 22nd International Conference on Photochemical Conversion and Storage of Solar Energy. (July-Aug. 2018, Hefei, China)

3. **Hong Pang**, Xianguang Meng, Hui Song, Jinhua Ye: "Constructing zinc sulfide photocatalysts for carbon dioxide reduction" Workshop on Emerging Nanoscience and Nanotechnology. (Jan. 2018, Tsukuba, Japan)

4. **Hong Pang**, Xianguang Meng, Hui Song, Jinhua Ye: "Constructing colloidal zinc sulfide photocatalysts for carbon dioxide reduction" MANA International Symposium 2018. (Mar. 2018, Tsukuba, Japan)

5. Guixia Zhao, **Hong Pang**, Guigao Liu, Peng Li, Huimi Liu, Huabin Zhang, Li Shi, Jinhua Ye: "Co-porphyrin/Carbon nitride hybrids for improved photocatalytic CO_2 reduction under visible light" IUMRS-ICA2016. (Oct. 2016, Qingdao, China)